UiT The Arctic University of Norway

The Faculty of Science and Technology - Department of Geosciences

Structurally controlled hydrothermal mineralization

A case study from Vanna island, northern Norway

Hanne-Kristin Paulsen

A dissertation for the degree of Philosophiae Doctor – December 2019

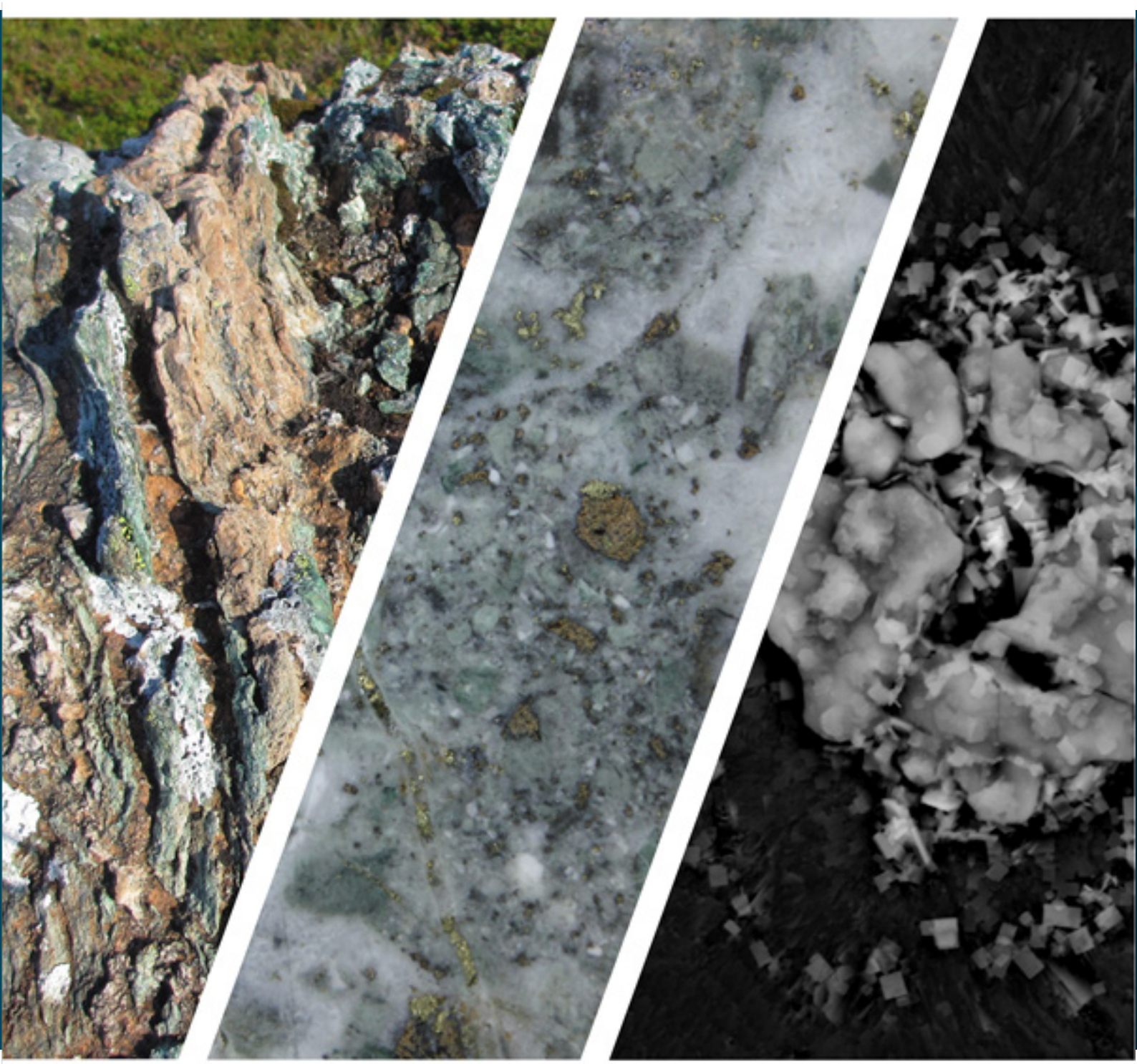

“Å eg veit meg eit land langt der oppe mot nord, med ei lysande strand
mellom høgfjell og fjord”
–Elias Blix

Abstract

The formation of mineral deposits is closely related to the tectonic setting in which they form. Structures create avenues of net permeability that allow ore-bearing fluids to transport and deposit mineralization. In a deeper crustal setting these structures can be ductile shear zones, while brittle faults and fractures are the dominant fluid pathways in the upper continental crust. The formation of local structures are strongly related to the regional tectonic setting. This work focusses on the metallogeny of Vanna, an island located in the northern part of the Archaean to Palaeoproterozoic West Troms Basement Complex. The complex is a part of the north-western margin of the Fennoscandian Shield, which is the most prolific mining area in Europe. Vanna has been subjected to a prolonged multiphased deformation history with several episodes of extension and compression. Paper I focusses on the geotectonic history of Vanna; normal faulting during the 2.2-2.4 Ga extension created rift basins that subsequently became inverted during the accretionary Svecofennian orogeny (c. 1.8-1.7 Ga), and possibly younger events. Inversion tectonics during crustal shortening resulted in the formation of low-grade fold and thrust belt structures in the basement rocks and metasedimentary cover sequence. This event also involved reactivation of the basin-bounding normal faults in the basement. Further, the youngest recorded tectonic event on Vanna is late-Paleozoic post-Caledonian extensional normal faults. This geological and structural framework outlined in Paper I forms the basis for understanding the metallogenic evolution of Vanna. Paper II and III each discuss a different style of hydrothermal mineralization. In paper II we show that emerald mineralization formed by hydrothermal fluids circulating in the Olkeeidet tectonic shear zone; a large, crustal scale dextral shear zone active during the contractile deformation that resulted in the formation of fold and thrust belt structures. Emerald mineralization is associated with extensive metasomatic alteration of the host rocks within the shear zone. This highly saline hydrothermal fluid likely originated as a magmatic fluid and strongly Na/K metasomatised the host rocks, and deposited quartz-tourmaline veins, dolomite and emerald. Emeralds were formed by Be sourced from the hydrothermal fluids, and Cr was likely sourced locally from chromite in an assumed metasedimentary unit. Paper III investigates hydrothermal Cu-Zn mineralization hosted by the Palaeozoic brittle Vannareid-Burøysund fault. Here, highly saline fluids composed of $CaCl_2$ and NaCl transported Cu and Zn as

chloride complexes using the brittle fault as a fluid conduit. The subsequent deposition of Zn in the form of sphalerite first, and Cu in the form of chalcopyrite second also shows that the fault progressively evolved and widened with time. Considered together, the three papers in this thesis show that mineralization on Vanna is structurally controlled, and the results can be used to discuss the mineralization potential and the key geological controls on mineralization more broadly.

Acknowledgements

First and foremost I would like to thank my two supervisors, Sabina Strmić Palinkaš and Steffen G Berg who have guided and supported me throughout these four years. Without your help, patience and inspiration I would never have made it this far. Thank you for allowing me to make mistakes, and for supporting me when trying to mend them. I am grateful for the opportunity to work with two scientists that each show passion and knowledge in each of your scientific fields. I have truly learned a lot from you.

I would like to thank my colleagues, who helped me develop and mature the work and my co-authors for scientific discussions and contributions to the papers. Paul Armitage - thanks for your company in the field and valuable discussions. In particular I am grateful to Siri Karlsen, Sofie Kolsum and Ida Rønningen for lively debates and constructive conversations. I would like to thank Trond Slagstad, Morgan Ganerød, and Asis Nasuti at NGU for Ar-Ar analyses and geophysics processing. Many thanks to Andrea Čobić for XRD analyses.

I would like to say thanks to the lab-staff - Trine, Karina, Ingvild and Matheus - for high-quality thin-sections, isotope analyses and help with SEM data. Kai - thanks for your enthusiasm and support with the SEM. Many thanks also goes to the administrative staff at IG, Matthias, John-Arne, Anders, Inger, Margrete, Cecilie and Andre - you always found time to offer a helping hand.

To my friends and fellow peers at IG, this could not have been accomplished without you. I would like to thank JB, Fredrik, Erland, Holger, Jiri, and Melanie for scientific discussions. To all the people whom I at one point have shared an office with - Harald, Yulia, Kai, Jack, Louise, Paul, Marina, and Stephan - thanks for listening when I inadvertently decided to explain something in great detail. In particular I would like to thank Carly Faber for patient proofreading and for always having time to explain the intricacies of metamorphic geology to me. Sina Marti - never stop asking those questions that seem so simple, but that in reality are the important ones. To Carly, Sina, Mariana, Calvin, Henry, Andrea, Lis and Torbjørn - what better way is there ponder the meaning of life than out and about climbing, hiking and skiing in the mountains. This journey

would have been way too bland without you.

Thanks to my big, loud and ever expanding family, mamma og pappa, Marianne, Britt, Sissel-Marie, Sven-Are, and Liza. To all of you - thank you for never letting me forget that there are new adventures waiting everywhere. All of your support, encouragement and love has been essential throughout this journey.

Figure 1: View of Vanna from the top of Vanntinden (1031 m.a.s.l.)

Preface

This thesis is the outcome of a 4-year PhD project starting in September 2015. The work was mainly funded by the UiT–The Arctic University of Norway, with additional financial support from Dynamics and Evolution of Earth and Planets (DEEP) at the University of Oslo. UiT The Arctic University of Norway is the degree-awarding institution. Associate professor Sabina Strmić Palinkaš and Professor Steffen G. Berg were my supervisors.

The PhD program requires that 25% of the four-year period is duty work. This was fulfilled through practical teaching of field courses, and assisting with exercises in general geology, mineralogy, structural geology, and regional geology. I also assisted MSc students with their thesis work and took part in outreach events including Forskningsdagene at UiT and UiO.

The following ECTS-accredited courses were completed as part of my PhD: Philosophy of science and ethics (UiT); Gold from bedrock to bullion: sustainable mining (University of Oulu); Communicating science: Scientific writing (UiT); Hydrothermal processes and mineral resources (University of Oulu); Solid Earth - fluid Earth interactions (DEEP PhD school at University of Oslo); Seafloor mineral resources and prospects of deep-sea mining: geological, environmental and technological challenges ahead (University of Bergen); and Deformation processes (UiT).

The thesis presented herein aims to discuss metallogeny of Vanna, an island located in the northern part of the West Troms Basement Complex in northern Norway. Fieldwork was carried out over four field seasons with the aim of understanding the structural and tectonic evolution of Vanna and its controls on hydrothermal mineralization.

This thesis consists of an introduction, a brief synthesis and three manuscripts. Parts of the work in this thesis has been presented at national and international conferences, and workshops.

The three papers are presented in this thesis are:

Paper I: Hanne-Kristin Paulsen, Steffen G. Bergh, Sabina Strmić Palinkaš, Siri Elén Karlsen, Sofie Kolsum, Ida U. Rønningen and Aziz Nasuti, **Fold-thrust structures and oblique faults on Vanna island, West Troms Basement Complex, and their relation to inverted metasedimentary sequences**, Manuscript

Paper II: Hanne-Kristin Paulsen, Steffen G. Bergh and Sabina Strmić Palinkaš **Hydrothermal emeralds: a shear zone hosted mineralization on Vanna Island, northern Norway** Manuscript

Paper III: Hanne-Kristin Paulsen, Steffen G. Bergh and Sabina Strmić Palinkaš . **Late Palaeozoic fault controlled hydrothermal Cu-Zn mineralization on Vanna Island, West Troms Basement Complex, northern Norway,** Manuscript submitted to Norwegian Journal of Geology

Conferences, workshops and meetings

2019 EGU General Assembly, Vienna Austria. PICO presentation

NGF Winter Meeting, Bergen Norway. Oral and poster presentation.

3rd general assembly Norwegian research school for Dynamics and Evolution of Earth and Planets, Sommarøy Norway. Poster presentation

2018 2nd general assembly Norwegian research school for Dynamics and Evolution of Earth and Planets, Bergen Norway. Poster presentation

AMGG annual meeting, Tromsø Norway. Oral presentation

Mineral Resources in the Arctic Workshop. Tromsø Norway. Oral presentation

2017 1st general assembly Norwegian research school for Dynamics and Evolution of Earth and Planets, Geilo Norway. Poster presentation

AMGG annual meeting, Tromsø Norway. Oral presentation

NGF Arctic days conference, Svolvær Norway. Oral presentation

Fennoscandian Exploration and Mining Conference. Levi Finland.

Geonor Conference. Mo i Rana Norway.

Broken Hill Deposit field trip. New South Wales Australia.

2016 32nd Nordic Geological Wintermeeting, Helsinki Finland. Poster presentation.

2015 Mineralklynge Norge workshop. Mo i Rana Norway.

Contents

List of Figures

1

Introduction

Ore deposits can form in a variety of geological and tectonic settings. However, their formation depend on the interaction between several key geological mechanisms. In particular, geological structures and mineral deposits are closely linked; for a significant ore-deposit to form, ore-forming fluids need to migrate though the crust in avenues of net permeability from its place of origin to a place where it can be deposited. This permeability can be faults, ductile shear zones, brittle fractures and fracture systems. The latter is particularly important as fluid pathways in the brittle upper continental crust (Gabrielsen and Braathen, 2014; Sibson et al., 1975). In addition to a fluid conduit, favourable physiochemical fluid properties are needed for transport and deposition of ore. The solubility, also expressed as the metal-bearing capacity of a fluid, is dependent on several factors. Fluid chemistry/salinity, temperature, pressure, pH and oxidation state all affect the fluid solubility to varying degrees. A fluid under favourable physiochemical conditions can therefore transport significant amounts of metal, and likewise deposit these metals in the solid state if the solubility decreases. The origin of such an ore-bearing fluid can be diverse; it can be magmatic, formed from metamorphic dehydration reactions or expulsion of pore fluids from compaction of sediments, or meteoric. A combination of one or more of these sources is also common. Regardless of origin, the fluid properties may also be modified by the interaction with host rock through which they migrate. Identifying these key geological mechanisms that results in the formation of ore deposits is essential to ensure continued supply of metals and minerals for further socio-economic development and for making the green shift.

Vanna island, with its excellent exposure and protracted geological history is an ideal place to investigate ore-forming processes. A suite of felsic and mafic intrusive rocks overlain by metasedimentary rocks have recorded a lengthy geotectonic history, from Archaean to late Palaeozoic, including multiple tectonic events of extension and compression. The island is located in the northern part of the West Troms Basement Complex, a basement horst interpreted to be the western continuation of the Archaean to Palaeoproterozoic Fennoscandian Shield - the most prolific mining district in Europe (Eilu, 2012).

On Vanna, two distinctly different mineral-occurrences are investigated, emerald mineralization at Olkeeidet and the Vannareid-Burøysund Cu-Zn occurrence. Detailed structural mapping done on each of these occurrences reveal a strong structural control, however they formed in different geotectonic settings; the former is hosted by a ductile shear zone formed in a contractile event that resulted in fold and thrust belt structures, while the latter is hosted by a brittle fault related to continental rifting. In addition, we analyse the hydrothermal ore-bearing fluid in each of these deposits by fluid inclusion investigations. Further, we indirectly investigate the fluid properties by analysing ore-minerals and minerals associated with hydrothermal fluid alteration by scanning electron microscope analyses, Raman spectroscopy, and X-ray diffraction. Although neither mineral occurrence currently has any economic value or exploitation potential, they do provide excellent examples of structurally controlled hydrothermal ore mineralization. By studying them in detail we gain not only information about how each of these occurrences formed but also where to search for new ore bodies.

1.1 Geological background

1.1.1 Northern Fennoscandian Shield

The Fennoscandian Shield is the largest exposed area of Archaean and Proterozoic rocks in Europe, and extends from the north-western part of Russia though Finland, Sweden and Norway (Fig. 1.1). The rocks get progressively younger towards the south-west. It is the most important metal mining district in Europe, and most known ore deposit types are present in this region. These ore deposits are distributed within several metallogenic areas, and their spatial and temporal distribution are related to different geotectonic events (Eilu et al., 2003; Eilu, 2012).

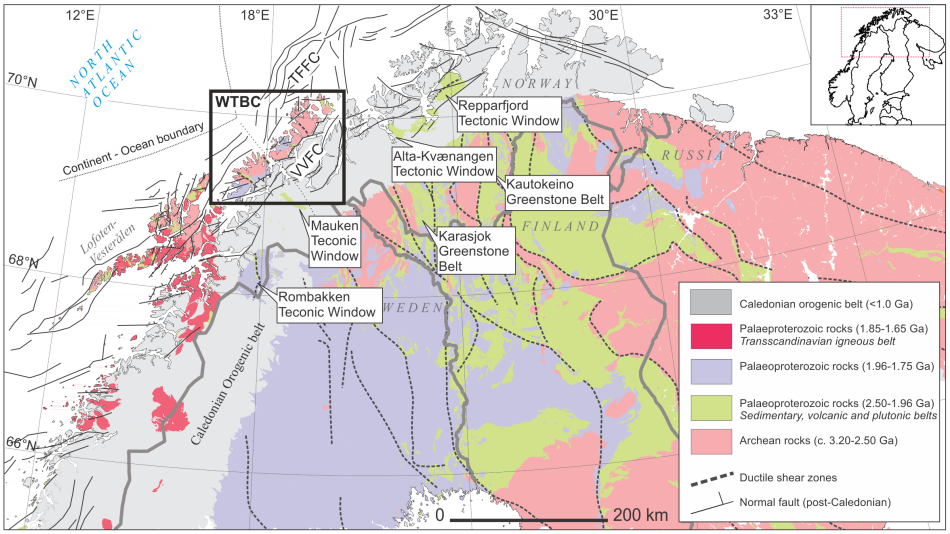

Figure 1.1: Northern Fennoscandian Shield after Koistinen et al., (2001). The West Troms Basement Complex is separated from the main Fennoscandian Shield by a c. 100 km wide section of Caledonian rocks. Post-Caledonian extensional faults are present along most of the North-Norwegian margin (Olesen et al., 2002; Indrevær et al., 2013; Davids et al., 2013; Koehl, 2013). TFFC - Troms-Finnmark Fault Complex, VVFC - Vestfjorden-Vanna Fault Complex

Archaean rocks are located in the northern and eastern part of the shield and are mainly partly migmatitic TTG-gneisses (tonalite, trondhjemite and granodiorite) and volcano-sedimentary supracrustal rocks deposited in rift-basins (Hölttä et al., 2008; Lahtinen et al., 2011). With the exception of banded iron formations like Bjørnevatn and Kostomuksha, the Archaean rocks are relatively unmineralized (Eilu, 2012).

The Archaean rocks are unconformably overlain by a number of **Palaeopro-**

terozoic sedimentary-volcanic successions and associated mafic sills and dikes ranging in age from c. 2505 to 1930 Ma, with a general decrease in age to the north-west (Hanski et al., 2001; Lahtinen et al., 2011; Eilu, 2012; Bingen et al., 2015). This tectonic rifting event in the Fennoscandian Shield has been correlated to a global record of Palaeoproterozoic breakup of an/several Archaean super-craton(s) (Bleeker, 2003).

The two main Palaeoproterozoic tectonic events in the Fennoscandian Shield are the **Lapland-Kola** (1.94-1.86 Ga) and the **Svecofennian** (1.92-1.79 Ga) orogenies. The Lapland-Kola event is a collisional belt containing both Archaean terrains, felsic granulites and juvenile Palaeoproterozoic crust (Daly et al., 2006). The Svecofennian Orogeny was the most important tectonic event in the Northern Fennoscandian Shield (Koistinen et al., 2001). It is an accretionary orogen that involved large-scale formation of new continental crust. Palaeoproterozoic passive margin sediments, juvenile arcs, and microcontinents were accreted on to the continent along an array of major north-west to north striking crustal scale shear zones which progressively developed across the Archaean and Palaeoproterozoic continents (Gaál and Gorbatschev, 1987; Nironen, 1997; Bark and Weihed, 2007; Angvik, 2014). This deformation was also the last major ductile event to shape the currently exposed penetrative structural grain of the rocks (Koistinen et al., 2001; Henderson et al., 2015). Emplacement of the Transscandinavian igneous batholith occurred along the south western margin of the Svecofennian protocraton (1.80-1.78 Ga) (Gaál and Gorbatschev, 1987; Högdahl et al., 2004). This NE to SW trending belt stretches from southern Sweden to Lofoten in Norway. It is composed of granitoid rocks with associated mafic intrusions.

The Svecofennian Orogeny is the most prolific metallogenic event in northern Fennoscandia (Weihed et al., 2005). It includes the formation of VMS deposits in intra-arc extensional settings prior to basin inversion. A number of economically important iron skarn-iron ores and Fe-apatite ores were also formed at this time, as well as porphyry copper and iron oxide copper gold (IOCG) deposits. Numerous orogenic gold deposits formed throughout the Proterozoic greenstone belts during syn- to post collisional stages (Eilu et al., 2003; Lahtinen et al., 2012).

In northern Norway, the Fennoscandian Shield with Palaeoproterozoic metasupracrustal belts is found as the Kautokeino and Karasjok Greenstone Belts, as basement windows exposed in the Caledonides - the Alta-Kvænangen, Repparfjord, Mauken, and Rombakken tectonic windows, and the West Troms Basement Complex horst exposed to the west of the Caledonian orogenic rocks (Fig. 1.1).

1.1.2 Caledonian orogenic rocks in northern Norway

In northern Scandinavia, Caledonian orogenic rocks are found in a c. 100 km wide belt mainly in eastern Norway and western Sweden (Fig. 1.2). The Caledonian Orogeny is a continent-continent collision between the continents Laurentia and Baltica that closed the Iapetus Ocean during the Ordovician and Silurian. Terrains that are exotic to Baltica were placed on top of a wedge of Neoproterozoic to early Palaeozoic passive margin sediments during the collision (Augland et al., 2014). This resulted in a nappe sequence of allochthons that are generally increasingly distal from the continental margin westward and upwards in the nappe-stack. These nappes cover large parts of northern Norway and the western part of Sweden, and the underlying Archaean and Proterozoic basement has been reworked to different degrees.

The Kalak Nappe Complex is the structurally lowest nappe, and it is separated from the basement by a thin Neoproterozoic to Cambrian autochthonous cover. It is comprised of Precambrian basement rocks and metapsammites with local mafic intrusive rocks. It also includes the Seiland igneous province - a large igneous province that intruded intracontinental rift zones prior to the opening of the Iapetus Ocean, around 610-550 Ma (Larsen et al., 2018). The Caledonian metamorphic grade increases upwards, with greenschist facies at its base and amphibolite facies metamorphism in the middle and upper units (Faber et al., 2019). The overlying Vaddas and Kåfjord Nappes are composed of high grade metasedimentary rocks with felsic and mafic intrusive rocks that records amphibolite to granulite facies metamorphism (Faber et al., 2019). A mylonitic high strain zone marks the boundary between the Kåfjord Nappe and the overlying Normannvik Nappe. The Normannvik Nappe is composed of migmatized garnet-mica schists and gneisses. A greenschist-facies shear zone marks the transition from the Nordmannvik Nappe to the overlying Lyngsfjell Nappe, which is composed of two distinctly different units; the Lyngen Magmatic Complex and the unconformably overlying Late Ordovician/Early Silurian Balsfjord Group. The Nakkedal and Tromsø Nappes are the stratigraphically uppermost nappes.

1.1.3 Collapse of the Caledonian orogenic rocks and opening of the Atlantic Ocean

During the collapse of the Caledonian orogeny, many of the nappe-bounding thrust faults were reactivated as normal faults. Continued extension and incipient rifting resulted in a series of NE-SE striking brittle normal faults in rhombic, zigzag-shaped fault trends that evolved to major fault zones like the Vestfjorden-Vanna fault complex and the Troms Finnmark fault complex. (Lippard and Prestvik, 1997; Olesen et al., 1997; Roberts and Lippard, 2005;

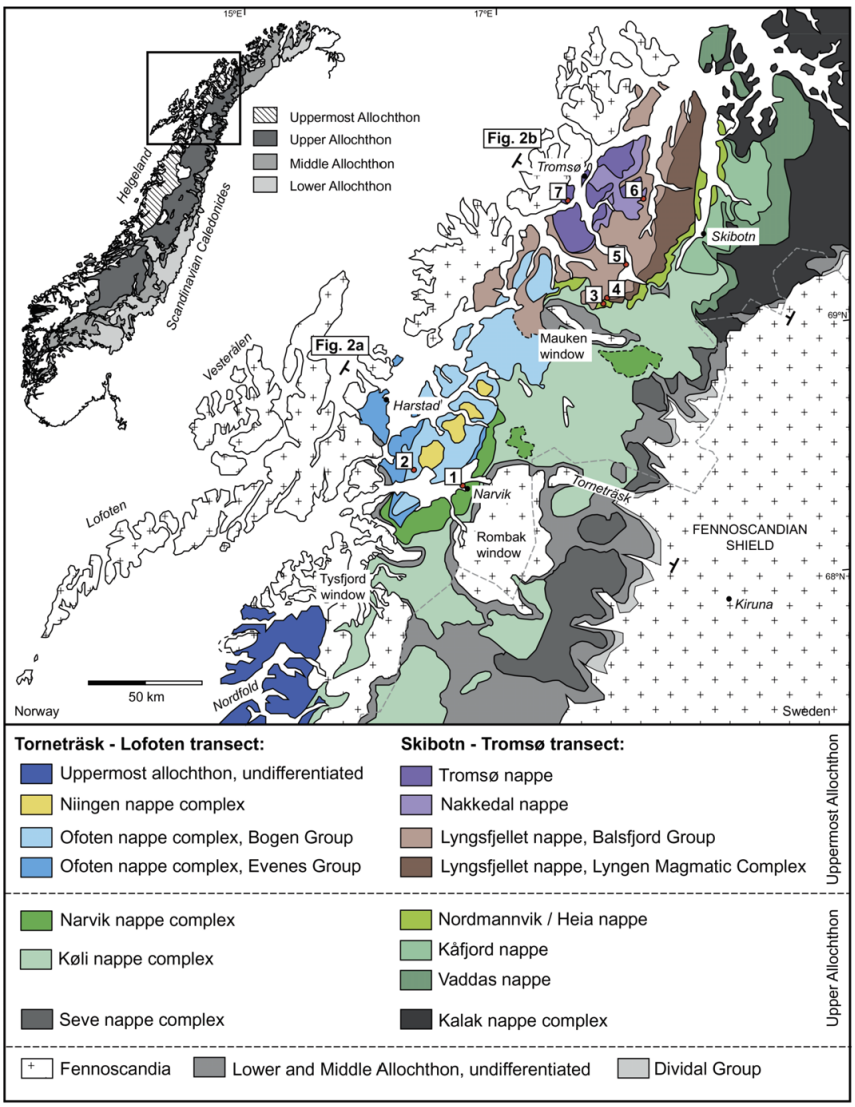

Figure 1.2: Caledonian orogenic rocks exposed in nothern Norway Figure from Augland et al., 2014.

Hansen et al., 2012; Davids et al., 2013; Indrevær et al., 2013; Koehl et al., 2018). The Vestfjorden-Vanna Fault Zone separates the West Troms Basement Complex horst, and the Vannareid-Burøysund fault that hosts Cu-Zn mineralization described in paper III, is a part of this fault zone. The Troms-Finnmark fault complex is an offshore fault zone that runs parallel to it. As rifting continued from incipient continental faulting, the wide part of the margin of the coast of Vanna became passive as faulting moved westward and further south to the Lofoten area (Fig. 1.1; Mosar, 2003; Davids et al., 2012; Indrevær et al., 2013). As a result, the continental margin along the Norwegian coast narrows

northward towards Lofoten, and then abruptly widens again to the north of the Senja fracture zone that acted as a transfer zone.

1.1.4 The geology of West Troms Basement Complex

The Archaean/Palaeoproterozoic West Troms Basement Complex horst is situated west of the Caledonian orogenic rocks (Fig. 1.2). It is interpreted to be a part of the Fennoscandian Shield (Henderson et al., 2015; Bergh et al., 2010), although a link with the Lewisian in Scotland has also been suggested (Bergh et al., 2012).

The West Troms Basement Complex is (Fig. 1.3) a basement window composed of TTG gneisses (2.9-2.6 Ga) (Bergh et al., 2010; Myhre et al., 2013). The basement rocks are all strongly deformed, partly migmatized by Neoarchaean orogenies (c. 2.8-2.6 Ga: Myhre et al., 2013) and intruded by mafic dyke swarms dated at c. 2.4 Ga (Kullerud et al., 2006). Numerous supracrustal cover units (greenstone belts) with variable ages, composition and metamorphic grade (Zwaan, 1989; Armitage and Bergh, 2005; Bergh et al., 2010) overlie the basement gneisses. The Archaean volcano-sedimentary Ringvassøya greenstone belt was deposited at c. 2.8 Ga (Zwaan, 1989; Motuza, 2000), while the metasedimentary Vanna Group was deposited between 2.2 and 2.4 Ga (Bergh et al., 2007). Peak metamorphism reached high-grade granulite and amphibolite facies in Senja and Lofoten/Vesterålen parts of the transect during the D1-D2 events (Zwaan, 1995). Ringvassøya was subjected to medium grade amphibolite facies, while medium- to low grade greenschist facies dominated in the north-east (Vanna island, this work, Opheim and Andresen, 1989). This presumed metamorphic gradient implies that the studied transect evolved from a hinterland (deep crust) in the south-west to a foreland (upper crust) in the north-east (Bergh et al., 2010).

A suite of granites (Ersfjord Granite) and mafic igneous rocks (Hamn Gabbro) formed synchronous with a major suite of 1.8–1.7 Ga plutonic rocks in Lofoten and Vesterålen (Griffin et al., 1978; Corfu et al., 2003; Corfu, 2004). The Ersfjord Granite may have formed by partial melting of the TTG crust (Haaland, 2018; Laurent et al., 2019) and emplaced during the waning stages of the Svecofennian Orogeny (1.92-1.78 Ga), as defined in the Fennoscandian Shield (Lahtinen et al., 2011). This Svecofennian deformation in West Troms Basement Complex affected the entire province. Early deformation generated a main ductile gneiss-foliation (S_1), SW- and NE-dipping thrusts (S_1), and NV-SØ trending tight (F_1). Continued deformation folded these early fabrics into upright (F_2) fold systems. During the late-stage, partly orogen-parallel event (D_3) steeply NW-SE plunging folds (F_3) and subvertical ductile shear zones (strike-slip faults) formed in the Senja Shear Belt, whereas SE-directed orogen-normal thrusts and steep NW-SE

striking lateral shear zones formed in the northeast, i.e. on Ringvassøya and Vanna. This D3 deformation is dated at c. 1.77-1.65 Ga in the Senja Shear Belt, a major ductile deformation zone (Fig. 1.3) (Bergh et al., 2015; Laurent et al., 2019), which involved polyphase crustal contraction and accretion (D1) and partitioned thrust and strike-slip deformation (D3-transpression) (Bergh et al., 2010).

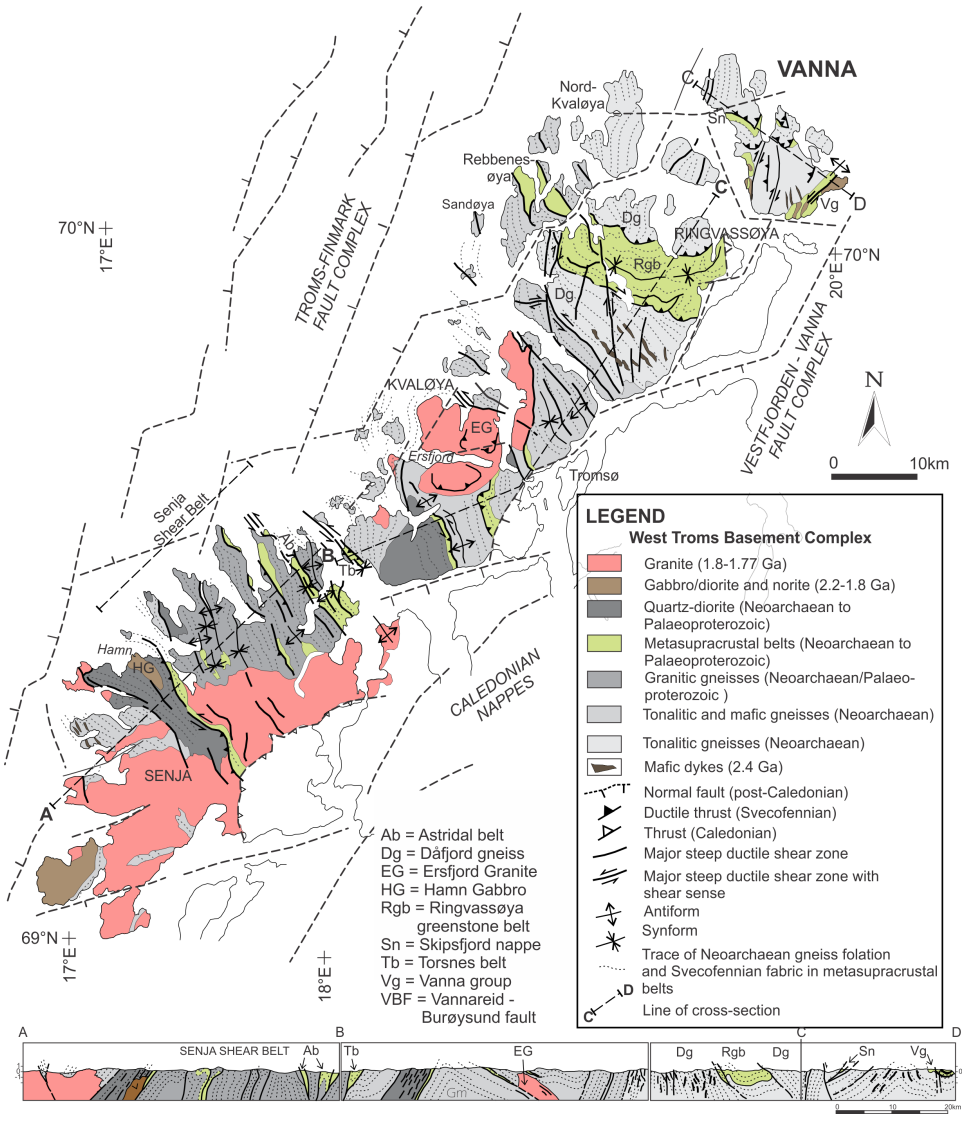

Figure 1.3: Geologic and tectonic map of the Archaean/Palaeoproterozoic West Troms Basement Complex (Bergh et al., 2010; Thorstensen, 2011; Haaland, 2018; Davids et al., 2013; Bergh et al., 2007). Archaean and Palaeoproterozoic basement blocks and Vanna Island is located at the northern end of the complex.

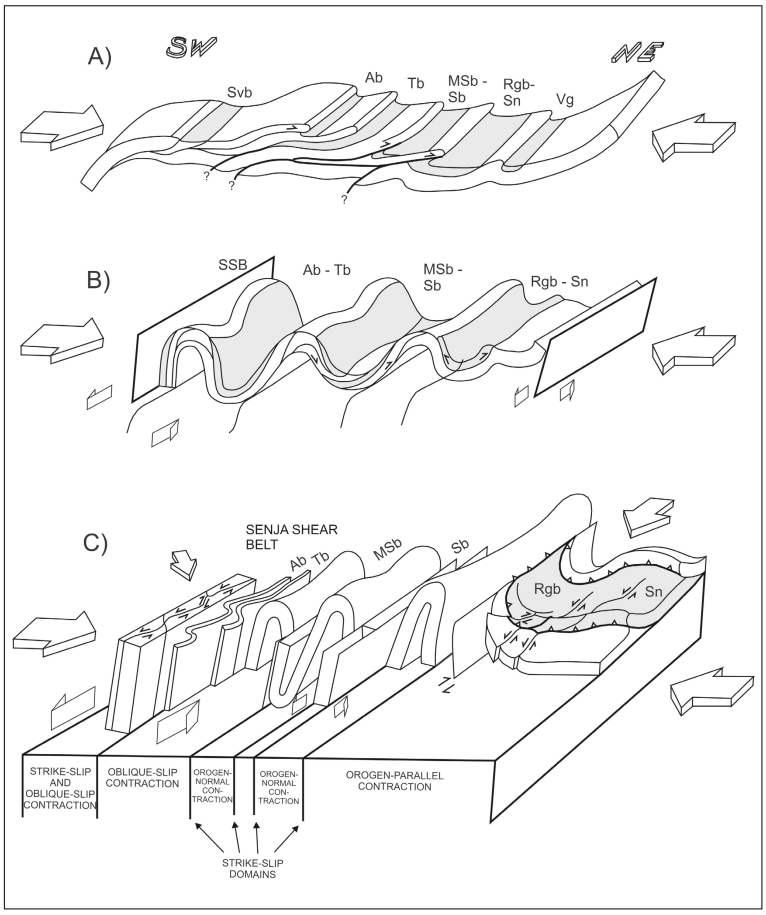

Figure 1.4: Schematic model displaying the development of presumed Svecofennian structures in the West Troms Basement Complex. (A) Formation of NE-directed thrusts and the main low angle mylonitic foliation (S1) in supracrustal belts from orogen-oblique NE-SW directed orthogonal shortening. (B) Continued orthogonal shortening produced upright macro-folds (F2) by folding of the earlier fabrics. (C) Late Svecofennian orogen-parallel to orogen-oblique directed contraction resulting in mostly sinistral strike-slip reactivation of steep macro-folds (D3). Figure from Bergh et al., (2010)

.

Whereas the Fennoscandian Shield in Finland, Sweden and Russia is well endowed in both base and precious metal deposits, few economic deposits have been found in the West Troms Basement Complex. Limited historic mining and exploration have mainly focused of base metals; Ni, Co, Cu ± PGE occurrences in layered mafic intrusions in the Hamm Gabbro was briefly mined in the 1860‘s (Bugge, 1935). During the same period, prospecting on Ringvassøya resulted in several known metal occurrences ranging from stratiform massive Fe-Cu sulphide deposits (assumed volcanic massive sulphide and/or sedimentary

exhalatory deposits) and several different precious metal type occurrences found within the 2.8(?) Ga Ringvassøya Greenstone Belt (Bratrein, 1989; Zwaan, 1989). Several smaller orogenic gold deposits were also recognized in the 1980's (Sandstad and Nilsson, 1998). Despite recent advances in the geological knowledge of the region, both the syngenetic mineralization processes and the hydrothermal alteration and potential metal remobilisation caused by the later Svecofennian deformation is still poorly understood.

1.1.5 Study area - the geology of Vanna island

Vanna island (Fig. 1.5) is the study area of this thesis. It is located in the north-eastern part of the West Troms Basement Complex (Fig. 1.3), and is mainly composed of Archaean tonalite gneisses cut by 2.4 Ga mafic dike swarms (Binns et al., 1980; Opheim and Andresen, 1989; Bergh et al., 2007). Several metasedimentary cover sequences unconformably overlie the basement; the largest of these is the well-studied Vanna Group along the southern coast. In addition, several smaller and less studied cover sequences are found along the western coast of the island at Kvalvågklubben and Hamre, and farther north as lenses in, and structurally below, the Skipsfjord Nappe. The age of these cover sequences is constrained at Vikan by the erosional contact with the 2.4 Ga mafic dikes in the basement, and a diorite sill (2.2 Ga; Bergh et al., 2007) that has intruded the metasedimentary sequence. In the north, highly strained parautochtonous sequences, the Skipsfjord Nappe, is composed of variously mylonitized tonalitic gneisses and intercalated lenses of metasedimentary and mafic intrusive rocks (Opheim and Andresen, 1989).

Vanna Group metasedimentary sequence

The first geological mapping on the island was carried out by Pettersen (1887), who suggested that the island consisted mainly of Precambrian gneisses overlain by Caledonian metasedimentary rocks along the south-eastern coast. Mapping carried out by Binns et al., (1980) focussed on the stratigraphy of this metasedimentary sequence, now termed the Vanna Group, and informally divided the low-grade metasedimentary rocks into the lower psammitic Tinnvatn formation and the overlying mixed lithological Bukkheia Formation. The Tinnvatn Formation is $<$ 80 m thick and unconformably overlie the basement tonalites. It consists of quartzitic, arkosic to subarkosic, and calcareous metasedimentary rocks deposited in a deltaic environment (Binns et al., 1980). Detailed sedimentary facies analysis carried out by Johannessen (2012) further suggested that the upper parts (8-10 m) of the Tinnvatn formation was deposited in a transgressive shallow marine environment and represents a foreshore facies, while the rest was deposited by tidal streams as an upper

shoreface facies. The much less studied overlying Bukkheia formation is thicker (< 150 m) and consists of partly calcareous mudstones with intermittent coarser sandstone layers. The Bukkheia formation is intruded by a diorite sill, locally up to 2 km thick. The diorite itself is composed of several intrusions ranging from intermediate to mafic, and whole-rock geochemical analyses show that the diorite has a continental tholeiitic signature (Johansen, 1987).

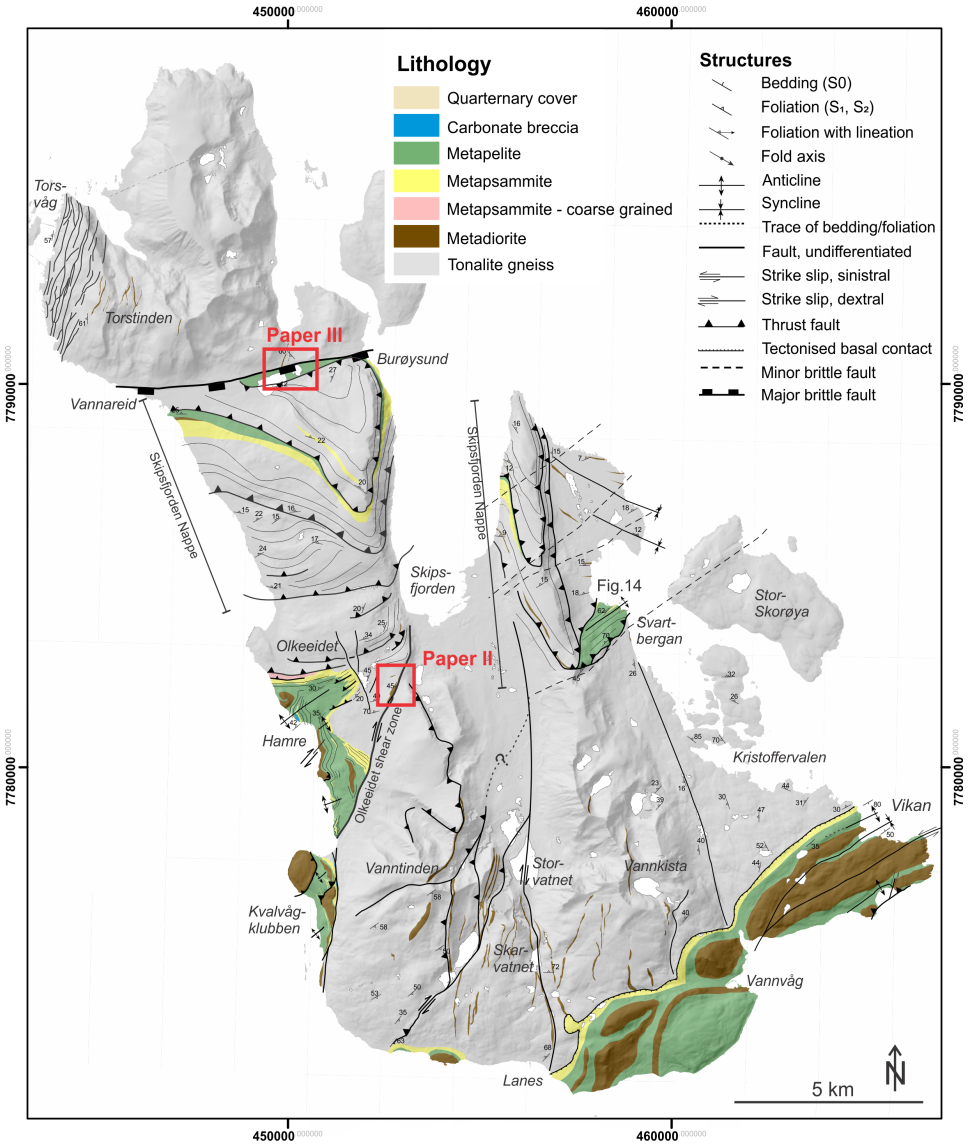

Figure 1.5: Geological and tectonic map of Vanna island (Modified after Bergh et al., 2007; Grogan and Zwaan, 1997; Opheim and Andresen, 1989; Roberts, 1974.) Red frames refer to the locations of Olkeeidet emerald occurrence in paper II and Vannareid Burøysund Cu-Zn mineralization in paper III.

Smaller metasedimentary sequences are also located at Hamre-Kvalvågklubben along the western coast of Vanna. These metasedimentary sequences have a similar stratigraphy as the Vanna Group, with metapsammites and quartzites overlain by intercalated metapelites, but the metamorphic grade is somewhat higher (upper-greenschist facies; this work; Bergh et al., 2007).

Skipsfjord Nappe

The parautochthonous Skipsfjord Nappe is a peculiar unit located in the northern part of Vanna (Fig. 2). It constitutes variously highly strained to mylonitized tonalitic gneisses and intercalated lenses of metasedimentary and mafic intrusive rocks of the Kvalkjeften Group (Opheim and Andresen, 1989). The metamorphic grade is generally higher than in the para-autochthonous units of the Vanna Group (lower amphibolite facies), and the rocks have a more pronounced foliation which coincides with ductile shear zones dipping gently NW. Individual units are separated by mylonitic high-strain ductile shear zones that dip gently NW and reveal mostly, top-to-the-SE thrust displacement. Oppheim and Andresen (1989) divided the Kvalkjeften Group into the lower mainly metapsammitic Geitdalen formation, and the upper mainly metapelitic Brattfjell formation. A depositional contact is suggested with the underlying mylonitic tonalite gneiss, however, strong deformation has obscured this relationship. A set of mafic dikes has intruded the upper parts of the Brattfjell formation.

Below the Skipsfjord Nappe, at Svartbergan (Fig. 1.5), recent mapping has unraveled a ca. 1km thick sequence of quartz-feldspathic metasandstones and siltstones, resembling rocks of the Vanna Group, although previously mapped as mylonitized basement gneisses. The strata are tilted to subvertical position, multiply folded, and truncated by the overlying Skipsfjord Nappe stack (Karlsen, 2019; Rønningen, 2019). The contact with basement gneisses below is marked by a moderate/steep oblique-slip shear zone at a high angle to the fold-thrust zones. In the north, the Skipsfjord Nappe is down-thrown > 3 km along the post-Caledonian brittle Vannareid-Burøysund normal fault (Opheim & Andresen 1989; Olesen et al. 1997), which hosts extensive Cu-Zn bearing quartz-carbonate veins (cf. paper III).

The Skipsfjord Nappe was originally suggested to be an allochtonous Caledonian thrust nappe correlated with the Kalak Nappe in Finnmark (Opheim and Andresen, 1989). Rice (1990) contradicted this interpretation and suggested that the rocks were a para-autochtonous basement-cover sequence. However, the Caledonian age of the Vanna Group deposition suggested by the similarities with the Cambro-Silurian Dividalen Group (Pettersen, 1887) and with Lyngsfjell Group (Landmark, 1973) was not disputed until Bergh et al., 2007 dated the

diorite sill in the metapelitic Bukkheia formation to be 2221 +- 3 Ma, thereby constraining a Palaeoproterozoic minimum age to the deposition of the Vanna Group. Further, Bergh (2007) showed that the provenance of the sediments were locally derived from Archaean tonalite gneisses of Ringvassøya, Kvaløya and Senja.

In this thesis, we suggest that complex fold-thrust belt structures of presumed late-Svecofennian age characterize the deformation of the basement tonalites and the Palaeoproterozoic metasedimentary and intrusive rocks. This further implies that the structures formed in the foreland/frontal part of a transpressional deformation system adjacent to a continental accretionary orogen (Paulsen et al., 2019). In this setting, Palaeoproterozoic sedimentary basins controlled the location, extent and character of late-Svecofennian basement-seated folds, thrusts and orogen-parallel/oblique shear zones. However, the age of this deformation is still unresolved. This will be discussed further in Paper I in this thesis.

1.2 Aims of the project

The aim of this thesis is to investigate the controls on mineralization in the Archaean/Palaeoproterozoic basement rocks on Vanna island, northern Norway using a combination of structural and lithological field mapping and a suite of geochemical techniques. Although ore-mineralization on Vanna has been known since the 1860's (Bratrein, 1989), few analytical studies have been carried out prior to the work in this PhD thesis. A further aim is to understand the formation of local structures, and their role as fluid pathways for ore-bearing fluids. In addition, an attempt is made to place the local structures in a larger tectonic setting. This work also sets out to understand the ore-bearing fluids, and the key mechanisms that ultimately lead to the deposition of mineralization.

2

Approach

The aims of this thesis are approached using a combination of field work together with an extensive suite of analytical techniques. The methods compliment each other well as they each resolve a part of the complex interplay of structures that control the hydrothermal fluid flow used as pathways, and to understand the physiochemical properties of the fluids that further control the mineralization and alteration assemblage.

2.1 Field mapping and structural analysis

Approximately ten weeks over four field seasons were spent mapping selected areas of Vanna island. Field studies forms the basis for all three papers presented in this thesis. Paper I comprises a structural field study that focussed on mapping of the metasedimentary cover sequences (Vanna Group) and their relation to the basement seated structures in Vanna. The key outcrops were the metasedimentary cover sequences, as they have recorded these structural fabrics very well. Mapping carried out in paper I also forms the structural framework for the more detailed field investigation of the structural controls on mineralization discussed in papers II and III. Field work for papers II and III also included selected sampling of mineralization, altered host rocks and their unaltered equivalents. For paper III, field work was combined with investigations of c. 800 m of existing diamond drill-core bored by Store Norske Gull in 2008 (Ojala et al., 2013). The drill-core provided unique 3D understanding

of the Vannareid-Burøysund fault, and its relationship to mineralization and hydrothermal alteration.

2.2 Analythical methods

A suite of different analytical methods were selected based on their usefulness to understand various properties involved in the deposition of ore-minerals in paper II and III, in particular to understand the metal-transport capabilities and deposition mechanisms of the ore-bearing fluid.

Scanning electron microscopy (SEM) including energy-dispersive X-ray spectroscopy (EDS), electron backscattered diffraction (EBSD), and cathodoluminescence (CL), was used to determine mineral chemistry, mineral parageneses, mineralogical changes, e.g. zonation in hydrothermal quartz, and textural relationships. The thin sections were coated with a thin carbon layer to avoid charging effects. All the analyses were carried out using a Zeiss Merlin VP Compact field emission SEM equipped with an X-max80 EDS detector and a Nordlys EBSD detector, both provided by Oxford Instruments, as well as a Zeiss valuable pressure secondary electron (VPSE) detector for CL imaging. The VPSE detector produces an image close to panchromatic CL under high vacuum conditions (Giffin et al., 2010). EDS chemical analysis of chlorite in fault rocks was used to estimate formation temperatures based on tetrahedral site occupancy (Cathelineau, 1988), which is accurate to within 30°C.

Fluid inclusions are microscopic bubbles of hydrothermal fluid trapped within a crystal, and are widely used to provide insight into the chemical and physical (pressure and temperature) properties of ore-forming fluids (Roedder, 1984; Wilkinson, 2001). Fluid inclusion studies were selected because it is one of the few methods that allows for semi-direct analysis of the fluids that deposited the various minerals, including ore-minerals. Fluid inclusion data were obtained from double polished wafers (100-250 µm thick) of hydrothermal gangue and ore minerals. Petrographic observations classified the fluid inclusions as primary, pseudosecondary or secondary based on their internal relationships with each other and their spatial distribution. Microthermometric measurements during the heating and freezing cycle allowed us to determine salinity, minimum fluid temperatures, and indicate the chemical composition of the fluid. All measurements were recorded using an Olympus BX 2 microscope coupled with a Linkam THMS 600 heating and cooling stage operating between -180 and +600°C at UiT-The Arctic University of Norway. For the equations used to calculate salinity and isochores see paper II and III. Despite the wide acceptance of usefulness of this method, there are several potential complications that can occur and lead to misinterpretations of the measurements. Fluid inclusions

commonly deform and/or recrystallise post deposition (Roedder, 1984). If not recognised, this can lead to over/underestimation particularly of pressures in calculated isochores (Tarantola et al., 2010). In addition, failure to recognise solid phases because of their small size making them invisible under the microscope, or metastability can further complicate measurements and the subsequent interpretation. Most of these issues can, however, be minimised by careful and detailed observations by the person performing the analyses.

In addition, qualitative measurements of key elements present in the hydrothermal fluid were obtained by **decrepitating fluid inclusions** (c. 500°C for 3-4 minutes) and analysing the resulting evaporate mounds formed on the sample surface using an SEM/EDS technique modified after Kontak (2004). We performed both spot analyses of specific mineral phases and a map scan over the whole evaporate mound. This technique was useful for determining the major components present in the fluid inclusions. Its usefulness is, however, limited by the unpredictability in which of the individual fluid inclusion will decrepitate, and further if microthermometric measurements have been obtained from that particular fluid inclusion.

Raman Spectroscopy is used to characterize the structure of geologically interesting materials such as minerals. It is particularly useful as a non-destructive method to identify Raman active species in fluid inclusions, including CO_2. Raman spectroscopy was conducted at the Department of Earth Science, the Faculty of Mathematics and Natural Sciences, University of Bergen (UiB). A JobinYvon LabRAM HR800 confocal Raman spectrometer equipped with a frequency doubled Nd-YAG laser (100 mW, 532 nm) and LMPlan FI 50× objective (Olympus) was used to identify minerals based on Raman spectra published in the literature (Lafuente et al., 2015). CO_2 densities were calculated according to Fall et al., (2011).

Stable isotopic measurements of $\delta^{13}C$ and $\delta^{18}O$ can indicate the source of the CO_2 that formed carbonates. These analyses were obtained using a ThermoFisher MAT253 IRMS with a Gasbench II at UiT (site.uit.no/sil). Samples were placed in 4.5ml Labco vials, then flushed with He, and 5 drops of water-free H_3PO_4 were added manually with a syringe. The results were normalised to the Vienna Pee Dee Belemnite (VPDB) standard by three in-house standards with a wide range of $\delta^{13}C$ and $\delta^{18}O$ values, and reported with an uncertainty of standard deviation $\leqslant$ 0.1 ‰.

X-ray diffraction (XRD) analyses were used to study the structure, composition and physical properties of minerals. It was particularly useful to identify the mineralogy of fine-grained ultracataclasite material. The analyses were conducted at the University of Zagreb on a Philips PW 3040/60 X'Pert PRO powder diffractometer (45 kV, 40 µA), with CuKα-monochromatized radiation

(Δ= 1.54056 Å) and θ-θ geometry. The area between 4 and 63°2θ, with 0.02° steps was measured with a 0.5° primary beam divergence. Compound identifications were based on a computer program X'Pert high score 1.0B and literature data.

For further detail on the analytical methods used, see paper II and III.

3

Synthesis of papers

Paper I

Paulsen, H.K., Bergh, S.G., Strmić Palinkaš, S., Karlsen, S.E., Kolsum, S. & Rønningen, I.U., Nasuti, A. **Fold-thrust structures and oblique faults on Vanna island, West Troms Basement Complex, and their relation to inverted metasedimentary sequences**, *Manuscript*

The aim of this paper is to portray and discuss the structural architecture and tectonostratigraphic evolution of Vanna island by using field structural and lithological mapping in combination with reprocessed magnetic susceptibility data. Resolving the structural evolution of Vanna significantly improves the understanding of the northernmost low-grade portion of the West Troms Basement Complex, and shows that Vanna could represent a fold-thrust belt system related to accretionary tectonism documented in this basement complex. Further, we compare these observations with the larger-scale tectonic evolution of northern Fennoscandian Shield. Further, understanding the formation of the structural fabrics found on Vanna is valuable from an economic perspective, and the results from this paper form a framework to understand the structural controls on mineralization presented in paper II and III.

This manuscript focusses on a series of metasedimentary sequences that unconformably overlie the Archaean to Palaeoproterozoic basement rocks on Vanna (Fig. 1.5). The para-autochthonous metasedimentary sequences in Vanna, including those in the autochthonous Skipsfjord and Svartbergan Nappes were

deposited in separate, pre-orogenic (2.4-2.2 Ga) rift basins bounded by NNW-SSE, NNE-SSW, and subordinate NE-SW trending, steep normal faults. The basins in Vanna comprise a lower series of metapsammites and overlying metapelites with subordinate horizons of peculiar calcareous metapelitic breccias, quartzites and conglomerates. Internal stratigraphy and preserved primary sedimentary structures indicate deposition in shallow marine, high-energy deltaic or tidal and shore face depositional environment.

Steep, pre-existing c. 2.4 Ga mafic dykes trending N-S in the tonalitic basement rocks of Vanna, provided favourable zones of weakness that helped localise the Palaeoproterozoic rift basins and their bounding normal faults. During the subsequent orogenic deformation, the rift-basins and enclosed metasedimentary sequences were subjected to two main shortening events (D_1-D_2). The D_1-event involved ENE-WSW shortening, basement-involved folding and steep reverse faulting/thrusting. Pre-existing N-S trending normal faults were reactivated as steep west-dipping reverse and low-angle thrust faults with up-to-the-east displacement. A dextral strike-slip component of the steep reactivated faults, including the Olkeeidet shear zone, is also observed. The D_2-event caused major SE-directed imbricate thrusting of the Skipsfjord and Svartbergan Nappes, basement-involved fold-thrust belt formation in the para-autochthonous Vanna Group in southeastern Vanna, and sinistral strike-slip reactivation of the steep N-S trending basement faults. These complex, two-stage fold- and thrust belt systems are considered to be Late-Svecofennian in age, from dating elsewhere in the West Troms Basement Complex. However, it is also possible that the D_2 phase is Caledonian in age, or reactivated during the Caledonian Orogeny. Regardless of the age of these contractile deformations, metasedimentary units and associated D_1-D_2 thrusts, steep strike-slip shear zones, and intrusive contacts in both the metasedimentary units and basement gneisses suffered mineralization and quartz-carbonate veining, emerald-quality beryllium, and fuchsite-bearing fabrics, suggesting strong ductile structural control on the mineralization described in paper II.

Paper II

Paulsen, H-K, Bergh, S. G, Palinkaš, S. S. **Hydrothermal emeralds: a shear zone hosted mineralization on Vanna Island, northern Norway** *Manuscript*

This paper investigates the hydrothermal origin of recently discovered emeralds hosted by the Olkeeidet shear zone (OSZ) on Vanna island (Fig. 1.5). The formation of emerald (the green coloured variety of beryl) is a geological contradiction - it requires interaction of two geochemically contrasting components; one that brings highly incompatible Be, and another rich in compatible

Cr. Although emeralds are rare, they can form in a variety of geological settings, most commonly from beryllium-bearing pegmatites that intrudes Cr-rich ultramafic rocks. This occurrence on Vanna is unique, and is evidence that emerald can be deposited from fluids and not just granitic melts.

Detailed mapping of structural relations shows that the OSZ is a c. 50 m wide ductile shear zone that cuts Archaean/Palaeoproterozoic tonalite and tonalite gneisses with amphibolite layers. Within the OSZ, an array of internal splay faults, including minor thrust faults and strike slip faults, form a set of duplexes that indicate dextral movement along the OSZ. Hydrothermal fluid flow through this shear zone is evident from extensive metasomatic alteration of the host rocks that resulted in the formation of albitites and fuchsite schists, and the deposition of hydrothermal dolomite, quartz, tourmaline and emerald. The protolith of the strongly metasomatised rock is speculated to include a small lens of metasedimentary rocks; similar metasedimentary rocks are also found along the OSZ further south at Kvalvågklubben. The mineralogy of emerald and the surrounding alteration assemblage is confirmed using SEM, and X-ray diffraction analyses as well as Raman Spectroscopy.

The OSZ acted as a conduit for hydrothermal fluid flow. In addition, metasomatic alteration of the host rocks likely furthered the porosity, thereby creating a positive-feedback loop that allowed for increasing metasomatic alteration. Fluid composition is investigated by fluid inclusion microthermometry and decrepitation, which reveal that the hydrothermal fluids were highly saline (30-43 wt. % NaCl equiv.) and composed of $H_2O+NaCl\pm CO_2\pm KCl$. Estimates of formation conditions reveal minimum temperatures of 320-350°C and 0.7 kbar pressure. In addition, the stable isotopic C-O compositions suggest that the fluids were, at least in part, magmatic in origin. As fluid can migrate considerable distances within a shear zone environment, a deeper crustal level magmatic degassing is speculated as a possible source of highly saline fluids and CO_2. A genetic link with granitoid-associated veins is thus suggested for the fluids. Such a magmatic fluid can also contain significant beryllium, the highly incompatible element, needed to form emerald. Chromium is likely sourced from the local, possibly metasedimentary host rocks. From this, we suggest that emerald mineralization is epigenetic and has formed as a result of hydrothermal growth associated with tectonic activity. This locality evidences that emerald can be deposited from hydrothermal fluids of a magmatic origin, in contrast to the classic emerald formation models where emerald is deposited from a granitic melt intruding an ultramafic host rock.

Paper III

Paulsen, H-K., Bergh, S. B., Palinkaš, S. S., **Late Palaeozoic fault controlled hydrothermal Cu-Zn mineralization on Vanna Island, West Troms Basement Complex, northern Norway,** *Manuscript submitted to Norwegian Journal of Geology*

This paper focusses on hydrothermal Cu-Zn mineralization hosted by the Vannareid-Burøysund fault (VBF). In this paper we aim to identify the structural and physiochemical controls on mineralization. We analyse the structural architecture and textural relationships of host rocks, cataclasites and hydrothermal veins hosted by the VBF and attempt to resolve its role as a fluid pathway for the ore-bearing fluids. A second part of this work aims to determine the characteristics of the ore-bearing fluid to indicate a potential fluid source, identify controls on metal solubility and transport capabilities, and investigate the depositional mechanisms. For this second part, we use a multi-technique analytical approach including fluid inclusion studies, mineral and whole-rock geochemical-, and stable isotope analyses.

The VBF is exposed on the northern part of Vanna, where it separates Archaean tonalite gneiss from highly strained Skipsfjord Nappe with enclosed metasedimentary lenses (Fig. 1.5). This fault is a part of the Vestfjord-Vanna Fault Complex that bounds the West Troms Basement Complex horst against Caledonian Nappes to the east. Existing K–Ar illite dating of this fault yielded a late Carboniferous through early Permian age (Davids et al., 2013); concurrent with incipient continental rifting that resulted in the opening of the North Atlantic Ocean. The Cu-Zn mineralization was discovered in 2008. Following a brief exploratory diamond drilling carried out by the company Store Norske Gull in 2012 this occurrence was informally interpreted as the stringer zone of a Palaeoproterozoic volcanic massive sulphide deposit, related to the deposition of the metasedimentary sequences in the Skipsfjord Nappe (Ojala et al., 2013). However the results from this paper contradicts that interpretation; we suggest that mineralization is epigenetic and strongly structurally controlled by late Palaeozoic normal fault movement.

A model is proposed to explain the complex Cu-Zn mineralization in the VBF. This model shows successive and/or repeated supply of over-pressurized hydrothermal fluids to the VBF in a tectonic environment characterised by crustal extension and normal faulting. Two main stages of faulting/fracturing is observed, where the initial stages of syn-ore brittle faulting along VBF generated massive proto/ortho-cataclasites in a relatively narrow core zone, and the porosity created by the fracturing allowed for the deposition of massive quartz-sphalerite veins. The second stage in the fault evolution was progressive widening of the fault, the development of spatially more extensive damage

zones, continued cataclasis, and injection of quartz-chalcopyrite veins. Additionally, during successive injection of quartz-sphalerite vein material, the initial fault core might have become partly or fully sealed, thus reducing the permeability and forcing the later fluids to flow into the damage zones. Although the fault cores acted as the main fluid conduits, the fluids also weakened the strength of the fault damage zones and contributed to the complex fault architecture.

Fluid inclusion microthermometry of inclusions hosted by quartz, sphalerite and calcite revealed that Cu and Zn were carried as chloride complexes in a highly saline (27-38 wt. % $NaCl+CaCl_2$ equiv.) fluid composed of $NaCl+CaCl_2+H_2O$ at temperatures conditions of c. 250-330°C. The propylitic alteration mineralogy assemblage suggests that the ore-bearing fluid was near neutral and possibly reducing. In such a highly saline fluid, the physiochemical properties that control metal solubility is mainly temperature and concentration of ligands. The successive deposition of quartz sphalerite veins followed by quartz-chalcopyrite veins is also reflected in the interpreted depositional mechanisms. Sphalerite ore minerals were deposited by isothermal fluid mixing - by diluting the highly saline fluid and thereby lowering the solubility. The later chalcopyrite minerals were deposited by a combination of fluid mixing with a cooler fluid and wall-rock interactions. Further, this implies an influx of cooler ground/meteroric water into the fault system as the fault widens. A magmatic source, or a significant magmatic contribution, of CO_2 in hydrothermal calcite is indicated by stable $\delta^{13}C_{VPDB}$ and $\delta^{18}O_{SMOW}$ analysis. In addition, the different stable isotopic composition of calcite found in the metasedimentary sequence in the Skipsfjord Nappe is not directly the source of metals and salinity of the ore bearing fluid, as suggested by previous workers. No late Palaeozoic magmatism is observed in the region, however, we suggest that the fluids might be derived from a deeper magmatic source that is not found on surface. This study demonstrates that hydrothermal Cu-Zn mineralization in northern Norway may occur not only in old Precambrian and Caledonian basement rocks, but also in much younger, Palaeozoic to Cretaceous, rift-related, brittle fault zones. This provides an additional regional mineral exploration model for structurally controlled ore deposits in northern Norway.

3.1 Synthesis

This thesis focusses on the structural and tectonostratigraphic evolution of Vanna, and its associated controls on mineralization. The three papers presented in this thesis relate well as each paper aims to explain a separate part. The first paper discusses the early tectonic and structural evolution of Vanna, with a focus on the contractile ductile deformations forming fold and thrust

belt structures. These contractionary fabrics are well-preserved in the metasedimentary strata that were deposited in Palaeoproterozoic continental rift basins that formed due to a E-W directed regional extension event. The subsequent multi-phase contractile deformation inverted these basins and their boundary faults and resulted in low-grade fold and thrust belt structures. The first phase (D_1) of deformation is caused by WSW-ENE compression, and the second more spatially extensive phase (D_2) was caused by later NNW-SSE compression. In paper II we investigate the Olkeeidet shear zone that hosts hydrothermal emerald mineralization deposited in relation to the dextral deformation. The Olkeeidet shear zone likely originated as a Palaeoproterozoic basin bounding normal fault, and the dextral movement along the fault suggests that the early D_1 deformation was active at the time of emerald formation. In paper III we investigate Cu-Zn mineralization hosted by the brittle Vannareid-Burøysund fault. This brittle fault is associated with incipient rifting related to the late Palaeozoic opening of the Atlantic Ocean.

Considered together, the three papers in this thesis can be used to discuss the mineralization potential and the controls more broadly. The three papers cover a prolonged geological history, and shows that various types of mineralization occur in different geotectonic settings. Although the occurrences found on Vannareid and Olkeeidet are small and at this stage in time uneconomic, neither type of mineralization is previously described from the West Troms Basement Complex. This study provides valuable insight into the mineralization potential, key mechanisms that control mineralization, and highlights the potential for further undiscovered and significant structurally controlled mineralization to be found.

3.1.1 A transect though a continental accretionary orogen

The data presented in paper I suggest that the structures on Vanna formed in the foreland/frontal part of a transpressional deformation system adjacent to a continental accretionary orogen, likely the Svecofennian Orogeny. Considering the presumed metamorphic gradient in the West Troms Basement Complex where the hinterland (deep crust) is represented by the high-grade rocks found in Lofoten/Vesterålen in the south-west, to a foreland (upper crust) at Vanna in the north-east, a near-complete coastal transect through an orogenic event can be found in the West Troms Basement Complex. The excellent exposures makes the this coastal transect a key area for studying regional-scale tectonics of a presumed Late-Svecofennian age.

3.1.2 Age of D2 deformation on Vanna

The discussion regarding the depositional age of the Vanna Group metasedimentary sequence; whether it is Caledonian (Pettersen, 1887; Landmark, 1973) or Svecofennian, was put to an end by Bergh et al., (2007) whom proved a Palaeoproterozoic depositional age. The age of deformation, however, still remains an open question. Although in paper I we suggest that the deformation is likely Svecofennian, preliminary and unpublished Ar^{40}/Ar^{39} data of metamorphically formed muscovite from mylonitised metasedimentary rocks within the Skipsfjord Nappe yield a Caledonian age (c. 420 Ma; NGU pers. comm., 2019). Further studies are needed to determine whether this preliminary data suggests that the entire D2 deformation event on Vanna is Caledonian or whether it simply suggests a weak Caledonian metamorphic overprint. It has previously been suggested that the West Troms Basement Complex has not been substantially subjected to Caledonian deformation (Dallmeyer, 1992; Corfu et al., 2003).

When considering a potential Caledonian age of this D2 deformation, it is natural to compare with the lowermost Caledonian Nappe exposed in the region, the Kalak Nappe (Fig. 1.2), thus supporting the suggestions by Opheim and Andresen (1989). The Kalak Nappe is exposed on the islands on Arnøya and Uløya located just east of Vanna, and is composed of low-grade Precambrian gneisses and metapsammites with local intrusive mafic rocks (Faber et al., 2019). However, the metapsammites are Neoproterozoic and much younger than those found at Vanna (Kirkland et al., 2007). On Arnøya and Uløya, the pervasive Caledonian mylonitic foliation, associated mineral lineations and stretching lineations also plunge shallowly to the NW or SE (Faber et al., 2019). The orientation of these structural fabrics are similar to foliations and stretching lineations found in the D2 deformational fabrics of the Skipsfjord Nappe on Vanna (Fig. 1.5). Despite similar orientations with Caledonian structural fabrics further studies are needed to confirm or disprove the hypothesis of the Caledonian age.

Further, if the D2-Vanna deformation of the Skipsfjord Nappe indeed is Caledonian, it also warrants further investigations into the formation age of the assumed Svecofennian-aged, semi-ductile D3 event in the southern parts of the West Troms Basement Complex (Fig. 1.4) in Bergh et al., (2007; 2010). Currently, this is interpreted to be Late Svecofennian orogen-parallel contraction that resulted in sinistral strike-slip reactivation of steep macro-folds. However, if the D2-Vanna deformation is Caledonian it is not unlikely that Caledonian aged structures also exist further south in the West Troms Basement Complex.

3.1.3 Hidden magmatism or deep-seated structures as a source of magmatic CO_2

Stable isotopic $\delta^{13}C$ and $\delta^{18}O$ analyses of emerald-hosting dolomite (paper II) in the assumed Palaeoproterozoic ductile OSZ and of hydrothermal calcite in the Palaeozoic VBF both show a significant component of magmatic CO_2 (Fig. 3.1). These analyses are in contrast to those analysed from the calcite cement of the Vanna Group (Johannessen, 2012), from calcite veins hosted by metasedimentary sequences within the Skipsfjord Nappe, and from calcite veins in the magmatic diorite sill within the Vanna Group - all of which plot much closer to the field of marine sandstone. The source of this magmatic CO_2 is, however, enigmatic as no magmatism is recorded on Vanna since the intrusion of the diorite sill at 2.2 Ga.

Regionally, several Svecofennian aged magmatic events, possible Palaeoproterozoic sources for the magmatic signature of the emerald-hosting dolomite are recorded in the West Troms Basement Complex. These include a suite of 1.8 to 1.7 plutonic rocks in Lofoten-Vesterålen, and the Ersfjord Granite (1.3) on Kvaløya. The latter intrusion is thought have formed from partial melting of the TTG gneisses and was emplaced during the waning stages of the Svecofennian Orogeny (Haaland, 2018).

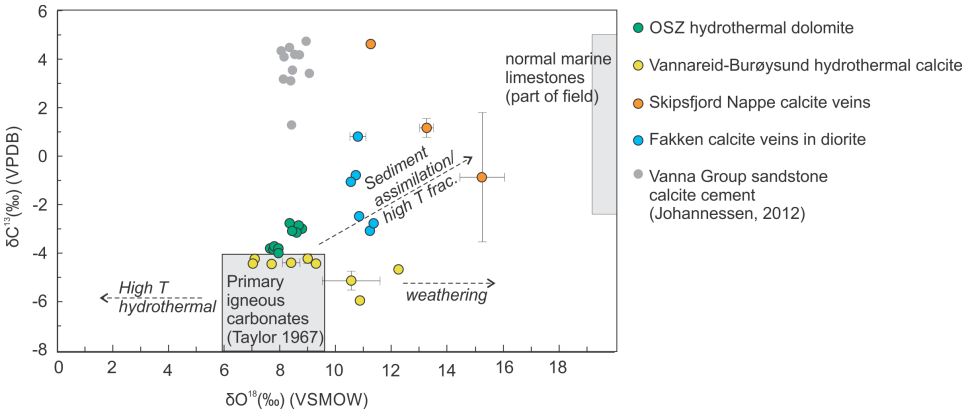

Figure 3.1: Isotopic compositions from Vanna

Regarding a possible magmatic source for some of the hydrothermal fluids in the much later brittle Palaeozoic Vannareid Burøysund fault, no direct evidence of a corresponding hot Permian magmatic and/or volcanic source/dike for the fluids have been observed in the Vanna island of western Troms. The closest in distance is the narrow (0.5 m wide) Carboniferous aged lamproite dike on Kvaløya farther south (Fig. 1.3) (Kullerud et al., 2011). Also, extensive rift-related mafic dike and sill intrusions of Carboniferous-Permian age do exist at northern Atlantic Ocean margins (Kirstein et al., 2006), including

the continental margin of northern Finnmark (Lippard and Prestvik, 1997; Roberts et al., 2003; Roberts, 2011; Rice, 2014; Nasuti et al., 2015). However, CO_2 degassing is common in continental rift systems, and volatiles can travel far from its source along faults and fractures (Brune et al., 2017).

Rather, this suggests that although no direct local source of the magmatic CO_2 is found in either of the mineralized faults, both of the faults are likely deep-seated structures that can source CO_2 bearing fluids from deeper in the crust, and therefore can source CO_2 from more distal/deeper reservoirs.

3.1.4 Fennoscandian source of salinity

Hydrothermal fluids may derive their salinity and metal contents from a variety of sources that include magmatic, various non-magmatic, or more commonly a mixed source. In paper II we suggest that the salinity and the fluids are sourced from a deeper magmatic source, likely associated with granitoid felsic melt.

However, widespread Na-metasomatism is documented in the Palaeoproterozoic volcano-metasedimentary rocks throughout the northern Fennoscandian Shield, resulting in the formation of albite and scapolite, commonly accompanied by formation of carbonate and tourmaline (Frietsch et al., 1997). Albitisation in shear zones is also described predating orogenic gold, where albitisation makes the rock more competent and favourable for gold deposition (Eilu 2007; Hulkki and Keinanen, 2007). The source of these Fennoscandian extensive Na and Cl rich fluids is elusive, but it is suggested that hypothetical evaporite sequences deposited in rift basins with mafic volcanism around 2500-2000 Ma is the source of these highly saline fluids (Meleznic et al., 2015).

3.1.5 Implications for mineral exploration

The results from paper III show that the brittle Vannareid-Burøysund fault can host hydrothermal mineralization. The VBF fault is a part of the Vestfjord-Vanna Fault Complex that developed due to post-Caledonian orogenic collapse and subsequent incipient rifting prior to the opening of the Atlantic Ocean. Age dating of illite obtained by Davids et. al., (2013) gave an age of the last movement along the fault of 306-284 Ma. With continued rifting, this wide part of the margin on the coast of Vanna became passive as faulting moved further south to the Lofoten area (Mosar, 2003; Davids et al., 2013; Indrevær et al., 2013), by leaving the VBF is a part of the innermost boundary fault system. This is visible in (Fig. 1.1) where the continental margin along the Norwegian coast narrows northward towards Lofoten, and then abruptly widens again to

the north of the Senja fracture zone that acted as a transfer zone.

Indrevær et al., (2013) suggested that these faults offshore could influence hydrocarbon migration and either act as fluid pathways for migration of fluids, or as hydrocarbon traps if the faults were sealed. The results from paper III also suggests that these faults could host hydrothermal mineralization and warrants further investigations into this extensive fault network that is found along most of the coastal margins of Norway.

3.2 Future research

The following suggestions on future research are given to further verify and/or evolve the results and models presented within this thesis:

- The age of the contractile deformation events on Vanna is uncertain. Absolute age dating of the ductile deformation that formed the fold and thrust belt system on Vanna would greatly improve the temporal relationship between the two ductile contractional phases (D1 & D2), and establish whether the deformation is late Svecofennian or Caledonian. Zircon age dating of the mafic layers in the Skipsfjord Nappe would also help constrain this age.

- The jump in metamorphic grade and age of supracrustal units from Ringvassøya to Vanna is not well understood, and further structural and lithological investigations of the islands of Nord-Kvaløya, Helgøy, Spenna and Nord-Fugløya could aid in understanding this gap.

- Further stable isotopic $\delta^{13}C$ and $\delta^{18}O$ studies of the various carbonate horizons and breccias found on the island, within the metasedimentary sequences and localised within various ductile and brittle faults, would further the understanding of the magmatic components in the hydrothermal fluids in paper II and III.

- The source of metals in the Vannareid-Burøysund fault could be further constrained by sulphur isotopic analyses of the sulphides sphalerite and chalcopyrite. Further, the source of the salinity in the fluid could be better constrained by analysing the halogen content of the fluid inclusions using a LA-ICP-MS method. In particular, measuring the Cr/Br ratio could indicate whether some of the salinity was derived from potential evaporites in metasedimentary sequences in the Skipsfjord Nappe. Further, this would aid exploration for similar metal occurrences to know whether such a source of salinity is needed to mobilise the metals.

- The verification of the brittle nature a Palaeozoic age of mineralization along the Vannareid-Burøysund fault warrants further investigations into other post-Caledonian extensional faults along the West Troms Basement Complex, including those described by Indrevær et al., (2013) and Koehl (2013).

Bibliography

Angvik, T. L. (2014). "Structural development and metallogenesis of Palaeoproterozoic volcano-sedimentary rocks of the Rombak Tectonic Window." PhD Thesis. UiT - the Arctic University of Tromsø (cit. on p. 4).

Armitage, P. E. B. and Bergh, S. G. (2005). "Structural development of the Mjelde-Skorelvvatn Zone on Kvaløya, Troms: a metasupractustal shear belt in the Precambrian West Troms Basement Complex, North Norway." In: *Norwegian Journal of Geology* **85**, p. 16 (cit. on p. 7).

Augland, L. E., Andresen, A., Gasser, D., and Steltenpohl, M. G. (2014). "Early Ordovician to Silurian evolution of exotic terranes in the Scandinavian Caledonides of the Ofoten - Troms area - terrane characterization and correlation based on new U-Pb zircon ages and Lu-Hf isotopes." In: *New perspectives on the Caledonides of Scandinavia and related areas.* Ed. by Corfu, F., Gasser, D., and Chew, D. M. Vol. 390. Special publication. London: The Geological Society of London, pp. 655–678 (cit. on pp. 5, 6).

Bark, G. and Weihed, P. (2007). "Orogenic gold in the new Lycksele-Storuman ore province, northern Sweden; the new Palaeoproterozoic Fäboliden deposit." In: *Ore Geology Reviews* **32**, pp. 431–451 (cit. on p. 4).

Bergh, S. G., Corfu, F., Myhre, P. I., Kullerud, K., Armitage, P. E. B., Zwaan, K. B., Ravna, E. J. K., Holdsworth, R. E., and Chattopadhya, A. (2012). "Was the Precambrian basement of Western Troms and Lofoten-Vesterålen in Northern Norway linked to the Lewisian of Scotland? A comparison of crustal components, tectonic evolution and amalgamation history." In: *Tectonics - recent advances*. Chap. 11 (cit. on p. 7).

Bergh, S. G., Corfu, F., Priyatkina, N., Kullerud, K., and Myhre, P. I. (2015). "Multiple post-Svecofennian 1750-1560 Ma pematite dykes in Archean-Palaeoproterozoic rocks of the West Troms Basement Complex, North Norway: geological significance and regional implications." In: *Precambrian Research* **266**, p. 15 (cit. on p. 8).

Bergh, S. G., Kullerud, K., Armitage, P. E. B., Zwaan, K. B., Corfu, F., Ravna, E. J. K., and Myhre, P. I. (2010). "Neoarchean to Svecofennian tectono-magmatic evolution of the West Troms Basement Complex, North Norway." In: *Norwegian Journal of Geology* **90**, p. 28 (cit. on pp. 7, 8, 9, 25).

Bergh, S. G., Kullerud, K., Corfu, F., Armitage, P. E. B., Davidsen, B., Johansen, H. W., Pettersen, T., and Knudsen, S. (2007). "Low-grade sedimentary rocks on Vanna, North Norway: a new occurrence of a Palaeoproterozoic (2.4-2.2 Ga) cover succession in northern Fennoscandia." In: *Norwegian Journal of Geology* **87**, p. 18 (cit. on pp. 7, 8, 10, 11, 12, 13, 25).

Bingen, B., Solli, A., Viola, G., Torgersen, E., Sandstad, J. S., Whitehouse, M. J., Røhr, T. S., Ganerød, M., and Nasuti, A. (2015). "Geochronology of the Palaeoproterozoic Kautokeino Greenstone Belt, Finnmark, Norway: Tectonic implications in a Fennoscandia context." In: *Norwegian Journal of Geology* **95**, pp. 365–396 (cit. on p. 4).

Binns, R. E., Chroston, P. N., and Matthews, D. W. (1980). "Low-grade sediments on Precambrian Gneiss on Vanna, Troms, Northern Norway." In: *Offprint NGU* **359**, p. 12 (cit. on p. 10).

Bleeker, W. (2003). "The late Archean record: a puzzle in ca. 35 pieces." In: *Lithos* **71**, p. 28 (cit. on p. 4).

Bratrein, H. D. (1989). *Karlsøy og Helgøy bygdebok: folkeliv, næringsliv, samfunnsliv 3: Fra år 1860 til 1925*. Vol. X. Springer, p. 656 (cit. on pp. 10, 13).

Brune, S., Williams, S. E., and Müller, R. D. (2017). "Potential links between continental rifting, CO_2 degassing and climate change through time." In: *Nature letters* **10**, pp. 941–946 (cit. on p. 27).

Bugge, C. (1935). *Rapport over Senjens nikkelverk*. Report. NGU (cit. on p. 9).

Cathelineau, M. (1988). "Cation site occupancy in chlorites and illites as a function of temperature." In: *Clay Minerals* **23**, p. 15 (cit. on p. 16).

Corfu, F. (2004). "U-Pb age, setting and tectonic significance of the anorthosite-mangerite-charnockite-granite suite, Lofoten-Vesterålen, Norway." In: *Journal of Petrology* **45**.9, p. 21 (cit. on p. 7).

Corfu, F., Armitage, P. E. B., Kullerud, K., and Bergh, S. G. (2003). "Preliminary U-Pb geochronology in the West Troms Basement Complex, north Norway:

Archean and Palaeoproterozoic events and younger overprints." In: *NGU Bulletin* **441**, p. 12 (cit. on pp. 7, 25).

Dallmeyer, R. D. (1992). "$^{40}Ar/^{39}Ar$ mineral ages within the Western Gneiss Terrane, Troms: evidence of polyphase Proterozoic tectonothermal activity (Svecokarelian and Sveconorwegian)." In: *Precambrian Research* **57**, p. 12 (cit. on p. 25).

Daly, J. S., Balagansky, V. V., Timmerman, M. J., and Whitehouse, M. J. (2006). "The Lapland-Kola orogen: Palaeoproterozoic collision and accretion of the northern Fennoscandian lithosphere." In: *Geological Society, London, Memoirs* **32**, pp. 579–598 (cit. on p. 4).

Davids, C., Benowith, J. A., Layer, P., Wemmer, K., Zwingmann, H., and Bergh, S. (2012). "$^{40}Ar/^{39}Ar$ dating of hydrothemally altered K-feldspar - Permian brittle faulting in northern Norway." In: *The 13th International Conference on Thermochronology*, p. 1 (cit. on p. 6).

Davids, C., Wemmer, K., Zwingmann, H., Kohlmann, F., Jacobs, J., and Bergh, S. (2013). "K-Ar illite and apatite fission track constraints on brittle faulting and the evolution of the northern Norwegian passive margin." In: *Tectonophysics* **608**, p. 16 (cit. on pp. 3, 6, 8, 22, 27).

Eilu, P. (2012). *Mineral deposits and metallogeny of Fennoscandia*. Special Publication 53. Geological survey of Finland (cit. on pp. 2, 3, 4).

Eilu, P., Sorjonen-Ward, P., Nurmi, P., and Niiranen, T. (2003). "A review of gold mineralisation styles in Finland." In: *Economic geology* **98**, p. 26 (cit. on pp. 3, 4).

Faber, C., Stünitz, H., Gasser, D., Jeřábek, P., Kraus, K., Corfu, F., Ravna, E. K., and Konopásek, J. (2019). "Anticlockwise metamorphic pressure–temperature paths and nappe stacking in the Reisa Nappe Complex in the Scandinavian Caledonides, northern Norway: evidence for weakening of lower continental crust before and during continental collision." In: *Solid Earth* **10**, pp. 117–148 (cit. on pp. 5, 25).

Fall, A., Tattitch, B., and Bodnar, R. J. (2011). "Combined microthermometric and Raman spectroscopic technique to determine the salinity of H_2O-CO_2-NaCl fluid inclusions based on clathrate melting." In: *Geochimica et Cosmochimica acta* **75**, pp. 951–964 (cit. on p. 17).

Gaál, G. and Gorbatschev, R. (1987). "An Outline of the Precambrian Evolution of the Baltic Shield." In: *Precambrian Research* **35**, p. 38 (cit. on p. 4).

Gabrielsen, R. H. and Braathen, A. (2014). "Models of fracture lineaments - joint swarms, fracture corridors and faults in crystalline rocks, and their genetic relations." In: *Tectonophysics* **628**, p. 19 (cit. on p. 1).

Giffin, B. J., Joy, D. C., and Michael, J. R. (2010). "A comparison of a luminescence-based VPSE and an electron-based GSED for SE and CL imaging in variable pressure SEM with conventional SE imaging." In: *Microscopy and Microanalysis* **160**, pp. 825–843 (cit. on p. 16).

Griffin, W. L., Taylor, P. N., Hakkinen, J. W., Heier, K. S., Iden, I. K., Krogh, E. J., Malm, O., Olsen, K. I., Ormaasen, D. E., and Tveten, E. (1978). "Archean and Proterozoic crustal evolution in Lofoten-Vesterålen, N Norway." In: *Journal of the Geological Society of London* **135**, p. 19 (cit. on p. 7).

Grogan, P. and Zwaan, B. (1997). *Geologisk kart over Norge, berggrunnskart Helgøy, M 1:250 000*. Report. Geological survey of Norway (cit. on p. 11).

Haaland, L. C. (2018). "Geometry and kinematic evolution of ductile shear zones in the Ersfjord Granite (1.79 Ga), West Troms Basement Complex: a Svecofennian accretionary thrust system." MSc Thesis. UiT - the Arctic University of Tromsø (cit. on pp. 7, 8, 26).

Hansen, J.-A., Bergh, S. G., and Henningsen, T. (2012). "Mesozoic rifting and basin evolution on the Lofoten and Vesterålen margin, North Norway; time constraints and regional implications." In: *Norwegian Journal of Geology* **91**, pp. 203–228 (cit. on p. 6).

Hanski, E., Huhma, H., and Vaasjoki, M. (2001). "Geochronology of northern Finland: a summary and discussion." In: *Special Paper 33*. Ed. by Vaasjoki, M. Geological Survey of Finland, pp. 255–279 (cit. on p. 4).

Henderson, I., Viola, G., and Nasuti, A. (2015). "A new tectonic model for the Palaeoproterozoic Kautokeino Greenstone Belt, northern Norway, based on high-resolution airborne magnetic data and field structural analysis and implications for mineral potential." In: *Norwegian Journal of Geology* **95**.3-4, p. 26 (cit. on pp. 4, 7).

Högdahl, K., Andersson, U. B., and Eklund, O. (2004). *The Transscandinavian Igneous Belt (TIB) in Sweden: a review of its character and evolution*. Geological Survey of Finland, p. 125 (cit. on p. 4).

Hölttä, P., Balagansky, V., Garde, A. A., Mertanen, S., Peltonen, P., Slabunov, A., Sorjonen-Ward, P., and Whitehouse, M. (2008). "Archean of Greenland and Fennoscandia." In: *Episodes* **13**.1, p. 7 (cit. on p. 3).

Indrevær, K., Bergh, S. G., Koehl, J.-B., Hansen, J.-A., Schermer, E. R., and Ingebrigtsen, A. (2013). "Post-Caledonian brittle fault zones on the hyper-extended SW Barents Sea margin: New insights into onshore and offshore margin architecture." In: *Norwegian Journal of Geology* **93**, p. 23 (cit. on pp. 3, 6, 27, 28, 29).

Johannessen, H. (2012). "Tinnvatnformasjonen i Vannas proterozoiske lagrekke: Sedimentære facies og avsetningsmiljø." MSc Thesis. UiT - the Arctic University of Tromsø (cit. on pp. 10, 26).

Johansen, H. (1987). "Forholdet mellom det prekambriske underlaget og overliggende sedimentære bergarter sør-øst på Vanna, Troms." MSc Thesis. UiT - the Arctic University of Tromsø (cit. on p. 11).

Karlsen, S. E. (2019). "Strukturell og kinematisk analyse av Skipsfjorddekket og underliggende bergarter i nordøstlige del av Vanna, Vest-Troms gneisregion." MSc Thesis. UiT - the Arctic University of Tromsø (cit. on p. 12).

Kirkland, C. L., Daly, J. S., and Whitehouse, M. J. (2007). "Provenance and Terrane Evolution of the Kalak Nappe Complex, Norwegian Caledonides: Implications for Neoproterozoic Paleogeography and Tectonics." In: *The Journal of Geology* **115**, pp. 21–41 (cit. on p. 25).

Kirstein, L. A., Davies, G. R., and Heeremans, M. (2006). "The petrogenesis of Carboniferous–Permian dyke and sill intrusions across northern Europe." In: *Contributions to Mineralogy and Petrology* **152**, pp. 721–742 (cit. on p. 26).

Koehl, J.-B. (2013). "Late Paleozoic-Cenozoic fault correlation and characterization of fault rocks in western Troms, North Norway." MSc Thesis. UiT - the Arctic University of Tromsø (cit. on pp. 3, 29).

Koehl, J.-B., Bergh, S., Henningsen, T., and Faleide, J.-I. (2018). "Middle to Late Devonian-Carboniferous collapse basins on the Finnmark Platform and in the southwesternmost Nordkapp basin, SW Barents Sea." In: *Solid Earth* **9**, p. 32 (cit. on p. 6).

Koistinen, T., Stephens, M. B., Bogatchev, V., Nordgulen, Ø., Wennerström, M., and Korhonen, J. (2001). *Geological map of the Fennoscandian Shield, scale 1:2 000 000*. Report. Geological surveys of Finland, Norway, Sweden, and the north-west department of ministry of Natural Resources of Russia (cit. on pp. 3, 4).

Kontak, D. J. (2004). "Analysis of evaporate mounds as a complement to fluid-inclusion thermometric data: case studies from granitic environments in Nova Scotia and Peru." In: *The Canadian Mineralogist* **42**, p. 16 (cit. on p. 17).

Kullerud, K., Skjerlie, K. p., Corfu, F., and de la Rosa, J. D. (2006). "The 2.40 Ga Ringvassøy mafic dykes, West Troms Basement Complex, Norway: The concuding act of early Palaeoproterozoic continental breakup." In: *Precambrian Research* **150**, p. 18 (cit. on p. 7).

Kullerud, K., Zozulya, D., Bergh, S., Hansen, H., and Ravna, E. J. K. (2011). "Geochemistry and tectonic setting of a lamproite dyke in Kvaløya, North Norway." In: *Lithos* **126**, p. 12 (cit. on p. 26).

Lafuente, B., Downs, R. T., Yang, H., and Stone, N. (2015). *Highlights in Mineralogical Crystallography*. *The power of databases: the RRUFF project*. Ed. by Armbruster, T. and Danisi, R. M. Berlin, Germany: W. De Gruyter, pp. 1–30 (cit. on p. 17).

Lahtinen, R., Hallberg, A., Korsakova, M., Sandstad, J. S., and Eilu, P. (2012). "Main metallogenic events in Fennoscandia: Summary." In: *Special Paper 53*. Ed. by Eilu, P. Geological Survey of Finland, pp. 397–401 (cit. on p. 4).

Lahtinen, R., Hölttä, P., Kontinen, A., Niiranen, T., Nironen, M., Saalmann, K., and Sorjonen-Ward, P. (2011). "Tectonic and metallogenic evolution of the Fennoscandian Shield: key questions with emphasis on Finland." In: *Special Paper 49*. Ed. by Neonen, K. and Nurmi, P. A. Geological Survey of Finland, pp. 23–33 (cit. on pp. 3, 4, 7).

Landmark, K. (1973). "Beskrivelse til de geologiske kartene Tromsø og Målselv II. Kaledonske bergarter." In: *Tromsø Museums Skrifter* **15**, pp. 1–263 (cit. on pp. 12, 25).

Larsen, R. B., Grant, T., Sørensen, B. E., Tegner, C., McEnroe, S., Pastore, Z., Fichler, C., Nikolaisen, E., Grannes, K. R., Church, N., ter Maat, G. W., and Michels, A. (2018). "Portrait of a giant deep-seated magmatic conduit system: the Seiland Magmatic Province." In: *Lithos* **299**.22, pp. 600–622 (cit. on p. 5).

Laurent, O., Vander, J., Bingen, B., Bolle, O., and Gerdes, A. (2019). "Building up the first continents: Mesoarchean to Paleoproterozoic crustal evolution in West Troms, Norway, inferred from granitoid petrology, geochemistry and zircon U-Pb/Lu-Hf isotopes." In: *Precambrian Research* **321**, pp. 303–327 (cit. on pp. 7, 8).

Lippard, S. J. and Prestvik, T. (1997). "Carboniferous dolerite dykes on Magerøy; new age determinations and tectonic significance." In: *Norsk Geologisk Tidsskrift* **77**, pp. 159–163 (cit. on pp. 5, 27).

Mosar, J. (2003). "Scandinavias North Atlantic passive margin." In: *Journal of Geophysical Research* **108**.B8, p. 18 (cit. on pp. 6, 27).

Motuza, G. (2000). *Description to the geological map of the central part of the Ringvassøya Greenstone Belt, Troms county, northern Norway*. Report. Geological survey of Norway (cit. on p. 7).

Myhre, P. I., Corfu, F., Bergh, S. G., and Kullerud, K. (2013). "U-Pb geochronology along an Archean geotransect in the West Troms Basement Complex, North Norway." In: *Norwegian Journal of Geology* **93**, p. 24 (cit. on p. 7).

Nasuti, A., Roberts, D., and Gernigon, L. (2015). "Multiphase mafic dykes in the Caledonides of northern Finnmark revealed by a new high-resolution aeromagnetic dataset." In: *Norwegian Journal of Geology* **95**.3-4, pp. 285–298 (cit. on p. 27).

Nironen, M. (1997). "The Svecofennian Orogen: a tectonic model." In: *Precambrian Research* **86**, p. 24 (cit. on p. 4).

Ojala, J. V., Hansen, H., and Ahola, H. (2013). "Cu-Zn mineralisation at Vannareid, West Troms Basement Complex: a new Palaeoproterozioc VMS occurrence in the northern Fennoscandian Shield." In: *12th Biennial SGA Meeting* (cit. on pp. 15, 22).

Olesen, O., Lundin, E., Nordgulen, Ø., Osmundsen, P. T., Skilbrei, J. R., Smethurst, M. A., Solli, A., Bugge, T., and Fichler, C. (2002). "Bridging the gap between the onshore and offshore geology in Nordland, northern Norway." In: *Norwegian Journal of Geology* **82**, p. 20 (cit. on p. 3).

Olesen, O., Torsvik, T. H., Tveten, E., Zwaan, K. B., Løseth, H., and Henningsen, T. (1997). "Basement structure of the continental margin in the Lofoten-Lopphavet area, northern Norway: constraints from potential field data, on-land structural mapping and palaeomagnetic data." In: *Norwegian Journal of Geology* **77**, pp. 15–30 (cit. on p. 5).

Opheim, J. A. and Andresen, A. (1989). "Basement-cover relationships on northern Vanna, Troms, Norway." In: *Norsk Geologisk Tidsskrift* **69**, p. 5 (cit. on pp. 10, 11, 12, 25).

Paulsen, H., Bergh, S., Strmic Palinkas, S., Armitage, P., Karlsen, S., Kolsum, S., Rønningen, I., and Nazuti, A. (2019). "Late-Svecofennian fold-thrust belt and oblique-slip structures on Vanna island, West Troms Basement Complex, and their relation to meta-sedimentary sequences." In: *Geological Society of Norway Wintermeeting*. Program with Abstracts. Bergen (cit. on p. 13).

Pettersen, K. (1887). *Den nord-norske fjeldbygning I*. Vol. 10. Tromsø Museums Årshefte. Tromsø Museum, p. 174 (cit. on pp. 10, 12, 25).

Rice, A. H. J. (1990). "A discussion: Basement-cover relationships on northern Vanna, Troms, Norway." In: *Norsk Geologisk Tidsskrift* **70**, p. 8 (cit. on p. 12).

Rice, A. H. N. (2014). "Restoration of the external Caledonides, Finnmark, North Norway." In: *Geological Society of London Special Publication* **390**, pp. 271–299 (cit. on p. 27).

Roberts, D. (1974). *Kartblad Hammerfest. Beskrivelse til det 1:250 000 berggrunnsgeologiske kart*. Report. Geological survey of Norway (cit. on p. 11).

Roberts, D. (2011). "Age of the Hamningberg dolerite dyke, Varanger Peninsula, Finnmark: Devonian rather than Vendian - a revised interpretation." In: *Norges Geologiske Undersøkelse Bulletin* **451**, pp. 32–36 (cit. on p. 27).

Roberts, D. and Lippard, S. J. (2005). "Inferred Mesozoic faulting in Finnmark: current status and offshore links." In: *NGU Bulletin* **443**, p. 6 (cit. on p. 5).

Roberts, D., Torsvik, T., Andersen, T. B., and Rehnström, E. F. (2003). "The Early Carboniferous Magerøy dykes, northern Norway; palaeomagnetism and palaeogeography." In: *Geological Magazine* **140**, pp. 443–451 (cit. on p. 27).

Roedder, E. (1984). *Fluid inclusions*. Vol. 12. Reviews in Mineralogy. Blacksburg, Virginia: U S geological Survey, p. 644 (cit. on pp. 16, 17).

Rønningen, I. U. (2019). "Geometrisk og kinematisk analyse av paleoproterozoiske duktile skjærsoner i Skipsfjorddekkets undre del, Vanna, Vest-Troms gneisregionen, og relasjon til metasedimentære bergarter i Vannagruppen." MSc Thesis. UiT - the Arctic University of Tromsø (cit. on p. 12).

Sandstad, J. S. and Nilsson, L. P. (1998). *Gullundersøkelser på Ringvassøy, sammenstilling av tidligere prospektering og feltbefaring i 1997*. Report. NGU (cit. on p. 10).

Sibson, R., Moore, J., and Rankin, A. H. (1975). "Seismic pumping - a hydrothermal fluid transport mechanism." In: *Journal of the Geological Society of London* **131**, p. 7 (cit. on p. 1).

Tarantola, A., Diamond, L. W., and Stünitz, H. (2010). "Modification of fluid inclusions in quartz by deviatoric stress I: experimentally induced changes in inclusion shapes and microstructures." In: *Contributions to Mineralogy and Petrology* **16**, p. 624 (cit. on p. 17).

Thorstensen, L. (2011). "Land-sokkel korrelasjon av tektoniske elementer i ytre del av Senja og Kvaløya i Troms." MSc Thesis. UiT - the Arctic University of Tromsø (cit. on p. 8).

Weihed, P., Arndt, N., Billström, K., Duchesne, J.-C., Eilu, P., Martinsson, O., Papunen, H., and Lathinen, R. (2005). "Precambrian geodynamics and ore formation: The Fennoscandian Shield." In: *Ore Geology Reviews* **27**, p. 49 (cit. on p. 4).

Wilkinson, J. (2001). "Fluid inclusions in hydrothermal ore deposits." In: *Lithos* **55**, p. 44 (cit. on p. 16).

Zwaan, K. B. (1989). *Berggrunnsgeologisk kartlegging av det prekambriske grønnsteisbelte på Ringvassøya, Troms*. Report. NGU (cit. on pp. 7, 10).

Zwaan, K. B. (1995). "Geology of the West Troms Basement Complex, northern Norway, with emphasis on the Senja Shear Belt: a preliminary account." In: *NGU Bulletin* **427**, pp. 33–36 (cit. on p. 7).

Fold-thrust belt structures and oblique faults on Vanna island, West Troms Basement Complex, and their relation to inverted metasedimentary sequences

Paulsen, H.K.[1], Bergh, S.G.[1], Strmic Palinkas, S.[1], Karlsen, S.[1], Kolsum, S. E.[1] & Rønningen, I.[1] and Nasuti, A.[2]

[1]University of Tromsø (UiT) – The Arctic University of Norway, 9037 Tromsø
[2] Geological Survey of Norway, 7491 Trondheim

Abstract

Complex fold-thrust and oblique, strike-slip accretionary tectonism of presumed Svecofennian age characterize the deformation of Neoarchaean basement gneisses (2.9-2.6 Ga), Palaeoproterozoic metasedimentary cover and intrusive rocks (2.2 Ga) on the island of Vanna, in the West Troms Basement Complex, northern Norway. Low-grade metasedimentary sequences occur in separate areas of the southeastern and western parts of the island as para-autochthonous and allochthonous units relative to a major thrust front in the north/central part. In the southeast, the Vanna Group sequence of metapsammites and calcareous metapelites, and an enclosed intrusive diorite sill dated at 2.2 Ga, were folded by SE-verging macrofolds together with the underlying basement gneisses, and truncated by low-angle, NW-dipping thrust zones that developed axial-planar to the macrofolds. In the western part of Vanna, a comparable sedimentary sequence and intrusive diorite sills are present at Hamre and Kvalvågklubben. These occurrences display a more complex internal deformation characterized by two sets of partly overturned folds verging NE and SE, with related NNW-SSE and NNE-SSW striking reverse faults, a dominant W-WSW dipping foliation, and steep, N-S striking ductile shear zones. The eastern boundary to the sedimentary sequences is a tectonic buttress contact against a steep, N-S to NNE-SSW striking reverse fault that merges into a dextral strike-slip shear zone northwards in the tonalitic basement gneisses, where the metasedimentary strata are folded, thrusted and partly inverted. In the north/central part of Vanna, a pronounced thrust system exists in the basement gneisses, termed the Skipsfjord Nappe, which emplaced repeated, imbricate sheets of foliated tonalitic and granitoid basement gneisses, metamorphosed sedimentary slivers, and intrusive mafic rocks over remnant medium-grade metasedimentary units. Individual sheets of the Skipsfjord Nappe are separated by mylonitic shear zones that dip gently NW and exhibit mainly top-to-SE thrust displacement, similar to deformation in the para-autochthonous Vanna Group in the south. Below the Skipsfjord Nappe at Svartbergan in the east is a c. 2 km thick para-autochthonous thrust sheet of quartz-feldspathic metasandstones and -pelites, resembling rocks of the Vanna Group, although previously mapped as mylonitized basement gneisses. These strata dip steeply NW and are internally folded and sheared, and truncated by the overlying gently dipping Skipsfjord Nappe. The underlying basement gneisses in southern Vanna display a similar thrust/reverse fault and oblique-lateral shear zone network, which is well expressed in high-resolution tilt-derivative aeromagnetic data acquired by the Geological Survey of Norway. The combined field and magnetic data are compatible with development of the structures in two major contractional events (D_1-D_2) for the Vanna deformation. The D_1 event involved ENE-WSW shortening, thick- and thin-skinned folding, thrusting and inversion of supracrustal rocks in western Vanna. The D_2 event caused major SE-directed thrusting of the Skipsfjord and Svartbergan nappes, basement-involved fold-thrust propagation in the para-autochthonous Vanna Group in southeastern Vanna, and sinistral strike-slip reactivation of steep N-S trending basement faults. These complex, two-stage fold-thrust systems are likely of Late Svecofennian age, supported by age determinations elsewhere in West Troms Basement Complex. In such a setting, Palaeoproterozoic sedimentary sequences/basins may have covered several crustal areas and controlled the location, extent and character of the Late Svecofennian fold-thrust and orogen-

oblique shear zones, concomitant inversion of metasedimentary sequences, and mineralization. Recent Ar-Ar age determination of muscovite in the Skipsfjord Nappe, however, reveals Caledonian (420 Ma) ages for the latest SE-directed fold-thrust event, which is at a high angle to most of the Svecofennian structures farther southwest, and calls into question or at least requires modification of previously proposed tectonic models for the northeastern parts of the West Troms Basement Complex. In economic terms, the thrusts, steep oblique shear zones, and intrusive contacts in both the metasedimentary units and basement gneisses exhibit mineralization and quartz-carbonate veining, locally with emerald-quality beryl and fuchsite-bearing fabrics, suggesting strong structural control on mineralization.

Introduction

The West Troms Basement Complex in northern Norway, situated west of the Scandinavian Caledonides (**Fig.** 1), consists of Meso/Neoarchaean and Palaeoproterozoic basement rocks preserved in a mid- to upper crustal transect (**Fig.** 2; Bergh et al. 2010; Myhre et al. 2013; Laurent 2019). These rocks are thought to be contiguous with autochthonous parts of the Fennoscandian Shield in Russia/Kola, Finland/Lapland and northern Sweden/Norrbotten (**Fig.** 1; Gorbatchov and Bogdanova 1993; Lahtinen et al. 2005, 2009; 2015; Hölttä et al. 2008; Bergh et al. 2012, 2014, 2015). The West Troms Basement Complex is a key area for studying the regional-scale tectonic architecture of a Late Svecofennian (1.77-1.65 Ga) accretionary orogen thanks to its long-lasting polyphase tectono-magmatic history (Bergh et al. 2015), and excellent 3-D bedrock exposures. The region hosts numerous volcano-sedimentary successions (greenstone belts) formed mainly by Palaeoproterozoic rifting (2.4-1.9 Ga) and a variety of magmatic/intrusive rocks dated at c. 1.8 Ga (Corfu et al. 2003; Myhre et al. 2011, 2013). In the present study, we explore the foreland portion of this mid-crustal transect and its basement-cover successions on the island of Vanna (**Figs.** 2, 3), which exhibits Neoarchaean basement gneisses and several overlying para-autochthonous metasupracrustal units dated at 2.4-2.2 Ga (Bergh et al. 2007), named the Vanna Group (Binns et al. 1980), and the allochthonous Skipsfjord Nappe (Opheim & Andresen 1989; Bergh et al. 2007). Recent studies show that these units experienced polyphase and possibly partitioned, basement-involved fold-thrust and strike-slip deformation of presumed Late Svecofennian age compatible with accretionary tectonism in higher-grade units farther west (Bergh et al. 2010; Paulsen et al. 2019c). These deformation events were also responsible for extensive hydrothermal alteration and emerald mineralization of the host rocks on Vanna (Bergh et al. 2007; Paulsen et al. 2019a), and may therefore have some importance for future mineral exploration in the area.

The boundary faults to the para-autochthonous metasedimentary units on Vanna (**Fig.** 3) are poorly exposed but, where observable, they seem to have controlled both the location of pre-/synorogenic Svecofennian magmatic intrusions and corresponding ductile fabrics, such as thrust faults and oblique strike-slip faults (Paulsen et al. 2019c). The main goal of the paper is to portray and discuss the structural architecture and evolution of the Vanna portion of the crustal transect, using field data and new magnetic susceptibility data acquired by the Geological Survey of Norway (Nasuti et al. 2015; Sandstad et al. 2015). We focus on the Palaeoproterozoic metasupracrustal successions and their boundary faults, and how the individual sedimentary units responded to Late Svecofennian accretionary orogenic deformation. We argue that the observed structures were developed by a basement-seated fold-thrust shortening event and oblique, partitioned lateral faulting event, both in the Palaeoproterozoic. The structural evolution on Vanna is also important in relation to accretionary tectonism in the West Troms Basement Complex farther southwest (Bergh et al. 2010), similarities with the northern Fennoscandian Shield and its tectonic evolution (cf. Nironen 1997; Bergman et al. 2001, 2006; Daly et al. 2006; Hölttä et al. 2007; Lahtinen et al. 2005, 2009, 2015), and for

consideration of Caledonian reworking of the region. Furthermore, understanding the tectonics of the Vanna segment of the West Troms Basement Complex crustal transect, and its possible relation to Caledonian structural overprint, is important from an economic perspective (Eilu, 2012).

The West Troms Basement Complex

The oldest rocks in the West Troms Basement Complex (WTBC) are Meso- and Neoarchaean TTG gneisses (2.9-2.6 Ga) that vary between tonalitic, granitoid and quartz-dioritic in composition (Bergh et al. 2010; Myhre et al. 2013). These rocks were all severely deformed and partly migmatized during Neoarchaean orogenies (2.8-2.6 Ga: Myhre et al. 2013), spatially separated by lensoidal terrane boundaries (Bergh et al. 2010), and cut by a mafic dyke swarm dated at c. 2.4 Ga (Kullerud et al. 2006). Metasupracrustal cover units (greenstone belts) with variable ages, composition and metamorphic grade overly the basement gneisses (Zwaan 1989; Armitage & Bergh 2005; Bergh et al. 2010). The depositional ages span from c. 2.7 Ga for parts of the Ringvassøya greenstone belt (Zwaan 1989; Motuza et al. 2000), 2.2-2.4 Ga for the Vanna Group (Bergh et al. 2007), to >1.9 Ga for the Torsnes supracrustal belt (Myhre et al. 2011). A suite of granites (Ersfjord Granite) and mafic igneous rocks (Hamn Gabbro) formed synchronously with a major suite of 1.8–1.7 Ga plutonic rocks in Lofoten and Vesterålen (Griffin et al. 1978; Corfu 2004). The Ersfjord Granite may have formed by partial melting of the TTG crust (Haaland 2018; Laurent et al. 2019) and was emplaced during waning stages of the Svecofennian orogeny (1.92-1.78 Ga) as defined in the Fennoscandian Shield (Lahtinen et al. 2008). This deformation is dated at c. 1.77-1.65 Ga in the Senja Shear Belt, a major ductile deformation zone (**Fig.** 2; Bergh et al. 2015; Laurent et al. 2019), which involved three phases of deformation: crustal contraction and accretion and partitioned thrust and strike-slip deformation (transpression) (Bergh et al. 2010). The Svecofennian deformation in the WTBC affected the entire province by generating an early-phase, ductile gneissic foliation, SW- and NE-dipping thrusts, and NW-SE trending tight, upright fold systems. During the late-stage event, steeply NW-SE plunging folds and subvertical ductile shear zones (strike-slip faults) formed in the Senja Shear Belt, whereas SE-directed orogen-normal thrusts and steep NW-SE striking lateral shear zones formed in the northeast on Ringvassøya and Vanna (**Fig.** 2; Bergh et al. 2010). Peak metamorphism reached high-grade granulite and amphibolite facies in the Senja and Lofoten/Vesterålen parts of the transect during the early-stage events (**Fig.** 2), whereas medium- to low-grade greenschist facies characterized the late-stage event in the northeast (Vanna island, this work), implying that the studied transect evolved from a hinterland (deep crust) in the southwest to a foreland (upper crust) in the northeast (Bergh et al. 2010).

Geology of Vanna

Vanna island is located in the northeastern part of the WTBC (**Fig.** 2) and is underlain by Neoarchaean tonalitic gneisses (2.9-2.6 Ga) with foliation-parallel 2.4 Ga mafic dykes (Opheim & Andresen 1989; Kullerud et al. 2006). A low-grade metasedimentary cover unit, the Vanna Group (Binns et al. 1980; Johansen 1987) is present along the southeastern coast between Vikan and Lanes (**Fig.** 3), and rests with a depositional contact on the basement gneisses. Despite strong, presumed Late Svecofennian contractional deformation (Bergh et al. 2007), primary features are locally well preserved. The lowest formation is deltaic arkosic sandstones (Binns et al. 1980), succeeded by shallow-marine calcareous mudstones and siltstones (>150 m thickness), intruded by a diorite sill dated at 2221 ± 3 Ma (Binns et al. 1980; Bergh et al. 2007) with an intracontinental tholeiitic geochemical signature (Johansen, 1987). The basement contact and overlying strata are deformed by SE-directed fold- and basement-seated thrust faults within and below the diorite sill (Bergh et al. 2007; Kolsum 2019). Similar but smaller and less studied para-autochthonous cover units exist in western and central parts of Vanna: at Hamre-Kvalvågklubben, Kvalshausen, Svartbergan, and at Skipsfjorden (**Fig.** 3) (addressed in this work).

These rocks are folded (N-S and NE-SW axial traces), foliated (WSW-dipping), and bounded by a steep NNE-SSW striking ductile shear zone in the basement gneisses on their eastern side (**Fig.** 3). The allochthonous Skipsfjord Nappe (Opheim & Andresen 1989) is located in the central part of Vanna (**Fig.** 3) and constitutes variously mylonitized tonalitic gneisses and intercalated lenses of metasedimentary and mafic intrusive rocks of the Kvalkjeften Group (Opheim & Andresen 1989). The metamorphic grade is generally higher than in the para-autochthonous units (lower amphibolite facies), and the rocks have a more pronounced foliation which coincides with ductile shear zones dipping gently NW. New structural investigations (this work) have uncovered a thrust contact and c. 500 m thick sequences of steeply tilted quartzites and metapelites below the Skipsfjord Nappe at Svartbergan (**Fig.** 3); this metasupracrustal series may correspond to the para-autochthonous units farther south (Opheim & Andresen 1989; Karlsen 2019; Rønningen 2019). In the north, the Skipsfjord Nappe is down-thrown >3 km along the post-Caledonian brittle Vannareid-Burøysund normal fault (Opheim & Andresen 1989; Davids et al. 2013), which hosts extensive Cu-Zn bearing quartz-carbonate veins (cf. Paulsen et al. 2019b).

Methods and workflow

In this paper we explore the new results of ongoing structural studies of the TTG basement gneisses and the above-mentioned metasedimentary units on Vanna. We focus on the nature of inferred Late Svecofennian contractional and strike-slip fabrics in the supracrustal units and underlying basement rocks, their spatial and temporal evolution, and kinematic (sense-of-shear) relationships. New magnetic susceptibility data from the Geological Survey of Norway (Nasuti et al. 2015; Sandstad et al. 2015) largely support the very complex structural architecture on Vanna, and allow us to explore and correlate fold-thrust structures and steep lateral faults that are compatible with a partitioned Palaeoproterozoic tectonic model (Bergh et al. 2010). Furthermore, we compare the structural pattern on Vanna with regional Svecofennian structures elsewhere in the WTBC and address links to similar settings in Fennoscandia. We also comment on new absolute age determinations of the fold-thrust structures on Vanna, some of which have yielded Caledonian ages (c. 420 Ma, cf. Opheim & Andresen 1989; Rice 1990). Another important issue is to discuss the structural control on mineralization on Vanna, e.g. hydrothermal alteration along contacts between the diorite and host rocks, and within shear zones in all domains of the studied metasupracrustal rocks (which are the main topics in other papers by Paulsen et al. 2019).

Results

Lithostratigraphic and structural data were obtained from five separate areas that contain metasedimentary successions (**Fig.** 3), including: (i) the Vanna group at Vikan-Larstangen, (ii) Hamre-Kvalvågklubben, (iii) Kvalkjeften Group in Skipsfjord Nappe, and (iv) Svartbergan Nappe. We describe and compare effects of the presumed Late Svecofennian orogenic deformation in these successions and in the para-autochthonous basement gneisses in the southern part of Vanna, arguing for polyphase folding, thrusting and oblique strike-slip faulting, and possible effect of Caledonian structural reworking. The relative timing of various ductile fabrics has been confirmed by superposition of structures, particularly in key outcrops at Kvalvågklubben and Hamre on the west side of the island, and along the boundary to basement gneisses on their eastern side between Vikan and Larstangen (**Fig.** 3), as outlined below.

Vikan-Larstangen

Vikan is the type area for the low-grade Palaeoproterozoic Vanna Group, where it unconformably overlies the tonalitic basement gneisses along its northern boundary (**Fig.** 4). The Vanna Group at

Vikan has been the subject of several previous studies, focusing on stratigraphic build-up and depositional facies reconstructions, and its presumed Late Svecofennian contractional deformation (e.g. Binns et al. 1980; Johansen 1989; Bergh et al. 2007, 2010; Pettersen 2007; Knudsen 2007, Johannessen 2012). An intrusive sill of diorite in the Vanna group was dated at 2221 ± 3 Ma (Bergh et al. 2007), and since 2.4 Ga mafic dykes in the basement gneisses do not cut the basal unconformity (Bergh et al. 2007), a Palaeoproterozoic 2.4-2.2 Ga depositional age is inferred for the Vanna Group, revoking a previously interpreted Neoproterozoic depositional age (Binns et al. 1980; Johansen 1987).

The unconformable contact with the basement gneisses at Vikan (**Fig.** 4) is steep to subvertical due to basement-involved folding, and is characterized by a c. 20 cm thick basal conglomerate (Bergh et al. 2007). Directly overlying is a c. 70 m thick sequence of shallow marine deltaic, arkosic sandstones (Tinnvatn Formation), with well-preserved sedimentary structures such as rhythmic lamination (**Fig.** 5a), trough cross-bedding (**Fig.** 5b) and wavy ripple marks. Southwards, the Tinnvatn Formation is overlain by a calcareous mud- and siltstone sequence (Bukkheia Formation, c. 100 m exposed thickness) displaying ripple marks and mud cracks (**Figs.** 5c, d), indicating a tidal marine deposition (Binns et al. 1980; Bergh et al. 2007). Units above the Bukkheia Formation are covered by the diorite sill, but a similar sequence of mudstones and siltstones reappears as aligned rafts both within the diorite and as a separate unit on the southern side of the diorite at Myra and Larstangen (Bergh et al. 2007; Knudsen 2007; Kolsum 2019).

The entire metasedimentary succession and the diorite sill at Vikan has been deformed together (see photos in Bergh et al. 2007) by SE-verging upright, tight, asymmetric major folds with associated NW-dipping axial-planar cleavages and thrust faults. Primary bedding (**Fig.** 4a) is preserved in most fold hinges at a high angle to foliation, but is mostly parallel to the main NW-dipping cleavage and thrust faults along the fold limbs (**Figs.** 4a, b). Typically, axial-planar thrusts repeat the stratigraphy of the Bukkheia mudstones and define a tectonic contact to the Tinnvatn Formation below (**Fig.** 4). In addition, a younger set of subvertical folds have refolded the tilted metasandstone beds in upright macrofolds, creating steep E-W to NW-SE striking mylonitic strike-slip shear zones, mostly with a sinistral shear sense (**Fig.** 4c). These steep shear zones are superimposed onto, and/or partly cut the main NW-dipping foliation at a low angle (Bergh et al. 2007).

South of the large composite diorite sill, at Myra and Larstangen (**Fig.** 4), the intrusive contact and bedding in the metapsammites is still preserved (**Figs.** 6a, 4g). However, the diorite in the contact is usually strongly foliated and mylonitized (**Fig.** 6b) in zones that dip moderately to the WNW (**Figs.** 4g-i). Farther east, at Myra, primary bedding in presumed Bukkheia Formation mudstones is less apparent, but when present, is multiply folded and cleaved. Progressive coaxial structures include tight E-W trending isoclinal folds (oldest) with a main axial-planar mylonitic foliation, refolded by upright E-W trending folds with subvertical axial surfaces (**Figs.** 6c, 4d, e). The gently NNW-dipping mylonitic foliation, which contains stretched clasts of calcareous siltstone indicating ESE thrusting (**Fig.** 4), is also folded by the later upright folds (**Fig.** 6d). Along the axial traces of such folds, steep NNE-SSW trending, mylonitic strike-slip shear zones are developed, accompanied by internal subvertical folds.

Although the diorite sill has been folded together with the metasedimentary strata, the diorite itself is largely massive and with a microcrystalline textures, however, contractional strain has been accommodated by a set of irregular ductile shear zones along both the diorite-sediment contact zone and inside the diorite itself (**Fig.** 4f: Kolsum 2019). The diorite contact zone at Myra is marked by a c. 5-10 m thick zone of intercalated mudstones and calcareous mafic schists and increased ductile deformation, i.e. tight folds and a mylonitic foliation. Internally in the diorite, a complex high-strain

mylonite zone (c. 20 m thick) contains a mylonitic foliation wrapping around sigmoidal lenses of massive diorite (**Fig.** 6e) and is itself irregularly folded (**Fig.** 6f). The mylonitic foliation contains stretching lineations that indicate SE-directed thrusting (**Fig.** 4f), and in places encloses large-scale tightly folded and transposed lenses of metasandstones/siltstones (**Fig.** 6g). The transposed metasandstone lenses are interpreted as internal xenoliths affected by strong ductile shearing in the diorite (Bergh et al. 2007; Knudsen 2007; Kolsum 2019). Notably, there is evidence of widespread hydrothermal fluid circulations in the diorite in the form of carbonate and quartz-rich veins, sulphides, and the retrogressive phases epidote, chlorite and adularia (**Figs.** 6e, h).

Hamre-Kvalvågklubben

Another metasedimentary sequence with several enclosed sill-like diorite bodies is present on the western side of the Vanna island (**Fig.** 3) along the shore in the area between Hamre and Kvalvågklubben (**Figs.** 7, 8). This unit is bounded to the northwest by the frontal thrust sheets of the Skipsfjord Nappe (Opheim & Andresen 1989) and to the east by para-autochthonous basement tonalites and a steep basement seated ductile shear zone, informally termed the Olkeeidet shear zone (Paulsen et al. 2019a). The metamorphic grade and intensity of deformation in the sequence is slightly higher, i.e. upper greenschist facies, compared to at Vikan-Larstangen. However, the tectono-stratigraphy is quite similar, marked by a lower metapsammitic series (<200 m thick) and an upper series of metapelites/schists with embedded diorite lenses >100 m thick (**Fig.** 7). A possible relict basement–cover contact dipping moderately SW is inferred in two localities, one near Hamrevatnan in the north below the frontal Skipsfjord Nappe (**Fig.** 7), and another at Kvalvågen in the south (**Fig.** 8). The stratigraphy is established in these areas, starting with a lower metapsammite unit and a conformably overlying metapelitic series (**Fig.** 7). The basal metapsammites strike E-W in the north at Hamrevatnan and can be traced westward to the shoreline, where the strata dip moderately south (**Fig.** 9a, 7a) and are overridden by the Skipsfjord Nappe frontal thrust (**Fig.** 9b) that dips NW (**Fig.** 7, cross-section A-A'). Possible cross-beds in the quartz-rich metasandstones of the lower series (**Fig.** 9c) indicate way up to the south. Muscovite-chlorite schists conformably overly the metasandstones and contain a peculiar, calcareous metapelite breccia (c. 100 m thick) with fragments of dismembered slate layers embedded in a calcite-dolomite matrix (**Fig.** 9d). This breccia marks the transition to metapelites of the upper series, is also present in the south between Kvalvågklubben and Mellomjordbukta (**Fig.** 8), and has been used as a tectono-stratigraphic marker for the upper metapelitic series together with the intrusive, presumed lens-shaped diorite sills.

The map pattern clearly reveals a change/bend in strike of the entire metasedimentary sequence, from E-W in the area north of Hamrebukta (**Figs.** 7a, b) to c. N-S farther south (**Figs.** 7c-e), and a corresponding southward narrowing. This change in attitude is interpreted to be caused by at least two ductile deformation events with macro- and mesoscale folding, thrusting, and lateral shearing of the entire metasedimentary sequence and enclosed diorites, as outlined below.

The primary stratigraphy and bedding relations in the metapelitic rocks are mostly obliterated by a penetrative foliation enriched with secondary calcite (**Fig.** 10a), which is also widespread in the diorites, where it is expressed as a mylonitic foliation. Attitude data from the metasedimentary rocks south of Hamrebukta and between Kvalen and Øra show that bedding is clearly folded by tight/isoclinal locally open, east-verging upright to overturned folds (**Fig.** 10b). These folds trend N-S to NNW-SSE, have fold axes plunging gently to the south, and axial-planar cleavage with a moderate dip to the WSW (**Fig.** 7c-e, 8c). The main foliation has a similar average dip and is interpreted to have developed parallel to the axial surface of these early-stage folds. Cross-section B-B' from Finneset (**Fig.** 7) illustrates well the relationship between primary bedding, possible early-stage folding and related axial-planar thrusting sub-parallel to the main foliation. In outcrop, steep to subvertical

metasandstone beds are overridden by a gently west-dipping ductile shear zone (thrust) composed of foliated, mylonitized metapelites (**Figs.** 10c, d) with peculiar, metre-thick quartz-carbonate breccia subparallel to the main foliation (**Fig.** 10e). Inside such thrust zones, small-scale, tight isoclinal folds with axial surfaces parallel to the mylonitic thrust fabrics (**Fig.** 10f), thrusts duplexes (**Fig.** 10g), sigmoidal lenses and stretching lineations (**Fig.** 10h) are present and consistent display top-to-ENE movement. On a map scale, the main mylonitic foliation wraps around mega-lenses/boudins (from c. 50 m up to 200 m in length) of the more competent and steeply dipping metapsammites, e.g. at Solbakken (**Fig.** 7).

Similar gently WSW-dipping thrust zones are also common within many of the foliated diorite bodies, e.g. at Kvalvågklubben (**Fig.** 11a) and Svartneset (**Figs.** 11b, c), and along their contacts to surrounding host rocks. When approaching the steep west-dipping Olkeeidet shear zone, which is exposed just east of Solbakken, Kvalvågen and Øra (**Figs.** 7, 8), most mesoscale thrusts are subparallel to this boundary fault. This suggests a kinematic (reverse) relationship (see discussion). Field studies along the contact with Olkeeidet shear zone in these areas (**Fig.** 11a) reveal a steep, N-S striking, partly mylonitic ductile shear zone, succeeded by metapsammites and -pelites with moderate to steep west dips (**Figs.** 8a-d). This boundary shear zone displays internal, very complex kinematic patterns, indicating both dip-slip thrusting to the ENE and lateral (dextral) movements.

The thrust zone south of Kvalvågen contains peculiar, up to 30 m thick hydrothermal quartz-carbonate breccias (**Fig.** 11d), in which coarse-grained carbonate is separated by narrow layers of bright green muscovite-fuchsite, and cross-cut by networks of quartz veins (**Fig.** 11e). Comparable breccias and hydrothermal mineralization are seen along strike of the boundary fault, and inside many steep shear zones present within the metasedimentary units and in the intrusive diorites (**Figs.** 11f-h). The steep shear zones in the supracrustal units are narrow, localized (<5m wide) steep, NE-SW trending and mostly strike parallel to the low-angle thrusts. Some merge into each other, for example within diorites at Kolvika, and into the surrounding host rocks, e.g. at Solbakken (**Fig.** 7). They have internal mylonitic fabrics such as transposed lenses, subvertical isoclinal folds (**Fig.** 11h), and asymmetric lenses/boudins, all recording both reverse movement to the east and lateral strike-slip shearing (mostly dextral).

The maps (**Figs.** 7, 8) and structural field studies further indicate the presence of a second group of structures superimposed on the early stage folds and main foliation/thrust-forming event. This can be demonstrated in the north at Hamrevatnan, where the entire metasedimentary sequence and the depositional basement-cover contact is folded by a macroscale tight, SE-verging and partly overturned anticlinal fold system with gently NE-plunging fold axes and gently NW-dipping limbs (**Fig.** 7). North of Hamrebukta, mesoscale SE-verging folds are observed in metapelites with fold axes that plunge gently to the SW, and they are considered to be parasitic to the larger map-scale fold. In many areas the main foliation, which in general has a fairly consistent and moderate dip to the west, is itself clearly folded by open, asymmetric SE-verging meso-folds with fold axes plunging gently to the SW, as in the sequence northeast of Mellomjordbukta (**Fig.** 8). The relatively younger age for these folds is confirmed by local refolding of the earlier N-S trending isoclinal folds and related axial-planar thrusts. Younger NW-dipping thrust faults are also present, for example along the contact with the diorite bodies at Hamreklubben and Svartneset in the north (**Fig.** 7) and at Straumsnes and Rishaugen in the south (**Fig.** 8). In all these localities, the thrusts are responsible for SE-ward displacement of the diorites and accompanied metasedimentary host rocks. An important observation is that the gently dipping thrust at Rishaugen splays out from the Olkeeidet shear zone near Kvalvågen and obliquely truncates the NNW-SSE striking main foliation in the hangingwall (**Fig.** 8); this is evidence of a

younger tectonic overprint (see discussion). Furthermore, the diorite contact at Svartneset (**Fig.** 7) is folded by NE-SW trending asymmetric folds as in the metasedimentary rocks.

Skipsfjord Nappe

In northern and central parts of Vanna the Skipsfjord Nappe (**Figs.** 3, 12a) is an allochthonous thrust sheet that includes several larger sheets and smaller lenses of highly strained, medium-grade metasedimentary, calcareous, and mafic-volcanic/intrusive rocks sandwiched in between imbricate slices of tonalite, variably foliated tonalitic and granitoid basement gneisses, and numerous mafic layers (**Figs.** 13c, d) (cf. Opheim & Andresen 1989). The Skipsfjord Nappe is centred at Skipsfjorden (**Fig.** 3) and bounded below by a thrust contact against a smaller, possible para-autochthonous slice/nappe unit east of Skipsfjorden termed the Svartbergan Nappe (Karlsen 2019; Rønningen 2019) (**Figs.** 12c). In the north the Skipsfjorden Nappe is down-faulted >3 km along the Permian aged Vannareid-Burøysund fault (Opheim & Andresen 1989; Davids et al. 2013).

The Kvalkjeften metasedimentary sequence (**Fig.** 12d; Opheim & Andresen 1989) defines mega-lenses within the Skipsfjord Nappe (**Fig.** 3) occurring between tonalite gneisses and with mylonitic upper and lower contacts. This sequence is more highly strained than similar units described elsewhere on Vanna although the metamorphic grade never exceeded greenschist facies (Opheim and Andresen 1989). A possible depositional contact is observed inside the mega-lenses, although it has been tectonized. Opheim and Andresen (1989) informally divided the metasedimentary sequence into two formations (**Fig.** 12d), a lower formation of metapsammites (**Fig.** 13a) and an upper formation dominated by calcareous metapelites and intercalated, thin siltstone layers (**Fig.** 13b). A striking feature of the Skipsfjord Nappe is the presence of widespread, variably deformed foliation-parallel mafic intrusive sheets intercalated with the calcareous metasedimentary rocks, e.g. north of Olkeeidet (**Fig.** 12a), varying in thickness from 20 cm to 2m (**Figs.** 13c, d). Thick dykes have strongly deformed rims, whereas smaller dykes are more intensively strained.

The main tectonic feature of the Skipsfjord Nappe rocks is a gently NW-dipping planar and uniform foliation (**Figs.** 13b, e). This fabric is locally irregular due to presence of abundant, less deformed tonalite lenses, mafic intrusions/sills, and secondary carbonate and quartz veins (**Fig.** 13e), i.e. similar to that of the metasedimentary sequence at Hamre and Kvalvågklubben. Gently NW-dipping mylonite zones often separate and/or juxtapose tonalite gneisses on top of and below the metasedimentary package. The high-strain mylonitic shear zones also dip gently NW and display stretching lineations and sigmoidal clasts (**Fig.** 13e) that indicate SE-directed thrust displacement (**Fig.** 12b). Transposed near-recumbent isoclinal folds (**Fig.** 13f) are aligned parallel to the mylonitic foliation that is always axial-planar to the isoclinal folds. In addition, open asymmetric SE-verging mesoscale kink folds of the main foliation has been observed in the underlying Svartbergan Nappe, but not in the Skipsfjord Nappe.

The dip angle of the strong planar foliation in the Skipsfjord Nappe changes in the north where it approaches the Permian Vannareid-Burøysund fault zone (Opheim & Andresen 1989; Davids et al. 2013), from gently NW-dipping to steeply south-dipping near the fault trace, which is likely caused by normal drag along the termination of the fault (see Paulsen et al. 2019a).

Svartbergan Nappe

Structural investigations in the area of Svartbergan (**Fig.** 3) have recently uncovered a thick sequence (>500 m) of possible metasedimentary rocks tectonically below the Skipsfjord Nappe rocks (**Fig.** 14), and above the autochthonous tonalitic basement. The strata crop out at a level that corresponds to the Tinnvatn Formation of the Vanna Group and the lower units of the metasedimentary sequence at Hamre and Kvalvågklubben farther west. This unit, not previously described, makes up a composite

tectonic wedge or mega-lens (**Fig.** 14), with thrust contacts aligned parallel to internally conformable, steeply dipping metapsammites and pelites (**Figs.** 15a, b). Locally also the unit contains small sheets and boudinaged lenses of granite tonalites and granites (**Fig.** 15c) that may be remnants of the underlying basement rocks. Characteristically, the main foliation of the entire unit dips 50-80° to the NW (**Fig.** 14b), locally also to the SE, and is superimposed on assumed primary sedimentary layers, evidenced by the presence of quartzitic metasandstone and intercalated muscovite schist horizons (**Figs.** 15a, b). A low-grade (greenschist facies) mineral assemblage, i.e. muscovite ±biotite in felsic rocks and amphibole+chlorite+epidote in mafic lithologies, defines the main foliation. The sequence is relatively homogeneous, but no valid stratigraphy can be established since the contacts to basement gneisses to the south (below), and to the overlying Skipsfjord Nappe, are defined by ductile thrusts (see below). Internally, the mylonitic fabric of these thrusts is parallel to the axial surface of transposed, isoclinal folds, and also includes a dip-slip stretching lineation plunging NW (**Fig.** 14b) as in the Skipsfjord Nappe (**Fig.** 14a).

On a larger scale, the entire steeply dipping sedimentary unit in the Svartbergan Nappe is tilted as part of a macroscale fold limb, where the flank is inverted against the overlying thrust contact (**Fig.** 14 A-A'). Such a fold, however, is not fully confirmed by the field studies. On the small scale, however, asymmetric kink folds (metre-scale) with fold hinges that plunge shallowly to the SW and NE (**Figs.** 14b, 15d), are prevalent and fold the steep layers, often displaying opposite SE and NW vergence with conjugate kink bands and cross-cutting crenulation cleavages (**Figs.** 15d, e). These conjugate kink folds indicate NE-SW shortening strain (**Fig.** 14b) relative to bedding and the tilting event (see discussion). Stretching lineations are also well developed on foliation surfaces, and importantly they are also clearly folded by the kink folds (**Fig.** 15e) suggesting that the folding post-dated the main thrusting (see discussion).

The upper contact with the Skipsfjord Nappe is a <20 m thick transition zone with several repeated and alternating planar-foliated proto-, ortho-, and ultra-mylonitic host rocks (**Fig.** 15f), including phyllonites, quartz-feldspathic and calcareous schists, that are also extensively kink-folded in the lower part of the transition zone (**Fig.** 15e). A marked gradual shallowing of the steep NW-dipping foliation in the lower part of the Svartbergan Nappe to c. 30° dip in the transition zone to overlying Skipsfjord Nappe rock is apparent (**Fig.** 14a), together with enrichment of secondary carbonate and quartz veins parallel to the main thrust fabric.

Para-autochthonous Neoarchaean basement gneisses

The Neoarchaean basement to the south of the Skipsfjord Nappe on Vanna is composed of dominantly massive tonalite and subordinate tonalitic gneisses, with or without intercalated massive amphibolites, and foliation-parallel mafic intrusive sheets, some dated at 2.4 Ga (Kullerud et al. 2006). Comparable basement rocks are present to the north of the Vannareid-Burøysund fault (**Fig.** 3).

The basement tonalites south of Svartbergan and Olkeeidet (**Fig.** 3) are generally massive, but typically contain an internal system of low-angle and high-angle ductile shear zones striking c. N-S and dipping consistently to the west (**Figs.** 16a-d). The low-angle shear zones in the massive tonalites are subparallel to a weak bench fabric, striking regularly N-S to NNW-SSE and with a moderate dip to the west, which is also parallel to a weak composite banding in areas where tonalitic gneisses appear. The bench and low-angle shear zone fabrics are also parallel to a set of very regular NNW-SSE trending mafic dykes with moderate dips to the west (**Figs.** 16c, d). The low-angle shear zones are mylonitic and range in thickness from 1m to 15 m. They dip consistently to the west and exhibit up-to-east shear, and are typically situated along mafic dyke margins (**Fig.** 16e). When not parallel to the dykes, these shear zones splay out from the dykes and distinctly truncate the bench fabric of the

surrounding tonalites (**Fig.** 16d), then rejoin the margins of other dykes and/or steep shear zones (see below) for several hundred metres along strike (**Figs.** 16b,d). Thus, they define a repeated, partly imbricate system within the basement gneisses (see **Fig.** 16a). Internal stretching lineations, sigmoidal lenses and asymmetric folds all support east- to ENE-directed thrusting (**Fig.** 16g). The overall picture is that the low-angle basement-seated thrusts have the same orientation and kinematic character as the main foliation and associated early-stage thrusts in the metasedimentary units at Hamre and Kvalvågklubben (**Figs.** 7, 8) (see discussion).

Frequent high-angle, steep to subvertical ductile shear zones are also recorded in the tonalitic basement, all striking N-S to NNW-SSE, which is parallel to the gneissic fabric and mafic dykes. These shear zones are seen on the geological map (**Fig.** 3) and magnetic map (**Fig.** 17, see below) as prominent lineaments along valleys and narrow depressions, and are traceable over large distances. Examples include lineaments between Skarvatnet and Storvatnet in south central Vanna (**Figs.** 16c, e, f), and along the previously mentioned Olkeeidet shear zone (**Fig.** 3). These lineaments define steep mylonitic shear zones that follow the gneiss fabric and mafic dykes, and merge into the gently dipping thrusts (**Fig.** 16e). Two sets of stretching lineations are observed on the steep mylonitic fault fabric at Skarvatnet (**Fig.** 16f), one set showing dip-slip reverse up-to-east shear sense (oldest) and another containing chlorite- and epidote-rich phyllonite indicating sinistral strike-slip.

The Olkeeidet shear zone is a prominent N-S to NNE-SSW striking linear feature fully embedded in basement tonalites, and which can be traced southwards from the frontal Skipsfjord Nappe at Olkeeidet as the boundary fault/contact to the metasedimentary sequence at Hamre and Kvalvågklubben (**Figs.** 7, 8). Just south of Olkeeidet, a c. 40-50 m wide remnant of a metasedimentary sequence occurs within the shear zone (**Fig.** 7). Here, the shear zone separates massive autochthonous tonalite on either side from a sequence of weakly foliated NW-dipping slivers of dismembered metasedimentary and mafic intrusive rocks, in contact with mylonitized amphibolite sheets in the tonalites on the western margin. Within this shear zone, an array of oblique, NW-SE trending and steep sigmoidal faults splay outward and merge into the main boundary shear zones, defining a prominent dextral strike-slip duplex structure. South of Kvalvågen (**Fig.** 8) the Olkeeidet shear zone bounds a moderately west-dipping imbricate thrust system in the metasedimentary rocks (**Fig.** 8) that becomes steeper to the east against the Olkeeidet shear zone (**Fig.** 11a). Associated small-scale, oblique-reverse faults and steep strike-slip faults with shallow to steep dips to the WSW kinematically classify the overall Olkeeidet shear zone as a combined reverse fault (in the south) and dextral-oblique strike-slip zone (in the north). In contrast, where the Olkeeidet shear zone terminates against the Skipsfjord Nappe in the north (**Figs.** 3, 12b1, 19b), the gently NW-dipping foliation in the Skipsfjord Nappe rocks is bent sinistrally into the Olkeeidet shear zone (**Figs.** 3, 12b), indicating sinistral strike-slip movement, which suggests that the Olkeeidet shear zone evolved from a dextral to a sinistral strike-slip shear zone (see discussion).

Another common feature for both the moderate and steeply dipping basement-seated shear zones is extensive hydrothermal alteration resulting in the precipitation of carbonate and quartz veins, breccias, and secondary minerals like albite, chlorite, and fuchsite. Similar hydrothermal minerals are found in all the major basement shear zones on Vanna, i.e. south of Kvalvågen (**Figs.** 11d, e), Skarvatnet (**Fig.** 16f) and Nord-Vannvågdalen (**Fig.** 3). The strike-slip portion of the Olkeeidet shear zone in the north (**Fig.** 7) is unique in that the hydrothermal alteration has resulted in the deposition of emerald-bearing carbonate and quartz breccias. Hydrothermal fluids have also caused local extensive albitisation of the surrounding host rocks and formation of fuchsite schists (see Paulsen et al. 2019b).

Aeromagnetic data

Reprocessed magnetic data were obtained from the Geological Survey of Norway's MINN project (Rodionov and Ofstad, 2012; Nasuti et al. 2015; Sandstad et al. 2015) and used to resolve and interpret the tectonic architecture of Vanna island. We interpreted data sets converted to total magnetic fields and tilt derivative fields (**Figs.** 17a, b) using the methods of Henkel (1991). In our analysis we referenced all previous knowledge of the bedrock geology and ground-truthed the interpretations. In particular, magnetic anomalies enabled us to separate: i) metasupracrustal units from the tonalitic basement gneisses, ii) mafic intrusive sills and their metasedimentary host rocks, iii) Neoarchaean and Palaeoproterozoic ductile fabrics, and in particular, iv) different generations and attitudes of mafic dykes. Such dykes show up well as semi-linear magnetic highs, whereas the tonalitic basement and metasedimentary rocks in general are weakly magnetic to non-magnetic (**Fig.** 17a). Major tectonic discontinuities (faults) are identified as displaced magnetic anomalies; e.g., ductile shear zones are postulated where a progressive displacement of the affected anomalies occurs, while brittle structures are observed to truncate abruptly the anomalies they intersect.

The magnetic data reveal several distinct anomaly patterns that seem to correspond well with the mapped bedrock structures and domains described above. *First* of all, the magnetic signatures of the rather weakly deformed low-grade metasedimentary sequences between Vikan and Lanes on the southeastern part of the island, and at Hamre-Kvalvågklubben on the west side, are shown by markedly contrasting high and low magnetic responses (**Fig.** 17). These contrasts are interpreted to be due to the strong magnetic response of the diorite intrusions, whereas the metasedimentary rocks have weak magnetic anomalies. *Second*, the more highly strained and metamorphosed mylonitic metasedimentary units of the Skipsfjord Nappe, and partly also the Svartbergan Nappe, show less contrast between the mapped diorite intrusions and metasedimentary host rocks, but evidently locate the allochthonous nappes well. We infer this lack of magnetic contrast to be a result of the penetrative flat-lying foliation and abundant mafic sheets in the Skipsfjord Nappe. *Third*, the magnetic signature of the massive basement tonalites that dominate the interior of the southern part of Vanna have a relatively weak and uniform magnetic signature. We consider the variably N-S, NNW-SSE and NNE-SSW trending strong magnetic anomalies to reflect both the gentle/moderate west-dipping mafic dyke swarms, the associated and closely linked thrusts, and the steep, ductile strike-slip shear zones, especially in the southern and western parts (**Fig.** 17a). *Fourth*, a much stronger magnetic signature is evident for the tonalites and tonalitic gneisses in northern Vanna, north of the Vannareid-Burøysund fault zone, which is well constrained as an E-W trending magnetic lineament (**Fig.** 17) separating the two basement domains. This northern basement area, however, is beyond the scope of the present paper.

Discussion

Below we use the presented field and magnetic susceptibility data to discuss the structural architecture of Neoarchaean basement and Palaeoproterozoic cover successions in the Vanna portion of the WTBC crustal transect in northern Norway. Our data to some extent support previous models for deposition of the Vanna Group sedimentary sequence (Binns et al. 1980; Bergh et al. 2007), but questions important issues such as the formation and linkage of other pre-orogenic supracrustal units on Vanna, and the nature and controlling factors of Palaeoproterozoic crustal deformation. Another subsidiary issue is the absolute timing of the deformation, especially since new Ar-Ar dating of muscovite in the Skipsfjord Nappe suggests a Caledonian age for thrusting of the Skipsfjord Nappe (NGU, pers. comm., 2019), such that previously proposed tectonic models for the Late Svecofennian frontal deformation on Vanna must be reconsidered (cf. Opheim & Andresen 1990; Bergh et al. 2007). In the discussion below, we focus first on the Palaeoproterozoic metasupracrustal sequences, their formation in possible

rift basins, depositional regime and basin architecture based on internal build-up and boundary contact relations; second, how the individual sedimentary units responded to Late Svecofennian (and/or younger) orogenic crustal deformation; and third, we discuss the regional implications of our findings with regard to the Late Svecofennian orogeny, and possible implications of a Caledonian age for the deformation.

Palaeoproterozoic sedimentation and basin formation

From worldwide studies, it is well known that the geometry and evolution of fold-thrust belts in frontal portions of orogenic belts may have been controlled by and/or have originated at the expense of pre-existing rift basins (and deposits) and their bounding faults, and with complex internal extensional architectures (see Gillcrist et al. 1987; Bond & McClay 1995; Corfield et al. 1996). Our studies show that the pre-orogenic setting for the Vanna basement gneisses likely included Palaeoproterozoic sedimentary rift sequences (basins) that may have covered a very large uniform extensional (?) basin and/or several smaller basins. We discuss this issue by first interpreting the depositional regime and basin configuration of the para-autochthonous metasedimentary sequences at Vikan, Hamre and Kvalvågklubben, and their bounding contacts to the Vanna basement gneisses described above. Then we compare these units to the more highly deformed supracrustal rocks in the Skipsfjord and Svartbergan nappes.

Our data show that the para-autochthonous units share many similarities in terms of internal stratigraphy/lithology, thicknesses, and sedimentary facies types (**Fig.** 18). For example, they are all composed dominantly of a lower series of metapsammites and overlying metapelites in successive order, but often with local internal variations, i.e. presence of subordinate horizons of peculiar calcareous metapelitic breccias, quartzites, conglomerates and, notably, diorite sills (**Fig.** 17) (cf. Bergh et al. 2007). On the other hand, the studied sequences are spatially separated and have varied depositional, thrust and strike-slip boundary contacts to the basement gneisses (**Figs.** 4, 7, 8). Based on the similarities in the established stratigraphic columns, we interpret the rocks to represent a correlative sequence formed in a system of linked continental rift basins. The onset of sedimentation in the basin(s) is well documented by a basal depositional contact to the Tinnvatn Formation of the Vanna Group at Vikan (**Fig.** 4) (Binns et al. 1980; Bergh et al. 2007). The Tinnvatn Formation consists of well-sorted rhythmic laminated arkosic sandstones with sedimentary structures indicating shallow marine, high-energy deltaic or tidal depositional environment and shore-face deposits (Binns et al. 1980; Bergh et al. 2007; Johannessen, 2012). A similar depositional setting is considered for the metapsammitic units on the western side of Vanna at Hamre and Kvalvågklubben (**Figs.** 7, 8), where relict cross-bedded and rhythmically laminated sandstones indicate a deltaic depositional environment as for the Tinnvatn Formation at Vikan.

We consider the thick successions of metapelites overlying the psammites both at Vikan, Hamre, and Kvalvågklubben (**Fig.** 18) to mark a primary fining upward tendency in the sedimentary sequences, although several internal thrust contacts has caused repetition and thickening of the sequences. The deposition of thick, alternating massive and laminated mudstones suggest that the Bukkheia Formation metapelites, and similar lithologies at Hamre and Kvalvågklubben (**Fig.** 18) formed in a subsiding basin, for example as outer shelf deposits (cf. Clifton et al. 1971). This interpretation is supported by the abundance of carbonate layers, and brecciated carbonate cement within mudstones and mudstone breccias at Hamrebukta, Finneset and Mellomjordbukta (**Figs.** 7, 8), which is a common feature in such shallow marine deposits. In addition, the numerous subordinate thin layers of sandstone found within the mudstone horizons could represent intermittent high-energy deposits, possibly storm deposit layers (Eriksson et al. 1998).

Correlation of the para-autochthonous metasedimentary units (i.e. Kvalkjeften Group) on Vanna with those of the allochthonous Skipsfjord and Svartbergan nappes (**Fig.** 18) is, however, more uncertain, since all primary relations are removed by the strong ductile shearing. However, supracrustal units in both of these nappes have quartzitic metapsammites at the base and an overlying thick pile of metapelites, now muscovite schists in the Skipsfjord Nappe and calcareous metapelites and siltstone horizons in the Svartbergan Nappe rocks (**Fig.** 18). Also, both units are intruded by a diorite sill structurally above the metasedimentary strata. This could suggest a genetic relationship with the para-autochthonous sequences at Hamre, Kvalvågklubben and Vikan, and that they were possibly all part of the same Palaeoproterozoic rift-basin succession.

Rift-basin architecture and controlling factors

In rift basins, the shape and topography of the palaeo-coastline or erosional boundary would control the transport and spatial extent of sedimentation which would preferentially be parallel to the presumed rift axis and bounding normal faults (cf. Bergh & Torske 1986, 1988). In the Vanna units, sedimentary transport directions were recently determined from palaeocurrent data in metapsammites of the Tinnvatn Formation at Vikan, yielding transport directions of deltaic streams along NNE-SSW and NNW-SSE trending coastlines (Johannessen 2012). This indicates that the Vanna Group basin between Vikan and Lanes was bounded by normal faults or scarps trending parallel to the presumed coastline, i.e. NNW-SSE and NNE-SSW (Johannessen 2012). A possible candidate for relict steep NNE-SSW trending bounding normal faults is the Olkeeidet shear zone, now a combined reverse and strike-slip fault (see discussion) to the east of the Hamre-Kvalvågklubben metasedimentary sequence (**Fig.** 7). Many other similarly oriented basement-seated faults have mapped in this work in southern Vanna (**Fig.** 3) and may be related to pre-orogenic extensional basins; such faults are also inferred from NNE-SSW trending linear anomalies on the aeromagnetic maps (**Fig.** 17).

The Vanna metasedimentary sequences were deposited between 2.4 and 2.2 Ga (Bergh et al. 2007) during a time of regional NE-SW extension in the northern Fennoscandian Shield (Balaganski et al. 2001). These Palaeoproterozoic extensional events followed a major c. 2.45 Ga break-up of the Archaean continent (Lahtinen et al. 2008) producing voluminous pulses of mafic magmatism (dyke swarms) in the Archaean craton (Amelin et al. 1995) that stretched even beyond the region now covered by the Caledonian Orogen and into Laurentia (Skyttä et al. 2019). The extension produced NW-SE trending rift basins and small oceans surrounded by normal faults, and elongate normal fault-bounded blocks (Lahtinen et al. 2008; Skyttä et al. 2019). In the WTBC, a similar extensional pulse has been documented by the intrusion of an extensive 2.4 mafic dyke swarm that covers most of the northern islands from Ringvassøya to Vanna (**Fig.** 2; Kullerud et al. 2006; Bergh et al. 2010). These mafic dykes to some degree may have controlled the location and spatial extent of the Palaeoproterozoic rift basins on Vanna, as outlined below.

On Vanna, we mapped a system of NNW-SSE trending mafic dykes within the basement tonalites that are consistently parallel to the basement-seated thrusts and steep reverse and strike-slip faults (**Fig.** 16). Our interpretation is that these dykes intruded along possible syn-extensional normal faults and fissures that likely also created subsiding basin(s) for the deposition of the Vanna Group and related sediments. The Olkeeidet shear zone likely originated as one of these extensional normal faults that was later reactivated as a combined (?) reverse and strike-slip fault (see below). The widths of the extensional basins are unknown because we only see one side of them. If the sediments formed as Palaeoproterozoic clastic shoreline deposits, with their orientation or extent controlled by the 2.4-2.2 Ga extensional event, then an undulating shoreline could account for the current arcuate shapes of the depositional basement cover contacts. In addition, the post-deposition contractional events could have further modified the orientation (see further discussion below).

Basement-involved fold-thrust structures, oblique faults, and basin inversion

Below we discuss and interpret the effects of the presumed Late Svecofennian orogenic deformation on Vanna on the basis of our interpretation of two major contractional events (D_1-D_2) for the Vanna deformation. The D_1 event includes various N-S striking fold-thrust fabrics at Hamre-Kvalvågklubben (**Figs.** 7, 8), whereas NE-SW trending fabrics in the para-autochthonous Vanna Group between Vikan and Larstangen, and the Skipsfjord and Svartbergan nappes in the north, are ascribed to the D_2 event (**Fig.** 19). We argue for the controlling effect of the pre-orogenic normal faults and associated mafic dykes in the Neoarchaean tonalitic basement rocks in localizing both D_1 and D_2 shortening strain and thrust/reverse fault reactivation.

Discussion of D_1 fold-thrust and oblique structures

We consider the rift basins and c. N-S striking bounding normal faults on Vanna to have controlled both the extent and resulting character of the D_1 fold-thrust structures at Hamre-Kvalvågklubben in western Vanna, and linked steep oblique N-S shear zones, as well as the nature of concomitant inversion of the metasedimentary sequences. The main argument in favour of such control, is overlap in attitude and spatial location of D_1 faults relative to the metasupracrustal sequences in these areas, and similarity with the orientation of basement-seated faults in the Neoarchaean tonalitic basement rocks (**Figs.** 3, 17). For example, shear zones (D_1) in the basement of southern Vanna define two major sets, one a set of N-S striking low-angle thrust that may have exploited the pre-orogenic traces of extensional mafic dykes with dips to the west, and the other a set of N-S trending high angle reverse and/or strike-slip faults with a steep to subvertical dip (**Figs.** 3, 16). The low-angle basement-seated thrusts have the same orientation and kinematic character as the main foliation and associated early-stage thrusts in the metasedimentary units at Hamre and Kvalvågklubben (**Figs.** 7, 8). The west dip of the low-angle faults, and the kinematic indicators that show slightly oblique top-to-east sense of shear confirm that they are thrust faults formed during the c. E-W contractile D_1 shortening event. Further, these thrusts in the basement commonly merge into the steep N-S strike-slip faults (**Figs.** 16d-e) creating a step-wise imbricate fault pattern, indicating that they formed separately and were controlled in further propagation by the steep faults. This kind of flat-ramp imbricate fault interaction is common in thin-skinned fold thrust belts where sedimentary strata control the thrust propagation (e.g. Boyer & Elliott 1982).

In the Hamre-Kvalvågklubben sequence flat-ramp related D_1 thrusts with kinematic indicators of top-to-ENE displacement are common (**Figs.** 10g-h). Flat thrusts are interpreted to have been localized to the axial surfaces of tight early folds, and parallel to a main penetrative foliation present in both the metasedimentary rocks and enclosed diorites (**Fig.** 11b). Possible thrust ramps are evident where thrusts propagated to higher stratigraphic levels in metapelites and truncated tilted, competent sandstone beds in the footwall of the thrusts (**Figs.** 10c, d) (cf. Jamison 1987). In addition, steep reverse and strike-slip faults are present (**Figs.** 11f-h), and since many of them merge into or splay outwards from each other, they are temporally linked to the D_1 event.

In the basement-involved portion of the east-directed D_1 fold-thrust belt (**Fig.** 16a) we interpret the step-wise propagation to be controlled by pre-orogenic low-angle mafic dykes and high-angle normal faults. Alternatively, if the steep normal faults became listric at depth, they could have acted as pre-existing detachments that controlled thrust ramp development toward east, as described from e.g. the Lewisian of Scotland (Tavarnelli 1996; Butler et al. 2007). In such a setting, individual thrust faults branched off the detachment and merged with a dyke at higher level in the basement. Continued compression from the west allowed the thrust system to further migrate towards the foreland in the

east during the D_1 contractional event (**Fig.** 11a). In this model, both the pre-orogenic normal faults and the 2.4 Ga mafic dykes are pre-existing zones of weakness in the basement that were reactivated as thrusts during the D_1 event. This D_1 basement-involved event on Vanna is thus an example of E-W directed horizontal shortening strain in a basement-cover segment accommodated by low-angle ductile thrusting and reactivation of pre-existing steep normal faults (see **Fig.** 19a). This would suggest that the pre-existing normal faults were reactivated as steep reverse faults during the D_1 event, thus enabling positive structural inversion of the rift basins. This model is supported by the Olkeeidet shear zone in its southern trace, where it probably acted as a steep buttress against eastward transport of low-angle thrusts into the basement, thus enabling positive inversion of the rift basin at Hamre-Kvalvågklubben (**Figs.** 7, 8).

The pattern defines a repeated, partly imbricate system within the basement gneisses (see **Fig.** 16a). Internal stretching lineations, sigmoidal lenses and asymmetric folds all support east- to ENE-directed thrusting (**Fig.** 16g). The low-angle basement-seated thrusts have the same orientation and kinematic character as the main foliation and associated early-stage thrusts in the metasedimentary units at Hamre and Kvalvågklubben (**Figs.** 7, 8).

Discussion of D_2 fold-thrust and oblique structures

The D_2 contractional event on Vanna is evidenced by: i) refolding of tight N-S trending (D_1) folds by asymmetric SE-verging folds (D_2) in the Hamre-Kvalvågklubben metasedimentary sequence (**Fig.** 7, 8), ii) the presence of SE-directed thrusts that splay out from the N-S trending Olkeeidet shear zone south of Kvalvågen (**Fig.** 8), iii) the presence of a large SE-directed thrust system involving the Skipsfjord and Svartbergan nappes (Opheim & Andresen 1990; Karlsen 2019; Rønningen 2019), which reshaped the early N-S trending D_1 structures in central Vanna, and iv) SE-directed fold-thrust structures developed in the para-autochthonous Vanna Group between Vikan and Lanes in southeastern Vanna (Bergh et al. 2007). A summary of the most important D_2 structures is shown in **Fig.** 19b, and discussed below in a profile from the frontal part in the south to the hinterland in the north.

In the southeast, at Vikan and Myra (**Fig.** 4), the para-autochthonous Vanna Group, its enclosed diorite sill and the basement-cover contact suffered progressive and coaxial tight folding followed by upright SE-verging folding and localized thrusting due to NW-SE contraction (e.g. Bergh et al. 2007). This interpretation is supported by consistent top-to-SE transport indicated by polyphase fold patterns (**Fig.** 6c) and kinematic indicators in the shear zones . The abundance of repeated thrusts cutting up-section from the basement into the Vanna Group cover rocks (**Fig.** 4, cross section) where they are localized to the diorite-sediment contacts and within the diorites themselves (**Fig.** 6), suggest that the D_2 foreland fold-thrust belt is a combined thick-skinned (basement-involved) and thin-skinned type in a typical, repeated thrust fan (Boyer & Elliott 1982). Imbricate thrust fans occur mainly in the frontal parts of orogenic belts in contrast to more internal parts of orogenic belts where crystalline basement slivers are present and attached in duplex structures (Morley 1986; Vann et al. 1986).

Farther north on Vanna, the D_2 event caused major SE-directed thrusting of the Skipsfjord and Svartbergan Nappes, and possibly partitioned dextral strike-slip reactivation of the basement-involved N-S trending D_1 faults (see **Fig.** 19b). Interpreted cross-sections of the Skipsfjord Nappe show a typical imbricate, foliation-parallel thrust system (**Fig.** 12a) with mixed slivers of tonalitic basement and metasedimentary rocks. Polyphase structures and uniform SE-directed kinematic indicators reveal a similar, presumed progressive evolution of internal structures as in the Vanna Group, advocating a temporal relationship between the D_2 structures from the foreland to hinterland. The steep dip of the

main strata and fabric in the Svartbergan Nappe below the Skipsfjord Nappe (**Fig.** 12c) could indicate that the Svartbergan Nappe formed behind and/or above a major NE-SW trending and NW-dipping thrust ramp (or buttress) in the frontal basement tonalites, tentatively a pre-existing NW-dipping normal fault bounding a smaller rift basin to the south, similar to that of the Vanna Group (**Fig.** 14, cross-section), but perpendicular to the Hamre-Kvalvågklubben basin. This inferred pre-existing normal fault in the basement then acted as a stiff, less strained zone, inverting the strata in the Svartbergan Nappe at a frontal thrust ramp. During this SE-ward movement the strata were tilted to subvertical attitude and pushed up the ramp. Consequently, we interpret the Svartbergan Nappe, at least, to be controlled by one or more even deeper thrust detachments that stepped upwards on reaching the pre-existing NE-SW trending normal fault barriers. Similar architectures and propagating thrusts are well known from many basement-involved fold-thrust belts, e.g. the Moine Thrust Belt in Scotland (Butler 1982) and in the Western Alps (Gillcrist et al. 1987; Wibberley 1997). In all these examples, basement sheets have been carried on a crustal-scale sole thrust from the hinterland to the foreland (cf. Nemčok 2005).

If the Svartbergan Nappe stalled towards such a normal fault ramp in the tonalitic basement, then the overlying Skipsfjord Nappe could have been thrusted SE-wards on top of the already stacked, steeply NW-dipping Svartbergan Nappe strata in the form of an out-of-sequence thrust system (cf. Morley 1988). This term, however, is usually ascribed to thin-skinned thrust belts, and requires complete truncation of older, in-sequence thrust structures (Butler 1982; Morley 1988). Our argument lies in the fact that the Svartbergan Nappe is steeply dipping, whereas the Skipsfjord Nappe has a gentle dip to the NW (**Figs.** 3, 12c, 14). Widespread subhorizontal kink folding and refolding of earlier-formed stretching lineations occurring in the Svartbergan Nappe rocks (**Figs.** 15e, g), whereas the Skipsfjord Nappe rocks only display structures formed by one uniform thrusting event, would support out-of-sequence thrusting of the Skipsfjord Nappe. An alternative interpretation for the contrast in internal dip of these D_2 thrust sheets is one of basement-involved duplexing (e.g. Butler et al. 2007). In this case, the Skipsfjord Nappe defines the roof thrust of a basement-cover involved duplex while the Svartbergan Nappe represent an internal splay fault system of the duplex.

We have argued above for the reactivation of NNW-SSE and NNE-SSW trending rift-basin normal faults as steep reverse and dextral strike-slip faults during the NE-SW directed D_1 shortening event, e.g. the Olkeeidet, Skardalen, and Nordvannvågdalen shear zones (**Fig.** 3). These shear zones were oriented almost parallel to the SE translation of the Skipsfjord and Svartbergan Nappes during the D_2 event, thus providing a favourable orientation for orogen-parallel strike-slip motion (see **Fig.** 19b). Such movement on steep faults is evidenced on a large scale by sinistral bending of the mylonitic foliation in the frontal portion of the Skipsfjord Nappe at Olkeeidet inward against the Olkeeidet shear zone (**Figs.** 7, 12b1-b3). On a smaller scale, sinistral strike-slip faults trending variably between N-S and NE-SW are common in the para-autochthonous Vanna Group and enclosed diorites south of Vikan (**Fig.** 4; Bergh et al. 2007; Kolsum 2019). The presence of subvertical S-shaped folds adjacent to such localized shear zones verifies overall sinistral shearing.

The spatial and temporal relationships between the Skipsfjord-Svartbergan Nappes in the north and the para-autochthonous Vanna Group sequence in the southeast reveal that both thick- and thin-skinned tectonics characterize the D_2 fold-thrust system (see **Fig.** 3, cross-section). In this regional transect, we first emphasize the importance of deep, basement-seated detachments in order to transfer orogenic contractional strain from deep to shallow crustal levels towards the less deformed foreland in the WTBC (cf. Dahlstrom 1970: Boyer & Elliott 1982; Coward & Butler 1985; Butler 1986). Second, the role of the pre-existing normal faults like the Olkeeidet shear zone, is more important than previously

thought for the lateral segmentation and partitioning of the D_1 and D_2 features, and in making barriers for thrust reactivation and inversion of the pre-existing rift-basin sequences.

In a regional perspective, our interpretation of the E-W directed D_1 shortening event on Vanna is that it marks the continuation of the dominant NE-SW contraction events farther south in the WTBC, whereas SE-directed thrusting of the Skipsfjord and Svartbergan Nappes and sinistral reactivation of oblique faults (**Fig.** 19b) occurred as a result of orogen-parallel movement relative to earlier events in the WTBC (Bergh et al. 2007, 2010).

Fault rocks and fluid interactions

Hydrothermal carbonate and quartz veins and chlorite-muscovite-fuchsite bearing mylonitic alteration zones are present along several of the basement-seated faults on Vanna, and suggest that fluids infiltrated and caused alteration during both the D_1 and D_2 fault movements. Consequently, phyllosilicate growth occurred in the tonalites (Wintsch et al. 1995), whereas in the mafic (diorite) rock, micas like biotite and chlorite replaced amphibole and plagioclase along zones of weakness such as faults. Phyllosilicates in granitoid/tonalitic rocks are generally weak, and faults rich in such aligned minerals can exhibit aseismic slip, which may also localize the strain to the fault zone and leave the surrounding wall rocks relatively unstrained (e.g. Wibberley 1999, 2005). We believe such a process may account for and explain why the D_1-D_2 ductile thrusts and steep shear zones in the basement of Vanna became so localized.

Temporal constraints on the D_1-D_2 events

The metasedimentary rocks of the Skipsfjord Nappe belonging to the Kvalkjeften Group (**Fig.** 12c), were previously thought to be remnant of Neoproterozoic Caledonian rocks attached to a Caledonian thrust sheet (Opheim & Andresen 1989; Rice 1990). These rocks are now interpreted to have a Palaeoproterozoic depositional age (2.4-2.2 Ga) and are correlative to the para-autochthonous Vanna Group farther south (Bergh et al. 2007, 2010). The D_1 event on Vanna, with E-W to NE-SW-directed shortening and eastward thrusting, is considered as a progressive continuation of the first and second shortening events farther south in the WTBC, whereas the SE-directed D_2 thrusting of the Skipsfjord Nappe is interpreted to result from the Late Svecofennian, orogen-parallel thrusting event (Bergh et al. 2007, 2010, 2015). However, the latter interpretation is uncertain since new preliminary ^{40}Ar-^{39}Ar dating of muscovite reveals a Caledonian age (c. 420 Ma) for the main D_2 foliation-forming event in the Skipsfjord Nappe (NGU, pers. comm., 2019). It is uncertain, however, whether this age represents the main D_2 thrusting event or a Caledonian reactivation of older thrust faults within the Skipsfjord Nappe. Further dating and re-consideration are needed to achieve a better interpretation the significance of the Caledonian Ar-Ar age.

Despite the uncertainty introduced by absolute age determinations, the relative ages of the D_1 and D_2 fabrics on Vanna are evidenced by superposition of structures, e.g. in key outcrops at Hamre and Kvalvågklubben (**Figs.** 7, 8) and along the boundary to basement gneisses on their eastern side (**Fig.** 3). In terms of similar mineral assemblages and metamorphic grade (upper greenschist facies), crustal contraction with closure of Palaeoproterozoic rift basins, and similar mineralization, all suggest that both D_1 and D_2 are of Svecofennian age (Skyttä et al. 2019). Therefore we prefer a Late Svecofennian age for both the D_1 and D_2 events, at least until new radiometric data becomes available.

Regional comparison and implications

Comparable Palaeoproterozoic metasedimentary successions like those on Vanna, which overlie Archaean basement gneisses and dating between c. 2505 to 1930 Ma (Bingen et al. 2015), are found both in tectonic basement windows of the Caledonides in northern Norway and in the Fennoscandian

Shield of northern Finland and Sweden (**Fig.** 1). The closest and most relevant are the Alta-Kautokeino Greenstone Belt that lies between Archaean basement complexes (Siedlecka et al. 1985; Henderson et al. 2015). The stratigraphy is that of a basal Jatulian fuchsite-bearing quartzite, the Masi Formation, hosting an albite–magnetite-rich mafic sill dated at 2220 ± 7 Ma (Bingen et al. 2015), overlain by the Bihkkačohkka, Likčá, and Čáravárri Formations composed of mudstones and siliciclastic metapsammites (Torske & Bergh 2004) and corresponding metavolcanics of the Čáscejas Formation. Notably, the Masi quartzite unit has been interpreted as part of an incipient early Palaeoproterozoic rift basin sequence deposited during early E-W directed rifting of the Archaean continental crust, which is analogue to the Vanna Group sequence.

The youngest, Bihkkačohkka, Likčá, and Čáravárri of the Kautokeino greenstone belt are correlated with the Raipas Group at Alta. This group is dated at c. 2100 Ma (Melezhik et al. 2015) and, in addition to basaltic volcanics, contains thick, well preserved arkosic sandstones (Skoadduvarri Sandstones) and associated dolomites and calcareous mudstones (Zwaan & Gautier 1980; Bergh & Torske 1986, 1988; Vik 1985; Melezhik et al. 2015). These units resemble those of the Tinnvatn and Bukkheia formations of the Vanna Group, but contrasts in being much thicker (<2 km), and the somewhat younger in age. The sandstones near Alta, however, display trough cross-bedding and numerous fluvio-deltaic structures, and are interpreted to have been deposited as distal tectonically induced fan deltas in an elongate N-S trending rift basin stretching from Kautokeino in the south to Alta (Bergh & Torske 1986; 1988; Torske & Bergh 2004). In terms of the known, long-lasting period of Palaeoproterozoic rifting (Skyttä et al. 2019), we consider the Raipas Group metavolcanic rocks to mark the later pulse of mafic magmatism and corresponding crustal extension (2.32-1.98 Ga) of the Karelian craton (Skyttä et al. 2019), creating elongate rift basins filled by clastic and calcareous sandstones and mudstones, as occur on Vanna. Later on, the entire Alta-Kautokeino greenstone belt succession was inverted, folded and thrusted due to E-W shortening and basin closure during the Svecofennian orogeny (c. 1.9-1.7 Ga) (Henderson et al. 2015). The western part of the NNW-SSE trending Kautokeino greenstone belt shows steeply dipping shear zones with both dip-slip and strike-slip kinematics, predominantly sinistral, but also with dextral kinematics (Henderson et al. 2015). In the Alta area, the Svecofennian orogenic event resulted in E-W trending macroscale anticline-syncline folds and local thrust systems (Zwaan & Gautier 1980) that may correspond to those of the D_1 shortening event on Vanna. These folds were later affected by a SE-directed refolding either due to oblique-partitioned refolding during the late stages (i.e. D_2) of the Svecofennian orogeny, or alternatively, due to Caledonian reworking.

Furthermore, we suggest correlation of the Skoadduvarri Sandstone with the Saltvatn Group in the Repparfjord Tectonic window succession (cf. Bingen et al. 2015). This group is the stratigraphically lowest unit in the Raipas Supergroup of the Repparfjord tectonic window and consists of arkosic sandstone, conglomerate and minor dolostone (Pharaoh et al. 1983; Jensen 1996; Nilsen & Nilsson 1996; Torgersen et al. 2015). By analogy to Alta and slightly in contrast to the Vanna Group, the Raipas Supergroup was deposited at c. 2100 to 2060 Ma (Perello et al. 2015) in a likely more NE-SW trending basin, but still somehow linked to the Alta-Kautokeino greenstone belt (Torgersen et al. 2015).

Other possible correlative sequences with the Vanna Group are clastic metasupracrustal rocks of the Karasjok Greenstone belt (e.g. Often, 1985; Siedlecka et al. 1985; Braathen & Davidsen 2000). This belt is traced southward from coastal eastern Finnmark into the Central Lapland and Kittilä Greenstone belt of northern Finland (e.g. Patison, 2007) and continues further into Russia (Hanski & Huhma 2005). The siliciclastic units there are thick arkoses and fuchsite-rich quartzites, and closely related to metapelites and volcaniclastic deposits (Braathen & Davidsen 2000; Melezhik et al. 2013).

Of importance to basin closure events, the Karasjok greenstone belt is bounded to the east by west-transported fold-thrust nappes formed by E-W crustal shortening (e.g. Krill 1985; Marker 1985) as part of the Lappland-Kola Orogen. This orogen affected portions of the reworked Archaean crust and enclosed rift basins at c. 1.95–1.91 Ga, by NE-SW transpressional continent-continent collision between the Kola craton and the Karelian craton (Daly et al. 2006; Lahtinen et al. 2008).

Fennoscandian metasupracrustal units farther south with similar build-up of quartzites, arkosic sandstones and mudstones as on Vanna, and showing approximately the same depositional ages, relationships with the basement, and intrusion of mafic sills exist in the Central Lapland Greenstone belt of Finland (Hanski & Huhma 2005) and in the Norrbotten Province of Sweden (Bingen et al. 2015; Bergman 2018).

Palaeoproterozoic volcano-sedimentary sequences in the Norrbotten province of Sweden (**Fig.** 1) define a system of NNW-SSE to NNE-SSW trending linear belts (Bergman 2018; Bergman et al. 2001) that record long-lived c. 2.2-2.1 Ga continental extension and sedimentary basin formation, and mafic-ultramafic intrusions (Martinsson, 1997; Melezhik and Fallick, 2010; Lynch et al. 2018). These basin sequences experienced tectonic inversion in response to NE-SW crustal shortening, and these events produced folds and partitioned reverse and strike-slip faults trending NNW-SSE, that resemble the two-phase shortening events on Vanna (e.g. Anderson et al. 2019). The field data described above from the Vanna Group and analogue sedimentary sequences, clearly indicate the sequences were deposited in possible extensional basins that were later inverted by successive NE-SW and NW-SE contraction, producing basement-involved fold-thrust structures and temporally and spatially related transverse, strike-slip shear zones, as documented from Vanna.

In summary, our data and regional comparison of the Palaeoproterozoic metasupracrustal sequences on Vanna outlined above, all can be accounted for by formation in rift-related basins due to break-up of the Archaean craton in northern Fennoscandia (2.4-2.1 Ga), followed by two major assumed Late Svecofennian crustal shortening events (D_1-D_2) that reactivated and inverted the rift basins along their bounding normal faults by first, NE-SW and second, NW-SE directed crustal shortening. The resulting structural architecture was that of basement-involved fold-thrust deformation and corresponding oblique strike-slip faults formed by partitioned transpression (cf. Bergh et al. 2010).

Conclusions

1) The para-autochthonous metasedimentary sequences on Vanna, including those in the allochthonous Skipsfjord and Svartbergan nappes, were deposited in separate, pre-orogenic (2.4-2.2 Ga) rift basins bounded by NNW-SSE, NNE-SSW, and subordinate NE-SW trending, steep normal faults. The basins on Vanna consist of a lower series of metapsammites and overlying metapelites with subordinate horizons of peculiar calcareous metapelitic breccias, quartzites and conglomerates. Internal stratigraphy and primary sedimentary structures indicate deposition in N-S trending narrow (?) basins from source areas in the south in shallow marine, high-energy deltaic or tidal and shore face depositional environment. Similar aged metasedimentary sequences are present both in the WTBC, in other tectonic basement windows in the Caledonides, and elsewhere in the Fennoscandian shield east of the Caledonides (**Fig.** 1).

2) The steep, pre-existing c. 2.4 Ga mafic dykes trending N-S in the tonalitic basement rocks of Vanna, provided favourable zones of weakness that localized the Palaeoproterozoic rift basins and their bounding normal faults.

3) The rift basins and enclosed metasedimentary sequences were subjected to two main shortening events (D_1-D_2). The D_1 event involved ENE-WSW shortening, thick- and thin-skinned folding and

steep reverse faulting/thrusting and reactivation of the pre-existing N-S trending normal faults (and along mafic dykes) as steep west-dipping reverse and low-angle thrust faults with up-to-east displacement. This caused up-east inversion of the metasedimentary rocks in western Vanna.

The D_2 event caused major SE-directed imbricate thrusting of the Skipsfjord and Svartbergan nappes, basement-involved fold-thrust belt formation in the para-autochthonous Vanna Group in southeastern Vanna, and sinistral strike-slip reactivation of the steep N-S trending basement faults and associated mafic dykes. This two-stage fold-thrust system is considered to of Late Svecofennian age, extrapolating from ages elsewhere in the WTBC.

4) The tectonic architecture of Vanna is strongly supported by high-resolution tilt-derivative aeromagnetic data acquired by Geological Survey of Norway. Magnetic anomalies enabled us to separate possible rift basins and bounding faults, metasupracrustal units and tonalitic basement, mafic dykes and sills, and D_1-D_2 low-angle (thrust) and steep basement-seated shear zones.

5) Regional comparison of the Palaeoproterozoic metasedimentary rift-basin sequences and orogenic fold-thrust systems on Vanna show many similarities with those found elsewhere in Fennoscandia, e.g. in the Alta-Kautokeino and Karasjok greenstone belts, Central Lapland Greenstone Belt of Finland, and in the Norrbotten Province of Sweden.

6) The metasedimentary units and associated D_1-D_2 thrusts, steep strike-slip shear zones, and intrusive contacts in both the metasedimentary units and basement gneisses developed mineralization, quartz-carbonate veins, emerald-quality beryl, and fuchsite-bearing fabrics, suggesting a strong structural control on the mineralization.

References

Amelin, Y.V., Heaman, L.M. & Semenov, V.S. 1995: U-Pb geochronology of layered mafic intrusions in the eastern Baltic Shield: implications for the timing and duration of Paleoproterozoic continental rifting. Precambrian Research 75, 31-46.

Andersson, J.B.H., Bauer, T. & Lynch, E.P. 2019: Evolution of structures and hydrothermal alteration in a Palaeoproterozoic metasupracrustal belt: Constraining paired deformation-fluid flow events in a Fe and Cu-Au prospective terrain in northern Sweden. Solid Earth Manuscript, 1-48.

Armitage, P.E.B. & Bergh, S.G. 2005: Structural development of the Mjelde-Skorelvvatn Zone on Kvaløya, Troms: a metasupracrustal shear belt in the Precambrian West Troms Basement Complex, North Norway. Norwegian Journal of Geology 85, 117-133.

Balagansky, V.V., Timmerman, M.J., Kozlova, N., Ye. & Kislitsyn, R.V. 2001: A 2.44 Ga syn-tectonic mafic dyke swarm in the Kolvitsa Belt, Kola Peninsula, Russia: implications for early Palaeoproterozoic tectonics in the north-eastern Fennoscandian Shield. Precambrian Research 105, 269-287.

Bergh, S.G., Corfu, F., Myhre, P.I., Kullerud, K., Armitage, P.E.B., Zwaan, K.B., Ravna, E.J.K., Holdsworth, R.E. & Chattopadhya, A. 2012: Was the Precambrian basement of western Troms and Lofoten-Vesterålen in northern Norway linked to the Lewisian of Scotland? A comparison of crustal components, tectonic evolution and amalgamation history, Tectonics - recent advances.

Bergh, S.G., Corfu, F., Priyatkina, N., Kullerud, K. & Myhre, P.I. 2015: Multiple post-Svecofennian 1750-1560 Ma pegmatite dykes in Archean-Palaeoproterozoic rocks of the West Troms Basement Complex, North Norway: geological significance and regional implications. Precambrian Research 266, 15.

Bergh, S.G., Kullerud, K., Armitage, P.E.B., Zwaan, K.B., Corfu, F., Ravna, E.J.K. & Myhre, P.I. 2010: Neoarchean to Svecofennian tectono-magmatic evolution of the West Troms Basement Complex, North Norway. Norwegian Journal of Geology 90, 21-48.

Bergh, S.G., Kullerud, K., Corfu, F., Armitage, P.E.B., Davidsen, B., Johansen, H.W., Pettersen, T. & Knudsen, S. 2007: Low-grade sedimentary rocks on Vanna, North Norway: a new occurrence of a Palaeoproterozoic (2.4-2.2 Ga) cover succession in northern Fennoscandia. Norwegian Journal of Geology 87, 301-318.

Bergh, S.G., Kullerud, K., Myhre, P.I., Corfu, F., Armitage, P.E.B., Zwaan, K.B. & Ravna, E.J.K. 2014: Archean elements of the basement outliers west of the Scandinavian Caledonides in northern Norway: architecture, evolution and possible correlation with Fennoscandia, In: Dilek, Y., Furnes, H. (Eds.), Evolution of Archean Crust and Early Life. Springer Science, Dordrecht, p. 24.

Bergh, S.G. & Torske, T. 1986: The Proterozoic Skoadduvarri sandstone formation, Alta, Northern Norway: a tectonic fan-delta complex. Sedimentary Geology 47, 1-26.

Bergh, S.G. & Torske, T. 1988: Palaeovolcanology and tectonic setting of a Proterozoic metatholeiitic sequence near the Baltic Shield margin, northern Norway. Precambrian Research 39, 20.

Bergman, S. 2018: Regional geology of northern Norrbotten County, In: Bergman, S. (Ed.), Geology of the Northern Norrbotten ore province, northern Sweden. Sveriges geologiska undersökning, pp. 9-18.

Bergman, S., Billström, K., Persson, P.-O., Skiöld, T. & Evins, P. 2006: U-Pb age evidence for repeated Palaeoproterozoic metamorphism and deformation near the Pajala shear zone in the northern Fennoscandian Shield. GFF 128, 7-20.

Bergman, S., Kübler, L. & Martinsson, O. 2001: Description of regional geological and geophysical maps of northern Norrbotten County (east of the Caledonian orogen), Sveriges geologiska undersökning, p. 110.

Bingen, B., Solli, A., Viola, G., Torgersen, E., Sandstad, J.S., Whitehouse, M.J., Røhr, T.S., Ganerød, M. & Nasuti, A. 2015: Geochronology of the Palaeoproterozoic Kautokeino Greenstone Belt, Finnmark, Norway: Tectonic implications in a Fennoscandia context. Norwegian Journal of Geology 95, 365-396.

Binns, R.E., Chroston, P.N. & Matthews, D.W. 1980: Low-grade sediments on Precambrian gneiss on Vanna, Troms, Northern Norway. Offprint NGU 359, 61-72.

Bond, R.M.G. & McClay, K.R. 1995: Inversion of a Lower Cretaceous extensional basin, south central Pyrenees, Spain, In: Buchanan, J.G., Buchanan, P.G. (Eds.), Basin Inversion. Geological Society Special Publications, pp. 415-431.

Boyer, S.E. & Elliott, D. 1982: Thrust systems. The American Association of Petroleum Geologists bulletin 66, 1196-1230.

Braathen, A. & Davidsen, B. 2000: Structure and stratigraphy of the Palaeoproterozoic Karasjok Greenstone Belt, north Norway - regional implications. Norsk Geologisk Tidsskrift 80, 33-50.

Butler, R.W.H. 1982: The terminology of structures in thrust belts. Journal of Structural Geology 4, 239-245.

Butler, R.W.H. 1986: Thrust tectonics, deep structure and crustal subduction in the Alps and Himalayas. Journal of the Geological Society of London 143, 857-873.

Butler, R.W.H., Matthews, S.J. & Morgan, R.K. 2007: Structural evolution of the Achnashellach Culmination, southern Moine Thrust Belt: testing the duplex model, In: Ries, A.C., Butler, R.W.H., Graham, R.H. (Eds.), Deformation of the Continental Crust: The Legacy of Mike Coward. The Geological Society of London, pp. 103-120.

Clifton, H.E., Hunter, R.E. & Phillips, R.L. 1971: Depositional structures and processes in the non-barred high-energy nearshore. Journal of Sedimentary Petrology 41, 651-670.

Corfield, S.M., Gawthorpe, R.L., Gage, M., Fraser, A.J. & Besly, B.M. 1996: Inversion tectonics of the Variscan foreland of the British Isles. Journal of the Geological Society of London 153, 17-32.

Corfu, F. 2004: U-Pb age, setting and tectonic significance of the anorthosite-mangerite-charnockite-granite suite, Lofoten-Vesterålen, Norway. Journal of Petrology 45, 21.

Corfu, F., Armitage, P.E.B., Kullerud, K. & Bergh, S.G. 2003: Preliminary U-Pb geochronology in the West Troms Basement Complex, north Norway: Archean and Palaeoproterozoic events and younger overprints. NGU Bulletin 441, 61-72.

Coward, M.P. & Butler, R.W.H. 1985: Thrust tectonics and the deep structure of the Pakistan Himalaya. Geology 13, 417-420.

Dahlstrom, C.D.A. 1970: Structural geology in the eastern margin of the Canadian Rocky Mountains. Bulletin of Canadian Petroleum Geology 18, 332-406.

Daly, S., Balagansky, V.V., Timmerman, M.J. & Whitehouse, M.J. 2006: The Lapland-Kola orogen: Palaeoproterozoic collision and accretion of the northern Fennoscandian lithosphere, In: Gee, D.G., Stephenson, R.A. (Eds.), European Lithosphere Dynamics. Geological Society, London, Memoirs, pp. 579-298.

Davids, C., Wemmer, K., Zwingmann, H., Kohlmann, F., Jacobs, J. & Bergh, S.G. 2013: K-Ar illite and apatite fission track constraints on brittle faulting and the evolution of the northern Norwegian passive margin. Tectonophysics 608, 196-211.

Eilu, P. 2012: Mineral deposits and metallogeny of Fennoscandia, Special Publication. Geological Survey of Finland, p. 401.

Eilu, P., Hallberg, A., Bergman, T., Feoktistov, V., Korsakova, M., Krasotkin, S., Kuosmanen, E., Livineko, V., Nurmi, P.A., Often, M., Philippov, N., Sandstad, J.S., Stromov, V. & Tontti, M. 2008: Metallic mineral deposit map of the Fennoscandian Shield, 1:2 000 000. Geological Survey of Finland, Geological Survey of Norway, Geological Survey of Sweden. The Federal Agency of use of mineral resources of the Ministry of Natural Resources of the Russian Federation.

Eriksson, P.G., Condie, K.C., Tirsgaard, H., Mueller, W.U., Altermann, W., Miall, A.D., Aspler, L.B., Catuneanu, O. & Chiarenzelli, J.R. 1998: Precambrian clastic sedimentary systems. Sedimentary Geology 120, 5-53.

Gillcrist, R., Coward, M. & Mugnier, J.-L. 1987: Structural inversion and its controls: examples from the Alpine foreland and the French Alps. Geodinamica Acta 1, 5-35.

Gorbatschev, R. & Bogdanova, S.V. 1993: Frontiers in the Baltic Shield. Precambrian Research 64, 19.

Griffin, W.L., Taylor, P.N., Hakkinen, J.W., Heier, K.S., Iden, I.K., Krogh, E.J., Malm, O., Olsen, K.I., Ormaasen, D.E. & Tveten, E. 1978: Archean and Proterozoic crustal evolution in Lofoten-Vesterålen, N Norway. Journal of the Geological Society of London 135, 19.

Haaland, L.C. 2018: Geometry and kinematic evolution of ductile shear zones in the Ersfjord Granite (1.79 Ga), West Troms Basement Complex: a Svecofennian accretionary thrust system. MSc thesis, Department of Geosciences. UiT the arctic University of Norway, Tromsø, p. 79.

Hanski, E. & Huhma, H. 2005: Central Lapland Greenstone belt, In: Lehtinen, M., Nurmi, P.A., Ramo, O.T. (Eds.), Precambrian Geology of Finland – Key to the evolution of the Fennoscandian Shield. Elsevier, Amsterdam, pp. 139-194.

Henderson, I., Viola, G. & Nasuti, A. 2015: A new tectonic model for the Palaeoproterozoic Kautokeino Greenstone Belt, northern Norway, based on high-resolution airborne magnetic data and field structural analysis and implications for mineral potential. Norwegian Journal of Geology 95, 26.

Henkel, H. 1991: Magnetic crustal structures in northern Fennoscandia. Tectonophysics 192, 57-79.

Hölttä, P., Balagansky, V., Garde, A.A., Mertanen, S., Peltonen, P., Slabunov, A., Sorjonen-Ward, P. & Whitehouse, M. 2008: Archean of Greenland and Fennoscandia. Episodes 13, 7.

Hölttä, P., Väisänen, M., Väänänen, J. & Manninen, T. 2007: Paleoproterozoic metamorphism and deformation in Central Lapland, Finland, In: Ojala, J.V. (Ed.), Gold in the Central Lapland Greenstone Belt, Finland. Geological Survey of Finland, pp. 7-56.

Jamison, W.R. 1987: Geometric analysis of fold development in overthrust terranes. Journal of Structural Geology 9, 207-219.

Jensen, P.A. 1996: The Altenes and Repparfjord tectonic windows, Finnmark, northern Norway. Remnants of a Palaeoproterozoic Andean-type plate margin at the rim of the Baltic Shield. PhD thesis. University of Tromsø, pp. 1-120.

Johannessen, H. 2012: Tinnvatnformasjonen i Vannas proterozoiske lagrekke: Sedimentære facies og avsetningsmiljø. MSc thesis, Department of Geology. University of Tromsø, Tromsø, p. 105.

Johansen, H. 1987: Forholdet mellom det prekambriske underlaget og overliggende sedimentære bergarter sør-øst på Vanna, Troms. Cand. scient thesis, Institutt for biologi og geologi. Universitetet i Tromsø, Tromsø, p. 136.

Karlsen, S.E. 2019: Strukturell og kinematisk analyse av Skipsfjorddekkets og underliggende bergarter i nordøstlige del av Vanna, Vest-Troms gneissregion. MSc, Institute of geosciences. UiT - the Arctic University of Norway, Tromsø, p. 80.

Knudsen, S. 2007: Strukturgeologi og petrologi i palaeoproterozoiske metasedimentære og intrusive bergarter på Vanna, Troms. MSc, Department of Geology. University of Tromsø, Tromsø, p. 113.

Koistinen, T., Stephens, M.B., Bogatchev, V., Nordgulen, Ø., Wennerström, M. & Korhonen, J. 2001: Geological map of the Fennoscandian Shield, scale 1:2 000 000. Geological surveys of Finland, Norway, Sweden, and the north-west department of ministry of Natural Resources of Russia.

Kolsum, S. 2019: Geometrisk og kinematisk analyse av duktile skjærsoner i metasedimentære og intrusive bergarter i Vannagruppen, Vest-Troms gneisregion, Troms, og deres relasjon til svekofenniske folde- og skyvestrukturer. MSc, Institute for geosciences. UiT - the Arctic University of Norway, Tromsø, p. 86.

Krill, A.G. 1985: Svecokarelian thrusting with thermal inversion in the Karasjok-Levasjok area of the northern Baltic Shield. NGU Bulletin 403, 16.

Kullerud, K., Skjerlie, K.P., Corfu, F. & de la Rosa, J.D. 2006: The 2.40 Ga Ringvassøy mafic dykes, West Troms Basement Complex, Norway: The concluding act of early Palaeoproterozoic continental breakup. Precambrian Research 150, 183-200.

Lahtinen, R., Garde, A.A. & Melezhik, V.A. 2008: Palaeoproterozoic evolution of Fennoscandia and Greenland. Episodes 31, 9.

Lahtinen, R., Huhma, H., Lahaye, Y., Kousa, J. & Luukas, J. 2015: Archean-Proterozoic collision boundary in central Fennoscandia: Revisited. Precambrian Research 261, 39.

Lahtinen, R., Korja, A. & Nironen, M. 2005: Palaeoproterozoic tectonic evolution of the Fennoscandian Shield, In: Lehtinen, M., Nurmi, P.A., Rämö, T. (Eds.), The Precambrian Bedrock of Finland—Key to the Evolution of the Fennoscandian Shield. Elsevier, Amsterdam, pp. 418-532.

Lahtinen, R., Korja, A., Nironen, M. & Heikkinen, P. 2009: Palaeoproterozoic accretionary processes in Fennoscandia, In: Cawood, P.A., Kröner, A. (Eds.), Earth Accretionary Systems in Space and Time. The Geological Society, London, pp. 237-256.

Laurent, O., Auwera, J.V., Bingen, B., Bolle, O. & Gerdes, A. 2019: Building up the first continents: Mesoarchean to Paleoproterozoic crustal evolution in West Troms, Norway, inferred from granitoid petrology, geochemistry and zircon U-Pb/Lu-Hf isotopes. Precambrian Research 321, 303-327.

Lynch, E.P., Hellström, F.A., Huhma, H., Jönberger, J., Persson, P.-O. & Morris, G.A. 2018: Geology, lithostratigraphy and petrogenesis of c. 2.14 Ga greenstones in the Nunasvaara and Masugnsbyn areas, northernmost Sweden, In: Bergman, S. (Ed.), Geology of the Northern Norrbotten ore province, northern Sweden. Sveriges geologiska undersökning.

Marker, M. 1985: Early Proterozoic (c.2000-1900Ma) crustal structure of the northeastern Baltic Shield: tectonic division and tectogenesis. Norges Geologiske Undersøkelse Bulletin 403, 55-74.

Martinsson, O. 1997: Tectonic setting and metallogeny of the Kiruna greenstones. PhD. Luleå University of Technology, pp. 1-162.

Melezhik, V.A., Bingen, B., Sandstad, J.S., Pokrovsky, B.G., Solli, A. & Fallick, A.E. 2015: Sedimentary-volcanic successions of the Alta-Kvænangen Tectonic Window in the northern Norwegian Caledonides: Multiple constraints on deposition and correlation with complexes on the Fennoscandian shield. Norwegian Journal of Geology 95, 40.

Melezhik, V.A. & Fallick, A.E. 2010: On the Lomagundi-Jatuli carbon isotopic event: The evidence from the Kalix Greenstone Belt, Sweden. Precambrian Research 179, 165-190.

Morley, C.K. 1986: A classification of thrust fronts. The American Association of Petroleum Geologists Bulletin 70, 12-25.

Morley, C.K. 1988: Out-of-sequence thrusts. Tectonics 7, 539-561.

Motuza, G. 2000: Description to the geological map of the central part of the Ringvassøya Greenstone Belt, Troms county, northern Norway. Geological Survey of Norway, Vilnius, p. 25.

Myhre, P.I. 2011: U-Pb geochronology of crustal evolution and orogeny. Contributions from Caledonide Spitsbergen and the Precambrian West Troms Basement Complex, North Norway. PhD thesis, Department of Geology. University of Tromsø, Tromsø, p. 125.

Myhre, P.I., Corfu, F., Bergh, S.G. & Kullerud, K. 2013: U-Pb geochronology along an Archean geotransect in the West Troms Basement Complex, North Norway. Norwegian Journal of Geology 93, 1-24.

Nasuti, A., Roberts, D., Dumais, M.-A., Ofstad, F., Hyvönen, E., Stampolidis, A. & Rodionov, A. 2015: New high-resolution aeromagnetic and radiometric surveys in Finnmark and North Troms: linking anomaly patterns to bedrock geology and structure. Norwegian Journal of Geology 95, 285-297.

Nemčok, M., Schamel, S. & Gayer, R. 2005: Thrustbelts - structural architecture, thermal regimes and petroleum systems. Cambridge University Press.

Nilsen, K.S. & Nilsson, L.P. 1996: Berggrunnskart: Vargsund, scale 1:50 000. Norges geologiske Undersøkelse.

Nironen, M. 1997: The Svecofennian Orogen: a tectonic model. Precambrian Research 86, 24.

Often, M. 1985: The early Proterozoic Karasjok Greenstone Belt, Norway: a preliminary description of lithology, stratigraphy and mineralisation. NGU Bulletin 403, 16.

Olesen, O., Lundin, E., Nordgulen, Ø., Osmundsen, P.T., Skilbrei, J.R., Smethurst, M.A., Solli, A., Bugge, T. & Fichler, C. 2002: Bridging the gap between the onshore and offshore geology in Nordland, northern Norway. Norwegian Journal of Geology 82, 243-262.

Opheim, J.A. & Andresen, A. 1989: Basement-cover relationships on northern Vanna, Troms, Norway. Norsk Geologisk Tidsskrift 69, 67-81.

Patison 2007: Structural Controls on Gold Mineralisation in the Central Lapland Greenstone Belt., In: Ojala, J.V. (Ed.), Gold in the Central Lapland Greenstone Belt, Finland. Gold in the Central Lapland Greenstone Belt, Finland, pp. 107-122.

Paulsen, H.-K., Bergh, S.G. & Palinkas, S.S. 2019a: Hydrothermal origin of shear zone hosted emeralds on Vanna Island, northern Norway. Manuscript.

Paulsen, H.-K., Bergh, S.G. & Palinkas, S.S. 2019b: Late Palaeozoic fault controlled hydrothermal Cu-Zn mineralization on Vanna Island, West Troms Basement Complex, northern Norway. Manuscript submitted to Norwegian Journal of Geology.

Paulsen, H.-K., Bergh, S.G., Palinkas, S.S., Armitage, P.E.B., Karlsen, S.E., Kolsum, S., Rønningen, I.U. & Nazuti, A. 2019c: Late-Svecofennian fold-thrust belt and oblique-slip structures on Vanna island, West Troms Basement Complex, and their relation to metasedimentary sequences, Geological Society of Norway Annual Meeting. Geological Society of Norway, Bergen, Norway, p. 75.

Pettersen, T. 2007: Strukturell analyse av metasedimentære bergarter på Vanna, Troms. MSc, Department of geology. University of Tromsø, Tromsø, p. 112.

Pharaoh, T.C., Ramsay, D. & Jansen, Ø. 1983: Stratigraphy and structure of the northern part of the Repparfjord-Komagfjord window, Finnmark, Northern Norway. Norges Geologiske Undersøkelse Bulletin 377, 1-45.

Rice, A.H.N. 1990: A discussion: Basement-cover relationships on northern Vanna, Troms, Norway. Norsk Geologisk Tidsskrift 70, 179-186.

Rodionov, A. & Ofstad, F. 2012: Helicopter-borne magnetic, electromagnetic and radiometric geophysical survey at Vanna, Karlsøy, Tromsø, NGU rapport. NGU, p. 23.

Rønningen, I.U. 2019: Geometrisk og kinematisk analyse av paleoproterozoiske duktile skjærsoner i Skipsfjorddekkets undre del, Vanna, Vest-Troms gneisregionen, og relasjon til metasedimentære bergarter i Vannagruppen. MSc, Institute for geosciences. UiT - the Arctic University of Norway, Tromsø, p. 110.

Sandstad, J.S. 2015: MINN - mineral resources in North Norway. Norwegian Journal of Geology 95, 211-216.

Siedlecka, A., Krill, A.G., Often, M., Sandstad, J.S., Solli, A., Iversen, E. & Lieungh, B. 1985: Lithostratigraphy and correlation of the Archaean and Early Proterozoic rocks of Finnmarksvidda and the Sørvaranger district. Norges Geologiske Undersøkelse Bulletin 403, 7-36.

Skyttä, P., Piippo, S., Kloppenburg, A. & Corti, G. 2019: 2. 45 Ga break-up of the Archaean continent in Northern Fennoscandia: Rifting dynamics and the role of inherited structures within the Archaean basement. Precambrian Research 324, 303-323.

Tavarnelli, E. 1996: The effects of pre-exisiting normal faults on thrust ramp development: an example from the northern Apennines, Italy. Geologische Rundschau 85, 363-371.

Torgersen, E., Viola, G. & Sandstad, J.S. 2015: Revised structure and stratigraphy of the northwestern Repparfjord Tectonic Window, northern Norway. Norwegian Journal of Geology 95, 397-421.

Torske, T. & Bergh, S.G. 2004: The Čaravarri Formation of the Kautokeino Greenstone Belt, Finnmark, north Norway; a Palaeoproterozoic foreland basin succession. NGU Bulletin 442, 18.

Vann, I.R., Graham, R.H. & Hayward, A.B. 1986: The structure of mountain fronts. Journal of Structural Geology 8, 215-227.

Vik, E. 1985: En geologisk undersøkelse av kobbermineraliseringene i Alta–Kvænangenvinduet, Troms or Finnmark. PhD, Geological Institute. NTH University of Trondheim, Trondheim, pp. 1-295.

Wibberley, C. 1999: Are feldspar-to-mica reactions necessarily reaction-softening processes in fault zones. Journal of Structural Geology 21, 1219-1227.

Wibberley, C. 2005: Initiation of basement thrust detachments by fault-zone reaction weakening, In: Bruhn, D., Burlini, L. (Eds.), High-Strain Zones: Structure and Physical Properties. Geological Society, London, pp. 347-372.

Wibberley, C.A.J. 1997: A mechanical model for the reactivation of compartmental faults in basement thrust sheets, Muzelle region, Western Alps. Journal of the Geological Society of London 154, 123-128.

Wintsch, R.P., Christoffersen, R. & Kronenberg, A.K. 1995: Fluid-rock reaction weakening of fault zones. Journal of geophysical research 100, 13021-13032.

Zwaan, K.B. 1989: Berggrunnsgeologisk kartlegging av det prekambriske grønnsteisbelte på Ringvassøya, Troms, NGU rapporter. NGU, p. 28.

Zwaan, K.B. & Gautier, A.M. 1980: Alta og Gargia. Beskrivelse til de berggrunnsgeologiske kart 1834 I og1934 IV. 1: 50 000. Norges Geologiske Undersøkelse Skrifter 357, 1-47.

Figures

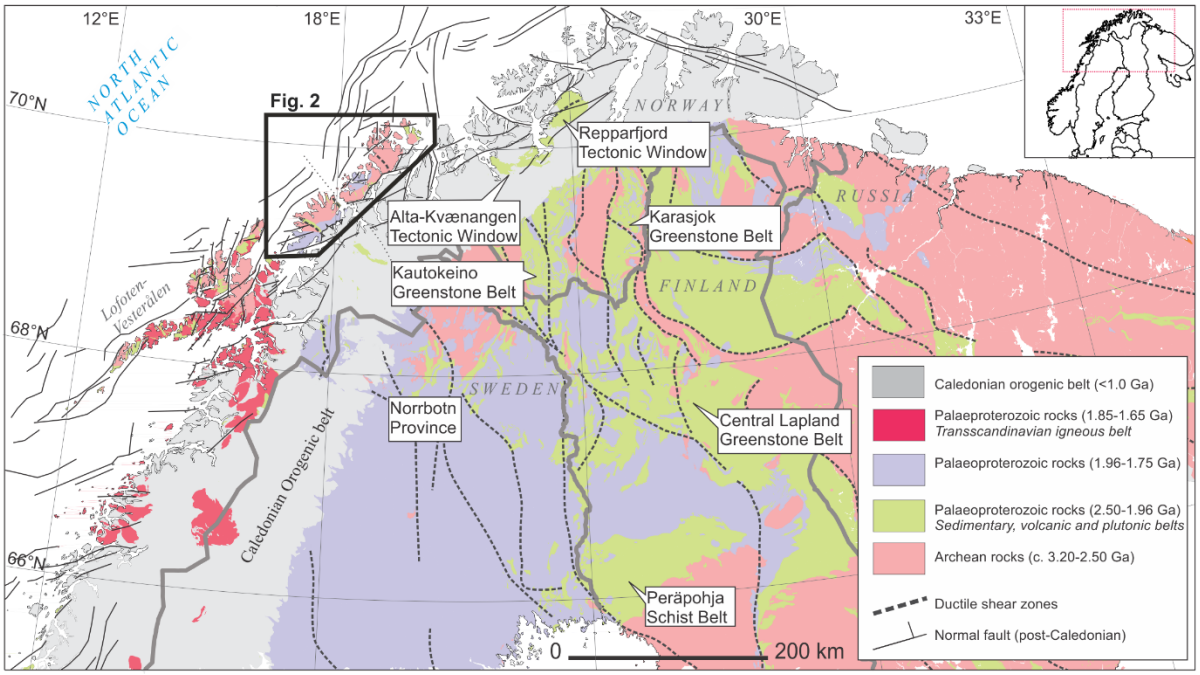

*Figure 1. Regional geological map of the northern Fennoscandian Shield (based on Koistinen et al. 2001; Olesen et al. 2002; Eilu et al., 2008 and Bergh et al. 2010). Basement windows include the West Troms basement Complex (outlined by the black frame; **Fig.** 2), Repparfjord, and Alta-Kvænangen. The latter extends to the Kautokeino Greenstone belt. Other supracrustal units exposed on the Fennoscandian Shield are the Karasjok Greenstone belt, Central Lapland Greenstone Belt, Peräpohja Schist belt and the Norrbotten Province.*

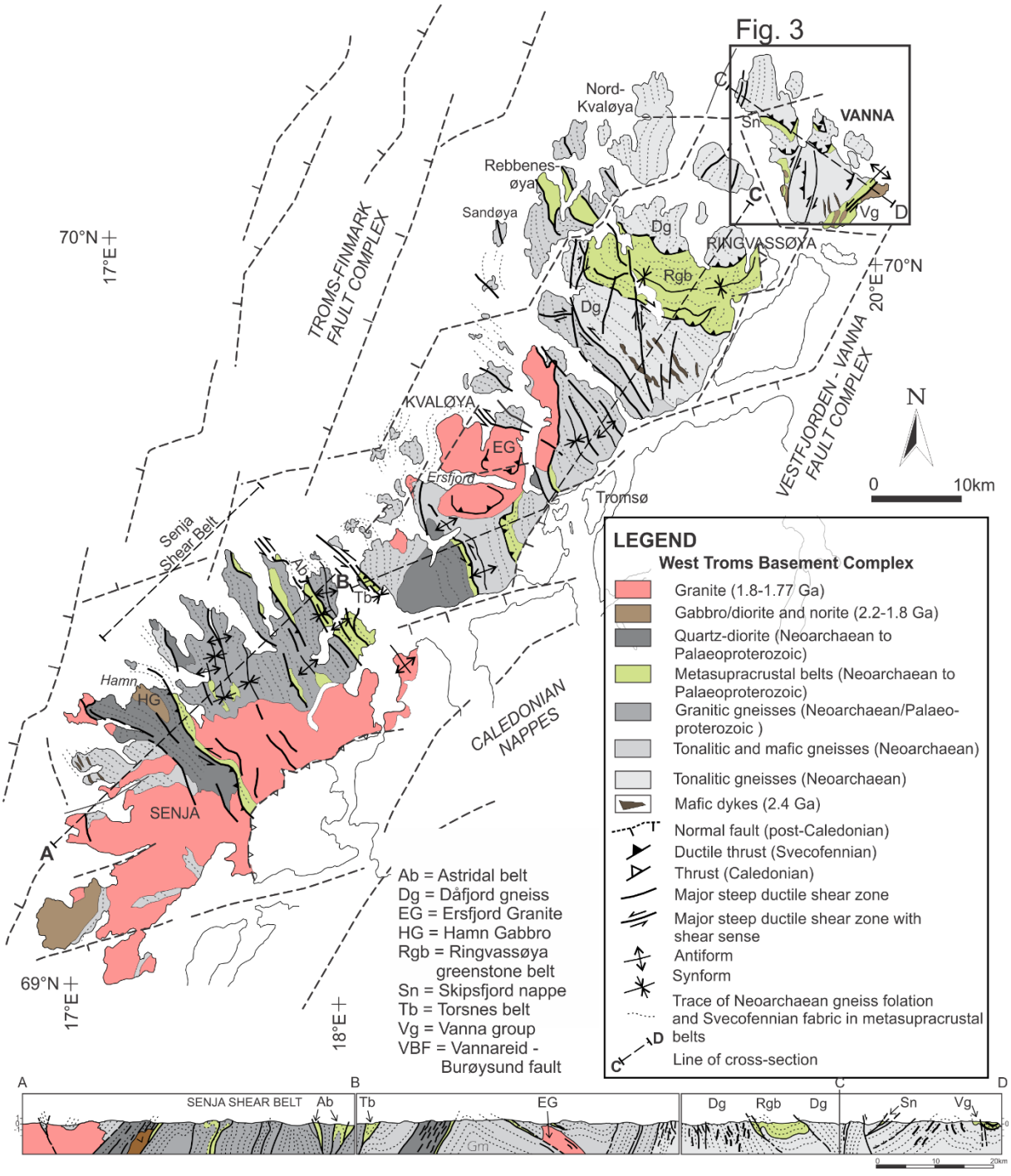

*Figure 2. Geologic-tectonic map and cross-section of the West Troms Basement Complex (modified after Kullerud et al., 2006; Bergh et al., 2007, 2010; Haaland 2019). Vanna island is located in the northern part of the complex and is outlined with a black frame (**Fig. 3**).*

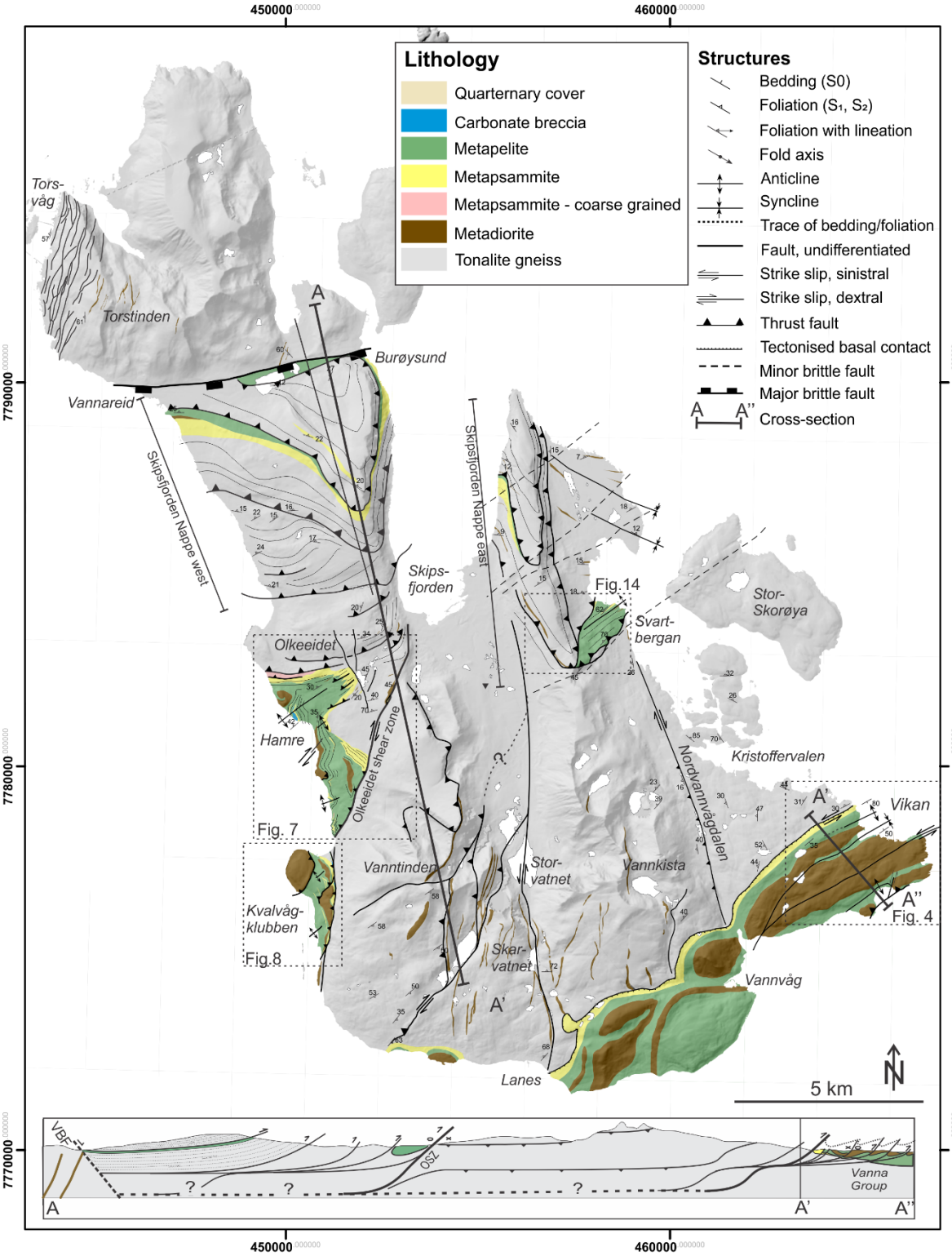

*Figure 2. Geologic-tectonic map and interpreted cross-section of Vanna island (modified after Bergh et al., 2007). The various metasedimentary sequences are outlined with black stippled frames: Vikan-Larstangen (**Fig.** 4), Hamre (**Fig.** 7), Kvalvågklubben (**Fig.** 8) and Svartbergan (**Fig.** 14).*

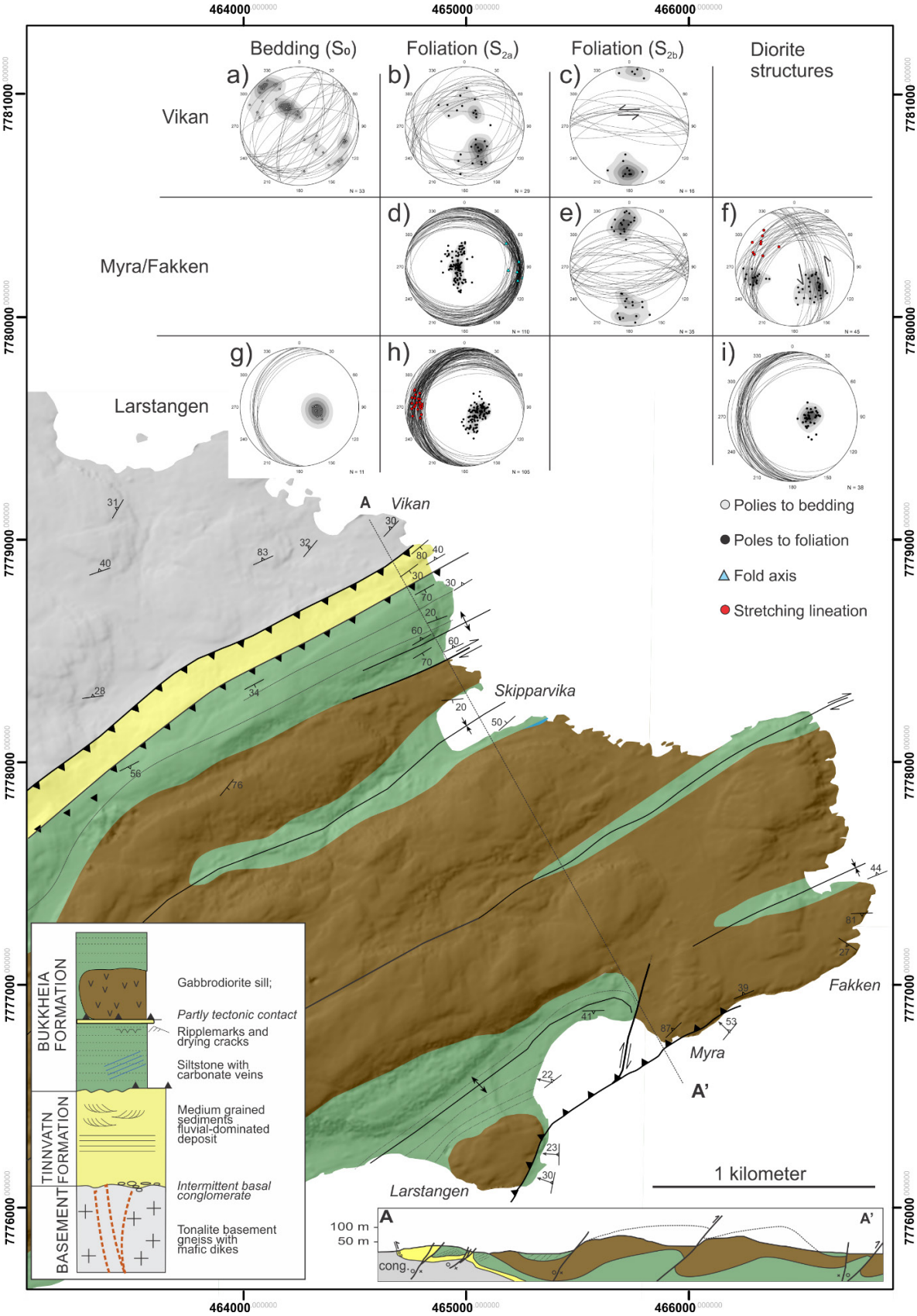

Figure 4. Geological and structural map with cross section of the transect between Vikan and Myra (Bergh et al., 2007). Pseudostratigraphic column is based on Binns et al., (1980). Equal area lower hemisphere stereonets (a-i) show poles and great circles to bedding (grey) and foliation (black), stretching lineations (red), and measured fold axis (blue). For location of map see ***Fig.*** *3.*

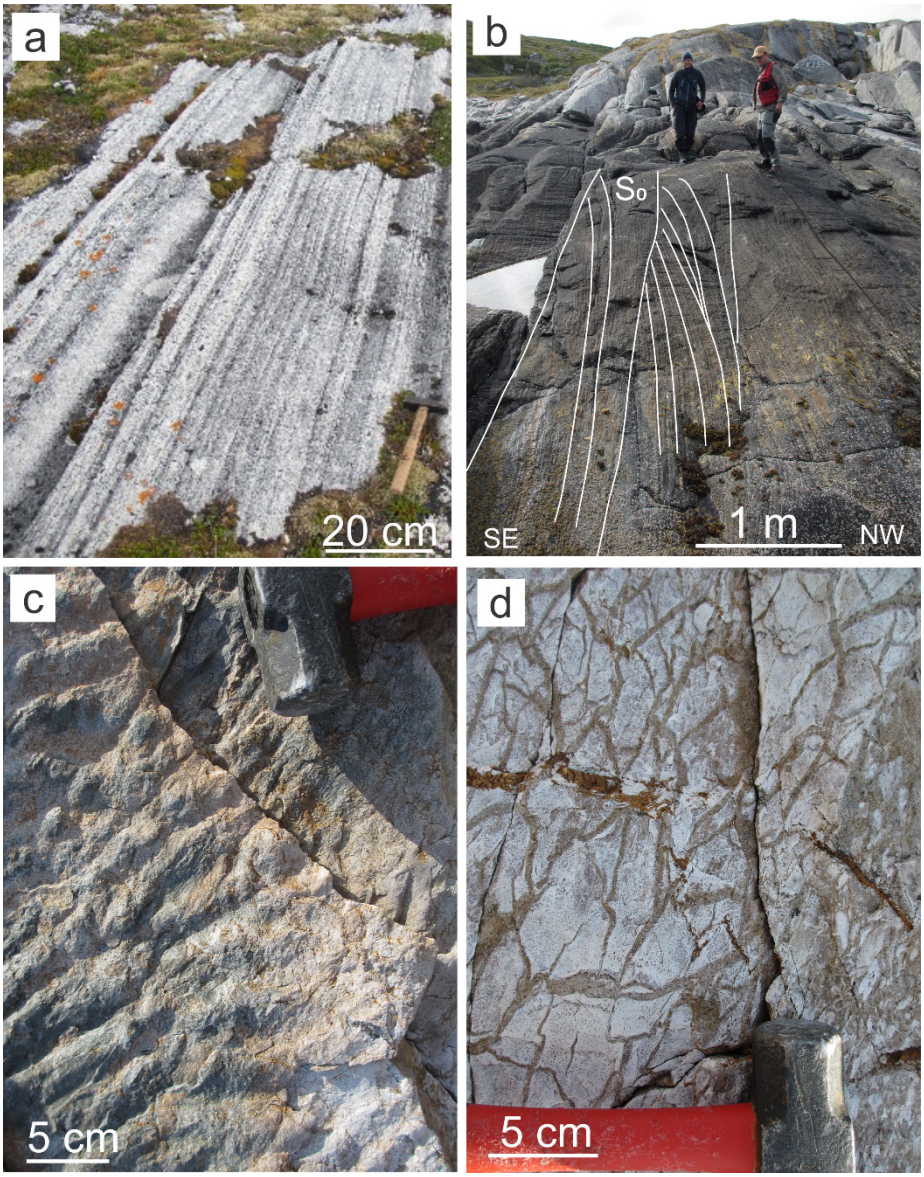

Figure 5. Primary sedimentary structures from Vikan. A) Rhythmic lamination in Tinnvatn Formation sandstone. B) Trough cross-bedding that indicates shallow marine deltaic deposition of sediments. The strata is tilted to near-vertical position because of basement involved folding. The depositional contact with the basement tonalite gneiss is c. 10m to the NW. C) Ripple marks and in silt and sandstone layers within the Bukkheia Formation. D) Mud cracks from the Bukkheia Formation indicating shallow marine environment.

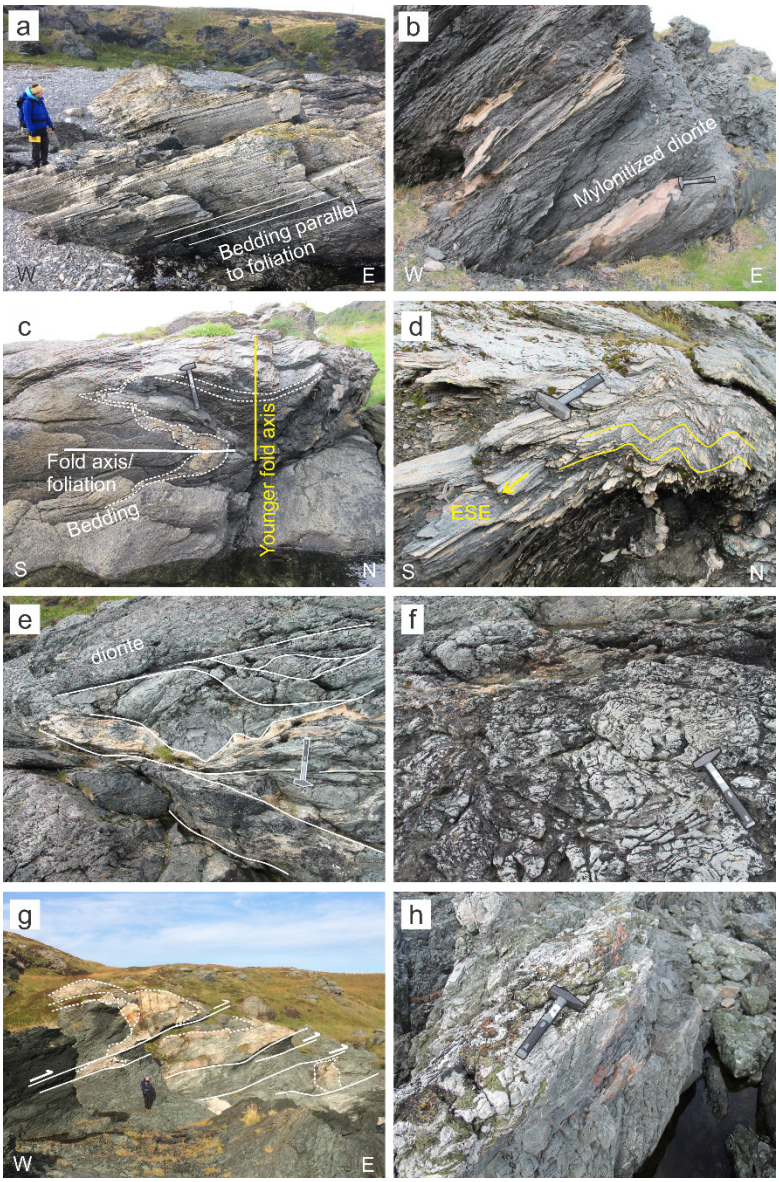

Figure 6. Field photos from Myra and Larstangen. A) Bedding in pale coloured metapsammites partly preserved and parallel with foliation. Diorite sill is visible along the top of the photo. Note person for scale. B) Mylonitized dark grey diorite at contact with metasediments. Lenses of pale metapsammite is parallel with mylonite. C) Bedding is folded by tight E-W trending isoclinal folds with the main axial planar mylonitic foliation (in white colour). This is refolded by upright E-W trending folds with subvertical fold axis (in yellow colour). D) Late E-W trending upright folds. E) Anastomosing mylonite zones internally within the diorite wraps around lenses of massive diorite. Hydrothermal carbonate (pale yellow colour on photo) is common in these mylonite zones. F) Irregular folding within diorite. G) Transposed lenses of metapsammitic xenoliths in mylonite zone in diorite sill that indicate SE directed thrusting. Note person for scale. H) Hydrothermal quartz, carbonate (white) and adularia (red) associated with chlorite (dark green), epidote (bright green) and sulphides are common in the diorite sill. Note hammer used as scale in photos is 30 cm.

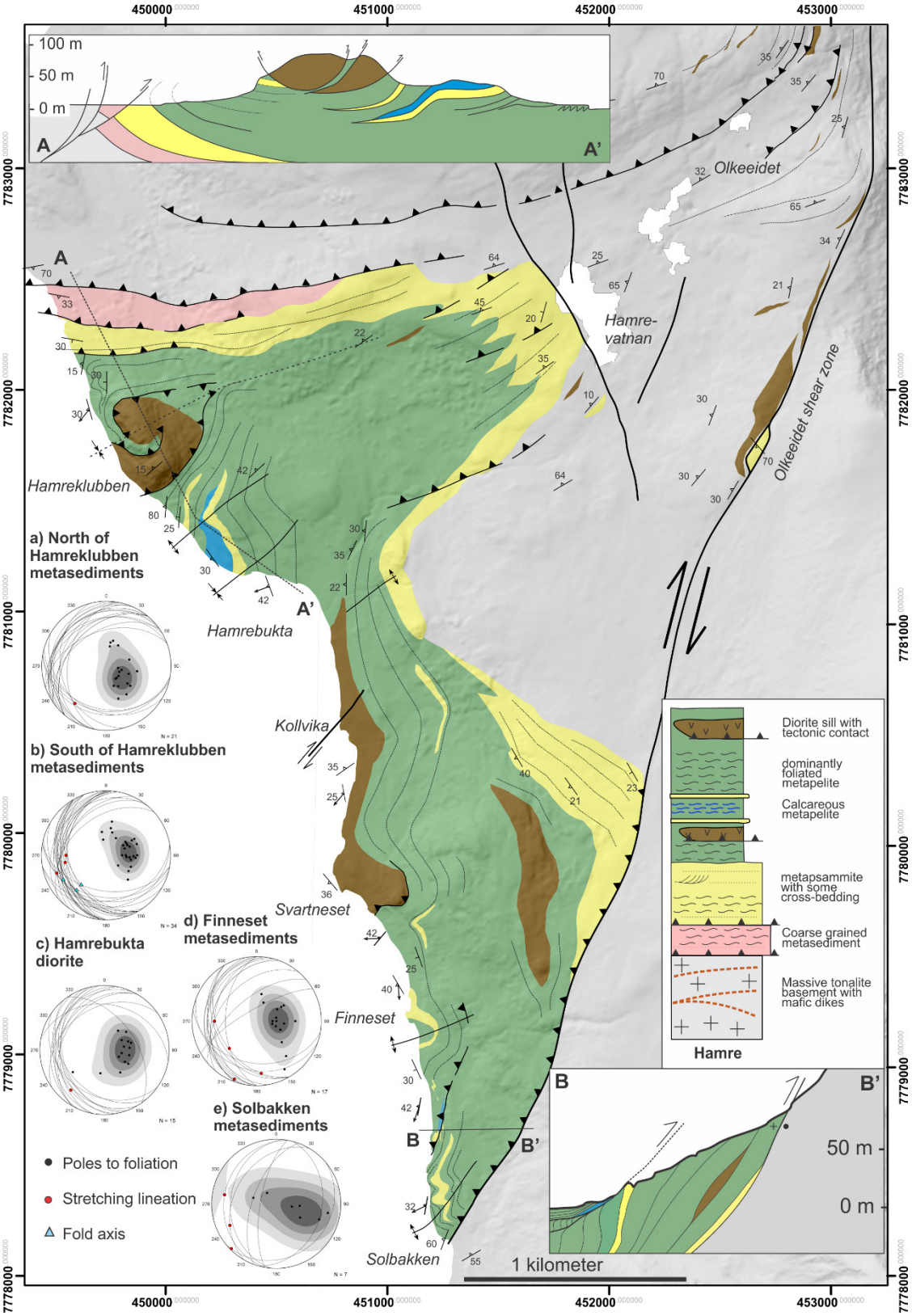

Figure 7. Geological and structural map of Hamre area. Cross-section A-A' shows the coastal transect between the basement-cover contact to Hamrebukta. Cross section B-B' shows a transect from, Solbakken/Finneset to the thrust contact with the basement tonalite. Pseudostratigraphic column show the interpreted stratigraphy. Equal area lower hemisphere stereonets (a-e) showing poles and great circles to foliation (black), stretching lineations (red), and measured fold axis (blue). For location of map see ***Fig.*** *3.*

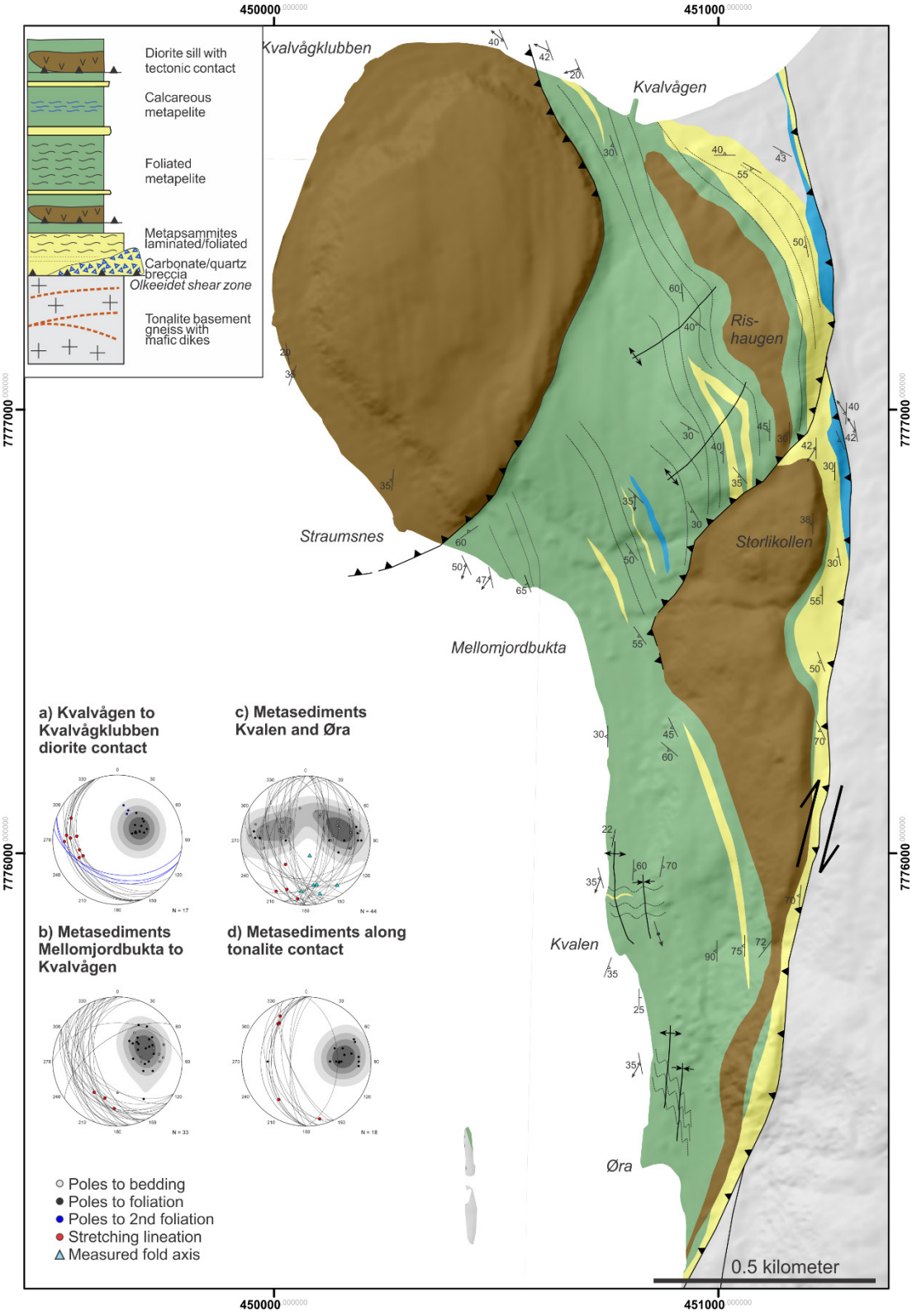

Figure 8. Geological and structural map of Kvalvågklubben area. Pseudostratigraphic column show the interpreted stratigraphy. Equal area lower hemisphere stereonets (a-d) showing poles and great circles to bedding (grey) and foliation (black and dark blue), stretching lineations (red), and measured fold axis (blue). For location of map see ***Fig.*** *3.*

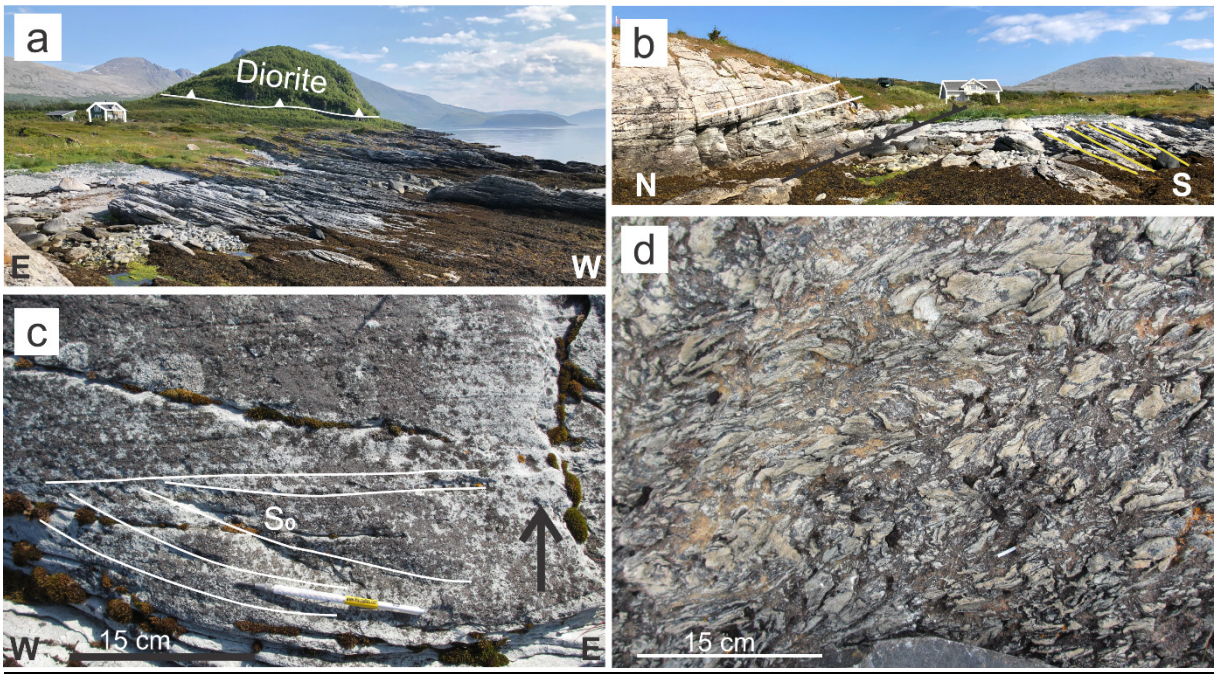

Figure 9. Field photos from northern parts of Hamre. A) Shallow south dipping foliation in metapelites north of Hamreklubben. Hamreklubben derives its name from a pronounced hill in the landscape, where a diorite sill outcrops. The diorite sill has a thrust contact with the underlying metapelites. Note two story house for scale. B) Shallow south dipping metapelites (to the right in the photo; yellow lines) is overridden by the frontal portion of the Skipsfjord Nappe. The thrust fault (black) and overlying metapsammites (white lines) dip to the NW. Note two story house for scale. C) Relict trough cross-bedding indicating way up to the south. D) Peculiar calcareous metapelite breccia with fragments of dismembered metapelite layers enclosed in a carbonate matrix

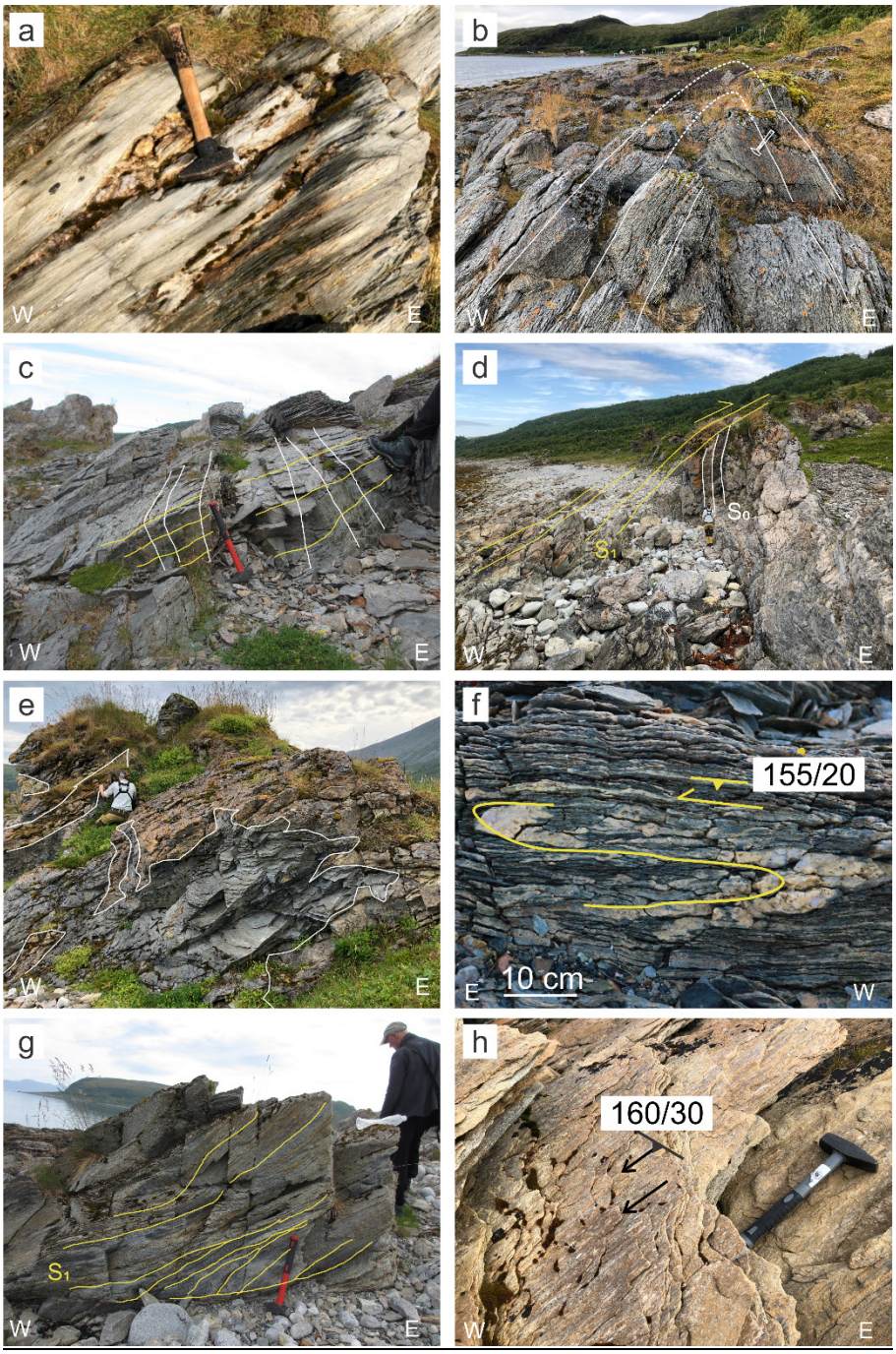

Figure 10. Field photos from Hamre and Kvalvågklubben areas. A) A penetrative foliation has almost obliterated the bedding. Secondary carbonate ± quartz (brown material under hammer) is commonly observed along foliation, and in fractures cross-cutting foliation. B) Open, upright and weakly east-verging folded metasediments at Kvalen. C) Relict bedding still visible (white lines) overprinted by a west dipping foliation. D) At Solbakken, steep to subvertical metasandstone beds (white lines) are overridden by a gently west-dipping ductile thrust fault (yellow lines). E) Carbonate breccia (brown colour outlined by while line) in metapelites (dark grey) sub-parallel to foliation. Note person for scale. F) Isoclinal fold within mylonite zone indicating top-to-ENE movement. G) Thrust duplex in metapelite indicating top-to-ENE movement. H) Stretching lineations in metapelites from Kvalvågen indicating top-to-ENE movement. Hammer used for scale is c. 30 cm.

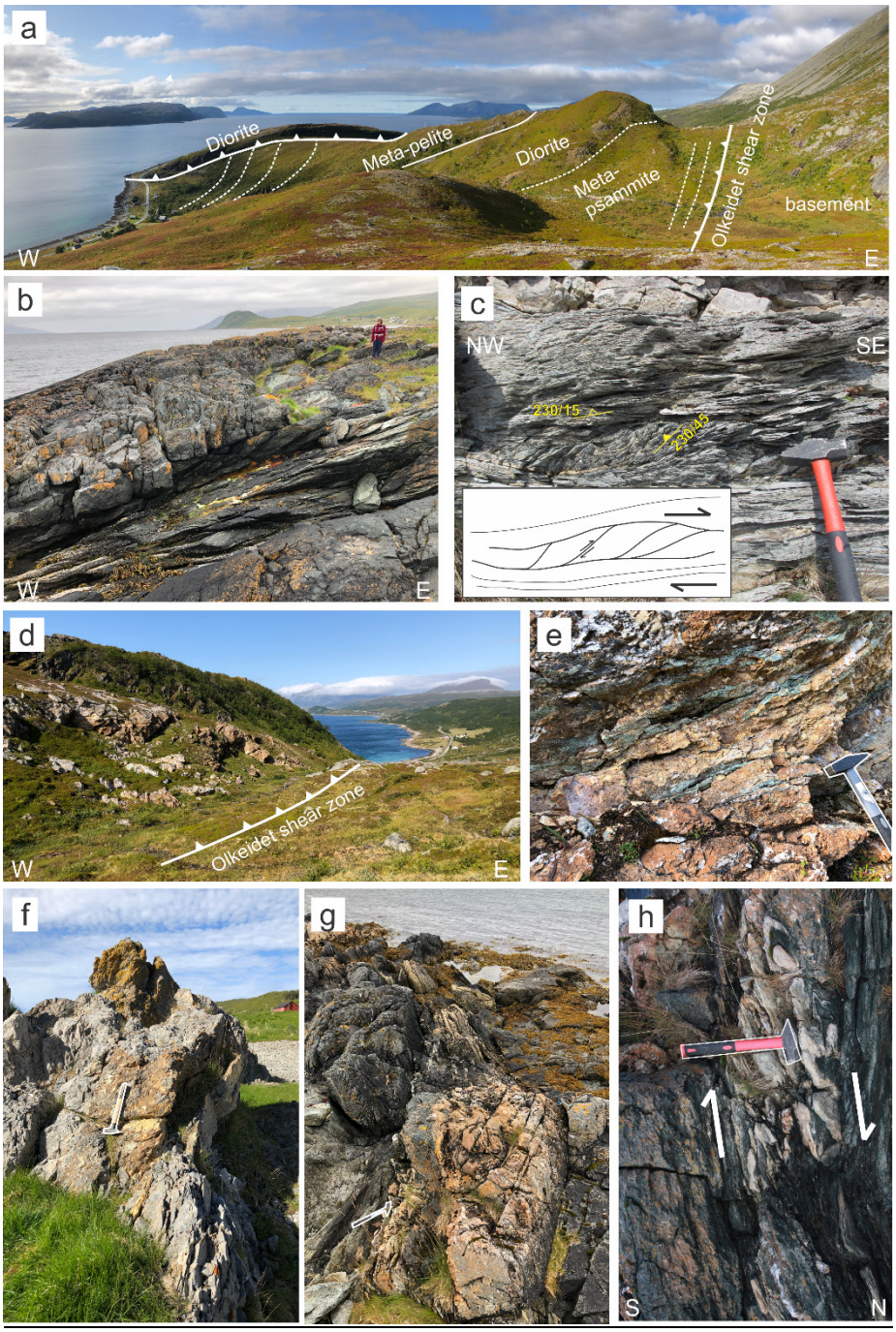

Figure 11. A) Overview photo of Kvalvågklubben. The Olkeeidet shear zone (reverse fault) separates the metasedimentary sequence from the basement gneisses. Two diorite layers/lenses makes pronounced hills in the terrain, and commonly have thrusted contacts with the surrounding metasediments. Note person for scale. B) Internal thrust zone in the diorite at Svartneset. C) Internal thrust zone at Hamreklubben with duplex formation. D) Hydrothermal quartz-carbonate breccia (c. 30 high brown coloured rock in outcrop) occurs in the hanging wall/west side of the Olkeeidet shear zone. This unit can be traced intermittently along the fault from Storkollen to Kvalvågen. E) Close-up of the hydrothermal showing coarse grained carbonate (brown colour) with foliation parallel fuchsite layers that are cut by a network of quartz veins (white). F) At Kvalvågen the hydrothermal breccia is associated with a steep shear zone, however the mineralogy is similar to (E). G) Hydrothermal quartz carbonate veins are found in steep shear zones internally within the diorite. H) Steep shear zone in diorite with isoclinal folds indicating dextral movement. Hammers used for scale are c. 30 cm.

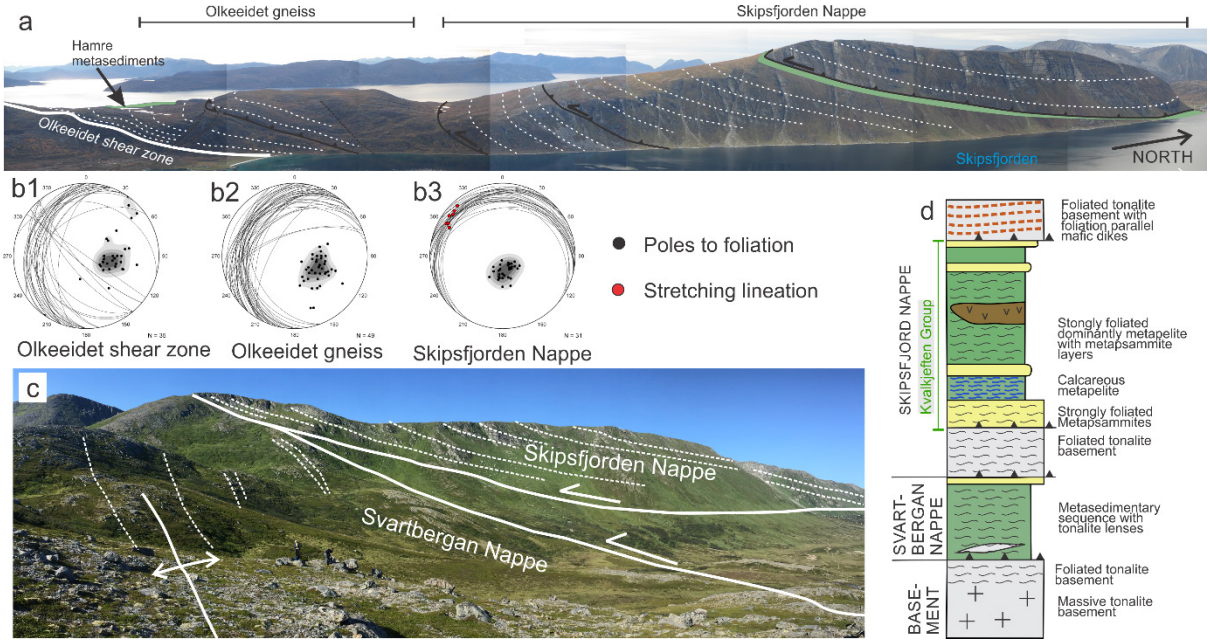

Figure 12. A) Photographic cross section of the western section of the highly strained Skipsfjord Nappe. The shallowly north-dipping strong foliation is (marked with white stippled lines) includes mafic mafic-volcanic/intrusive layers sandwiched between imbricate slices of tonalite basement gneiss. Note how the foliation flattens northward. The metasedimentary Kvalkjeften group is coloured green on the map and marks the base of a second thrust sheet. B) Equal area lower hemisphere stereonets (B1-B3) showing poles and great circles to foliation (black) and stretching lineations (red). The foliation changes from the Olkeeidet shear zone (B1) where the moderately dipping foliation strikes almost N-S, to a NE-SW foliation is the basement gneiss just north of the Olkeeidet shear zone (B2) to a shallow dipping E-W strike in the Skipsfjord Nappe (B3). C) Photographic cross section of the eastern part of the Skipsfjord Nappe and the underlying Svartbergan Nappe. The foliation steepens to the south, and the thrust contact with the basement horst is just south of the photo. D) Pseudostratigraphic column of the Svartbergan and Skipsfjord Nappes. The Kvalkjeften Group (Opheim & Andresen, 1989) is outlined.

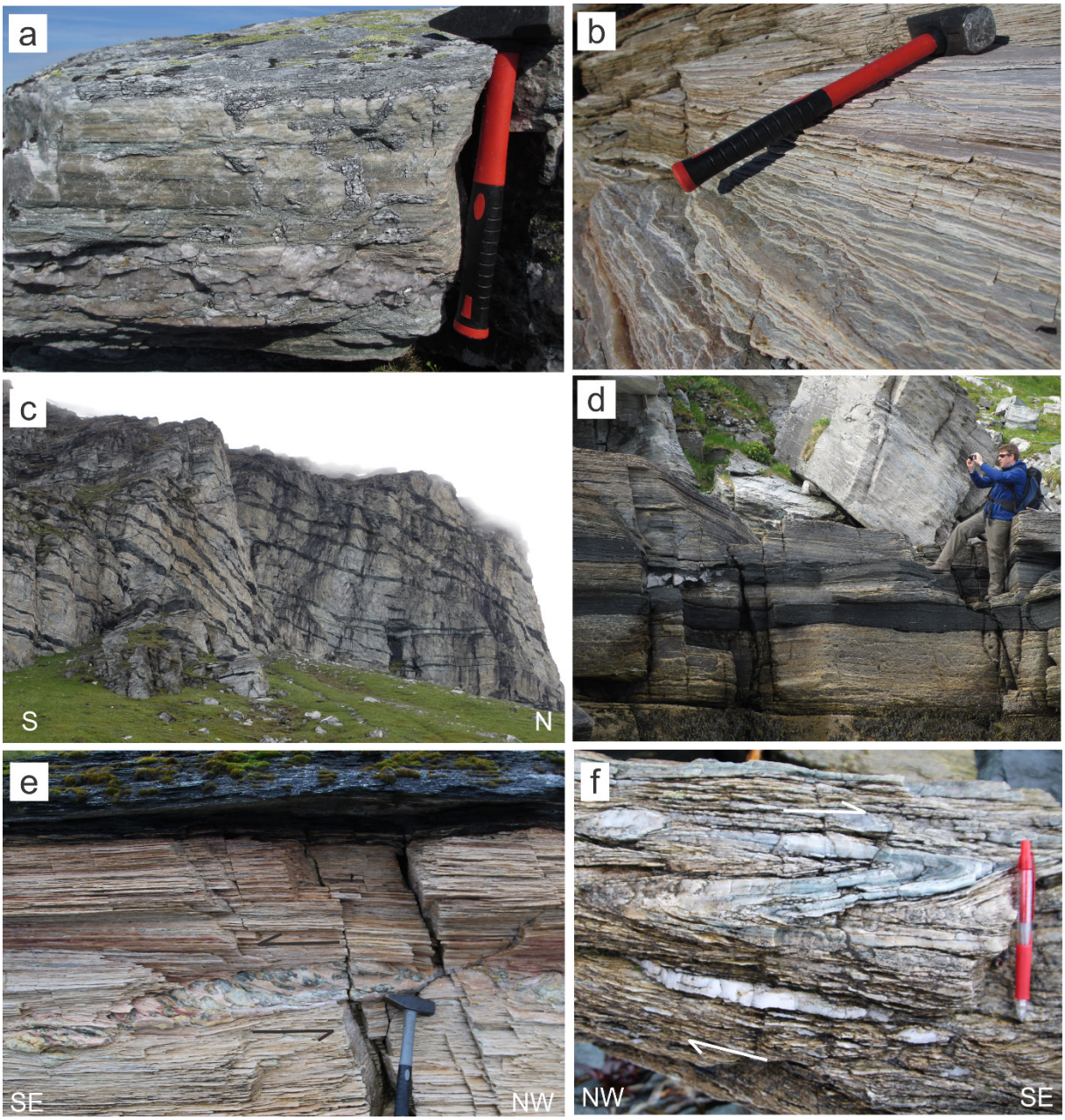

Figure 13. Field photos of the western Skipsfjord Nappe. A) Metapsammites from the lower parts of the Kvalkjeften Group. B) Highly foliated metapelites from the upper parts of the Kvalkjeften group. C) Typical outcrop photo of the Skipsfjord Nappe with mafic intrusive sheets varying in size from 20 cm to 2 m in thickness. The foliation is planar and uniform. Outcrop is c. 100 m high. D) Close-up of highly strained metasediments with mafic layers. E) Lenses of hydrothermal quartz-carbonate veins show top to SE directed thrust movement. F) Transposed near-recumbent isoclinal folds are aligned with the mylonitic foliation and indicate top-to-SE movement.

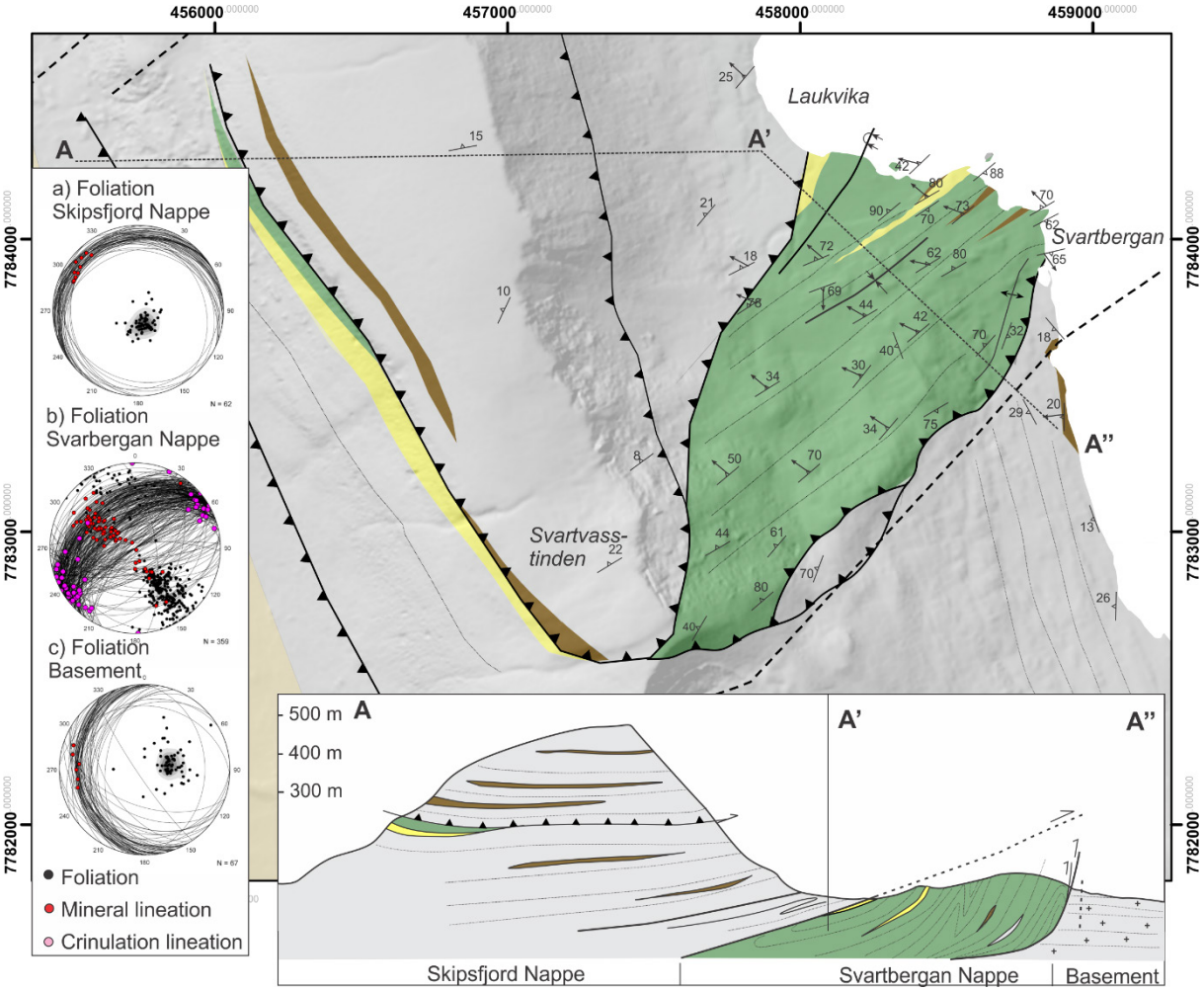

Figure 14. Geological and structural map of Svartbergan area. Cross-section A-A'' shows a composite transect across the Skipsfjord Nappe and the Svartbergan Nappe towards the steep basement-cover contact. Equal area lower hemisphere stereonets showing poles and great circles to foliation (black), stretching lineations (red), and crenulation lineations (purple). For location of map see ***Fig.*** *3.*

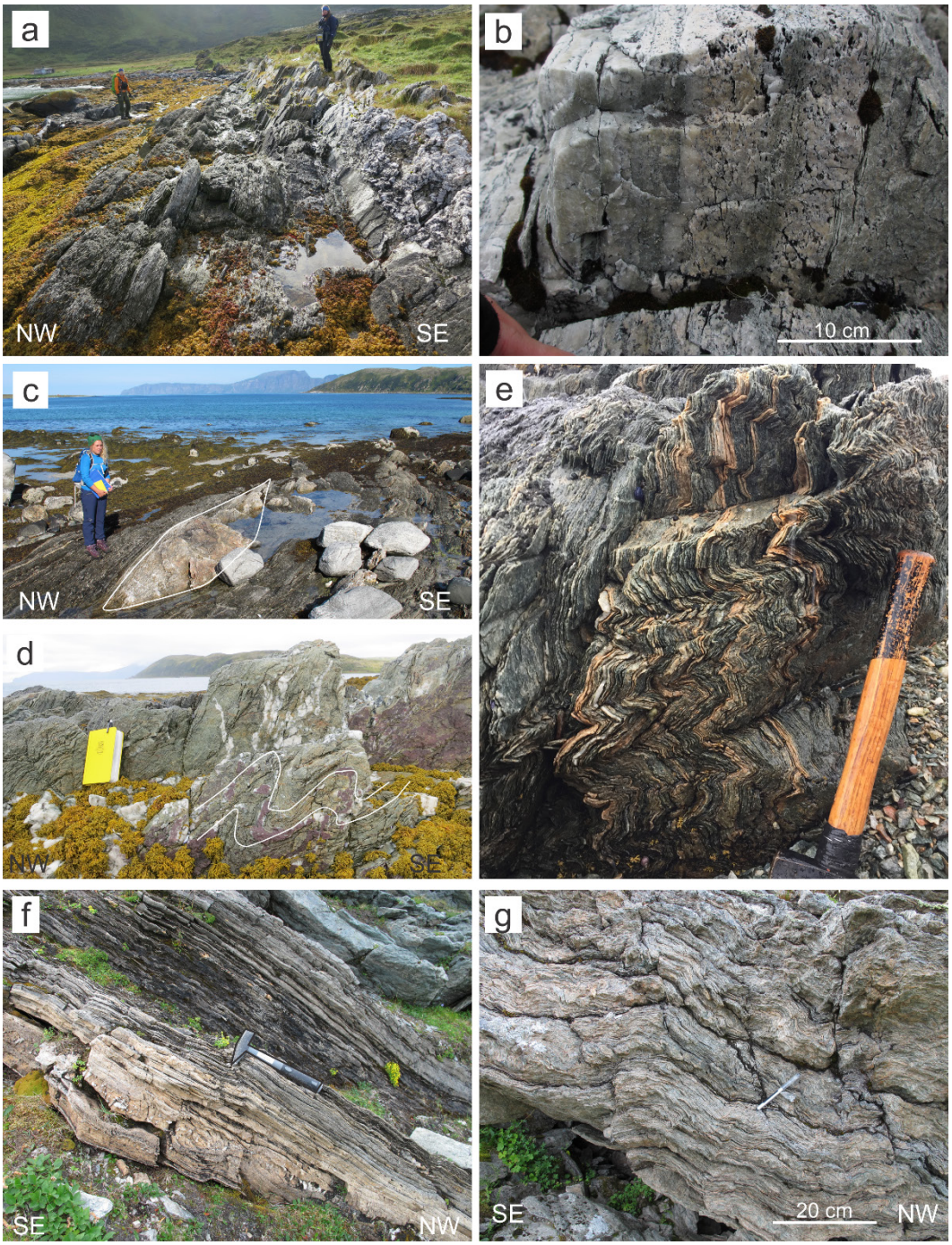

Figure 15. Field photos of the Svartbergan Nappe. A) Internally conformable, steeply dipping metapelites. B) Steeply dipping metapsammites with relict primary beds are observed at Laukvika. C) Lenses of basement tonalite gneiss are found within the metasedimentary sequence. These are interpreted as remnants of the underlying basement rocks. D) Meter-scale, asymmetric, SE verging folds likely represent macro-scale folding observed on the map-scale. Book for scale is 15 cm. E) Small-scale kink folds show NE-SW shortening strain. F) Mylonite formed along the contact with the overlying Skipsfjord Nappe. G) Extensive kink-folding in the lower part of the transition zone between the Svartbergan Nappe and the Skipsfjord Nappe. Hammer used for scale is c. 30 cm.

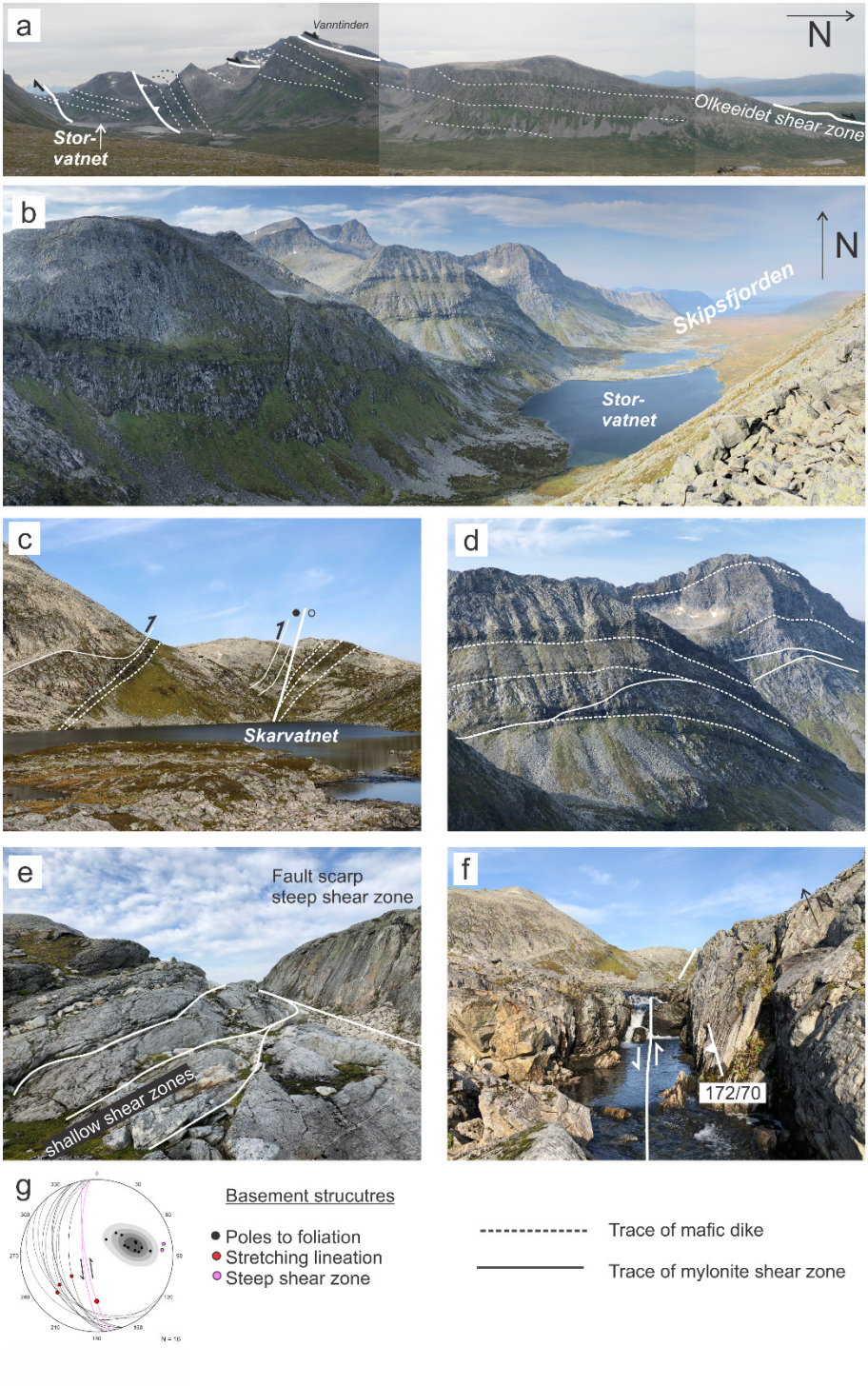

Figure 16. Field photos of basement rocks on southern Vanna. A) Photographic cross-section from Skarvatnet to the Olkeeidet shear zone. The massive tonalites are weakly foliated and contain foliation sub-parallel mafic intrusive sheets. An internal system of low-angle and high-angle ductile shear zones strike c. N-S and dips consistently to the west B) Overview photo of the basement rocks viewed from the north. C&D) The mylonitic low-angle shear zones are generally subparallel to the mafic dikes, and also splay out from the dikes and truncate the weak tonalite gneiss foliation. Steep sinistral mylonitic shear zones merge into the shallow shear zones. E) Shallow shear zones merge with the steeper shear zones. F) The marked lineament from Skarvatnet is a steep almost NS trending shear zone that displays sinistral movement. G) Equal area lower hemisphere stereonets showing orientation relationship between the weak west dipping basement foliation (black), stretching lineations (red), and steep shear zone with sinistral movement (purple).

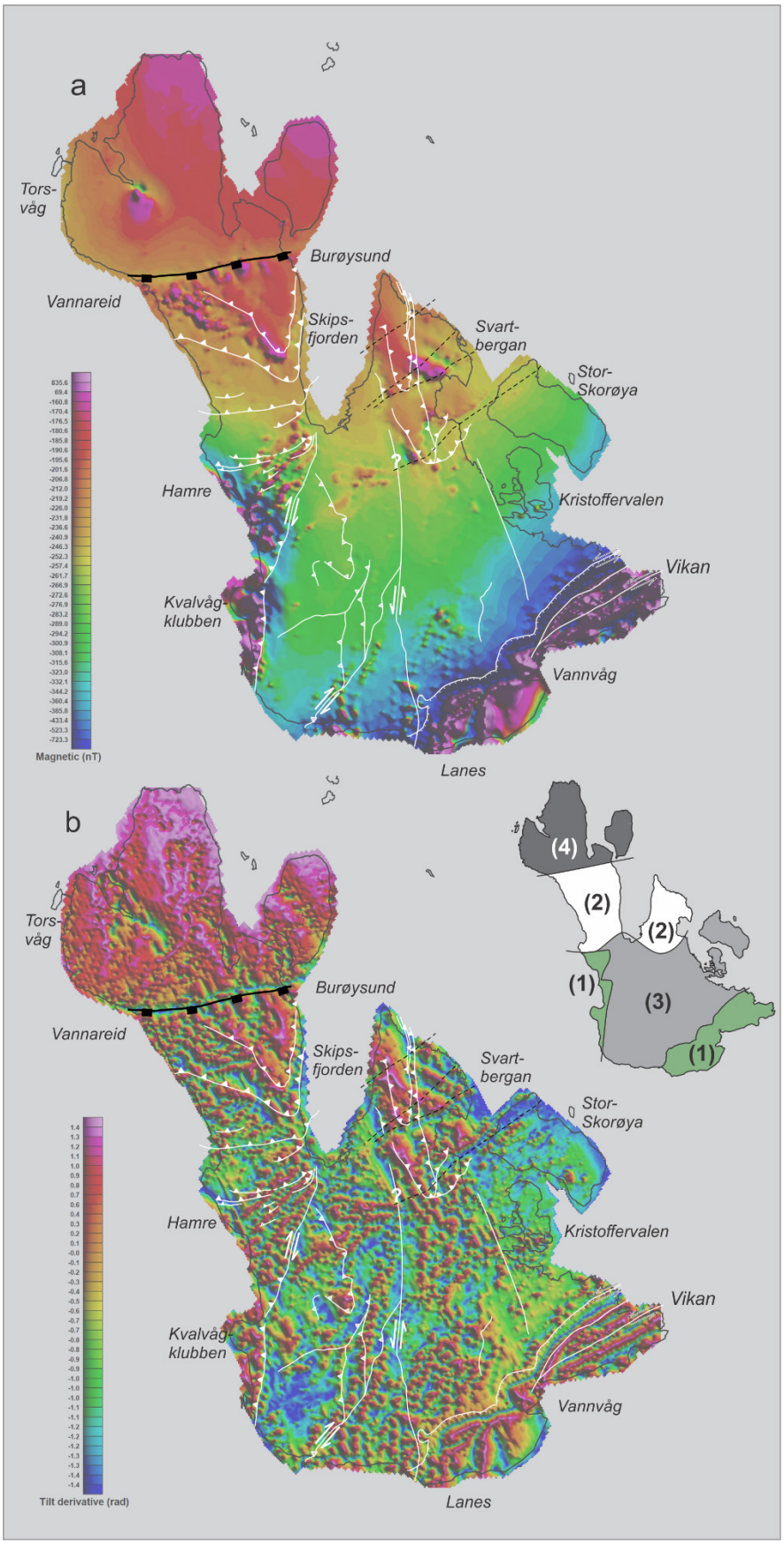

Figure 17. Aeromagnetic data from the Geological Survey of Norway's MINN program for Vanna island showing a) total magnetic field and b) tilt derivative maps (Rodionov and Ofstad, 2012; Nasuti et al. 2015; Sandstad et al. 2015). Major tectonic discontinuities (faults) are identified as displaced magnetic anomalies; e.g. ductile shear zones (white) are postulated where a progressive displacement of the affected anomalies occurs, while brittle structures are observed to truncate abruptly the anomalies they intersect (black). Small inset map show the four areas that show distinct geophysical patterns: (1) Deformed metasedimentary sequences with interpreted high magnetic response of the diorite intrusions and low magnetic response of the metasedimentary strata; (2) Highly strained Skipsfjord Nappe show less contrast between diorite and metasedimentary strata because of the flat-lying foliation; (3) Massive tonalite with relatively low magnetic signature with various N-S, NNW-SSE and NNE-SSW trending high magnetic anomalies reflecting a set of mafic dikes; (4) A much higher magnetic signature is evident for the tonalites and tonalitic gneisses in northern Vanna, north of the Vannareid-Burøysund fault zone, which is well constrained as an E-W trending low magnetic lineament.

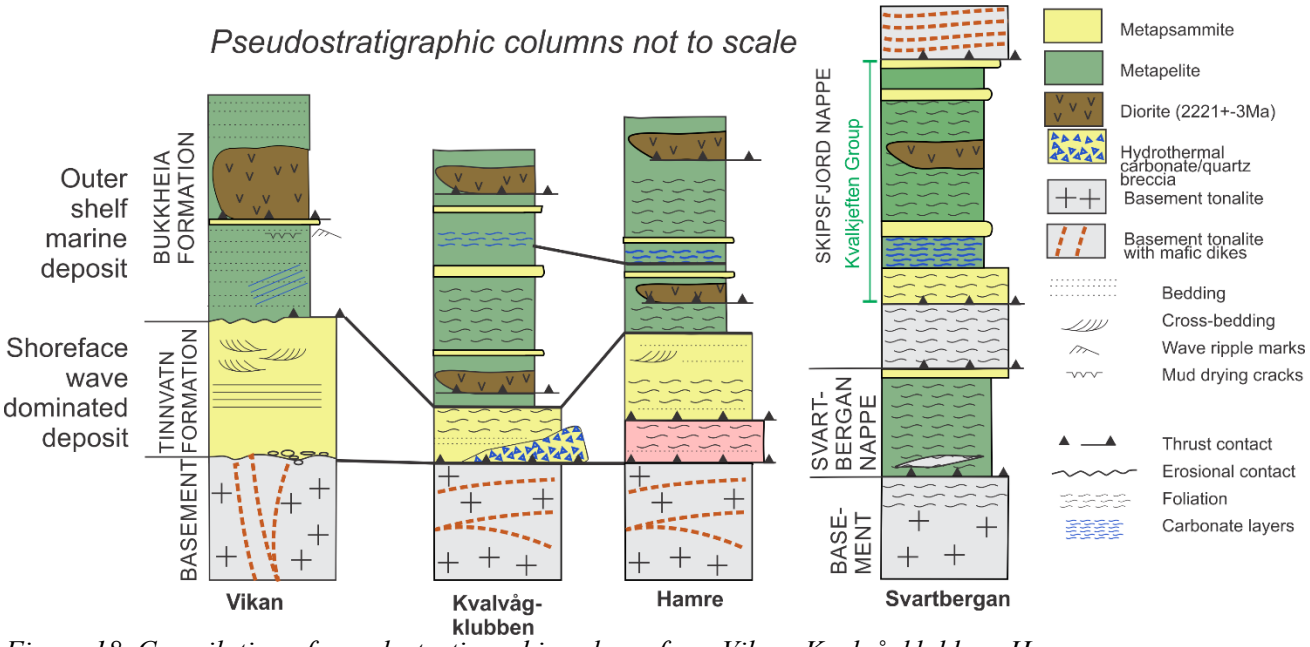

Figure 18. Compilation of pseudostratigraphic column from Vikan, Kvalvågklubben, Hamre, Svartbergan and Skipsfjord Nappe showing that they are all composed dominantly of a lower series of metapsammites and overlying metapelites in successive order. The similarities observed suggests that they represent a correlative sequence formed in a system of linked continental rift-basins. Note that the pseudostratigraphic columns are not to scale.

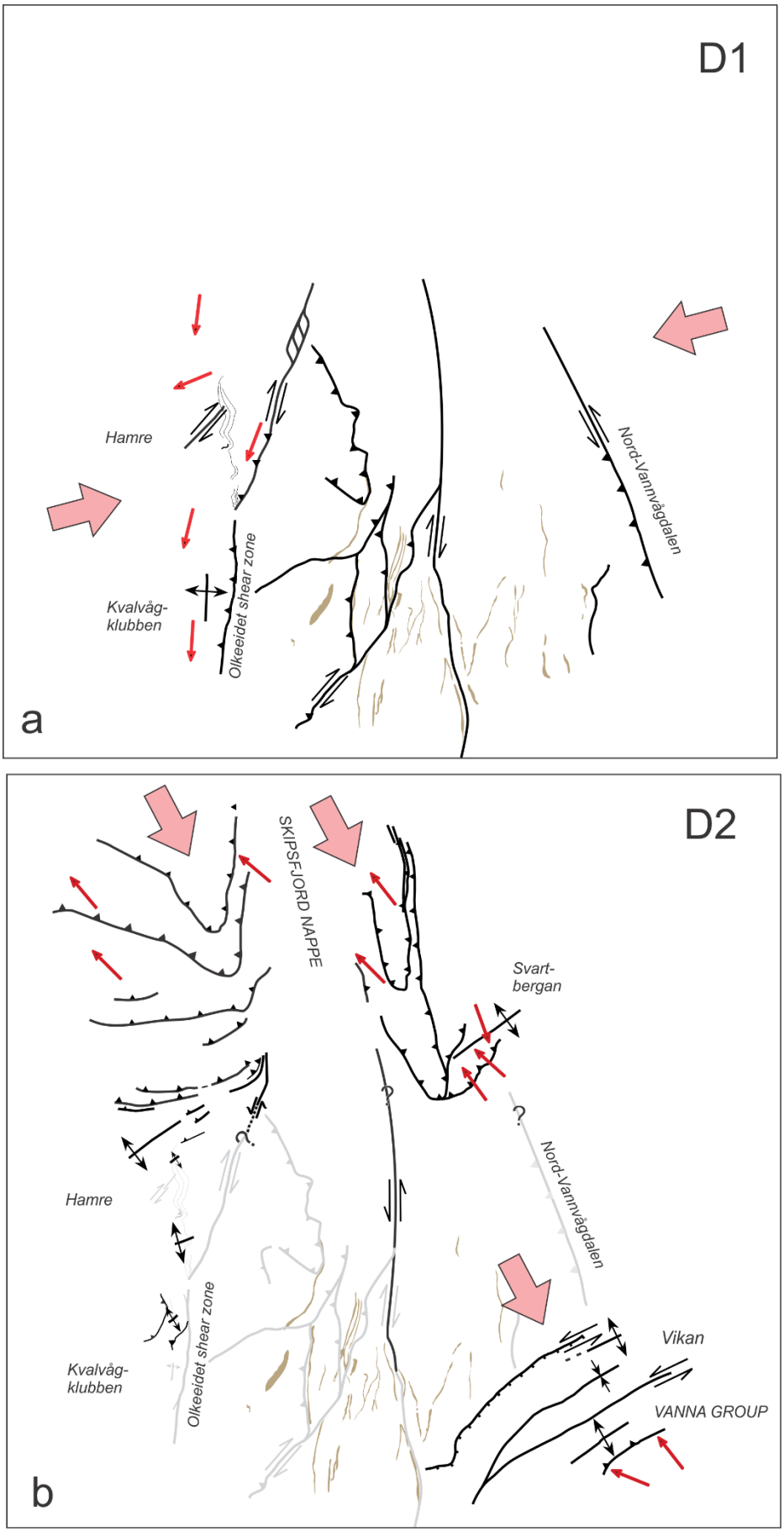

Figure 19. Schematic map view of interpreted D1 and D2 structures on Vanna. A) D1 structural fabrics are found mainly in the Southern part of Vanna within the metasedimentary strata at Hamre and Kvalvågklubben, and the along the boundaries of the mafic dikes (brown lines) in the basement. Pink arrows indicate ENE-WSW shortening direction, while red arrows are mineral lineations. B) D2 structural fabrics are most prominent within the Skipsfjord Nappe and in the Vanna Group metasedimentary strata at Vikan/Larstangen. Folding of earlier D1 foliation is observed at Hamre, and some reactivation of the basement structures is interpreted. Mineral lineations (red arrows) also support SE directed compression as indicated by the pink large arrows.

Hydrothermal emeralds: a shear zone hosted mineralization on Vanna Island, northern Norway.

Hanne-Kristin Paulsen[1], Steffen G. Bergh[1], Sabina Strmić Palinkaš[1]

[1] University of Tromsø (UiT) – The Arctic University of Norway, N-9037 Tromsø, Norway

hanne-kristin.paulsen@uit.no

Abstract

Emerald, a green Cr-bearing beryl, has been discovered within a ductile shear zone (the Olkeeidet shear zone) on Vanna Island, northern Norway. The Olkeeidet shear zone (OSZ) separates Archaean tonalitic gneiss with amphibolite layers in the hanging wall from massive tonalite in the footwall. The shear zone itself is comprised of rocks altered to albitite and fuchsite schist. Emerald is hosted by hydrothermal dolomite lenses in the albitite within the OSZ. The albitite rocks within the shear zone are deformed in a complex duplex structure. The protolith of the albitites is unclear and the original mineralogy has been almost completely replaced by albite and phyllosilicates. Hydrothermal quartz-tourmaline veins are also associated with this alteration. Fluid inclusion microthermometric measurements reveal that emerald was deposited from hypersaline (30-43 weight percent NaCl equivalent) H_2O+NaCl±CO_2±KCl hydrothermal solution. Minimum emerald formation conditions have been set at 320-350°C and 0.7 kbar. Chemical analyses show that the green colour of emerald is caused by Cr substitution of Al. In addition, chemical analyses of tourmaline, chlorite, and fuchsite found in hydrothermal veins and metasomatised host rocks show higher Cr values than when these minerals are found in unaltered host rocks. This suggests that the Cr required for the formation of emerald, and also responsible for the Cr enrichment in other minerals, was likely supplied by the hydrothermal fluid, and possibly remobilised locally from a Cr-rich meta-sedimentary strata. The stable isotope composition of dolomite ($\delta^{13}C$ vs. $\delta^{18}O$) suggest a strong contribution of magmatic CO_2. As fluid can migrate considerable distances within a shear zone environment, a deeper crustal level magmatic degassing is speculated as a possible source of highly saline fluids and CO_2

Introduction

Emerald, the green colored variety of beryl, is one of the most valuable gemstones, and forms where minor amounts of Cr and/or V substitute Al in crystal lattice of beryl ($Be_3Al_2Si_6O_{18}$). Although emeralds are rare, they can be formed in various geological settings (Walton 2004; Groat et al., 2008) but their formation always requires interaction of two geochemically contrasting components; one that brings highly incompatible Be and another rich in compatible Cr. The upper continental crust represents the main geological reservoir of Be with an average content between 1.5 and 3.1 ppm (Rudnik and Gao, 2003). Partial melting of felsic magmatic rocks and/or Al-rich meta-sedimentary rocks can produce melts with a significantly high Be content (Barton and Young, 2002). Chromium, on the other hand, is associated with mafic or ultramafic rocks, but can also be enriched in black shales (Rudnik and Gao, 2003).

Although the classic model for emerald formation involves a felsic pegmatite that intrudes an ultramafic rock (Vapnik et al, 2006), more recent studies show that emerald can form without a direct igneous component by a combination of magmatic (Laurs et al,. 1996), metamorphic (Grundmann and Morteani, 1989; Zwaan, 2006), and/or hydrothermal processes (Cheilletz and Giuliani, 1996; Banks et al, 2000; Groat et al., 2008). In this paper, we describe a case study from Vanna, northern Norway, which shows that emerald mineralization can be deposited from hydrothermal fluids circulating in a shear zone. At Vanna, this mineralization occurs within a poly-deformed shear zone, here referred to as the Olkeeidet shear zone (OSZ) within Archean to Palaeoproterozoic rocks of the West Troms Basement Complex. The OSZ has previously been described as a lineament (Grogan and Zwaan, 1997; Bergh et al., 2007), and its geological history is poorly understood. We present results from detailed mapping of structural relations, descriptions of the host lithology, as well as mineral and chemical characterization of hydrothermal and metasomatic alterations and the mineralization. Mineral parageneses are identified by a combination of petrographical observations, scanning electron microscope (SEM) analyses, Raman spectroscopy, and X-ray diffraction. Fluid composition and pressure-temperature conditions during emerald formation are investigated using fluid inclusion microthermometry and decrepitation. Here, we define hydrothermal as a process where the minerals have formed or precipitated from a hydrothermal fluid. The term metasomatism is used to describe the process where the bulk chemical composition of a rock in the solid state is changed by the introduction of components from an external source (Barton et al., 1991). This external source can be a hydrothermal fluid. This paper examines the results from the combination of analytical methods described above to discuss the hydrothermal formation of emeralds and associated hydrothermal fluid alterations in the polydeformed OSZ on Vanna.

Geological setting

Vanna is an island located in the northern part of the Neoarchaean-Palaeoproterozoic West Troms Basement Complex in northern Norway (**Fig.** 1; Bergh et al., 2010). This basement province is considered as be a western continuation of the Fennoscandian Shield separated by early Palaeozoic Caledonian Nappes to the east that are down-faulted by late Palaeozoic faults (Davids et al., 2012, Koehl et al., 2018, Indrevær et al., 2014). The West Troms Basement Complex is composed of segmented crustal blocks of tonalitic, trondhjemitic to granitic gneisses (2.9-2.6 Ga) overlain by supracrustal units (2.8-1.9 Ga; Armitage and Bergh 2005, Myhre et al., 2011, 2013) and intruded by felsic and mafic igneous rocks (c. 1.8 Ga; Corfu et al., 2003; Bergh et al., 2010). In the north, on the islands of Ringvassøy and Vanna, a mafic dike swarm (2.2-2.4 Ga) has intruded the basement gneisses (Kullerud et al., 2006).

At Vanna, a para-autochthonous meta-sedimentary sequence, the Vanna Group, unconformably overlies the basement gneisses. Its maximum age is constrained by an intrusive diorite sill dated at 2.2 Ga (**Fig.** 2: Binns et al., 1980; Johansen 1987; Bergh et al., 2007). The Vanna Group meta-sedimentary rocks are composed of arkosic, shallow deltaic sandstones and calcareous mud- and siltstones (Binns et al., 1980; Johannessen 2012). The main source and provenance for these meta-sedimentary rocks is considered to be the

basement rocks on the nearby islands of Ringvassøya, Kvaløya, and Senja (**Fig.** 1; Bergh et al,. 2007). While in the southern parts of Vanna these supracrustal units are relatively undeformed, in the northern parts of the island they occur both as relict lenses/layers of mylonites that alternates with highly sheared tonalites and mafic layers in the Skipsfjorden Nappe (Binns et al., 1980; Opheim and Andresen, 1989), with thrust contacts to autochthonous gneisses in the south. The deformation of these cover units and the tonalitic basement of Vanna is thought to be a result of Late Svecofennian and/or younger contractional deformation at lower to upper green-schist facies conditions (Johansen 1987; Opheim and Andresen 1989; Sen 2012; Dallmeyer 1992; Bergh et al., 2007, 2010; Myhre et al., 2013).

The OSZ is a c. 12 km long, NNE-SSW trending shear zone on south-western Vanna (**Fig.** 2). In the study area it cuts and deforms Archaean tonalitic gneisses. Further south, at Kvalvågklubben, it represents the unconformity between Vanna Group rocks and underlying basement. It is thought to have a complex multiphase history, and possibly originated as a Palaeoproterozoic extensional normal fault that was reactivated during the Svecofennian and/or younger contractional deformation (Bergh, et al. 2007; Paulsen et al., 2019).

Samples and methods

Fieldwork focussed on structural measurements, lithological mapping, and sampling. Samples were collected of hydrothermal vein material, unaltered host rocks (tonalite gneiss and amphibolite), and their metasomatically altered equivalents.

Scanning electron microscope (SEM) analyses combined with energy-dispersive X-ray spectroscopy (EDS) was used to highlight textural relationships as well as to determine chemical compositions of the mineralization and associated host rock alterations. Polished thin sections were coated with a thin carbon layer to avoid charging effects. All analyses were carried out at UiT The Arctic University of Norway using a Zeiss Merlin VP Compact field emission SEM equipped with an X-max^{80} EDS detector provided by Oxford Instruments. EDS measurements were done at 20 kV acceleration voltage and a 60-µm aperture size. The AZtec software by Oxford Instruments was used for data acquisition and further post-processing of the EDS data. Backscatter images (BSE) were acquired under the same conditions as EDS measurements. The vacuum conditions were higher than $1x10^{-5}$ mbar within the sample chamber.

X-ray diffraction (XRD) analyses were performed on emerald, dolomite, albite, muscovite/fuchsite, chlorite and tourmaline. The analyses were conducted at the University of Zagreb using a Philips PW 3040/60 X'Pert PRO powder diffractometer (45 kV, 40 µA), with CuKα-monochromatized radiation (λ = 1.54056 Å) and θ-θ geometry. The area between 4 and 63° 2θ, with 0.02° steps was measured with a 0.5° primary beam divergence. Compound identifications were based on a computer program X'Pert high score 1.0B and literature data.

Fluid inclusion petrographic descriptions and microthermometric measurements were obtained from double polished wafers (100-250 µm thick) of emerald, quartz, and dolomite. Petrographic descriptions are based on the ratio of liquid (L), vapour (V) and solid (S) phases at room temperature. Homogenisation temperatures (T_h), halite melting temperatures (T_s),

clathrate melting temperatures (T_{clath}), ice melting temperatures ($T_{m\ ice}$), and eutectic temperatures (T_e) were recorded using an Olympus BX 2 microscope coupled with a Linkam THMS 600 heating and cooling stage operating between -180 and +600°C at UiT The Arctic University of Norway. Fluid inclusions were classified according to Roedder (1984) and Sheperd (1985). Salinities and minimum trapping pressures for inclusions that homogenised by halite dissolution were calculated by the use of the Excel spreadsheet Hokieflincs_H_2O-NaCl (Steele-MacInnis et al., 2012) using the equations by Lecumberri-Sanchez et al., (2012). Salinities and minimum trapping pressures of the H_2O-NaCl±CO_2 system were calculated using the Excel spreadsheet mmc2 by Steele-MacInnis (2018).

Qualitative measurements of major elements present in the hydrothermal fluid were obtained by decrepitating fluid inclusions (c. 500°C for 3-4 minutes) and analysing the resulting evaporate mounds formed on the sample surface using SEM/EDS according to the procedure modified after Kontak (2004). We performed both spot analyses of specific solid phases and used map scan analyses to estimate the average composition of the whole evaporate mound.

Raman spectroscopy was conducted at the Department of Earth Science, the Faculty of Mathematics and Natural Sciences, University of Bergen. A JobinYvon LabRAM HR800 confocal Raman spectrometer equipped with a frequency doubled Nd-YAG laser (100 mW, 532 nm) and LMPlan FI 50× objective (Olympus) were used to identify emerald, dolomite, albite, muscovite/fucsite, chlorite and tourmaline. Mineral identifications were based on Raman spectra published in the literature (Lafuente et al., 2015). CO_2 in emerald-hosted fluid inclusions were also identified and CO_2 densities were calculated according to Fall et al., (2011).

$\delta^{13}C$ and $\delta^{18}O$ stable isotope analyses of dolomite were obtained using a Thermo-Fisher MAT253 IRMS with a Gasbench II at UiT The Arctic University of Norway (site.uit.no/sil). Samples were placed in 4.5ml Labco vials, then flushed with He, and 5 drops of water free H_3PO_4 were added manually with a syringe. Replicates of the samples were run at 60°C and 80°C and the reaction time was from 6 to 23 hours. The results were normalised to Vienna Pee Dee Belemnite (VPDB) standard by three in-house standards with a wide range of $\delta^{13}C$ and $\delta^{18}O$ values (Rosenbaum and Sheppard, 1986; Kim et al., 2007), and reported with an uncertainty of standard deviation ≤ 0.1 ‰.

Geological characteristics of the emerald mineralization

The emerald-hosting OSZ (**Fig.** 2) have preserved structures that indicate a long-lived system and multiphase deformation events. The OSZ is 40-50 m wide, NNE-SSW trending, and has a moderate to shallow (45-30 degrees) dip to the west. (**Fig.** 3; stereoplot). Massive autochthonous basement tonalite forms the footwall. The hanging wall consists of weakly foliated tonalitic gneiss with amphibolite layers subparallel to foliation. Amphibolite layers likely originated as mafic dikes (Kullerud et al., 2006; Bergh et al., 2007). The gneissic foliation in the hanging wall varies somewhat with a general moderate dip to the NW. Localised mainly within the shear zone is a sequence of highly altered rocks, mainly albitites and fuchsite schists. Further, the albitites within the shear zone are intruded by dolomite veins

that host emerald mineralization, and quartz-tourmaline veins. Lenses of unaltered tonalite gneiss and amphibolite layers are also present within the OSZ (**Fig.** 3).

Along the eastern margin of the OSZ, at the boundary with the massive tonalite, a < 0.5-2 m wide mainly mylonitic zone occurs. This strongly deformed zone has incorporated boudins and lenses of hydrothermal vein material, indicating that the hydrothermal veins intruded, at least partly, prior to or during fault movement (**Fig.** 4a). The western margin of the shear zone is less defined and is recognised by a gradual decrease in alteration and deformation.

Within the OSZ, an array of internal splay faults form a set of duplexes. These faults include minor thrust faults (**Figs.** 4b-d) and strike slip faults (**Fig.** 4e) with shallow to steep dips to the WSW (**Fig.** 3; stereoplot), indicating dextral movement along the OSZ. The internal faults in the duplex express themselves as half meter to meter scale shear zones that juxtapose the various rock types. A penetrative foliation with a steep to moderate NE dip is most pronounced within the duplexes. Although most of the structures are distributed ductile, some of the deformation is cataclasites that has formed in relation to the duplexes.

Massive tonalite gneiss that forms the basement rocks on Vanna (and the footwall of the OSZ) is characterized by a phaneritic texture and leucocratic mineral assemblage (**Fig.** 5a). On the microscale (**Figs.** 5b, c), the typical mode is observed as irregular grains of sericitised plagioclase (30%) and aggregates of finer-grained recrystallized polygonal quartz (40%) and microcline (10%). Fine-grained parallel-oriented biotite (10%), and amphibole (5%) occur in aggregates. Grains of microcline (5%) display tartan-twinning. Epidote, calcite, titanite and tourmaline are present in accessory amounts.

The **tonalite gneiss** in the hanging wall has a similar modal composition to the massive tonalite in the footwall. The weak gneissic foliation is defined by the alignment of planar minerals – typically biotite. **Amphibolite layers** (0.5 to 5 m wide) occur sub-parallel to foliation in the hanging wall. The primary mineralogy and igneous texture is now partly transformed into an amphibole-biotite-feldspar schist (**Fig.** 5d), particularly along their boundaries with surrounding tonalite gneiss. On a microscale (**Figs.** 5e, f), the typical mode observed is 50 % medium-grained (< 5 mm) calcic amphibole, 10 % chlorite, 20 % albite (Ab_{98-100}), 10 % biotite, with minor (3-5 %) amounts of microcline, epidote, and quartz. Accessory minerals include magnetite, ilmenite, rutile and titanite. The composition of amphibole ranges from actinolite to ferrotschermakite (**Fig.** 13d).

Metasomatic alteration of host rocks and hydrothermal vein deposition

The emerald mineralization (**Fig.** 6a) is hosted along the outer rims of a c. 30 m wide hydrothermal dolomite lens enclosed by the internal splay faults in the duplex (**Fig.** 3). The dolomite forms a hill in the landscape, and the weathered surface of dolomite is pale brown (**Fig.** 6b). Numerous smaller dolomite veins are mostly found enclosed in the metasomatically altered rocks (**Fig.** 6c), but dolomite also occurs in form of smaller lenses and veins in other rock types (**Fig.** 4a). The dolomite is coarse grained with equant grains (< 20 mm). In thin section, abundant small fluid inclusions (<10 μm) causes a cloudy appearance in the core of dolomite grains. Some deformation twins also occur in the core of these grains (**Figs.** 6d, e).

The outer rims of the dolomite grains do not contain fluid inclusions and have well developed twins that suggest the dolomite, at least, in part, has recrystallized.

A network of hydrothermal quartz veins, < 1 to 50 cm wide, is associated with and partly crosscut the dolomite lens (**Fig.** 6b), particularly along cleavage planes of dolomite crystals (**Fig.** 6d). This relationship of quartz crosscutting albitite is also observed at a microscopic scale (**Figs.** 7b, c).

The hydrothermal emerald-bearing dolomite is associated with intense metasomatic alteration that has almost completely overprinted the original mineralogy of the host rocks (now albitite and fuchsite schists). Although the contact relationships between the different host rock units, their highly altered equivalents, and hydrothermal veins have been partly to significantly juxtaposed by the (later and/or concurrent) movement along the shear zone (**Fig.** 3), a distinct metasomatic zonation can still be discerned. Such zonation patterns are commonly observed in other emerald deposits around the world (Alexandrov et al., 2001). They are considered a typical feature of infiltration metasomatism and can form sharp metasomatic fronts. Metasomatic alteration in the OSZ has resulted in the formation of two distinct zones outward from the dolomite contact; 1) albitisation that has resulted in an albite ± quartz ± rutile rock (albitite), 2) fuchsite schists that have formed mainly along the mylonitic contact with footwall tonalite gneiss. These two units will be described in further detail below.

Albitisation is visible as a characteristic pale or reddish alteration that mainly affects the rocks within the OSZ (**Fig.** 7a), but also to a much lesser extent amphibolite and tonalite outside of it. On a microscale, this rock is composed of fine-grained (< 2 mm) albite + rutile ± quartz ± white mica ± carbonate ± biotite ± chromite (**Figs.** 7b, c) in varying proportions.

Rutile is found both in clusters of fine grained subhedral rutile, and as equant, isolated, and small (<2 μm grains) grains. Layers of small (< 5μm), cubic chromite grains associated with fine grained rutile are observed partly enclosed in dolomite grains (**Fig.** 7d) or albite (**Fig.** 7e). A thin chlorite layer is observed along the contact with dolomite (**Fig.** 7f). Although the proportions of albite feldspar vary, the term albitite will be used in the following when referring to these highly altered albite rich rocks.

Fuchsite schists occurs mainly along the contact with tonalite basement rocks as a < 2 m wide, bright green, and strongly foliated to mylonitic unit (**Fig.** 8a). Smaller lenses of fuchsite schist also occur within the internal shear zones and thrust faults of the duplex (**Figs.** 4d, e). On a microscale, the original host rock mineralogy is observed as completely replaced by albite and fuchsite, with accessory amounts of microcline, rutile and carbonates (**Figs.** 8b, c). Fuchsite, which is the green Cr-rich variety of muscovite, forms spaced, undulatory bands, forming a schistosity that separates layers of albite. Rutile commonly occur as fine-grained aggregates within fuchsite layers. Albite has a cloudy appearance and flame-shaped deformation twins, which is characteristic of metasomatic albite (Passchier and Trouw, 2005). The cloudy appearance is caused by fluid inclusions and mineral inclusions of white mica, carbonate, rutile, and Fe-oxide.

Hydrothermal tourmaline+quartz ±albite veins cross cut the strongly albitised rocks. These veins occur as foliation parallel veins and as matrix infill in cataclasites (**Fig.** 9a). In

outcrop, tourmaline occurs as aplitic black felted masses (**Fig.** 9b). On a microscale, tourmaline is discerned as very fine grained (< 20 μm), and colour zoned. SEM map scan analyses reveal that this zonation is caused by variations in Mg and Cr (**Fig.** 9c). Narrow (< 2 cm) tourmaline bearing quartz veins enveloped by an intense epidote salvage are also observed to cut the amphibolite.

Mineral geochemistry

Beryl composition and mineral structure

Beryl is identified based on XRD and Raman analyses. A typical XRD pattern obtained from the beryl is shown in **Fig.** 10a. In the Raman spectra from analysed beryl (**Fig.** 11a) the main bands at 398 (ring), 667 (ring), and 1069 (Be-O bond), 1010 and 1123 cm^{-1} (shoulders) are in accordance with the Raman data published for beryl (e.g., Moroz et al., 2000).

The green colour of emerald is caused by the substitution of Al in beryl with low amounts of Cr and or V). Substitution of Al by Fe^{2+} and Fe^{3+} in different coordination can also cause colours range from yellow, green and blue (Schwarz and Schmetzer, 2002). The beryl from Vanna shows the Cr_2O_3 content around 0.5 wt. %, the FeO content around 0.3 wt. % and V_2O_3 below 0.2 wt. % (Table 1; **Fig.** 12). The emerald composition compared to emerald from other localities (e.g., Groat et al., 2008, Loughrey et al., 2013) reveals that the Vanna emeralds are enriched in Cr_2O_3 and depleted in FeO and V_2O_3 when compared to other localities in Norway (Byrud Mine; Loughrey et al., 2013). But shows geochemical trends to those from Madagascar, Pakistan, and Zimbabwe (**Fig.** 12); emerald from all three localities formed by pegmatitic fluid interactions with mafic host rocks (Groat et al., 2008)

Compositions and mineral structures of other minerals

XRD patterns (**Fig.** 10), Raman spectroscopy spectra (**Fig.** 11) and SEM mineral chemistry (**Fig.** 13; Table 1) from various hydrothermal, metasomatically altered and host rock minerals are described below.

The XRD pattern from analysed **fuchsite** in the fuchsite schist is shown in **Fig.** 10b. In **Fig.** 11d, the 420 and 700 cm^{-1} peaks in the Raman spectra is typical for Al-rich dioctahedral K-micas like muscovite (Wang et al., 2015). SEM analysis confirms the high Cr content in fuchsite (Table 1). In addition, the Cr (a.p.f.u.) content shows a general negative correlation with Al (**Fig.** 13a), and further suggests that Cr substitutes for Al in the crystal formula and is responsible for the bright green colour of fuchsite.

Two groups of **tourmaline** are identified from the OSZ based on their geochemistry (Table 1; **Fig.** 13b). Tourmaline in veins hosted by amphibolites are schorl with lower Mg/(Mg+Fe) ratios and lower Cr (a.p.f.u.) values compared to dravite from veins hosted by albitite. Colour zonation is also observed in dravite, and is caused by variations in Cr, Fe, and Mg content (**Fig.** 9c). XRD patterns and diffraction lines for dravite are shown in **Fig.** 10c. Raman spectra for tourmaline are characteristic cyclosilicate spectra, and the broad patterns and peak at 769 cm^{-1} confirm that the tourmaline is dravite (**Fig.** 11f; Hoang et al., 2011). The relatively large variation between spectra (e.g. prominence of the 719 cm^{-1} peak) is caused by the angle of the beam to the c axis of the mineral.

SEM analyses of **chlorite** also show two groups of chlorite (**Fig.** 13c). Chlorites hosted by host rock amphibolite, probably a retrograde metamorphic chlorite, have lower Mg/(Mg+Fe) ratios and lower Cr (a.p.f.u.) values than those formed at the margins of dolomite (**Fig.** 7f). Raman spectra of Mg-rich chlorites (**Fig.** 11e) show three major Raman peaks at 683, 552, 203 cm^{-1}, indicating that the chlorite is Mg-rich trioctahedral chlorite (Wang et al., 2015).

The XRD pattern of **dolomite** is shown in **Fig.** 10a. Raman spectra for dolomite show a dominant peak at 1098 cm^{-1} (**Fig.** 11b) which is a characteristic peak for MgCa carbonate (Herman et al., 1987). SEM analysis show minor amounts of Fe present in addition of Mg and Ca (Table 1).

SEM analyses of **biotite** show that biotite from host rock amphibolite (**Fig.** 5d-f) show lower Mg/ (Mg+Fe) ratios and lower Cr (a.p.f.u.) than rare phlogopite found at the contact zone with dolomite vein within metasomatically altered albitites and fuchsite schists (**Fig.** 13d).

Amphibole from host rock amphibolite layers (**Figs.** 5d-f) have very low Cr values (Table 1). Their composition varies from ferro-tchermakite to actinolite (**Fig.** 13e).

The XRD pattern of **albite** is show in **Figs.** 10b and c. Raman spectra from analysed **albite** show typical feldspar triplet peaks between 450 and 520 cm^{-1}. The peak at 507 cm^{-1} is characteristic for low albite (Freeman et al., 2008; **Fig.** 11c). SEM analyses for albite (Table 1) show that the albite component is $Ab_{0.99}$.

Fluid inclusion data

Fluid inclusion petrography

Emerald (**Fig.** 14a) hosts at least two generations of inclusions; primary and secondary. Primary inclusions are the most abundant in emerald and can be divided into three subgroups based on their shape and phase relationships at the room temperature: (1) E1 inclusions (**Fig.** 14b) are sub-rounded $L+V+S_1 \pm S_2$ inclusions with 10-20 vol. % vapour, a cubic solid phase (10-15 vol. %), and commonly a second very small (< 2 μm) birefringent solid phase; (2) E1b inclusions (**Fig.** 14c) are L+V+S and have a very elongate shape (100-300 μm long by 3-5 μm wide). These very elongate plane-related inclusions show a necked-down appearance, and/or are modified by trails of secondary inclusions that cross-cut them. These E1b inclusions are therefore not measured. (3) E2 type inclusions (**Fig.** 14d) are L_1+L_2+V inclusions with 80 vol. % liquid H_2O, 20 vol. % vapour CO_2 and traces of liquid CO_2. Raman Spectroscopy (**Fig.** 11) confirms the presence of CO_2 in these inclusions. Secondary inclusions (E3) are grouped into discrete linear trails and are small (<20 nm) L+V or L+V+S inclusions, with a gas phase of 20-30 vol. %, and with negative crystal shapes.

Two types of primary inclusions are hosted by quartz: Q1 (**Fig.** 14e) and Q2 (**Fig.** 14f) with similar petrographic characteristics to E1 and E2 inclusions in emerald. Q1 inclusions are $L+V+S_1 \pm S_2$, 50-100 μm in size, and with shapes that vary from irregular to sub-irregular. The inclusions contain a cubic solid that occupies up to 20 vol. %, and commonly one very small birefringent solid phase (<2μm). The vapour phase is 20-30 vol. %. Q2 inclusions are L+ V inclusions that contain liquid CO_2. Q1 and Q2 inclusions do not occur within the same fluid inclusion assemblages.

Fluid inclusions are numerous in dolomite, and both V-only, L+V, and L+V+S inclusions were observed. These fluid inclusions are very small (< 10μm) and accurate microthermometric measurements were difficult to obtain. In addition, measurements were further precluded by decrepitation in those inclusions that were large enough to measure.

Fluid inclusion microthermometry

During the cryometric runs, freezing was observed as shrinking of the vapour bubble. First melting (T_e) for all inclusions was recorded around -25 to -21°C, indicating a NaCl-KCl-H_2O system. Microthermometric data is summarised in Table 2, and **Fig.** 15.

For **E1** inclusions T_h V-L occurred at temperatures around 270-300°C. Total homogenisation by melting of the cubic solid (S_1) was around 270-350°C (E1), indicating that the cubic solid was NaCl and salinities are between 36-43 wt. % NaCl equiv. The very small solid (S_2) was insoluble during heating (< 350°C). At room temperature**, E2** inclusion contain a characteristic double bubble indicating the presence of CO_2. Raman microscopy spectra show weak bands at 1283 and 1387 cm^{-1} that confirms CO_2 in emerald-hosted fluid inclusions (Frezzotti 2012). No E2 inclusions were measured because of decrepitation at temperatures below T_h. Most secondary **E3** inclusions showed $T_{m\ ice}$ between -13 and -20°C, indicating salinities of 17 to 22 wt. % NaCl equiv. One E3 inclusion also contained a solid that melted at 260°C, giving a salinity of 36 wt. % NaCl equiv. T_h V-L occurred at temperatures of 190-280°C.

For **Q1** inclusions, T_h V-L occurred at 130-170°C. Total homogenisation by melting of the cubic solid (S_1) occurred around 200-250°C, indicating salinities of 33-36 wt. % NaCl equiv. The very small solid phase (S_2) was insoluble during heating (< 350°C). At room temperature, **Q2** inclusions also contain a characteristic double bubble indicating the presence of CO_2. Clathrate melting was observed around -0.3 to +2.2°C, indicating salinities of 13-16 wt. % NaCl equiv. Homogenisation of V_{CO2} to L_{CO2} was consistent around 31-35°C. Total homogenisation occurred by vapour to liquid ranging from < 223 to 270°C. However, 70% of measured Q2 inclusions decrepitated during the heating cycle before homogenisation temperatures could be obtained. Minimum homogenisation temperatures (< 223°C) for these inclusions are based on the 30% inclusions within the assemblage that could be measured successfully, and the temperatures where the fluid inclusions involuntarily decrepitated.

L+V+S inclusions in dolomite, decrepitated around 210-300°C with both vapour bubble and partly dissolved cubic solid still present in the inclusions, indicating salinities above c. 30-39 wt. % NaCl. No V-only inclusions were measured.

Pressure temperature conditions

Minimum trapping conditions of fluid inclusions that homogenise by halite dissolution can be calculated directly according to Lecumberri-Sanchez et al., (2012). Minimum emerald formation conditions from primary inclusions (E1) are c. 320°C and 0.7 kbar. CO_2 densities calculated from Raman spectra collected from E2 fluid inclusions in emerald are 0.14 g/cm^3 (Fall et al., 2011). Primary inclusion (Q1) assemblages in quartz show median temperatures of 220°C and pressures range between 1.2 and 1.9 kbar (see table 2).

The partitioning of the albite component between coexisting microcline and plagioclase solid-solutions can be applied as a pressure dependant geothermometer according to Stormer and Whitney (1977). This geothermometer was applied on using EDS compositions (Table 1) of the albite-microcline feldspars from fuchsite schist and yielded temperatures of 240°C at 1 kbar and 250°C at 3 kbar.

Fluid composition

Qualitative chemical analyses of major elements (Na, Cl, and K) in the fluid inclusions hosted by quartz were carried out by decrepitation of fluid inclusions and measuring the composition of evaporate mounds that formed on the surface. For comparison, both average compositions from map-scan analyses that covered the entire evaporate mound and spot analysis of individual crystals was done. Plots of Na vs K (**Fig.** 16) show a positive correlation of Na/K ratio that range from 10:1 to 1:1, where the majority of the inclusions have high Na/K values. The compositional ratios were consistent in the average map scan analyses and in spot analyses.

$\delta^{13}C$ and $\delta^{18}O$ stable isotopes

Stable isotopes of hydrothermal dolomite are analysed and compared to carbonates from other localities on Vanna (**Fig.** 17; Johannessen, 2012; Paulsen et al., in press). The hydrothermal dolomite stable isotopes from the OSZ all yielded $\delta^{13}C$ values of -4 to -2 ‰, which is slightly above, and $\delta^{18}O$ values (+7 to +9 ‰) within the same range as the values of primary igneous carbonates (Taylor et al., 1967). In comparison, hydrothermal calcite from the Palaeozoic Vannareid-Burøysund fault returned values $\delta^{13}C$ values in the range of -5.7 to -4.0 ‰, and $\delta^{18}O$ values from +7.1 to +12.3 ‰, also overlapping with the field of primary igneous carbonates. In contrast, calcite from hanging wall Skipsfjord Nappe, samples from veins and breccia in diorite of the Vanna Group meta-sedimentary rocks and values for calcite cement in meta-sandstones of the Vanna Group (**Fig.** 2: Johannessen, 2012) differ from all the other analysed samples and suggest a different origin.

Discussion

Emerald formation conditions (P-T estimates)

Beryl can form under a wide range of pressures and temperatures (Barton, 1986). At Vanna, primary fluid inclusions in emerald (E1) suggest that minimum formation conditions for emerald are 320-350°C and c. 0.7 kbar. Isochoric projections from fluid inclusion microthermometric measurements are plotted in a pressure-temperature diagram (**Fig.** 18). Similar formation conditions are also reported for Brazilian emeralds (1.0-1.1 kbar and 290-360°C; Cheilletz et al., 1994), and emerald from Byrud in Norway (< 1 kbar and 160-385°C), while Colombian emeralds (1.5 kbar and 300°C; Giuliani et al., 1994), and emerald from Madagascar (1.5 kbar and 250-450°C; Vapnik et al., 2006) have formed under higher pressures. The estimated P-T conditions for emerald at Vanna overlap with conditions of upper greenschist facies (350-500°C) as estimated by the mineral assemblage amphibole-chlorite-albite-calcite±epidote found in the host rock amphibolites.

Minimum estimates of temperature and salinity from fluid inclusions in dolomite are > 230°C and > 32 wt. % NaCl equiv. (Table 1). Although the salinity and homogenisation

temperatures for dolomite are poorly constrained because of decrepitation before total homogenisation could be measured, the minimum estimates overlap with E1 inclusions in emerald. Further this supports the textural relationship observed in outcrop (**Fig.** 6a) that dolomite and emerald deposited together, or as a part of the same hydrothermal event.

Hydrothermal quartz veins cross-cut dolomite (**Fig.** 6b). Q1 and Q2 inclusions are primary inclusions and both inclusion types have total homogenised over the same temperature range (220-270°C). However, these inclusion types have different salinities; Q1 homogenised by halite dissolution and represent a highly saline fluid (32-36 wt. % NaCl equiv.) while Q2 inclusions homogenised by vapour to liquid and yield lower salinities (13-16 wt. % NaCl equiv.; **Fig.** 15). This trend of similar homogenisation temperatures and different salinities is commonly attributed to a boiling fluid. However, petrographic observations show that Q1 and Q2 inclusions are not present in the same fluid inclusion assemblage and are therefore interpreted to represent two different fluids, or fluid end-members, with significantly different salinities. Secondary E3 inclusions in emerald show similar microthermometric properties as primary inclusions in quartz (**Fig.** 15), which supports that emerald (and dolomite) deposited prior to quartz.

Stable isotope data and potential fluid source

$\delta^{18}O$ and $\delta^{13}C$ data obtained from OSZ dolomites plot close to those of primary igneous carbonates (**Fig.** 17), and the narrow compositional range of $\delta^{13}C$ strongly supports a magmatic origin of CO_2. Stable isotope ratios can be affected post deposition by diagenetic, hydrothermal or metamorphic fluids, and oxygen isotopes are much more easily affected by exchangeable oxygen from these processes than carbon isotopes (Taylor et al, 1967, Fairchild et al., 1990). With the exception of organic diagenesis, carbon isotopes are effectively buffered by the dissolving carbonate precursor. However, the narrow $\delta^{18}O$ compositional range suggests that post-depositional weathering has not affected the isotopic ratio of O.

$\delta^{18}O$ and $\delta^{13}C$ isotopic ratios from elsewhere on Vanna are more variable. Calcite from veins in the Skipsfjord nappe, and Vanna Group sedimentary rocks, display much higher values of $\delta^{13}C$ and $\delta^{18}O$, larger compositional variations, and more variable trends than calcite in the Vannareid-Burøysund hydrothermal calcite and OSZ. This suggests a different origin, and/or possibly more diverse enrichment history of these carbonates on Vanna.

Hydrothermal fluid evolution

The stable isotopic signature of the CO_2 that formed the dolomite is dominantly magmatic, and fluid inclusion microthermometry and analysis of fluid inclusion evaporate mounds show a fluid composed of $NaCl+KCl+H_2O\pm CO_2$. The highly saline fluids from E1 fluid inclusions that homogenise by halite dissolutions and the association with tourmaline mineralization also suggest a genetic link with granitoid-associated veins (Wilkinson 2001; Thomas et al., 2003; Lecumberri-Sanchez 2012) or pegmatite related emerald occurrences (Giuliani et al., 1994; Vapnik and Moroz, 2002; Bodnar 2008). Zwaan (2006) suggested that fluids could migrate a considerable distance from a source, especially through strongly sheared rock. At Vanna, this strongly sheared rock is represented by the OSZ. This mechanism for emerald mineralization

is also suggested for Zimbabwean emerald (Zwaan 2006) and Habachtal emeralds in Austria (Grundmann and Morteani, 1989; **Fig.** 12).

Fluids generated from magma degassing commonly evolve from a volatile (CO_2 rich) fluid, that is produced in the early stages as the magma degasses, to a saline (> 50 wt. % NaCl equiv.) water rich fluid that can contain constituents like Cl-, Na+, and K+ (Sharma and Srivastava, 2014). These magmatic fluids can also contain significant beryllium (Thomas et al., 2011) and boron (Audétat, 1998). Thomas et al., (2011) studied the beryllium concentrations in fluid and melt inclusion in granite-pegmatite systems and suggested a strong enrichment of beryllium in the fluid and volatile-rich phase relative to melt. This provides a process by which ore-grade concentrations of beryl in magmatic fluids can be obtained. In contrast, Alexandrov et al., (2001) suggest that such a distant concentrated source of beryllium is not necessary as the amount of beryllium needed to form major amounts of beryl can be sourced locally within even a small radius. This could provide an alternative source for beryllium, and it is possible that Be was sourced from and remobilised by fluid circulation within and proximal to the OSZ.

Our geochemical analyses show that the green colour of emeralds found at Vanna is caused by Cr substitution of Al in its crystal lattice. Notably, Cr is also found in fuchsite, tourmaline, chlorite and biotite hosted by albitite rocks. In comparison, the same minerals found within relatively unaltered amphibolite layers contained only trace or below detection amounts of Cr. This, combined with chromite grains in the albitite (**Fig.** 8), suggests that the Cr for emerald formation is sourced locally and likely from the original albitite protolith. Although Cr is a compatible element with a low solubility in fluids, Cr mobility increases with increasing salinity and can therefore be mobile in a highly saline fluid such as the fluids at OSZ (Klein-BenDavid et al., 2011; Watenpuhl et al., 2014).

Possible albitite protolith

The percolation of highly saline fluids out of equilibrium with the host rocks caused extensive Na-metasomatic alteration resulting in the formation of the albitite within the OSZ. A likely protolith analogue to these strongly altered albitite rocks is the Vanna group meta-sedimentary sequence. These meta-sedimentary rocks are found along and bounded by the OSZ farther SW along the coast of Vanna. The OSZ is interpreted to be a reactivated Palaeoproterozoic normal fault that controlled the basin formation in which the Vanna group sediments deposited. Hence, it is likely that a small pocket of meta-sedimentary rocks also was deposited at Olkeeidet. Alternatively, a lens of meta-sedimentary rocks from further south along the OSZ could be reworked by the dextral movement along this shear zone into its current position. Local variations in grain size and composition of albitite may also be attributed to existing protolith variations. Johannessen (2012) described primary bedding sequences that range from quartzite, arenite and pelite within the Vanna group meta-sedimentary sequence. Similar meter-scale metasomatic alteration pockets composed of albite-quartz-rutile are found within a diorite sill from Fakken on southern Vanna (**Fig.** 3). Knudsen (2007) interpreted these as meta-sedimentary xenoliths.

Bergh et al., (2007) inferred that the provenance area for the Vanna group meta-sedimentary rocks is the nearby Archaean and Palaeoproterozoic basement rocks from the islands of

Vanna, Ringvassøya and Kvaløya (for location see **Fig.** 2). This provenance area also includes plagioclase phyric and gabbronorite dikes that has intruded the basement prior to the deposition of the Vanna group meta-sedimentary strata (Kullerud et al., 2006). In particular, the gabbronorite dikes contain < 3000 ppm chromium and could be a source of chromium that is found in the albitised meta-sedimentary rocks at Olkeeidet in the form of chromite (**Fig.** 7d, e). This suggests that in addition to beryllium potentially being sourced from the local host rocks, a potential local meta-sedimentary source of chromium is also likely.

Fault rocks, fluid interactions and metasomatic exchange of components

Faults and shear zones are well known fluid conduits, promoting permeability by various deformation processes (e.g. Sibson, 1994). Deformation along the OSZ could therefore have further contributed to enhanced fluid flow and also the formation of fuchsite schist. Fluid interactions in fault zones that run through feldspar-rich host rocks like tonalite gneiss, amphibolite or meta-sedimentary rocks commonly promote formation of phyllosilicates from the breakdown of feldspar (Wintsch et al., 1995; Wibberley, 1999) according to the reactions:

$3NaAlSi_3O_8 + K^+ + 2H^+ \rightarrow KAl_3Si_3O_{10}(OH)_2 + 6SiO_2 + 3Na^+$ (Albite → Muscovite + silica)

$3KAlSi_3O_8 + 2H^+ \rightarrow KAl_3Si_3O_{10}(OH)_2 + 6SiO_2 + 2K^+$ (K-feldspar → Muscovite + silica)

The chemical composition of an exotic fluid that intrudes the fault zone may also affect the composition of the minerals formed (Wintsch et al., 1995). This interaction between shear zone movement, host rock compositions, and highly saline Na>K rich fluids, that also likely carried/remobilised a significant amount of chromium (Klein-BenDavid et al., 2011; Watenpuhl et al., 2014), is likely responsible for the fuchsite schist formed at the mylonitic margin of the shear zone (**Fig.** 8a).

Further, the porosity of meta-sedimentary rocks is likely higher than the tonalite gneisses and could further channel the fluids within the shear zone system (**Fig.** 7d). Their red staining is also an indication of fluid infiltration. Sub-solidus replacement of feldspar is discussed by Putnis et al., 2007, where plagioclase reacts with fluids and forms K-feldspar pseudomorphs that co-precipitates with hematite, which further causes the red colouration. Drake et al. (2008) has shown that the red-staining process where plagioclase is replaced by albite, K-feldspar and sericite increase porosity, a process that would further increase fluid flow thought the OSZ as a positive feed-back mechanism for metasomatic alteration. The iron that is responsible for the red staining could be sourced from the metasomatic alteration of mafic minerals like amphibole and biotite in the amphibolite, and to a lesser extent the mafic minerals in the meta-sedimentary rocks.

Based on the field relationships, microstructures, mineral chemistry and isotopes we interpret that a highly saline fluid with a significant magmatic portion migrated through the OSZ. The composition of the rocks (meta-sedimentary), combined with the deformation, facilitated fluid infiltration and enhanced flow, thereby causing pervasive alteration of the fault zone rocks. The hydrothermal fluid transformed the meta-sedimentary rocks into albitites and fuchsite schists, provided CO_2 for the formation of dolomite, and also potentially remobilised chromium and beryllium for the formation of hydrothermal emeralds on Vanna.

Conclusions

1) At Vanna we suggests that emerald is epigenetic and has formed as a result of hydrothermal growth associated with tectonic activity. This locality evidences that emerald can be deposited from hydrothermal fluids of a magmatic origin, in contrast to the classic emerald formation models where emerald is deposited from a granitic melt intruding an ultramafic host rock.

2) Emerald formed from a highly saline fluid (30-43 wt. % NaCl equiv.) at minimum temperatures of 320-350ºC and 0.7 kbar pressure. The stable isotopic signature of dolomite suggest that fluids are at least partly magmatic in origin. As fluid can migrate considerable distances within a shear zone environment, a deeper crustal level magmatic degassing is speculated as a possible source of highly saline fluids and CO_2. This fluid used the OSZ as a fluid conduit. Extensive metasomatic alteration of the surrounding meta-sedimentary host rocks is associated with emerald mineralization. Deformation in the shear zone likely enhanced fluid flow, and the porosity of the meta-sedimentary sequence allowing for fluid circulation was likely furthered by albitisation creating a positive-feedback loop for increasing metasomatic alteration.

3) The green colour of emerald is caused by Cr (and Fe) substitution of Al. A local meta-sedimentary sequence was likely the source of Cr that was partly remobilised by the highly saline fluid. Beryllium could be sourced either from the partly magmatic component of the fluid, or it could be sourced from the fluids that circulate in the meta-sedimentary sequence.

References

Alexandrov, P., Giuliani, G. & Zimmermann, J.-L. 2001: Mineralogy, age, and fluid geochemistry of the Rila emerald deposit, Bulgaria. *Economic Geology* 96, 1469-1476.

Armitage, P.E.B. & Bergh, S.G. 2005: Structural development of the Mjelde-Skorelvvatn Zone on Kvaløya, Troms: a metasupracrustal shear belt in the Precambrian West Troms Basement Complex, North Norway. *Norwegian Journal of Geology* 85, 117-133.

Audétat, A., Detlef, G. & Heinrich, C.A. 1998: Formation of a magmatic-hydrothermal ore deposit: Insights with LA-ICP-MS analysis of fluid inclusions. *Science* 279, 2091-2094.

Aurisiccho, C., Conte, A.M., Medeghini, L., Ottolini, L. & De Vito, C. 2018: Major and trace element geochemistry of emerald from several deposits: Implications for genetic models and classification schemes. *Ore Geology Reviews* 94, 351-366.

Banks, D.A., Giuliani, G. & Yardley, B.W.D. 2000: Emerald mineralisation in Colombia: fluid chemistry and the role of brine mixing. *Mineralium Deposita* 35, 699-713.

Barton, M.D. 1986: Phase equilibria and thermodynamic properties of minerals in the system BeO-Al_2O_3-H_2O, with petrologic applications. *American Mineralogist* 71, 277-300.

Barton, M.D., Ilchik, R.P. & Marikos, M.A. 1991: Metasomatism, In: Kerrick, D.M. (Ed.), *Contact metamorphism*. Mineralogical society of America, pp. 321-351.

Barton, M.D. & Young, S. 2002: Non-pegmatitic deposits of beryllium: mineralogy, geology, phase equilibria and origin. *Reviews in Mineralogy and Geochemistry* 50, 591-691.

Bergh, S.G., Kullerud, K., Armitage, P.E.B., Zwaan, K.B., Corfu, F., Ravna, E.J.K. & Myhre, P.I. 2010: Neoarchean to Svecofennian tectono-magmatic evolution of the West Troms Basement Complex, North Norway. *Norwegian Journal of Geology* 90, 21-48.

Bergh, S.G., Kullerud, K., Corfu, F., Armitage, P.E.B., Davidsen, B., Johansen, H.W., Pettersen, T. & Knudsen, S. 2007: Low-grade sedimentary rocks on Vanna, North Norway: a new occurrence of a Palaeoproterozoic (2.4-2.2 Ga) cover succession in northern Fennoscandia. *Norwegian Journal of Geology* 87, 301-318.

Binns, R.E., Chroston, P.N. & Matthews, D.W. 1980: Low-grade sediments on Precambrian gneiss on Vanna, Troms, Northern Norway. *Offprint NGU* 359, 61-72.

Cheilletz, A., Féraud, G., Giuliani, G. & Rodriguez, C.T. 1994: Time-pressure and temperature constraints on the formation of Colombian emeralds: an Ar40/Ar39 laser microprobe and fluid inclusion study. *Economic Geology* 89, 361-380.

Cheilletz, A. & Giuliani, G. 1996: The genesis of Colombian emeralds: a restatement. *Mineralium Deposita* 31, 359-364.

Corfu, F., Armitage, P.E.B., Kullerud, K. & Bergh, S.G. 2003: Preliminary U-Pb geochronology in the West Troms Basement Complex, north Norway: Archean and Palaeoproterozoic events and younger overprints. *NGU Bulletin* 441, 61-72.

Dallmeyer, R.D. 1992: $^{40}Ar/^{39}Ar$ mineral ages within the Western Gneiss Terrane, Troms: evidence of polyphase Proterozoic tectonothermal activity (Svecokarelian and Sveconorwegian). *Precambrian Research* 57, 195-206.

Davids, C., Wemmer, K., Zwingmann, H., Kohlmann, F., Jacobs, J. & Bergh, S.G. 2013: K-Ar illite and apatite fission track constraints on brittle faulting and the evolution of the northern Norwegian passive margin. *Tectonophysics* 608, 196-211.

Deer, W.A., Howie, R.A. & Zussman, J. 1972: An introduction to the rock-forming minerals. Longman Group Limited, London.

Drake, H., Heim, C., Hogmalm, K.J. & Hansen, B.T. 2014: Fracture zone-scale variation of trace elements and stable isotopes in calcite in a crystalline rock setting. *Applied Geochemistry* 40, 11-24.

Fairchild, I.J., Marshall, J.D. & Bertrand-Sarfati, J. 1990: Stratigraphic shifts in carbon isotopes from Proterozoic stromatolitic carbonates (Mauritania): influence of primary mineralogy and diagenesis. *American Journal of Science* 290, 46-79.

Fall, A., Tattitch, B. & Bodnar, R.J. 2011: Combined microthermometric and Raman spectroscopic technique to determine the salinity of H_2O-CO_2-NaCl fluid inclusions based on clathrate melting. *Geochimica et Cosmochimica acta* 75, 951-964.

Freeman, J.J., Wang, A., E., K.K., Jolliff, B.L. & Haskin, L.A. 2008: Characterization of natural feldspars by Raman spectroscopy for future planetary exploration. *The Canadian Mineralogist* 46, 1795-1818.

Frezzotti, M.L., Tecce, F. & Casagli, A. 2012: Raman spectroscopy for fluid inclusion analysis. *Journal of Geochemical Exploration* 112, 1-20.

Giuliani, G., Cheilletz, A., Dubessy, J. & Rodriguez, C.T. 1994: Chemical composition of fluid inclusions in Colombian emerald deposits. *Eight Quadrennial IAGOD symposium*.

Groat, L.A., Giuliani, G., Marshall, D.D. & Turner, D. 2008: Emerald deposits and occurrences: a review. *Ore Geology Reviews* 34, 26.

Grogan, P., & Zwaan, K. B. (1997). Geologisk kart over Norge, berggrunnskart Helgøy

Grundmann, G. & Morteani, G. 1989: Emerald mineralization during regional metamorphism: the Habachtal (Austria) and Leydsdorp (Transvaal, South Africa) deposits. *Economic Geology* 84, 1835-1849.

Henry, D.J., Novák, M., Hawthorne, F.C., Ertl, A., Dutrow, B.L., Uher, P. & Pezzotta, F. 2011: Nomenclature of the tourmaline-supergroup minerals. *American mineralogist* 96, 895-913.

Herman, R.G., Bodgan, C.E., Sommer, A.J. & Simpson, D.R. 1987: Discrimination among carbonate minerals by Raman Spectroscopy using the laser microprobe. *Applied Spectroscopy* 41, 437-440.

Hoang, L.H., Hien, N.T.M., Chen, X.B., Minh, N.V. & Yang, I.-S. 2011: Raman spectroscopic study of various types of tourmalines. *Journal of Raman Spectroscopy* 42, 1442-1446.

Indrevær, K., Stunitz, H. & Bergh, S.G. 2014: On Palaeozoic-Mesozoic brittle normal faults along the SW Barents Sea margin: fault processes and implications for basement permeability and margin evolution. *Journal of the Geological Society of London* 171, 831-846.

Johannessen, H. 2012: Tinnvatnformasjonen i Vannas proterozoiske lagrekke: Sedimentære facies og avsetningsmiljø. MSc thesis, Department of Geology. University of Tromsø, Tromsø, p. 105.

Johansen, H. 1987: Forholdet mellom det prekambriske underlaget og overliggende sedimentære bergarter sør-øst på Vanna, Troms. Cand. scient thesis, Institutt for biologi og geologi. Universitetet i Tromsø, Tromsø, p. 136.

Kim, S.-T., Mucci, A. & Taylor, B.E. 2007: Phosphoric acid fractionation factors for calcite and aragonite between 25 and 75 °C: Revisited. *Chemical Geology* 246, 135-146.

Klein-BenDavid, O., Pettke, T. & Kessel, R. 2011: Chromium mobility in hydrous fluids at upper mantle conditions. *Lithos* 125, 122-130.

Knudsen, S. 2007: Strukturgeologi og petrologi i palaeoproterozoiske metasedimentære og intrusive bergarter på Vanna, Troms. MSc thesis, Department of Geology. University of Tromsø, Tromsø, p. 113.

Koehl, J.-B., Bergh, S.G., Osmundsen, P.T., Redfield, T.F., Indrevær, K., Lea, H. & Bergø, E. 2018: Late Devonian-Carboniferous faulting in NW Finnmark and controlling fabrics, *manuscript*, p. 67.

Kontak, D.J. 2004: Analysis of evaporate mounds as a complement to fluid-inclusion thermometric data: case studies from granitic environments in Nova Scotia and Peru. *The Canadian Mineralogis*t 42, 1315-1330.

Kullerud, K., Skjerlie, K.P., Corfu, F. & de la Rosa, J.D. 2006: The 2.40 Ga Ringvassøy mafic dykes, West Troms Basement Complex, Norway: The concluding act of early Palaeoproterozoic continental breakup. *Precambrian Research 150,* 183-200.

Lafuente, B., Downs, R.T., Yang, H. & Stone, N. 2015: The power of databases: the RRUFF project, In: Armbruster, T., Danisi, R.M. (Eds.), *Highlights in Mineralogical Crystallography*. W. De Gruyter, Berlin, Germany, pp. 1-30.

Laurs, B.M., Dilles, J.H. & Snee, L.W. 1996: Emerald mineralization and metasomatism of amphibolite, Khaltaro granitic pegmatite-hydrothermal vein system, Haramosh Mountains, northern Pakistan. *The Canadian Mineralogist* 34, 34.

Leake, B.E., Woolley, A.R., Birch, W.D., Burke, E.A.J., Ferraris, G., Grice, J.D., Hawthorne, F.C., Kisch, H.J., Krivovichev, V.G., Schumacher, J.C., Stephenson, N.C.N. & Whittaker, E.J.W. 2003: Nomenclature of amphiboles: additions and revisions to the international mineralogical association's 1997 recommendations. *The Canadian Mineralogist* 41, 1355-1362.

Lecumberri-Sanchez, P., Steele-MacInnis, M. & Bodnar, R.J. 2012: A numerical model to estimate trapping conditions of fluid inclusions that homogenize by halite disappearance. *Geochimica et Cosmochimica acta* 92, 14-22.

Loughrey, L., Marshall, D., P., I. & Jones, P. 2013: Boiling as a mechanism for colour zonations observed at the Byrud emerald deposit, Eidsvoll, Norway: fluid inclusion, stable isotope and Ar-Ar studies. *Geofluids* 13, 18.

Moroz, I., Roth, M., Boudeulle, M. & Panczer, G. 2000: Raman microspectroscopy and fluorescence of emeralds from various deposits. *Journal of Raman Spectroscopy* 31, 485-490.

Myhre, P.I., Corfu, F. & Bergh, S.G. 2011: Palaeoproterozoic (2.0-1.95 Ga) pre-orogenic supracrustal sequences in the West Troms Basement Complex, North Norway. *Precambrian Research* 186, 89-100.

Myhre, P.I., Corfu, F., Bergh, S.G. & Kullerud, K. 2013: U-Pb geochronology along an Archean geotransect in the West Troms Basement Complex, North Norway. Norwegian *Journal of Geology* 93, 1-24.

Opheim, J.A. & Andresen, A. 1989: Basement-cover relationships on northern Vanna, Troms, Norway. *Norsk Geologisk Tidsskrift* 69, 67-81.

Passchier, C.W. & Trouw, R.A.J. 2005: Microtectonics, 2. ed. Springer, Berlin Heidelberg.

Paulsen, H.-K., Bergh, S.G. & Palinkaś, S.S. in press: Late Palaeozoic fault controlled hydrothermal Cu-Zn mineralization on Vanna Island, West Troms Basement Complex, northern Norway. *Submitted to Norwegian Journal of geology*.

Paulsen, H.-K., Bergh, S.G., Palinkaś, S.S., Armitage, P.E.B., Karlsen, S.E., Kolsum, S., Rønningen, I.U. & Nazuti, A. 2019: Late-Svecofennian fold-thrust belt and oblique-slip structures on Vanna island, West Troms Basement Complex, and their relation to meta-

sedimentary sequences, *Geological Society of Norway Annual Meeting abstracts*. Geological Society of Norway, Bergen, Norway, p. 75.

Putnis, A., Hinrichs, R., Putnis, C.V., Golla-Schindler, U. & Collins, L.G. 2007: Hematite in porous red-clouded feldspars: Evidence of large-scale crustal fluid–rock interaction. *Lithos* 95, 10-18.

Roedder, E. 1984: Fluid inclusions. U S geological Survey, Blacksburg, Virginia, p. 644.

Rosenbaum, J. & Sheppard, S.M.F. 1986: An isotopic study of siderites, dolomites and ankerites at high temperatures. *Geochimica et Cosmochimica acta* 50, 1147-1150.

Rudnik, R.I. & Gao, S. 2003: The composition of the continental crust, In: Rudnik, R.I. (Ed.), *Treatise on Geochemistry*, pp. 1-64.

Schwarz, D. & Schmetzer, K. 2002: The definition of emerald. *ExtraLapis English* 2, 74-78.

Sen, J.A. 2012: Elementmobilitet under metasomatiske prosesser i dioritt på Vannøya. MSc thesis, Department of Geology. University of Tromsø, Tromsø.

Sharma, R. & Srivastava, P.K. 2014: Hydrothermal fluids of magmatic origin, In: Kumar, S., Singh, R.N. (Eds.), *Modelling of magmatic and allied processes*, pp. 181-208.

Sheperd, T.J. 1985: A practical guide to fluid inclusions. Blackie & Son Ltd, p. 235.

Sibson, R.H. 1994: Crustal stress, faulting and fluid flow. *Geological Society of London Special Publication* 78, 69-84.

Steele-MacInnis, M. 2018: Fluid inclusions in the system H_2O-NaCl-CO_2: An algorithm to determine composition, density and isochore. *Chemical Geology* 498, 31-44.

Steele-MacInnis, M., Lecumberri-Sanchez, P. & Bodnar, R.J. 2012: HokieFlincs_H_2O-NaCl: A Microsoft Excel Spreadsheet for interpreting microthermometric data from fluid inclusions based on the PVTX properties of H_2O-NaCl. *Computers and Geosciences* 49, 334-337.

Stormer, J.C. & Whitney, J.A. 1977: Two-feldspar geothermometry in granulite facies metamorphic rocks. Sapphirine granulites from Brazil. *Contributions to Mineralogy and Petrology* 65, 123-133.

Taylor, H.P., Frechen, J. & Degens, E.T. 1967: Oxygen and carbon isotope studies of carbonatites from the Laacher See District, West Germany and the Alnö District, Sweden. *Geochimica et Cosmochimica acta* 31, 407-430.

Thomas, R., Förster, H.-J. & Heinrich, W. 2003: The behaviour of boron in a peraluminous granite-pegmatite system and associated hydrothermal solutions: a melt and fluid inclusion study. *Contributions to Mineralogy and Petrology* 144, 457-472.

Thomas, R., Webster, J.D. & Davidson, P. 2011: Be-daughter minerals in fluid and melt inclusions: implications for the enrichment of Be in granite–pegmatite systems. *Contributions to Mineralogy and Petrology* 161, 483-495.

Vapnik, Y. & Moroz, I. 2002: Compositions and formation conditions of fluid inclusions in Emerald from the Maria deposit (Mozambique). *Mineralogical Magazine* 66, 201-213.

Vapnik, Y., Moroz, I., Roth, M. & Eliezri, I. 2006: Formation of emeralds at pegmatite-ultramafic contacts based on fluid inclusions in Kianjavato emerald, Mananjary deposits, Madagaskar. *Mineralogical Magazine* 70, 141-158.

Walton, L. 2004: Criteria for colored gemstone deposits in the Yukon, In: *Survey, Y.G. (Ed.), Open file*, p. 184.

Wang, A., Freeman, J.J. & Jolliff, B.L. 2015: Understanding the Raman spectral features of phyllosilicates. *Journal of Raman Spectroscopy* 46, 829-845.

Watenphul, A., Schmidt, C. & Jahn, S. 2014: Cr(III) solubility in aqueous fluids at high pressures and temperatures. *Geochimica et Cosmochimica acta* 126, 212-227.

Wibberley, C. 1999: Are feldspar-to-mica reactions necessarily reaction-softening processes in fault zones. *Journal of Structural Geology* 21, 1219-1227.

Wilkinson, J.J. 2001: Fluid inclusions in hydrothermal ore deposits. *Lithos* 55, 44.

Wintsch, R.P., Christoffersen, R. & Kronenberg, A.K. 1995: Fluid-rock reaction weakening of fault zones. *Journal of Geophysical Research* 100, 13021-13032.

Zane, A. & Weiss, Z. 1998: A procedure for classifying rock-forming chlorites based on microprobe data. *Rendiconti Lincei* 9, 51-56.

Zwaan, J.C. 2006: Gemmology, geology and origin of the Sandawana emerald deposits, Zimbabwe. *Scripta Geologica* 131, 1-211.

Figures

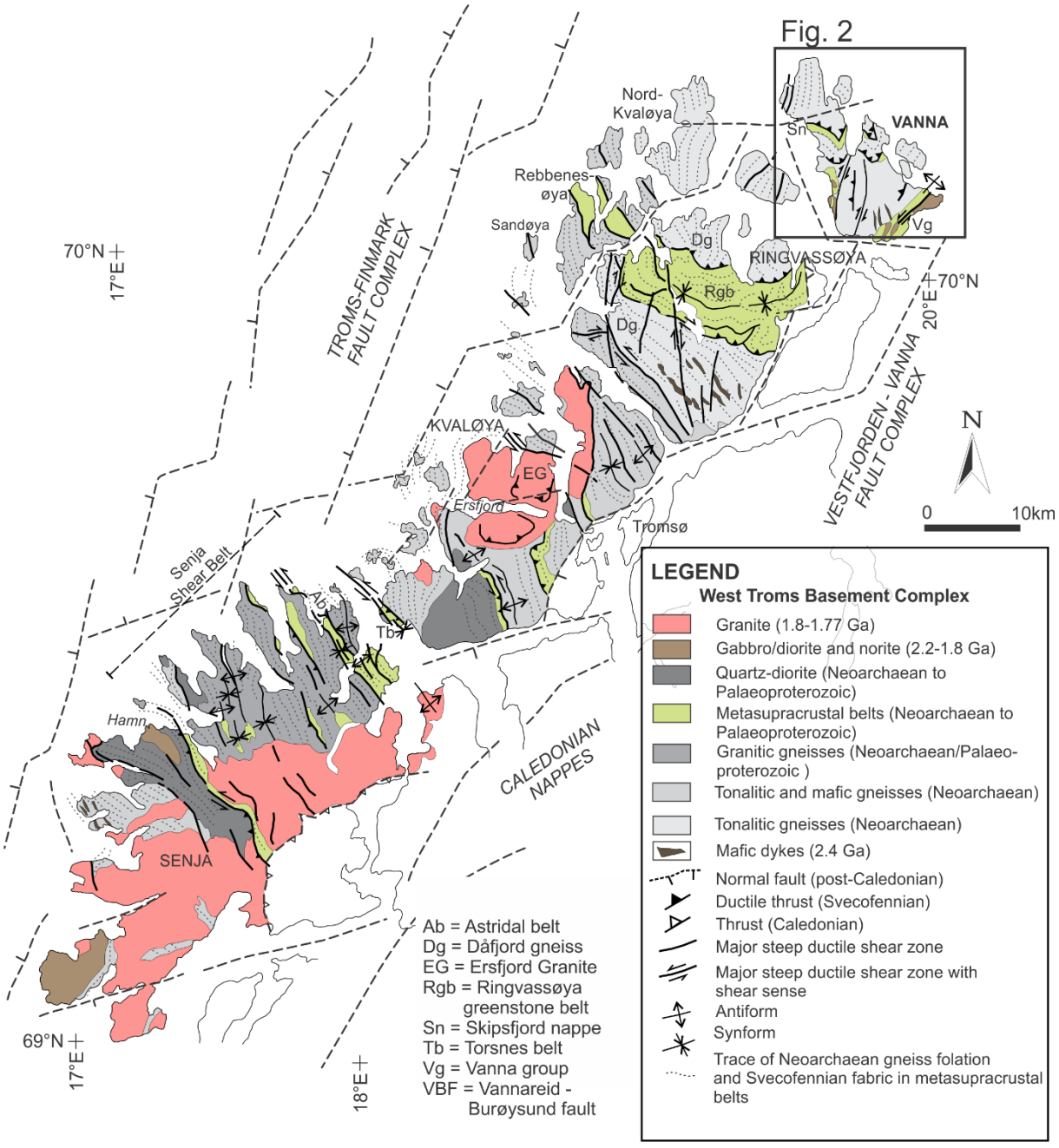

*Figure 1 Geology and cross-section of the Archaean/Palaeoproterozoic West Troms Basement Complex (Bergh et al. 2010; Thorstensen 2011; Davids et al. 2013; Haaland 2018). Vanna Island is located at the northern end of the complex and is marked on the map with a black frame (**Fig. 2**).*

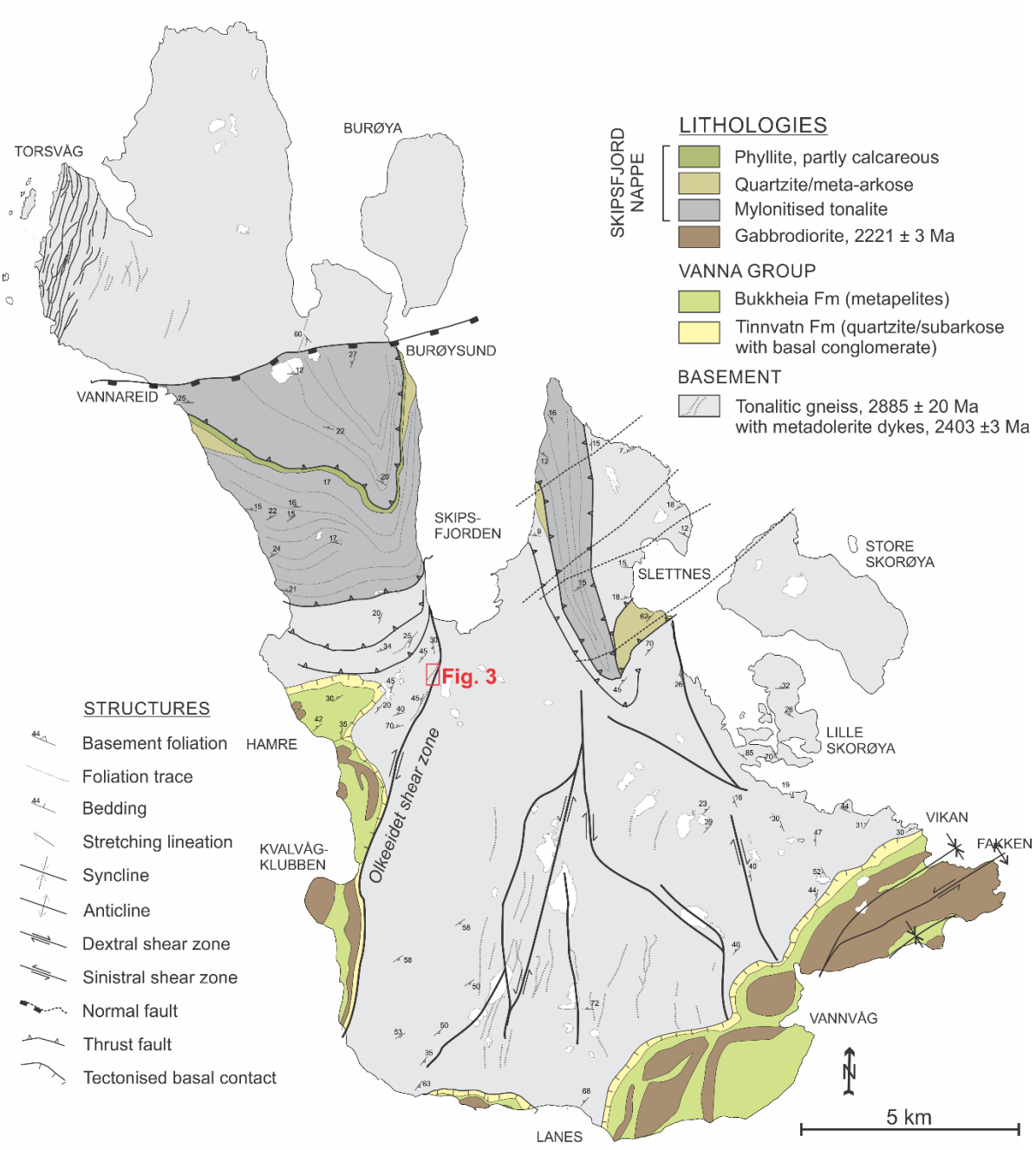

*Figure 2 Geological map showing Vanna Island. Location of emerald occurrence within Olkeeidet shear zone is marked in red frame (**Fig. 3**).*

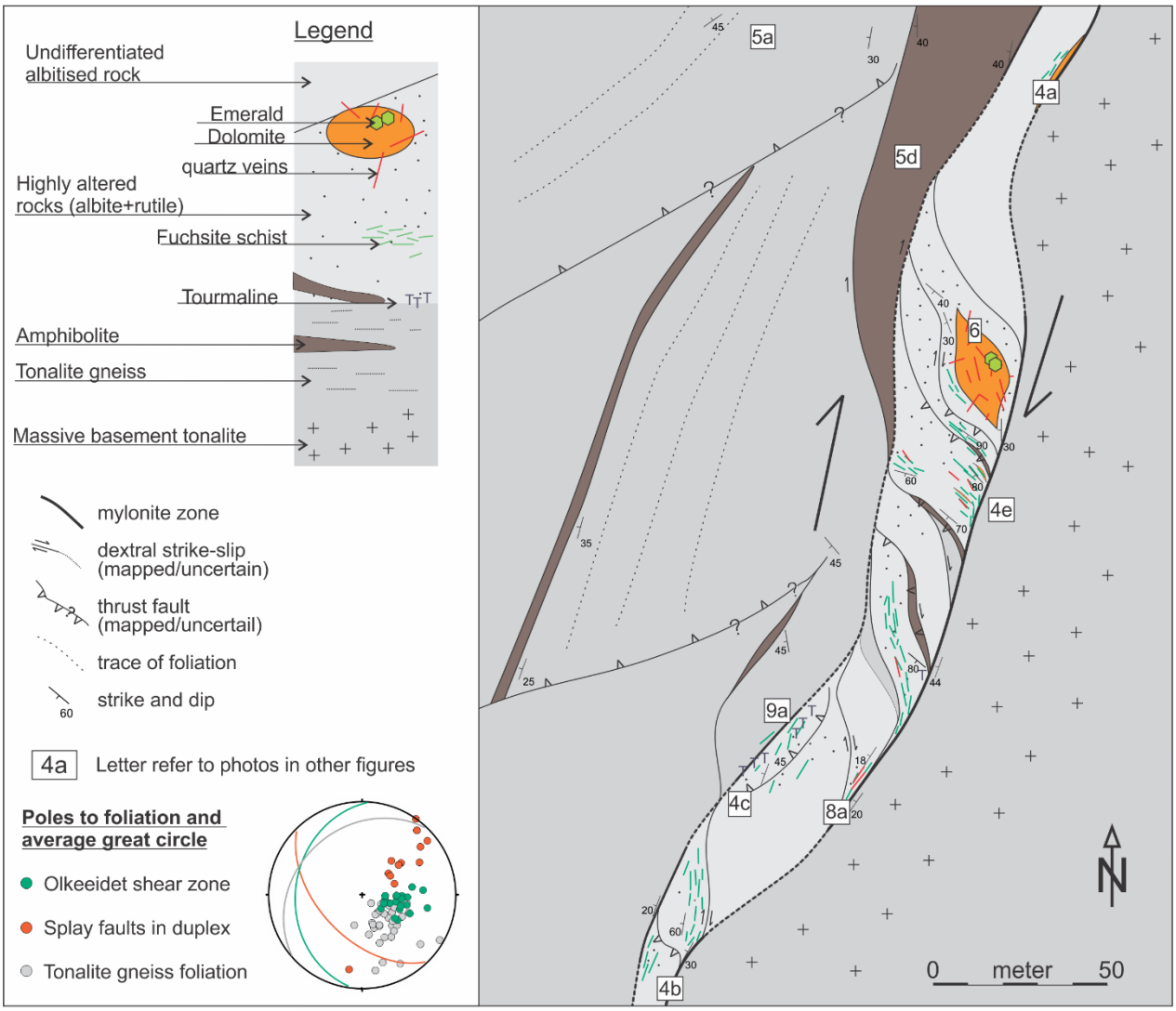

Figure 3 The Olkeeidet shear zone separates massive tonalite in the footwall from weakly foliated tonalite gneiss with amphibolite lenses in the hanging wall. The shear zone encloses a sequence of highly metasomatised rocks, mainly albitite and fuchsite schists, that are deformed in a complex duplex structure indicating dextral movement along the shear zone. Emerald is hosted by hydrothermal dolomite lenses in the albitite. Lower hemisphere equal area stereoplot at the bottom left show poles to foliation and averages in great circle of the Olkeeidet shear zone (green), internal splay faults in the duplex (red), and hanging wall tonalite gneiss foliation (grey).

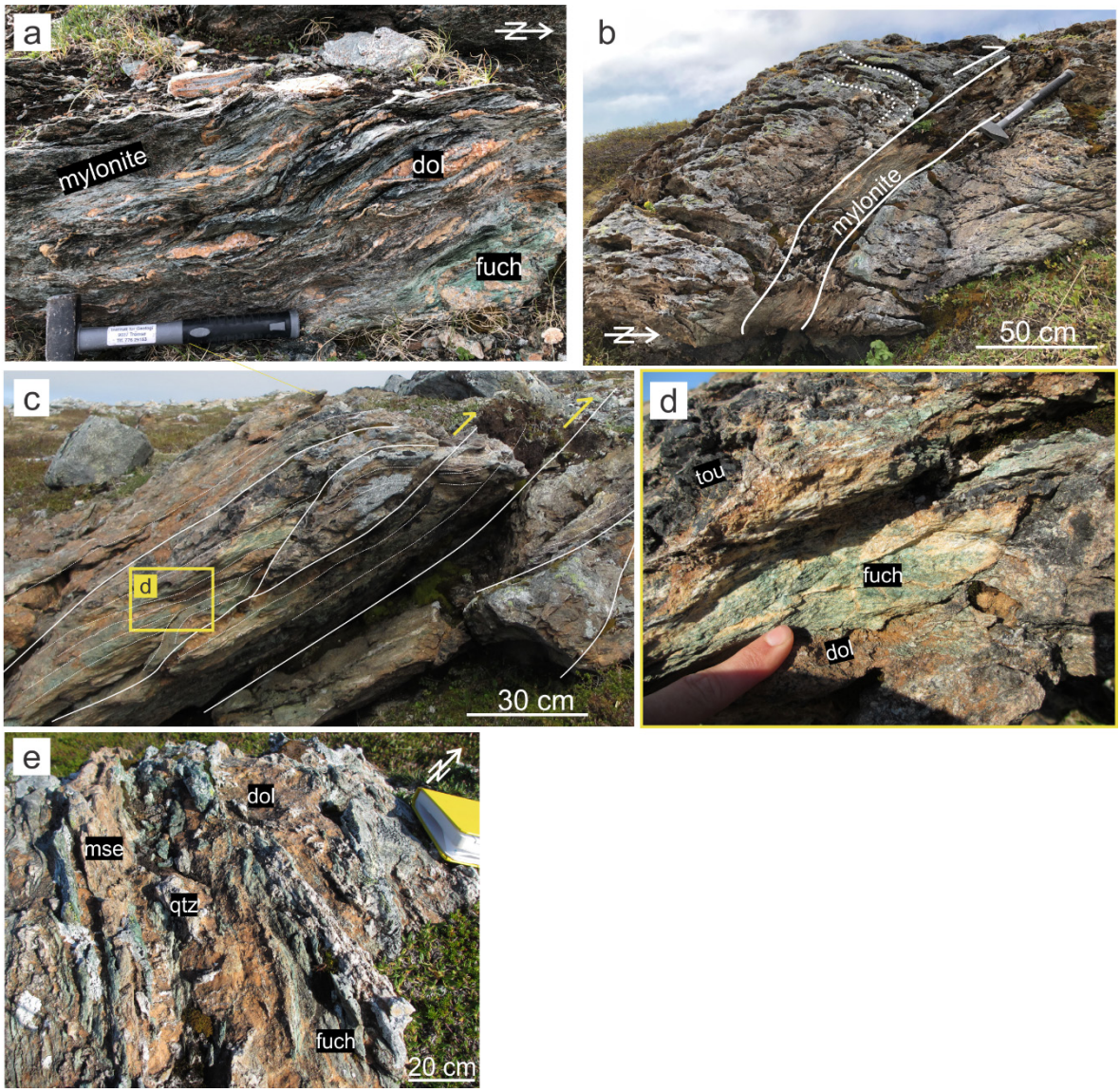

Figure 4 Structural relationships of the Olkeeidet shear zone. For location of photos, see figure 3. a) Mylonite zone along margins of shear zone with sigmoidal lenses of dolomite, quartz and bright green fuchsite rich rock. Hammer for scale (30 cm) b) mylonite formed in thrust fault internally within duplexes. Note drag-folding along hanging-wall host rocks. c) Thrust fault with top to the east movement juxtaposing different rock types in the shear zone. d) Close up of c). Note the black felted masses of tourmaline, bright green fuchsite schist, and brown weathering surface of dolomite e) Juxtaposed, highly strained and near vertical layers of metasomatised sediments(reddish brown) with lenses of fuchsite schist (green), dolomite (brown) and quartz veins (white). Abbreviations; dol=dolomite, fuch=fuchsite, tou=tourmaline

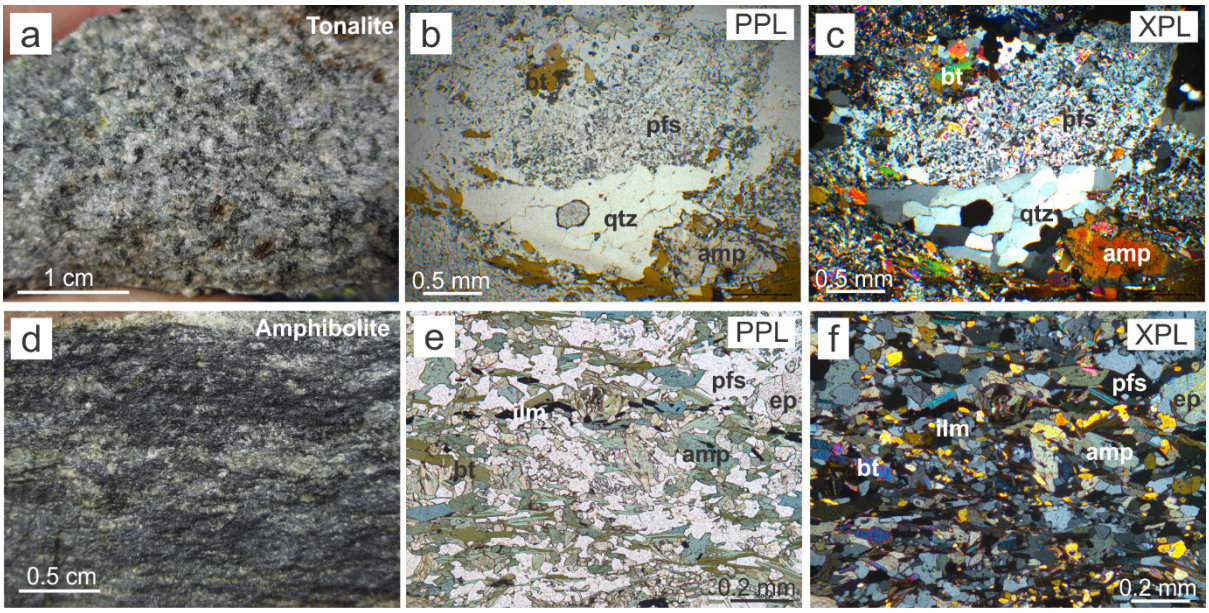

Figure 5 Images of typical and relatively unaltered host rocks. a) Massive tonalite gneiss in outcrop. b&c) Microphotograph of tonalite gneiss with sericitised plagioclase, biotite aggregates and polycrystalline grains of quartz, and amphibole (b-PPL & c-XPL). d) Outcrop photograph of weakly foliated amphibolite; e&f) Microphotograph of weakly foliated amphibolites with feldspar, amphibole, epidote, biotite and ilmenite. Abbreviations; PPL = plane-polarised light, XPL = cross-polarised light, bt= biotite, pfs=plagioclase feldspar, qtz= quartz, amph=amphibole, ep=epidote, ilm=ilmenite

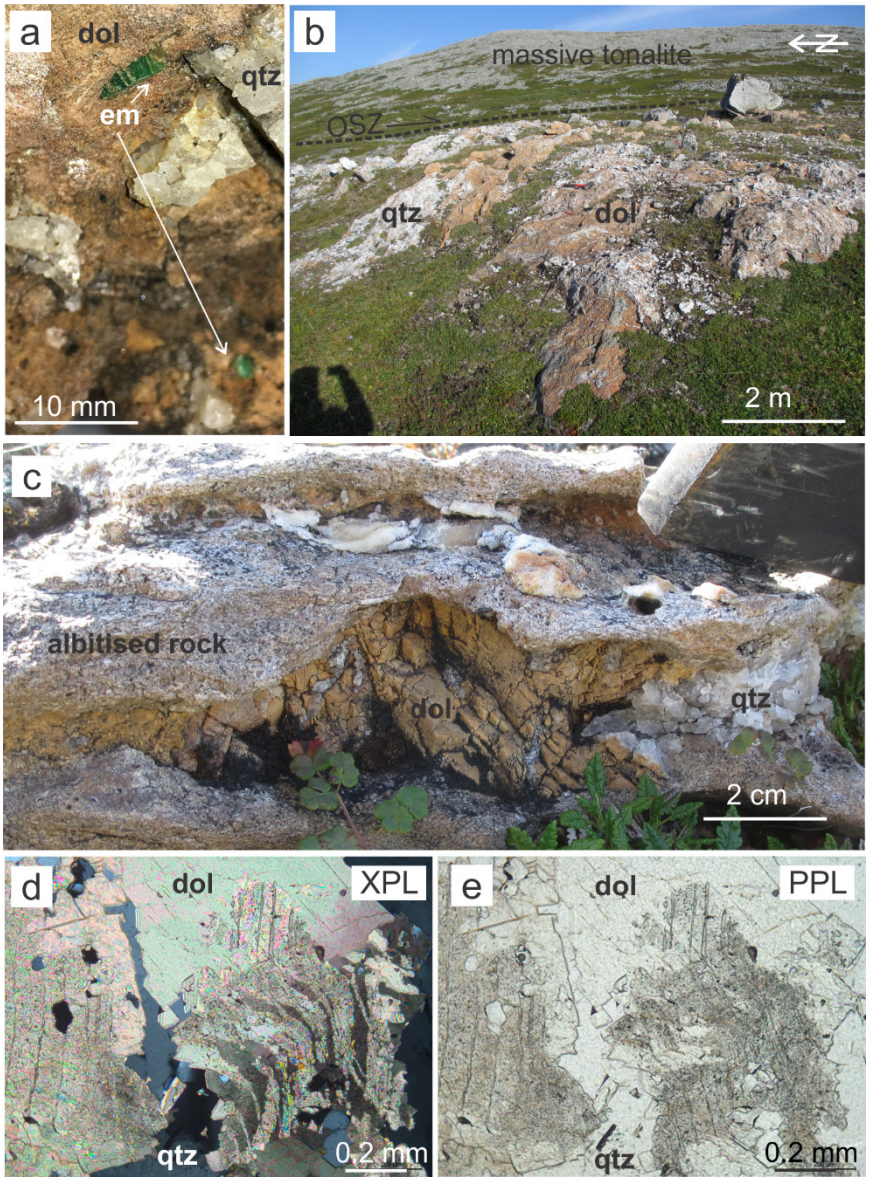

Figure 6 Images of dolomite a) outcrop photos of bright green emerald crystals hosted by dolomite veins with quartz. b) Dolomite lens with brown weathering surface forms a brown hill in the landscape. The shear zone is hidden just behind the dolomite hill, and its approximate location is shown with a stippled line. Massive tonalite in the footwall forms the mountain in the background. c) Outcrop photo of small dolomite vein hosted by albitised meta-sedimentary rock. d) Microphotograph of dolomite grain with cloudy appearance and deformation twinning in the core of the grain, and relatively undeformed rims (XPL). e) PPL of d. Abbreviations: XPL = cross-polarised light, PPL - plane polarised light, dol=dolomite, qtz=quartz.

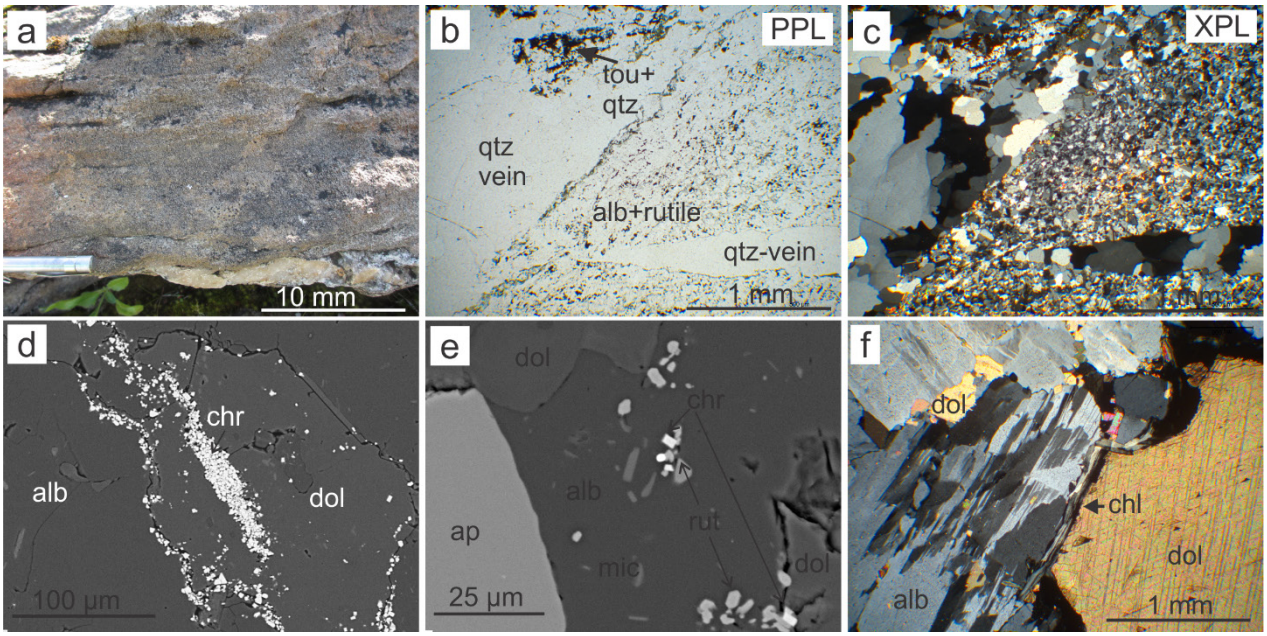

Figure 7 Photos of strongly albitised (albitite) rock. a) Outcrop photo of pale red albitised host rock. b) Thin section microphotograph of strongly albitised rock to the right in the photo (labelled alb+rutile). In the top left of the photo is a clast of a quartz tourmaline vein. Later quartz veins cross cut both albitised rockt and tourmaline vein. c) XPL of b). d) SEM image of clusters of small <5µm grains of chromite interstitially between albite and dolomite and also within dolomite rain. e) SEM image of aggregates of cubic chromite and elongate rutile grains in an albite matrix. f) Chlorite in contact between albite and dolomite. Abbreviations: XPL = cross-polarised light, PPL = plane polarised light, qtz=quartz, tou=tourmaline, ap=apatite, alb=albite, mic=microcline, dol=dolomite, chl=chlorite, chr=chromite

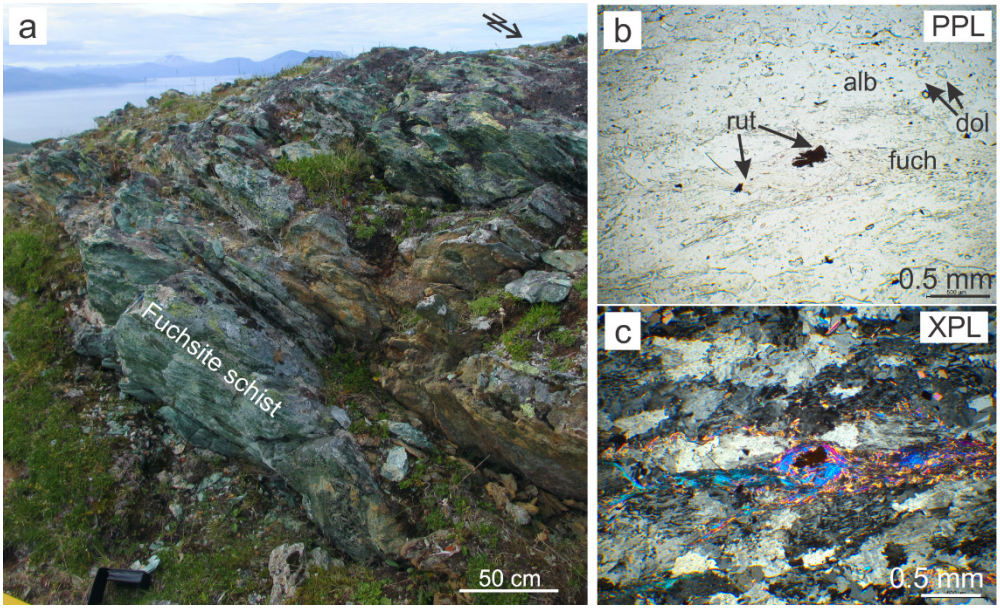

Figure 8 a) outcrop photo of strongly foliated bright green fuchsite schist. b&c) plane-polarised and cross-polarised microphotographs of fuchsite schist. Note flame shaped deformation twins in albite separated by fuchsite with spaced cleavage. Granular rutile has formed within fuchsite bands. Abbreviations; PPL = plane-polarised light, XPL = cross-polarised light, alb=albite, fuch=fuchsite, rut=rutile, dol=dolomite

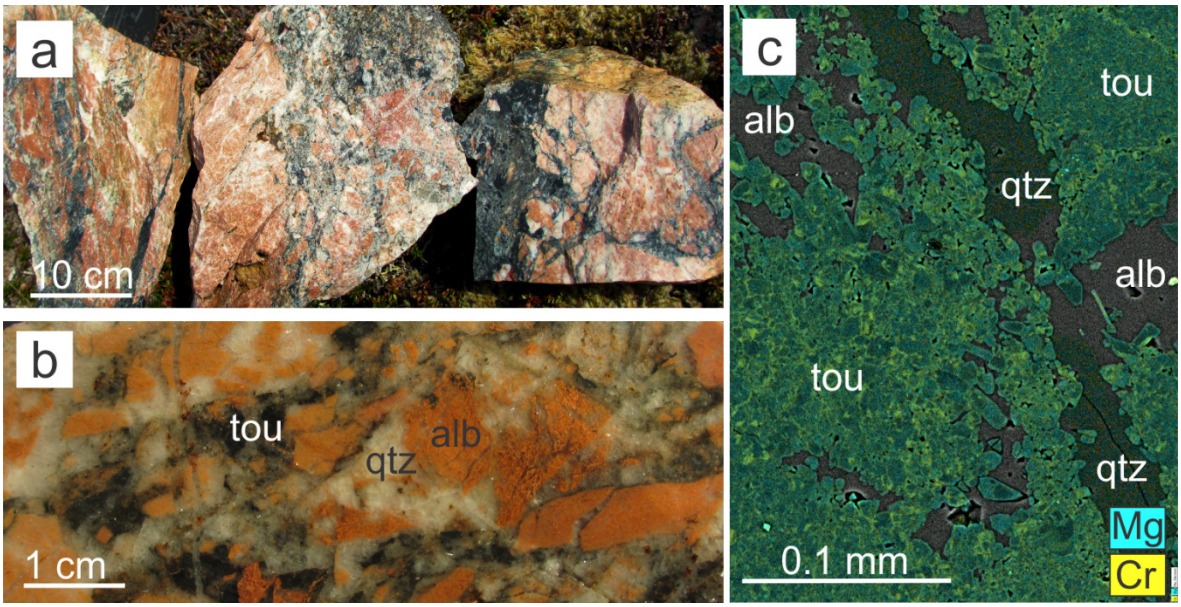

Figure 9 a) outcrop photograph of dark red albitised host rock cut by black tourmaline+quartz veins. b) Cut slab photo of a) showing dark red albitite cataclasite cataclasite with black tourmaline and transparent quartz infill. c) SEM image of massive and felted tourmaline grains (green) with albite and quartz. Colour overlay reflect compositional zoning of Mg (light blue) and Cr (yellow).

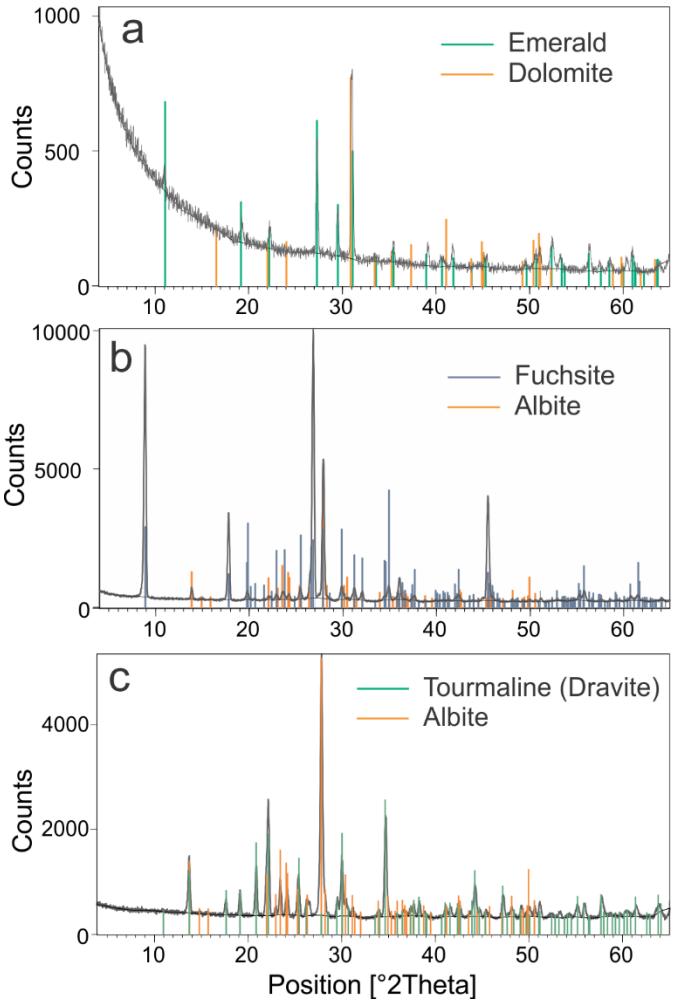

Figure 10 X-ray diffraction spectra of a) emerald and dolomite b) fuchsite and albite c) tourmaline and albite.

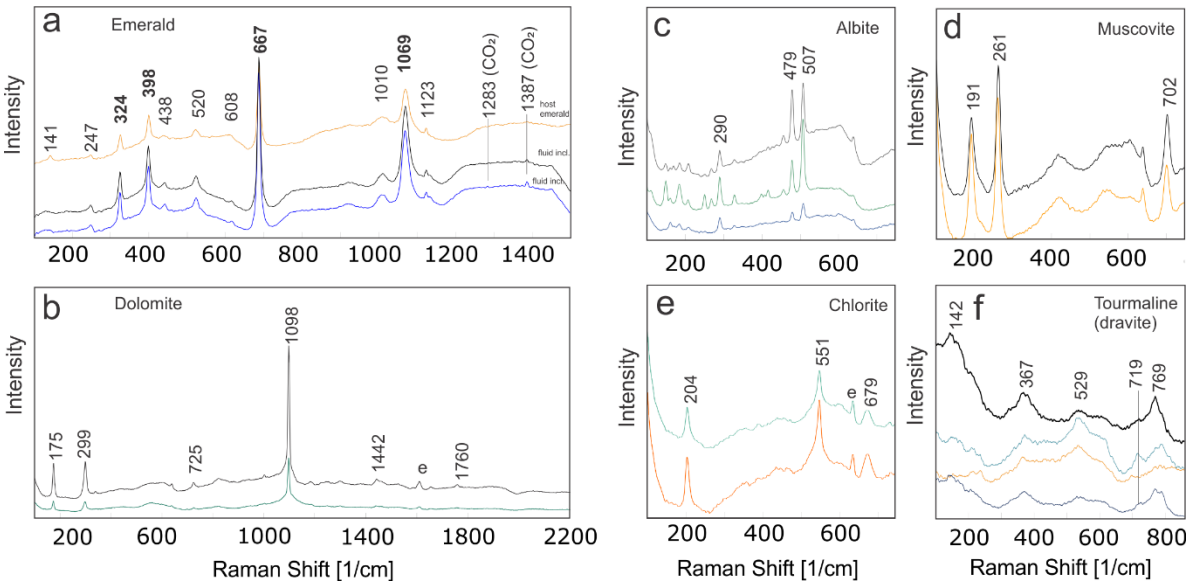

Figure 11 Raman spectroscopy results with major peaks annotated. a) Host beryl/emerald spectre (orange) and spectra of fluid inclusions with CO_2 in beryl (black and blue). b) Dolomite spectra. "e" denotes peak from accidental analysis of epoxy. c) Albite spectra from albitite. d) Muscovite (fuchsite) spectra from fuchsite schists. e) Chlorite spectra from dolomite contact. f) Tourmaline spectra.

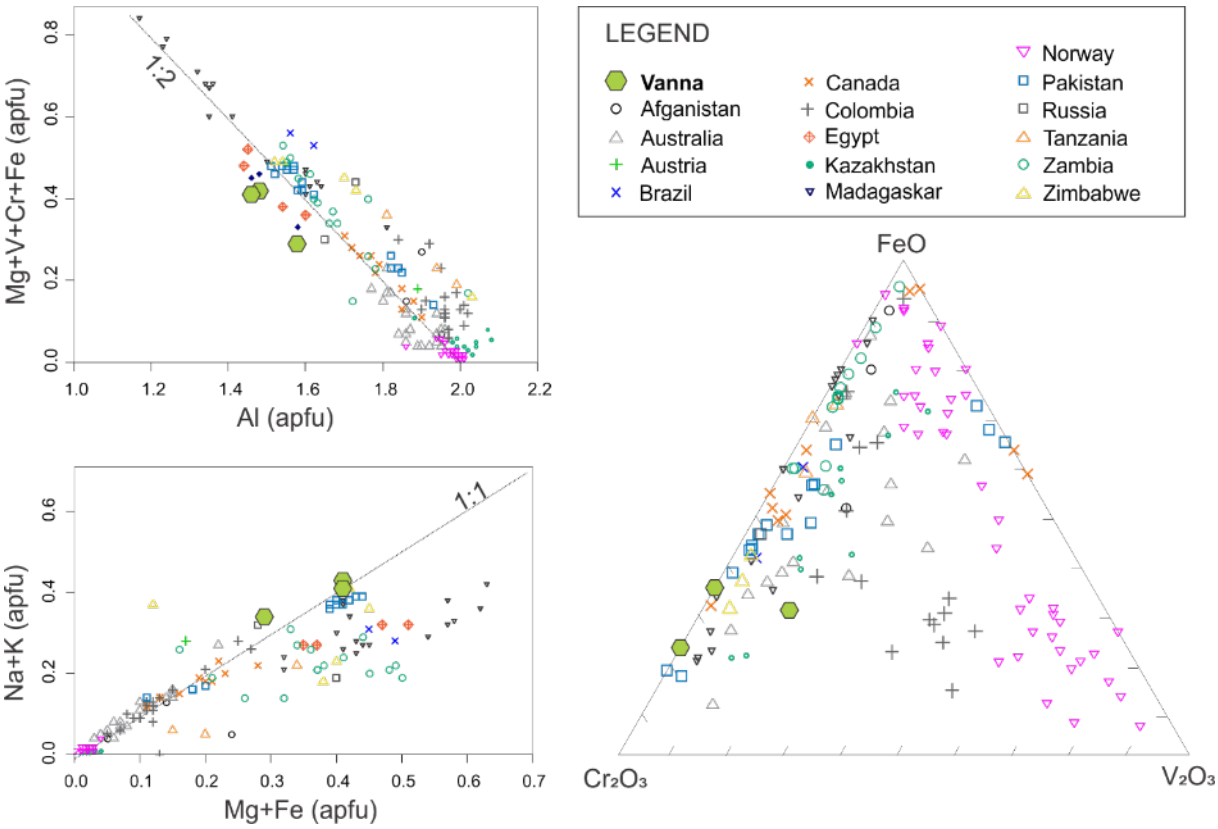

Figure 12 Emerald compositions of Vanna emerald superimposed on worldwide emerald data compiled from literature (Groat et al., 2008; Loughrey et al., 2013; Aurisiccho et al., 2018). Top left diagram show Al versus the sum of other Y-site cations in emerald in atoms per formula unit (a.p.f.u.). Bottom left diagram shows Mg+Fe versus monovalent channel-site cations (a.p.f.u.). Triangular diagram shows the distribution of FeO, Cr_2O_3 and V_2O_3 in wt. %. Vanna emeralds are Cr-rich and this is responsible for the green colour.

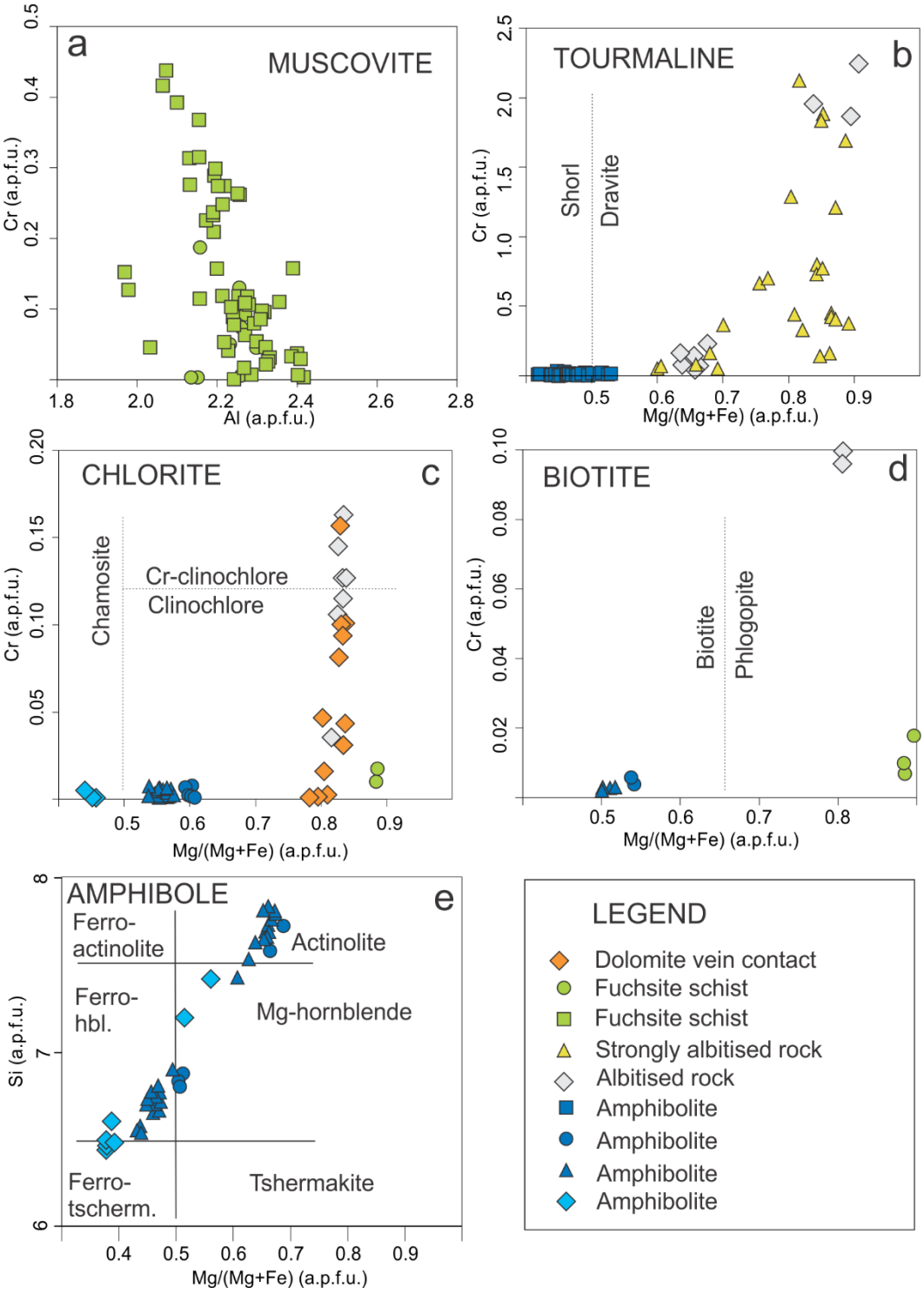

Figure 13 Plots that illustrate the variations in mineral chemistry and nomenclature of different samples. b-d also compares the chemistry of minerals from relatively unaltered amphibolites to strongly metasomatised albitised rock and fuchsite schist. a) Al vs Cr content in fuchsite showing a negative correlation. b) Mg/ (Mg+Fe) versus Cr in tourmaline. Nomenclature from Henry et al., (2011). c) Mg/ (Mg+Fe) versus Cr values from chlorite. Nomenclature based on (zwaan and Weiss, 1998). d) Mg/ (Mg+Fe) versus Cr in biotite (Deer et al., 1972). e) Amphibole composition plotted as Mg/ (Mg+Fe) versus Si. (Nomenclature after Leake et al., 2003). Legend shows different colour and symbols by rock type. All values are in atoms per formula unit (a.p.f.u.)

Mineral	Beryl*		Amphibole		Biotite			Chlorite			Muscovite		Tourmaline			Albite	Microcline	Dolomite	Rutile
Sample	H-Em	H-Em	M202	M202	M202	S203	H84B	M202	S300	H84J	H84G	H84G	M201	S300	H84B	H84G	H84G	H84G	H84A
SiO_2 (wt%)	59.49	56.69	52.06	46.09	37.67	36.77	40.28	26.77	28.31	30.52	45.83	47.901	36.89	35.102	36.105	68.57	67.28	0.12	0.22
Al_2O_3	13.47	12.94	4.03	10.33	15.52	15.65	16.01	20.83	20.53	19.67	25.66	29.21	29.44	19.4	23.93	19.73	19.22	-	0.16
FeO	0.31	0.27	13.34	17.38	18.57	14.04	11.55	21.62	9.28	11.33	2.26	1.87	12.303	2.81	3.49	-		3.32	0.13
MgO	2.79	2.70	14.8	10.2	12.09	16.6	16.14	17.82	25.96	26.06	2.31	2.47	6.15	8.14	8.01	-		19.26	-
MnO	-	-	0.23	0.28	0.06	-	-	0.17	0.07	0.03	-	0.05	0.04	0.03	0.07	-		0.16	-
Na_2O	2.26	2.33	1.01	2.42	0.05	0.12	0.12	0.05	0.05	0.07	0.27	0.39	2.54	2.79	2.82	11.71		-	0.03
CaO	-	-	11	9.8	0.15	0.07	0.06	0.11	0.05	0.1	0.04	-	0.31	0.24	0.16	-		29.37	-
K_2O	-	-	0.11	0.38	9.71	8.08	10.1	0.04	-	-	10.4	10.67	0.03	0.05	-	-	17.22	0.05	0.06
Cr_2O_3	**0.58**	**0.53**	**0.17**	**0.13**	**0.1**	**0.05**	**1.21**	**0.08**	**1.63**	**0.63**	**8.09**	**1.84**	**-**	**14.42**	**9.63**	**0.06**		**-**	**1.34**
V_2O_3	**0.16**	**-**	**0.12**	**0.01**	**0.03**	**0.18**	**0.38**	**0.07**	**0.21**	**0.05**	**0.48**	**0.24**	**0.13**	**2.00**	**1.86**	**-**		**-**	**0.69**
TiO_2	-	-	0.03	0.32	1.94	1.33	1.48	0.05	0.02	0.04	0.58	0.53	0.16	0.19	0.18	-		-	98.16
BeO	*12.38*	*11.80*	-	-	-	-	-	-	-	-	-	-	-	-	-	-		-	-
Total	91.45	87.26	96.92	97.22	95.96	92.92	97.24	87.57	86.13	88.43	95.95	95.14	87.96	85.13	86.38	100.12	104.1	52.27	100.7
Formula Ox	18	18	23	23	11	11	11	14	14	14	11	11	31	31	31	8	8	3	2
Si (a.p.f.u.)	5.53	5.44	7.58	6.88	2.84	2.78	2.89	2.76	2.79	2.94	3.14	3.23	6.08	6.03	6.02	2.99	2.99	0.01	-
Al	1.48	1.46	0.69	1.82	1.38	1.40	1.35	2.53	2.39	2.23	2.07	2.32	5.72	3.92	4.70	1.02	1.01	-	-
Fe	0.02	0.02	1.62	2.17	1.17	0.89	0.69	1.87	0.77	0.91	0.13	0.11	1.70	0.40	0.49	-	-	0.13	-
Mg	0.39	0.39	3.21	2.27	1.36	1.87	1.72	2.74	3.82	3.75	0.24	0.25	1.51	2.08	1.99	-	-	1.36	-
Mn	-	-	0.03	0.04	-	-	-	0.02	0.01	-	-	-	0.01	-	0.01	-	-	0.01	-
Na	0.41	0.43	0.29	0.70	0.01	0.02	0.02	0.01	0.01	0.01	0.04	0.05	0.81	0.93	0.91	0.99	0.01	-	-
Ca	-	-	1.72	1.57	0.01	0.01	-	0.01	0.01	0.01	-	0.00	0.05	0.04	0.03	-		1.49	-
K	-	-	0.02	0.07	0.93	0.78	0.92	0.01	-	-	0.91	0.92	0.01	0.01	-	-	0.99	-	-
Cr	0.04	0.04	0.02	0.02	0.01	-	0.07	0.01	0.13	0.05	0.44	0.10	-	1.96	1.27	-	-	-	0.01
V	0.01	-	0.01	0.00	-	0.01	0.02	0.01	0.01	-	0.02	0.01	0.02	0.28	0.25	-	-	-	0.01
Ti	-	-	-	0.04	0.11	0.08	0.08	-	-	-	0.03	0.03	0.02	0.02	0.02	-	-	-	0.98
Be	*3.00*	*3.00*	-	-	-	-	-	-	-	-	-	-	-	-	-	-	-	-	-
B	-	-	-	-	-	-	-	-	-	-	-	-	*3.00*	*3.00*	*3.00*	-	-	-	-
OH	-	-	-	-	-	-	-	-	-	-	-	-	*4.00*	*4.00*	*4.00*	-	-	-	-
Li****	-	-	-	-	-	-	-	-	-	-	-	-	*0.03*	*0.33*	*0.28*	-	-	-	-
Cation total	10.88	10.78	15.20	15.56	7.83	7.83	7.77	9.96	9.93	9.91	7.01	7.01	18.96	19.01	18.94	5.00	5.00	3.00	1.00
Mg/(Mg+Fe)			0.66	0.51	0.54	0.68	0.71	0.60	0.83	0.80	0.65	0.70	0.47	0.84	0.80				

*Table 1 EDS compositional analysis of representative minerals. Calculated values are marked with italics. * BeO and H_2O content in beryl is calculated on the basis of stoichiometry with 3 Be in the mineral formula. ** Tourmaline is calculated on the basis of stoichiometry with 3 B and 4 OH in the mineral formula.*

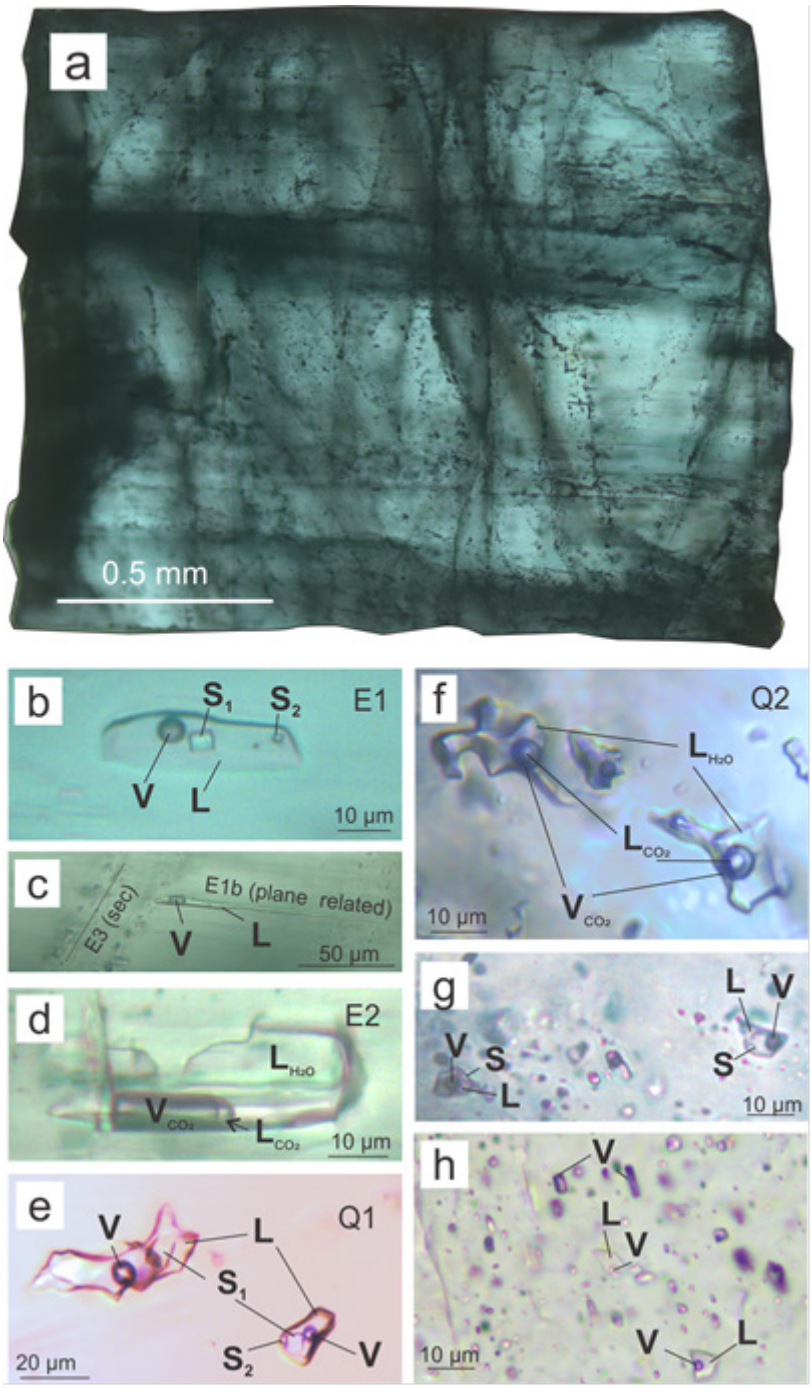

Figure 14 Fluid inclusion petrography. a) Polished emerald overview. b) E1 L+V+S_1+S_2 inclusions in emerald. b) E2 CO_2 bearing L+L+V inclusions in emerald. d) E1b plane related inclusions and E3 secondary L+V inclusions. e) Q1 L+V+S_1+S_2 inclusions in quartz. f) Q2 CO_2 bearing L+L+V inclusions in quartz. g) L+V+S fluid inclusions in dolomite. h) Numerous L+V and L-only fluid inclusions in dolomite.

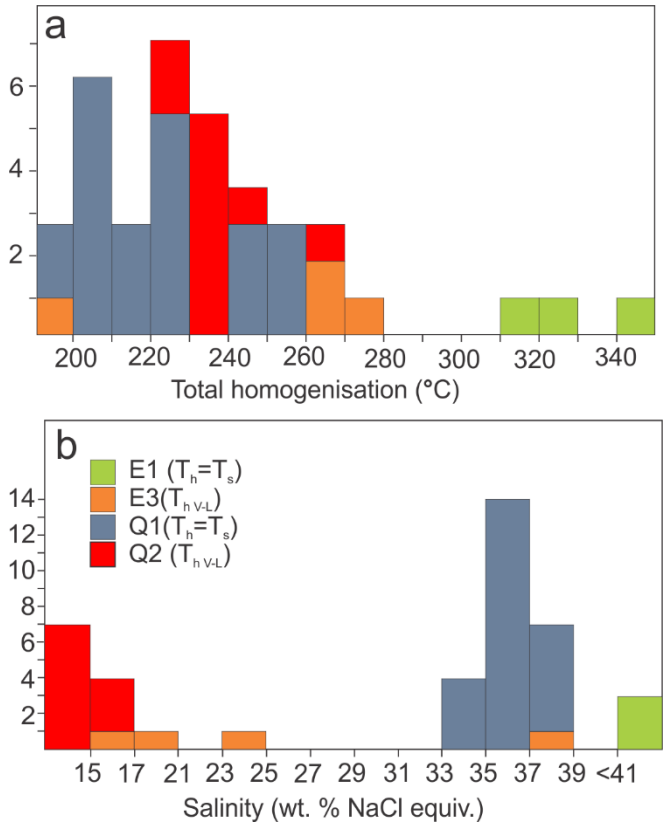

Figure 15 Histograms summarising fluid inclusion microthermometric measurements. a) T_h - total homogenisation temperature (°C). b) Calculated salinity in wt. % NaCl equivalent.

Host mineral	Inclusion type	Genetic type	Microthermometric data												
			T_{clath} (°C)		T_{im} (°C)		T_{s1} (°C)		T_h (°C)		Salinity (NaCl wt. % equiv)		Pressure (kbar) at $T_{h\text{-}tot}$	density (g/cm³)	n
			Range	Mdn±σ	Range	Mdn±σ	Range	Mdn±σ	Range	Mdn±σ	Range	Mdn±σ	Range		
Quartz	**E1a** ($L+V+S_1±S_2$)	Primary			-13.0 to -20.3	-15 ±2.9	320-350	330 ± 12.5	275-300	284 ± 10.3	40.4-43.0	41.2 ± 1.1	704-682	1.1	3
	E3 ($L+V$)	Secondary					260		190-280	243 ± 36.0	16.9-35.8	20.5 ± 7.4			4
	Q1 ($L+V+S_1±S_2$)	Primary					200-222	210 ± 7.8	130-140	134 ± 4.2	32.6-33.9	33.2 ± 0.5	1925-1251	1.2	6
	Q1 ($L+V+S_1±S_2$)	Primary					208-210	209 ± 1.0	140-178	158 ± 13.6	32.6-33.2	33.0 ± 0.2	1455-630	1.2	4
	Q1 ($L+V+S_1±S_2$)	Primary					221-249	222 ± 12.0	128-132	130 ± 1.4	33.8-35.3	33.8 ± 0.7	2626-1881	1.2	4
	Q1 ($L+V+S_1±S_2$)	Primary					241-263	253 ± 7.9	149-152	150 ± 1.1	35.0-36.4	35.8 ± 0.5	2404-1916	1.2	4
	Q1 ($L+V+S_1±S_2$)	Primary					210-214	212 ± 2.0	152		33.1-33.3	33.2 ± 0.1	1204-1244	1.2	2
	Q1 ($L+V+S_1±S_2$)	Primary					220-242	230 ± 7.8	145-166	150 ± 7.9	33.7-35.1	34.3 ± 0.5	1914-1304	1.2	4
	Q2 ($L+V$)	Primary	-0.3 to 2.2	1.3 ± 0.8					> 223-270	240 ± 11.7	13.0-15.9	14.1 ± 0.9	1594-1504	1.0	10
Dolomite	**D** ($L+V+S_1±S_2$)	Primary					>210-230		> 210-230		>32.4				4

Table 2 Summary of microthermometric data from fluid inclusions hosted by emerald, quartz, and dolomite. T_{clath} = clathrate melting temperatures, T_{im} = ice melting temperature, T_{S1} = solid dissolution temperature, T_h = homogenisation temperature, Mdn±σ = median plus/minus standard deviation, $T_{h\text{-}tot}$ = total homogenisation by halite dissolution, n= total number of microthermometric measurements. ">" symbol indicate that inclusions decrepitated at or near this temperature (±solid) and represents minimum temperatures and salinities.

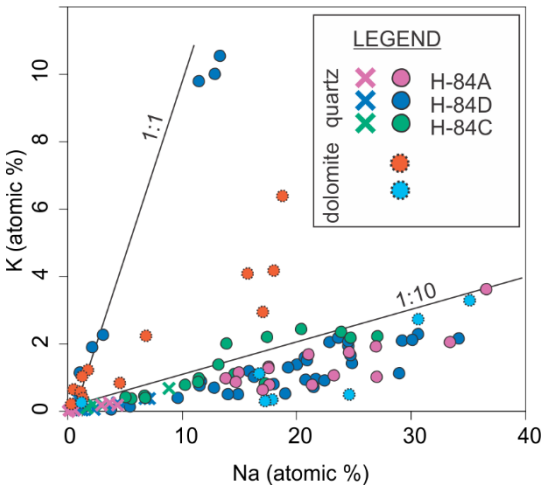

Figure 16 Qualitative geochemical measurements of evaporate mounds from fluid inclusions hosted in quartz. Map scan analyses yielding average compositions of the whole evaporate mound are marked with a cross and spot analysis of individual crystals are marked with a circle. Na versus K plot indicate two fluid trends with 10:1 and 1:1 Na/K ratios.

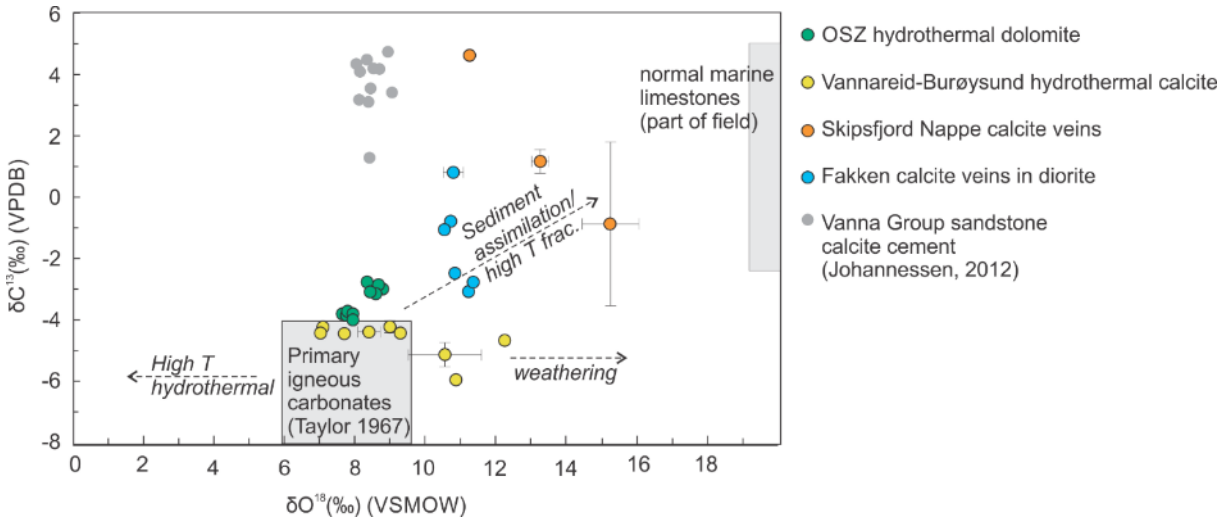

Figure 17 Plot with stable $\delta^{18}O$ and $\delta^{13}C$ isotopes from emerald-hosting dolomite in the OSZ. Data from Vannareid-Burøysund hydrothermal calcite, Skipsfjord Nappe calcite veins and Fakken calcite are from Paulsen et al., (in press). Vanna Group sandstone calcite cement is from Johannessen, (2012).

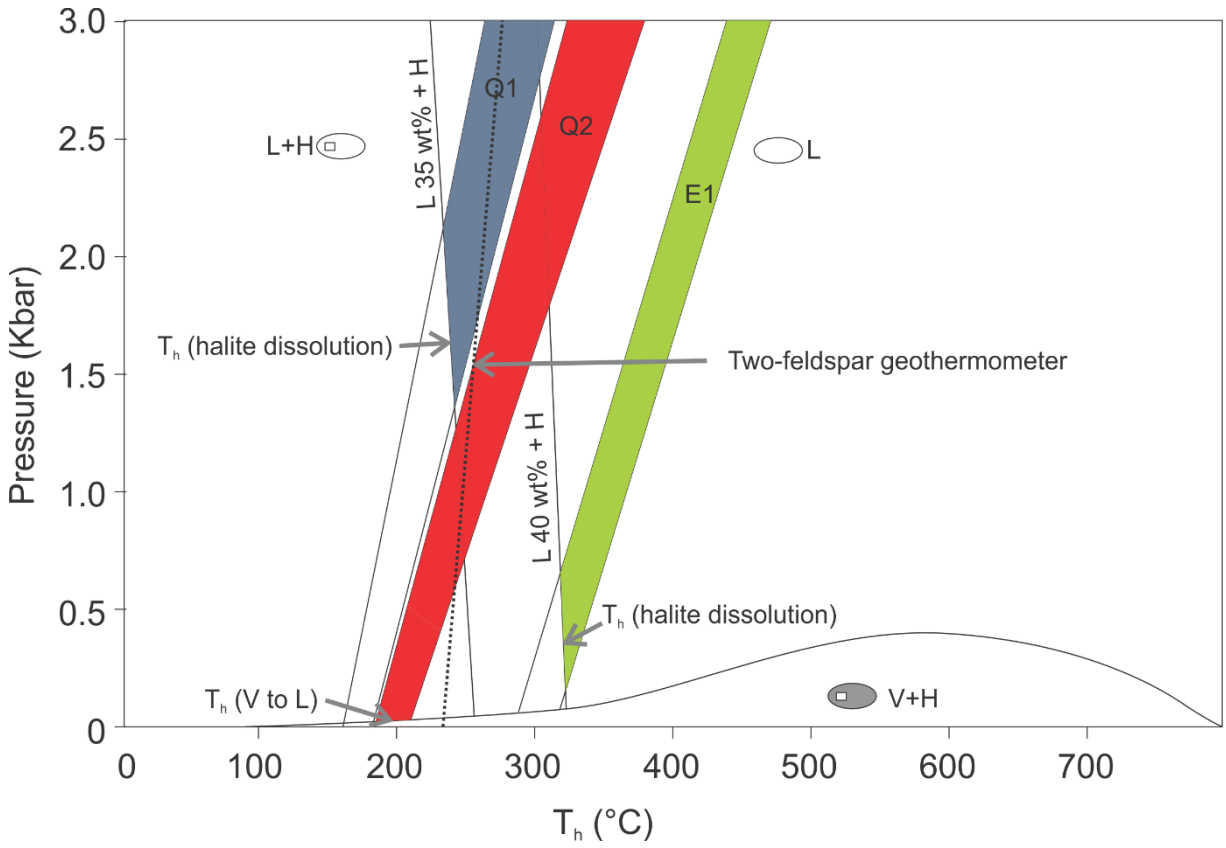

Figure 18 Pressure-temperature diagram with constructed isochores from fluid inclusion microthermometric data. E1 and Q1 inclusions show minimum formation temperatures by halite dissolution, and Q2 inclusions by vapour to liquid homogenisation. Two feldspar geothermometry from albite and microcline in fuchsite schist calculated according to Stormer and Whitney (1977) is also plotted as a stippled line. Liquidus and field boundaries for the 35 and 40 wt. % NaCl isopleths were interpolated using the data from Bodnar 2003. Abbreviations: T_h = homogenisation temperature, L = liquid, V = vapour, H = halite.

Late Palaeozoic fault controlled hydrothermal Cu-Zn mineralization on Vanna Island, West Troms Basement Complex, northern Norway.

Hanne-Kristin Paulsen[1], Steffen G. Bergh[1], Sabina Strmić Palinkaš[1]

[1] University of Tromsø (UiT) – The Arctic University of Norway, N-9037 Tromsø, Norway

hanne-kristin.paulsen@uit.no

Abstract

The Vannareid-Burøysund fault is a major, brittle normal fault in northern Norway, with cohesive fault rocks (cataclasites) that host Cu-Zn bearing quartz-carbonate veins. The fault is exposed on the island of Vanna in the Neoarchaean to Palaeoproterozoic West Troms Basement Complex, separating variably deformed tonalitic gneisses in the footwall from mylonitized meta-sedimentary rocks and tonalites in the hanging wall. Radiometric dating (K–Ar illite) of normal fault movement along the Vannareid-Burøysund fault yielded a late Permian age, concurrent with incipient post-Caledonian continental rifting. The fault evolution and internal architecture of the Vannareid-Burøysund fault largely controlled the spatial distribution of mineralization, and two main phases of the Cu-Zn mineralization have been discerned. Early quartz-sphalerite veins are deposited in the cataclastic fault core zone, where initial movement along the fault created a fluid conduit that allowed for fluid flow and sphalerite deposition. With subsequent movement and widening of the fault zone, a later and spatially more extensive generation of quartz-chalcopyrite veins were deposited in both the fault core and damage zones. Fluid inclusion microthermometry revealed that the ore-forming fluids were highly saline aqueous solutions (20-37 wt. % $NaCl+CaCl_2$) that carried base metals and sulphur. Further, the isotopic composition of hydrothermal carbonates indicates a magmatic source of CO_2. The structural data and obtained geochemical results indicate that the Cu-Zn mineralization in the Vannareid-Burøysund fault was epigenetic and strongly controlled by extensional brittle faulting and cataclasis during early stages of post-Caledonian (Permian) continental rifting, thus providing a new model for exploration of post-Caledonian hydrothermal ore deposits in basement rocks of northern Norway.

Introduction

Cu-Zn mineralization is found in a variety of geological settings, such as volcanogenic massive sulphide (VMS) deposits (Franklin et al. 1981; Galley et al. 2007), skarn deposits (Meinert et al. 2005), black shale hosted Cu-Zn deposits (Kupferschiefer; Kucha and Pawlikoswki, 1986; Oszczepalski 1999), sediment hosted Cu-Zn deposits (Perello et al. 2015), and hydrothermal vein deposits (Corbett and Leach 1998; Simmons et al. 2005). Key factors that may control the deposition of significant Cu-Zn mineralization include a source of metals (Rye and Ohmoto 1974; Boiron et al. 2010), an aqueous fluid capable of transporting metal complexes (Hemley and Cygan 1992; Zhong et al. 2015), rock permeability that allows fluid flow (Sibson et al. 1975; Ingebritsen and Manning 2010), and favourable physicochemical conditions for Cu and Zn deposition (Seward and Barnes 1997; Vaughan and Craig 1997; Corbett and Leach 1998). In crystalline rocks in the upper crust, brittle faults and fracture systems represent important conduits for ore-bearing fluids in otherwise non-permeable rocks (Braathen and

Davidsen 2000; Gabrielsen and Braathen 2014; Schmid and Handy 1991; Sibson 1977; Wise et al. 1984).

In this study, we analyse a major brittle normal fault in northern Norway, the Late Palaeozoic/Permian Vannareid-Burøysund fault (VBF), and its cohesive brittle fault rocks (cataclasites) hosting Cu-Zn bearing quartz-carbonate veins. The fault is situated along the contact between Neoarchaean tonalitic basement gneisses and an overlying, mixed basement and meta-sedimentary thrust unit, the Skipsfjord Nappe (Opheim and Andresen 1989; Monsen, 2014). The Cu-Zn mineralization was discovered in 2008 and briefly explored in 2012 when an exploration company (Store Norske Gull) bored eight drill holes totalling a length of 880 m, and informally interpreted the mineralized occurrence as a Palaeoproterozoic VMS type (Ojala et al. 2013). Follow-up studies showed Cu-Zn and sulfide enrichment in vein and brecciated/cataclastic fault rocks indicating extensive hydrothermal alteration (Monsen, 2014). This paper expands the goals to explore ore-forming processes based on fault rock architectures, ore-hosting vein and host rock mineral geochemistry, fluid inclusion microthermometry and decrepitation studies, and stable isotope data.

These goals are achieved by studying the brittle fault zone architecture (domains in section across the fault) and meso- and micro-scale textures of the resulting fault rocks in relation to ore-hosting hydrothermal quartz-carbonate veins. The mineralogical and geochemical changes of the host rock during infiltration of ore-bearing fluids and the mineralization process are studied in detail. In addition, P-T-X conditions estimated by use of microthermometric data obtained from fluid inclusions in quartz, sphalerite and calcite in hydrothermal veins are discussed. These data are also used to calculate the fluid composition in order to discuss metal mobility and depositional mechanisms of mineralization relative to the brittle faulting events. Fluid composition and stable isotope geochemistry of carbonates are used to infer potential sources of the Cu-Zn-bearing hydrothermal fluids.

Geological setting

Vanna is a coastal island located in the Neoarchaean-Palaeoproterozoic West Troms Basement Complex (WTBC) in northern Norway (**Fig.** 1; Bergh et al. 2010). This basement province is located west of, and structurally below, the much younger Palaeozoic Caledonian thrust nappes (Augland et al. 2014; Roberts and Lippard 2005), which to the east are down-faulted several km by the regional Vestfjord-Vanna Fault Complex (**Fig.** 1; Olesen et al. 1997; Indrevær et al. 2013). The WTBC (**Fig.** 2) is composed of segmented crustal blocks of tonalitic, trondhjemitic to granitic gneisses (2.9-2.6 Ga) overlain by supracrustal units (2.8-1.9 Ga; Armitage and Bergh 2005; Myhre 2011; Myhre et al. 2013), and intruded by felsic and mafic igneous rocks (c. 1.8 Ga; Bergh et al. 2010; Corfu et al. 2003). In the north of the WTBC, on the islands of Ringvassøy and Vanna, mafic dike swarms (2.4 Ga) intruded the basement gneisses (Kullerud et al. 2006).

In southern parts of Vanna (**Fig.** 3), a para-autochthonous meta-sedimentary sequence, the Vanna Group, unconformably overlies the basement gneisses (Binns et al. 1980; Johansen 1987). Its age is constrained by the older 2.4 Ga dikes present below the unconformity, and an intrusive diorite sill in the meta-sedimentary rocks dated at 2.2 Ga (Bergh et al. 2007). The Vanna Group meta-sedimentary rocks are composed of arkosic, shallow deltaic sandstones and calcareous mud- and siltstones (Binns et al. 1980; Johannessen 2012). These cover units and the tonalitic basement in Vanna were all affected by contractional deformation and low-grade metamorphism (greenschist facies) during the Svecofennian orogeny (c. 1.8-1.77 Ga) and/or during younger Caledonian tectono-thermal events (Bergh et al. 2010; Bergh et al. 2007; Dallmeyer 1992; Myhre et al. 2013). The Svecofennian event produced a foreland fold and thrust belt in Vanna (Bergh et al. 2007), which in the northern part of the island included the Skipsfjord Nappe (Binns et al. 1980; Opheim and Andresen 1989; Rice 1990). The Skipsfjord Nappe consists of repeated thrust sequences of locally highly strained and mylonitized basement tonalites, alternating with lenses/sheets of relict Vanna Group meta-sedimentary rocks, and sheared mafic and felsic intrusive rocks. Its thrust contact to autochthonous gneisses is exposed in the south at Skipsfjorden and Slettnes (**Fig.** 3).

In the northern part of Vanna island (**Fig.** 3), the Skipsfjord Nappe is down-faulted in the hanging wall by the VBF (Bergh et al. 2007; Opheim and Andresen 1989). This fault is a splay fault to the regional, ENE-WSW trending, zigzag-shaped Vestfjord-Vanna Fault Complex (**Fig.** 2) that bounds the WTBC horst against Caledonian nappes to the east (Forslund 1988; Olesen et al. 1997; Indrevær et al. 2013, 2014). Offshore to the northwest the WTBC horst abuts against the Troms-Finnmark Fault Complex (Indrevær et al. 2013) (**Figs.** 1 & 2). The WTBC horst and its bounding normal faults all formed during incipient rifting of the North Atlantic Ocean in the Early Permian-Triassic (**Fig.** 1; Blystad et al. 1995; Mosar et al. 2002; Faleide et al. 2008; Davids et al. 2013, 2018; Gabrielsen and Braathen 2014; Koehl et al. 2018a, b), and this rifting event affected the entire North-Norwegian passive continental margin (Mosar 2003).

The present study focuses on a mineralized segment (**Fig.** 4) of the VBF (Opheim and Andresen 1989) that hosts Cu-Zn mineralization. The VBF is a brittle oblique-normal fault striking ENE-WSW and dipping c. 50-60° to the SSE. It separates variably deformed Neoarchaean tonalitic gneisses intruded by mafic dikes (2.2-2.4 Ga), diorite and gabbro, in the footwall from mylonitized tonalites and meta-sedimentary rocks of the Skipsfjord Nappe in the hanging wall, with a minimum vertical throw in the order of 2-3 km (Opheim and Andresen 1989). A section through the VBF shows a < 100 m wide fault complex including fault gouge core and damage zones. K-Ar illite dating and $^{40}Ar/^{39}Ar$ dating of K-feldspar in the fault gouge core yielded Late-Carboniferous (348.5 Ma) through Early Permian (283.9 Ma) ages (Davids et al. 2013, 2018), concurrent with known periods of incipient rift-margin extensional faulting and associated fluid infiltration and reactivation (Indrevær et al. 2014; Davids et al. 2018).

We analyse the VBF and its mineralized sections, and attempt to resolve its role as a pathway for hydrothermal fluids and the conditions that caused ore mineral deposition along the VBF. The results may have important implications for understanding ore genesis and for exploration purposes of Cu-Zn deposits in northern Norway.

Methodology

Field work and drill core data

Fieldwork (c. five days) and structural analysis of the VBF focussed on characterization of the fault core and damage zones surrounding the mineralized fault segment and adjacent host rocks. These studies were combined with four days of detailed core logging of c. 880 m of non-oriented drill cores bored by Store Norske Gull (SNG) in 2012, to identify and describe fault rocks, fabric domains, and cross-cutting relationships of fabrics and hydrothermal veins. Sixty-one drill core samples and five outcrop rock samples were collected from the VBF core zones, damage zones, hydrothermal mineralized veins, and the surrounding host rocks. Microtextural analysis of polished thin-sections was undertaken using conventional transmitted and reflected light microscopy. We used an existing dataset obtained by SNG of 783 drill core assays (0.15-2 m sample length) of host rocks, fault rocks, and mineralized hydrothermal veins analysed by ALS-Geochemistry Analytical Lab. This dataset contains analyses of whole rock geochemistry (analysed fused pellets using XRF) and a 48-element suite (analysed using four-acid digest and ICP-MS finish). Samples with ore grade Zn and Cu (> 10 000 ppm) were re-analysed using sodium peroxide fusion with an ICP-AES finish.

Scanning electron microscope data

Scanning electron microscope (SEM) analysis including energy-dispersive X-ray spectroscopy (EDS), electron backscattered diffraction (EBSD), and cathodoluminescence (CL), was used to determine mineral chemistry, mineral parageneses, mineralogical changes, e.g. zonation in hydrothermal quartz, and textural relationships. The thin sections were coated with a thin carbon layer to avoid charging effects. All the analyses were carried out using a Zeiss Merlin VP Compact field emission SEM equipped with an X-max^{80} EDS detector and a Nordlys EBSD detector, both provided by Oxford Instruments, as well as a Zeiss variable pressure secondary electron (VPSE) detector for CL imaging. The VPSE detector uses the CL signal and produces an image close to panchromatic CL under high vacuum conditions (Griffin et al., 2010). EDS measurements were done at 20 kV acceleration voltage and a 60 µm aperture size. For EBSD, the sample was tilted to 70 degrees; 20 kV acceleration voltage and a 240 µm aperture was applied. A step-size of 5 µm was chosen for EBSD mapping and a minimum number of 6 detection bands was applied for indexing. The AZtec software by Oxford Instruments was used for data acquisition further post-processing of the EDS and EBSD data. Backscatter images (BSE) were acquired under the same conditions as EDS measurements. For VPSE imaging an acceleration voltage of 20 kV was applied as well as an aperture of 120 µm. The vacuum conditions were higher than

$1x10^{-5}$ mbar within the sample chamber. EDS chemical analysis of chlorite in fault rocks was used to estimate formation temperatures based on tetrahedral site occupancy (Cathelineau, 1988), which is accurate to within 30°C. EDS measurements were standardised using a cobalt standard.

X-ray diffraction data

X-ray diffraction (XRD) analyses were performed on consolidated fault rocks (cataclasites) to determine mineralogy of very fine-grained samples. The analyses were conducted at the University of Zagreb on a Philips PW 3040/60 X'Pert PRO powder diffractometer (45 kV, 40 μA), with CuKα-monochromatized radiation (λ = 1.54056 Å) and θ-θ geometry. The area between 4 and 63° 2θ, with 0.02° steps was measured with a 0.5° primary beam divergence. Compound identifications were based on a computer program X'Pert high score 1.0B and literature data.

Fluid inclusion data

Fluid inclusion data were obtained from double polished wafers (100-250 μm thick) of hydrothermal quartz, sphalerite, and calcite. Homogenisation temperatures (T_h), halite melting temperatures (T_s), final ice melting temperatures ($T_{m\,Ice}$), and eutectic temperatures (T_e) were recorded using an Olympus BX 2 microscope coupled with a Linkam THMS 600 heating and cooling stage operating between -180 and +600°C at UiT-The Arctic University of Norway. Fluid inclusions were classified according to Roedder (1984) and Sheperd (1985). Salinities of the H_2O-NaCl-$CaCl_2$ system were calculated in NaCl+$CaCl_2$ weight percent using known eutectic temperature as well as halite and ice melting temperatures (Bodnar and Vityk 1994; Steele-MacInnis et al. 2011). In addition, qualitative measurements of key elements and complexes present in the hydrothermal fluid were obtained by decrepitating fluid inclusions (c. 500°C for 3-4 minutes) and analysing the resulting evaporate mounds formed on the sample surface using SEM/EDS technique according to the procedure modified after Kontak (2004). We performed both spot analysis of specific mineral phases and a map scan over the whole evaporate mound.

Stable isotope data

We achieved twenty-two $\delta^{13}C$ and $\delta^{18}O$ stable isotope analyses of hydrothermal calcite veins, calcite from host rock mica-schists in the Skipsfjord Nappe hanging wall to the VBF, and calcites from veins and hydrothermal breccia adjacent to an intrusive diorite sill in the Vanna Group farther south (see **Fig.** 3 for location). These analyses were obtained using a Thermo-Fisher MAT253 IRMS with a Gasbench II at UiT (site.uit.no/sil). Samples were placed in 4.5ml Labco vials, then flushed with He, and 5 drops of water free H_3PO_4 were added manually with a syringe. The results were normalised to Vienna Pee Dee Belemnite (VPDB) standard by three in-house standards with a wide range of $\delta^{13}C$ and $\delta^{18}O$ values, and reported with an uncertainty of standard deviation ≤ 0.1 ‰.

Results

Fault geometry and textural subdivision

From a regional perspective, the VBF is discernible on ortho-photos and digital elevation maps as an ENE-WSW trending linear valley between Vannareid and Burøysund on the island of Vanna (**Fig.** 3). The fault itself is partly exposed in a road section in this valley (**Fig.** 4), but is otherwise mostly covered by glacial and valley debris. The surrounding basement gneisses in footwall and meta-psammites and schists of the Skipsfjord Nappe in hanging wall, are however, well exposed along the shores of Vanna both to the east and west. Where exposed, splays of the VBF strike ENE-WSW and dip 45-50° to the SSE (**Fig.** 4; Opheim and Andresen 1989; Monsen 2014). The foliation of the quartz-mica schists in the hanging wall of VBF strikes mostly ENE-WSW and dips gently to the NNW, but adjacent to the VBF the foliation on a large scale is tilted to a c. 50° dip to the SSE. This change in dip may be due to drag folding caused by normal, down-to the SSE movement of VBF.

This study focuses on the mineralized part of the VBF (**Figs.** 4 & 5). The surface expression of the fault is a scarp with c. 10 m thick core zone that can be followed for c. 25 m along strike. In outcrop, the fault zone is pronounced (**Fig.** 6A) and made up of pale green chlorite-rich proto- and ultracataclasite cut by networks of irregular quartz and calcite veins with sphalerite and chalcopyrite (**Fig.** 6B). Where exposed, the fault surface itself is planar and coated with green-coloured chlorite and epidote (**Fig.** 6A). Local presence of epidote slickenside fibres indicate normal-oblique, down-to the SSE movement along the fault.

Combined surface mapping, logged drill-core, and petrographic data show six textural domains across the c. 120 m thick VBF (**Fig.** 5). These include two fault core zones (**Fig.** 5; domains A1 & A2), characterized by various types of cataclastic fault rocks (**Figs.** 6 & 7), and two damage zones (**Fig.** 5; domains B1 & B2), with complex internal veins and fracture networks (**Figs.** 8 & 9). The remaining domains, domain C and domain D, occur in the surrounding host rocks of hanging wall (**Fig.** 10) and footwall, respectively. Notably, the fracture networks in both core and damage zones contain an extensive number of hydrothermal quartz-calcite veins with pronounced Cu-Zn mineralization (**Fig.** 11), described below.

Domain A1 (core zone) is c. 15 m thick and the principal fault core zone located in the footwall, at the contact between host rocks of tonalitic gneiss and a gabbroic dike. It is characterized by multiple generations of cohesive cataclasites with 20-50% sub-rounded, polymict clasts of tonalite gneiss, older cataclasite, sphalerite, and quartz in a pale green fine-grained quartz-chlorite matrix (**Figs.** 7 & 11A). Multiple generations of hydrothermal veins are identified within the cataclasites of domain A1 and make up c. 60 % of the material in this core zone (**Fig.** 11A).

In thin section, the cataclasites have a dismembered texture with sub-rounded to rounded, consolidated clasts of at least two generations of fine-grained cataclasite embedded as new clasts within a third generation (**Fig.** 7A-C). The matrix of all generations of cataclasite is microcrystalline with internal grain size of 0.1 to 5 mm, and composed of quartz (c. 98 %), chlorite, microcline and minor albite and cookeite (based on XRD and SEM analyses).

Along strike farther west, the texture and mineralogy of core zone A1 changes and is a c. 15 m wide complex cataclasite containing decimetre-sized clasts of mainly calcite and sphalerite cemented by calcite veins (**Fig.** 11B).

Domain A2 (core zone) defines a c. 4 m thick cataclasite zone, which is texturally similar to that of domain A1, but which affected weakly foliated tonalite gneiss host rocks of the footwall. This domain has the same types and amount of cohesive cataclasites and surrounding matrix components as domain A1 (**Fig.** 7), and also contain an extensive network of hydrothermal veins ranging in width from 1 mm to >1 m, which makes up c. 60% of the material in this zone. This vein material is are also present as matrix cement enclosing rounded to sub-angular, polymict clasts of embedded older cataclasite, tonalites, and fractured hydrothermal quartz and sphalerite grains (**Figs.** 11C & D). In addition, this core zone contains abundant networks of pale green ultra-cataclasites with internal banding (**Figs.** 8A-D & 11C-D). Thin section observations show that the apparent banding of the ultracataclasites is caused by minor variations in grain size (**Figs.** 8A-B), and that these ultra-cataclasites fill open space between quartz veins (**Fig.** 8C), and/or define consolidated sub-angular clasts within quartz breccias (**Figs.** 8 D-E & 11C). Acicular grains observed within the ultra-cataclasites (**Fig.** 8E) suggests grain-growth and that the original grain size was smaller.

Domain B1 (damage zone) is c. 40 m thick and located in tonalitic gneisses of the footwall to the VBF. It defines a link zone or fracture corridor between core zones A1 and A2 (**Fig.** 5), and is characterized by heavily fractured, weakly foliated tonalite gneiss with narrow (<60 cm thick) localized cataclastic zones parallel to the main and subsidiary fault surfaces of the VBF. Most of the fractures are infilled with multiple cross-cutting stock work veins (**Fig.** 11E), ranging in thickness from 1 mm to c. 80 cm.

In thin section, the relict gneiss foliation in the tonalitic gneiss host rock is observed as of 1-2 mm long composite bands of muscovite (**Fig.** 9C). This fabric is cut at a low angle by semi-brittle, chlorite-rich shear bands (**Figs.** 9A-C), indicating the fracturing produced a retrogressed shear band texture. Larger (<2 mm) plagioclase grains have commonly healed microfractures filled by microcrystalline quartz and chlorite; some are dilated by hydrothermal veinlets (**Fig.** 9C).

Domain B2 (damage zone) is c. 15 m thick and present in the footwall of core zone A1 (**Fig.** 5). This fractured zone is located mainly within a thick, foliated meta-gabbro dike, and it is truncated by networks of irregular brittle fractures, locally with narrow (<40 cm thick) cataclasite zones. Most of the fractures are filled by chalcopyrite-bearing quartz and calcite veins (**Figs.** 11F & G). In contrast to the damage

zone of domain B1, the quartz veins define parallel sets of sheeted veins close to the core zone, changing texturally into stock work vein networks with a more random orientation when farther from the core zone.

The typical mode of the foliated meta-gabbro identified in thin section is 70 % dark green, strongly pleochroic amphibole, 20 % partly sericitised plagioclase, 10 % fine-grained quartz as well as trace magnetite, garnet and ilmenite. In the fractured meta-gabbro, amphibole and ilmenite/magnetite grains are partly to completely replaced by chlorite, quartz, anorthite feldspar, and minor pyrite, titanite, apatite and rutile. Hydrothermal alteration of the meta-gabbroic host rock is outlined texturally as haloes along contacts to quartz veins and stock networks (**Fig.** 11F).

Domain C (hanging wall) represents the down-dropped hanging wall strata of the Skipsfjord Nappe (**Fig.** 5) with strongly foliated quartz-mica schists and intercalated mafic schists and lenses (**Fig.** 10A). In contrast to the core and damage zones of the VBF, the hanging wall schists are less fractured and comprise no Cu or Zn bearing hydrothermal mineralization (**Fig.** 5). The contact with cataclasites of the VBF itself (**Fig.** 5, domain A2) is marked by a narrow c. 1-2 m thick zone of unconsolidated, green-coloured fault gouge with sub-rounded clasts of quartz (≤ 1 cm) in a fine-grained, clay-rich matrix (**Fig.** 10B), made of illite and smectite–vermiculite (cf. Davids et al. 2013). This gouge zone is irregular in shape and may disappear along strike, but where present, it truncates (post-dates) the cataclasites of domain A2. No hydrothermal veining or mineralization is observed in the gouge material.

In thin section, alternating layers of recrystallized quartz (50%), white mica (40%), and plagioclase (10%) make up the ductile foliation of the Skipsfjord Nappe schists with accessory tourmaline (dravite), apatite, and uranothorite. The foliation itself shows clear evidence of internal shearing, by sigmoidal quartz porphyroblasts, mica fish and remnants of intrafolial tight folds (**Fig.** 10C). These ductile fabrics are all truncated by the brittle VBF.

Domain D (footwall) represents weakly foliated basement tonalite gneiss in the footwall to the VBF. This domain is weekly fractured and contain no significant mineralization.

Hydrothermal veins hosting Cu-Zn mineralization

Hydrothermal networks of Cu-Zn-mineralized quartz and calcite veins exist in variable amounts and geometric relationships both in the core (domains A1-A2) and damage zones (domains B1-B2) of the VBF (**Fig.** 11). In the core zones, matrix-bearing cataclasites are the main mineralized zones, whereas in the damage zones, secondary quartz and calcite are present as mineralized stock-work and/or parallel/sheeted veins. Notably, complex and multiphase microtextural and cross-cutting relationships of the Cu-Zn bearing veins are observed (**Figs.** 11H-L). These relations provide the basis for evaluating temporal and mineralogical changes of the hydrothermal veins/fluids. By use of such criteria, we propose a succession of veining from early to late-stage as: (i) quartz-sphalerite (QS) veins (10-30 mm

wide; **Fig.** 11A), (ii) quartz-chalcopyrite (QCp) veins ± calcite (1 mm to 1 m wide; **Figs.** 11C, D, F & G), (iii) calcite (Ca) veins (5 mm-1 m wide; **Fig.** 11B), and (iv) minor narrow (<10 mm wide) quartz-calcite-fluorite-sulfosalt veins (QCF) (**Figs.** 11H, I). Further details of these vein types are as follows:

QS veins (stage i) are mainly restricted to core zone A1 (**Fig.** 5) and are characterised by euhedral, zoned and massive quartz associated with sphalerite mineralization (**Figs.** 11A, H & I). Sphalerite is brown to deep orange in colour (**Figs.** 11A, B & H), commonly colour zoned, and is observed both as small (<1 mm) inclusions within larger (<10 mm) quartz grains and as interstitial material between quartz grains (**Fig.** 11I). In addition to vein style mineralization (**Fig.** 11H), individual grains of quartz and sphalerite are partly dismantled and now present as clasts within even younger generations of cataclasites (**Figs.** 11A-B & J-L), and truncated by a younger generation of quartz-chalcopyrite veins (QCp veins; **Figs.** 11J-L). These textural relationships indicates that the QS veins are the earliest observed hydrothermal veins.

QCp veins (stage ii) are composed of quartz and chalcopyrite with minor calcite. They are the most voluminous and spatially most extensive generation of quartz veins, and are in contrast to QS veins present in both the core and damage zones. Within the core zones (Domains A1, A2) quartz of the QCp veins exist as fine-grained matrix and as massive to euhedral grains in a hydrothermal breccia, enclosing rounded to sub-angular, displaced polymict clasts of basement tonalite gneiss, injected cataclasite (**Fig.** 11C), and earlier generations pf hydrothermal quartz and sphalerite (QS veins; **Fig.** 11A). Within the damage zones (Domains B1, B2), these quartz-chalcopyrite veins define cross-cutting stockwork-veins or parallel sets of sheeted-veins (**Figs.** 11E-G). In both cases, chalcopyrite is commonly deposited as a rim around clasts or at the inner edges of the veins (**Fig.** 11C), in direct contact with Fe-bearing minerals like chlorite or pyrite, or in contact with chlorite-rich cataclasite (**Figs.** 8C & 11D)

Notably, within the core zone of domain A2, multiple repeated quartz veins and injected ulatracataclasites are observed (**Figs.** 8A, B), outlined by euhedral quartz grains growing from the vein wall and having zoned cores and feathery/plumose textures on the rims (**Figs.** 8C-E). In addition, injected cataclasite is also present as fracture infill (**Fig.** 8D) and as matrix within broken hydrothermal quartz clasts (**Fig.** 8E). Multiple criss-cross networks of QCp veins exist, but an attempt to separate them into further generations and/or sub-stages has not been succesful.

Ca veins (stage iii) are characterised by various barren carbonate (calcite) veins cross-cutting previous generations of veins, or in conjunction with minor sphalerite and chalcopyrite. Calcite, however, is also present in all other vein types, where it represents the last infill stage in veins, and such calcite clearly post-dates the deposition of sphalerite (**Figs.** 11J-L), since sphalerite grains are fractured and show a jig-saw pattern. Calcite matrix observed in a coarse-grained breccia at the top of core zone A1 (**Fig.** 11B) with a high number of sphalerite clasts is also interpreted to be a late phase Ca vein. However, the lack of cross-cutting relationship with QCp veins makes this interpretation uncertain.

QCF veins (stage iv) are the youngest veins observed in the VBF, and they are only identified locally in core zone A1. These are narrow veins (<4 mm) of equant grains of massive quartz, calcite, fluorite and notably with Pb-As-Ag-Bi sulphides (**Figs.** 11J-L). This vein type will not be analysed further because of its limited spatial extent.

Alteration mineralogy and chlorite geochemistry

The secondary minerals associated with each of the above described vein types is commonly expressed as alteration haloes along rims of quartz-veins, but the mineral assemblages changes as these veins extended into different host rock types. Chlorite is the dominant alteration mineral and gives the altered rocks a pale green colour. In cataclasites, chlorite is found in close association with the main gangue minerals such as quartz and calcite, but also with minor albite, clinozoizite, titanite, rutile, apatite and cookeite. In tonalite host rock gneisses of the footwall to VBF, chlorite (±titanite) replaces host rock biotite and amphibole. Some epidote alteration of feldspar is also observed. In the gabbroic dike host rock tabular amphibole is replaced by chlorite and titanite/rutile; most feldspar is partly or fully replaced by epidote/clinozoizite; and ilmenite/magnetite is partly replaced by pyrite/chalcopyrite and titanite (**Fig.** 12). XRD analyses of very fine-grained ultracataclasite rocks show that quartz, chlorite, chalcopyrite and minor aggregates of microcline have completely replaced the original mineralogy.

We analysed the mineral chemistry of fine-grained chlorite present as matrix in cataclasites in core zones A1 and A2 of the VBF (**Fig.** 13), with an aim to estimate temperature of the hydrothermal alteration (Table 1). Chlorites were selected for analysis based on textural proximity to Cu-Zn bearing veins, to ensure that they were formed synchronously.

The chemical composition classifies the chlorite as clinochlore to chamosite (Table 1), with formation temperatures ranging from 280-305°C ± 30°C (Cathelineau, 1988). For example, chlorite analysed from surface outcrops of cataclasite in core zone A2 indicated a temperature of 280°C (**Fig.** 13A), whereas analysed chlorite from core zone A1 in drill cores at 70 m depth yielded a temperature of c. 295°C. In addition, at 93 m depth in domain B2, two generations of chlorite in the gabbroic host rocks (**Fig.** 13B) displayed a drop in the Mg/Fe ratio from core to rim, where the Mg-rich chlorite in the core indicates a formation temperature of 285°C, while the Fe-rich rim indicates growth at 305°C (cf. Table 1).

Fluid inclusions

The fluid inclusion study was conducted on quartz, calcite, and sphalerite from three generations of hydrothermal veins (i.e, QS veins, **Fig.** 14A; QCp veins, **Fig.** 14B; and Ca-veins, **Fig.** 14C). The microthermometric measurements were used to determine the salinity and density of the hydrothermal fluids that circulated along VBF as well as to indicate P-T-X conditions during faulting events. Further, the resulting fluid properties are used to infer the metal solubility potential of the ore-forming fluids and investigate the depositional mechanisms.

Fluid inclusion petrography

Primary fluid inclusions occur along growth zones and within isolated clusters. Primary fluid inclusion assemblages are usually cross-cut by trails of less common pseudosecondary and secondary inclusions (**Fig.** 14K). The microthermometry was conducted only for primary and pseudosecondary fluid inclusions, whereas a small size of secondary inclusions (<2 μm) precluded reliable measurements. Based on their petrographic characteristics, primary and pseudosecondary inclusions from all three generations of veins can be divided into three types:

Type 1 represents primary multiphase (liquid-vapour-solid) inclusions (**Fig.** 14D) containing an aqueous liquid (70 vol. %), a vapour bubble (15 vol. %), and a cubic solid phase (halite) (15 vol. %). Occasionally, assumed incidentally entrapped phases of elongated/tabular or fibroradial minerals are also observed (**Fig.** 14E). Type 1 inclusions are generally sub-rounded or with negative crystal shapes. These inclusions are found in all vein-types, but mostly in QS veins, in both quartz (**Fig.** 14D) and sphalerite (**Fig.** 14F). In QCp veins they are much less frequent and are hosted within the cores of euhedral and zoned quartz. Type 1 inclusions are also found in Ca veins.

Type 2 inclusions are also primary in their origin but, in contrast to Type 1, they do not contain a cubic solid phase. According to their petrographic properties, inclusions of this type can be divided into two subtypes, Type 2a and 2b. Type 2a inclusions are two-phase inclusions (liquid-vapour) that have sub-rounded to negative crystal shapes and contain a liquid phase (80 vol. %) and a vapour phase (20 vol. %; **Figs.** 11G & H). Type 2a inclusions are found in sphalerite and in calcite. Type 2b inclusions are irregularly shaped and can in addition to liquid (75-80 vol. %) and vapour (15-20 vol. %) also contain between <1 to 10 vol. % of solid phase (s) that are irregular, tabular, or radiating tabular in shape (**Figs.** 14I & J). Type 2b inclusions are found in quartz from both QS and QCp vein.

Type 3 inclusion are pseudosecondary inclusions grouped in narrow trails of coexisting, small (<20 μm), L+V and monophase L-only inclusions (**Fig.** 14K). The L+V inclusions have c. 90-98 vol. % liquid and 2-10 vol. % vapour, while L-only inclusions (at room temperature) commonly developed a vapour bubble during the freezing cycle. Type 3 veins are found in QS vein quartz.

Fluid inclusion microthermometry

Microthermometric measurements were performed on fluid inclusions in quartz, calcite and sphalerite, but the most numerous data, however, were obtained from fluid inclusions in quartz, because they are generally larger and easier to measure accurately. By contrast, fluid inclusions in sphalerite were usually too dark for phase changes to be observed, whereas calcite-hosted inclusions are too small (<20 μm).

During the freezing cycle, all fluid inclusions were undercooled to -100 to -130°C. Upon heating, frozen inclusions would turn dark brown around -80°C followed by first melt occurring around T_e of around -52°C indicating a fluid composed of H_2O-NaCl-$CaCl_2$ (cf. Roedder 1984; Steele-MacInnis et al. 2011).

Fluid inclusions in the of H_2O-NaCl-$CaCl_2$ system are notorious for metastable behaviour, which includes absence of phases that are expected to be present and occurrence of phases that are not expected to be present (Chu et al., 2016). In the following, we will describe the behaviour of each type of fluid inclusion and also note assumptions, possible metastable behaviour, and present alternative calculations for salinities. Despite uncertainties in the salinity calculations, the accuracies of the salinities presented is acceptable within the scope of this paper.

Type 1 (L+V+H) inclusions froze to a dark fine-grained mass during the freezing cycle. When heated the inclusions would turn dark brown around -80°C followed by first melt occurring around T_e of around -52°C. Ice, observed as a globular transparent phase, melted over a large range of temperatures from -52.3 to -37.5°C. It is assumed that antarcticite that melts at the eutectic temperature. Upon further heating, the isotropic solid in Type 1 inclusions melted around +70 to +151°C, and total homogenisation was characterized by a vapour to liquid transition in the temperature range from +70 to +239°C. The elongated solid in was insoluble up to 400°C. Based on the eutectic temperature of -52°C, total salinities are expressed as NaCl + $CaCl_2$ wt. % according to Steele-MacInnis et al. (2011). The total salinity for Type 1 inclusions was calculated from the peritectic $T_{m\,Ice}$ and final melting temperature of halite (T_s) based on the methods of Vanko et al., (1988). This resulted in salinities (33-36 wt. % NaCl+$CaCl_2$; Table 1). However, it should be noted that in some Type 1 inclusions, poor optical properties hindered accurate measurement of $T_{m\,Ice}$ and for these inclusions salinities are calculated based on ice (and antarcticite) melting at the eutectic; this assumption yields higher salinities (up to 5 wt. % NaCl+$CaCl_2$) and higher NaCl/$CaCl_2$ ratios (up to 0.5). Further, salinities for Type 1 inclusions can also be calculated as NaCl wt. % equivalents using halite melting temperatures according to Bodnar and Vityk (1994); such a calulation would yield salinities in the range of 27 to 30 wt. % NaCl equivalents. $T_{m\,Ice}$ temperatures observed below the eutectic possible for the $CaCl_2$ system (< -52°C; Steele-MacInnis et al. 2011) were interpreted as metastable (Wilkinson 2001). Salinities for these inclusions were calculated based on $T_{m\,Ice}$ of -52°C.

Type 2 inclusions showed two styles of freezing when cooled; 1) the inclusion froze to a dark fine-grained mass; or 2) the inclusion did not freeze and no phase transitions was observed. No correlation between the content of the fibroradiate solids and freezing style was observed. Upon warming the frozen inclusions would turn dark brown around -80°C followed by first melt occurring around T_e of around -52°C. Ice, observed as a globular transparent phase, melted over a large range of temperatures from -54.4 to -18.3°C. Total homogenisation occurred by a vapour to liquid transition in the temperature range from +35 to +220°C. The various fibroradiate solids observed in Type 2b inclusions were insoluble up to 400°C. Salinities were calculated as wt. % NaCl + $CaCl_2$ according to Steele-MacInnis et al. (2011; Table 1). It was not possible to identify which phase melted at the eutectic, antarcticite or hydrohalite, however, the differences in salinity (< 0.2 wt. % NaCl+$CaCl_2$) and NaCl/$CaCl_2$ ratios (<0.03) calculated for either option is negligable. In addition, metastable behaviour is

suspected for inclusions where no freezing behaviour was be observed (Chu et al., 2016). Alternatively, it is possible that freezing in these inclusions were hindered by small amounts of lithium in the fluid (Dubois et al., 2010).

Type 3 inclusions showed similar microthermometric behaviour to Type 2 inclusions; first melting was observed at T_e, and $T_{m\,Ice}$ occurred at -48.2 to -40.3°C, resulting in salinities of 28.6-30.6 wt. % NaCl + $CaCl_2$. The majority of Type 3 inclusions were liquid only at room temperature, but several developed vapour bubbles during freezing and T_h occurred by vapour to liquid transition at 19 to 36°C.

The microthermometric results of fluid inclusions in quartz, sphalerite and calcite from QS, QCp and Ca veins is summarised in Table 2 and **Fig.** 15A. **Fig.** 15A displays the last phase melting temperature on the X-axis; for Type 1 inclusions this is the cubic solid (halite), and for Type 2 and 3 inclusions ice melting ($T_{m\,Ice}$) is the last phase observed. Homogenisation temperatures (T_h) are plotted on the Y-axis. All together, the multiphase, two-phase and monophase fluid inclusions show that the fluids were low- to moderate temperature (<240°C) and moderate to highly saline (13-37 wt. % $CaCl_2$ + NaCl). **Fig.** 15B plots total salinity versus T_h and two clusters of fluid inclusions; Type 1 inclusions with higher salinities (33-36 wt.% NaCl+$CaCl_2$) and Type 2 and Type 3 inclusions with lower salinities (20-31 wt.% NaCl+$CaCl_2$). A salinity gap from c. 31-33 wt. % total salinity separates Type 1 from Type 2 and Type 3 inclusions in the **Fig.** 15B. This gap could be caused by metastability by failing to nucleate NaCl near the saturation point (Roedder, 1984), or it could be a result of the assumptions used to calculate the salinities of Type 1 inclusions as outlined above.

The temporal relationships between the vein-types as established by the cross-cutting relationships above are also included in the legend of **Fig.** 15B, and the data displayed are described accordingly. Overall the dataset shows a general positive correlation between total salinity and T_h. This positive correlation is also observed in sphalerite-hosted inclusions in QS veins (Type 1 and Type 2a) that show a weak positive correlation between total salinities (27-35 wt. % NaCl+$CaCl_2$) ranging over a rather narrow temperature range (155-218°C). Quartz-hosted inclusions (Types 1 and 2b) from QS veins are also highly saline inclusions (25-36 wt. % NaCl+$CaCl_2$) that homogenise over a larger T_h span (70-205°C). Inclusions in individual QS quartz veins (displayed as light and dark green colours) show overlap, however the light green vein has more inclusions with higher salinities than the vein plotted with darker green. Quartz hosted inclusions from QCp veins show two trends, the pale grey vein (inclusion type 1 and 2b) show similar T_h and salinities to those from QS veins. The pale blue and dark blue coloured dots representing Type 2b inclusions show relatively narrow range of salinities (25-31 wt.% NaCl+$CaCl_2$) over a large range of T_h (35-210°C). Type 3 pseudosecondary inclusions from QS veins show a weak overlap with these low-temperature Type 2b inclusions from QCp veins. Type 1 and 2a inclusions from Ca veins show the largest range in salinities (20-36 wt. % NaCl+$CaCl_2$), also with a positive correlation with T_h (94-175°C).

Fluid inclusion decrepitation

Qualitative chemical analyses of major elements in fluid inclusions in quartz were carried out by decrepitating individual inclusions and analysing the evaporate mounds formed on the sample surface (**Fig.** 16). SEM spot analyses of individual crystals enabled us to identify three major phases in the mounds: NaCl, $CaCl_2$, and $CaSO_4$ (anhydrite/gypsum; **Figs.** 16A, B). SEM map-scan analyses are presented in **Figs.** 16C-F and highlight the chemical composition of the mounds. Relative concentrations of Na, Ca, K, Cl and S are plotted in **Fig.** 17, and show two general trends based on the sulphur content: (1) mounds with varying amounts of Na, Ca, S, Cl and very minor K (e. g.); (2) mounds without S but with Na, Ca, Cl and very minor amounts of K. These trends likely reflect two different fluids.

Hydrothermal alteration of host and fault rocks

In order to resolve geochemical changes in fault and host rocks during deposition of the VBF hydrothermal mineralization, we performed lithogeochemical analyses of unaltered host tonalite gneiss and gabbro from footwall domain D. The obtained data were compared with the data gathered from altered host rock equivalents, including mineralized veins and cataclasites from core zones A1 and A2 (**Fig.** 5). The lithogeochemical data were used for construction of isocon diagrams (**Fig.** 18), following the method proposed by Grant (1986). In the diagrams, Al_2O_3 and TiO_2 are considered immobile and are for each sample used to delineate a second reference line, which takes into account apparent depletion of elements in the host rock when injected by hydrothermal quartz and calcite veins.

Separate isocon diagrams are constructed for the alteration of host rock tonalite gneiss (**Fig.** 18A) and gabbro (**Fig.** 18B), respectively. For both rock types, similar mobility trends are observed for ore-bearing elements: Zn and Cu are the major metals hydrothermally added to the system, together with minor amounts of S, Pb, As, Bi, Cd, Li, Ag and trace Sb. On the other hand, the major elements (expressed as oxides) show much larger variations; e.g. Na_2O is depleted in both of the altered host rocks of core zones A1 and A2, relative to unaltered host rocks (domain B2), whereas MgO and Fe_2O_3 is enriched. Other oxides like K_2O are slightly depleted in altered tonalite gneiss and enriched in altered gabbro, while MnO show opposite trends in altered tonalite gneiss versus gabbro, respectively.

$\delta^{13}C$ and $\delta^{18}O$ stable isotope data

Stable isotope data of calcite from various geological settings on Vanna were analysed, in order to infer potential sources of CO_2. Analysed samples show a wide range of $\delta^{13}C$ and $\delta^{18}O$ isotope values (**Fig.** 19). The hydrothermal vein calcites from VBF yielded $\delta^{13}C$ values in the range of -5.7 to -4.0 ‰, and $\delta^{18}O$ values from +7.1 to +12.3 ‰, overlapping with igneous carbonates (Taylor et al. 1967). In contrast, calcite from hanging wall Skipsfjord Nappe (for location see **Fig.** 5) shows distinctly higher $\delta^{13}C$ (-1 to +5 ‰) and $\delta^{18}O$ values (+11 to +16 ‰) than hydrothermal calcite in the VBF. Calcite samples from veins and breccia in diorite of the Vanna Group meta-sedimentary rocks (see **Fig.** 3 for location; Bergh

et al. 2007) all yielded $\delta^{13}C$ (-4 to +1 ‰) and $\delta^{18}O$ isotope values (+8 to +12 ‰), i.e. consistently higher than for the VBF calcites, but lower than for calcites in the Skipsfjord Nappe. By comparison, $\delta^{13}C$ (+1 to +5 ‰) and $\delta^{18}O$ (+8 to +10‰) values for calcite cement in meta-sandstones of the Vanna Group (Johannessen, 2012) differ from all the other analysed samples.

Discussion

The data presented above show that the Cu-Zn mineralized zones in the VBF resulted from a multiphase history of fracturing, cataclasis, and hydrothermal vein injections into Neoarchaean gneisses as host rocks and the VBF acting as a conduit for the hydrothermal fluids. Mineral chemistry, fluid inclusion microthermometry, and stable isotope results were used to gain insight into the ore-forming processes and P-T-X conditions during mineralization. Based on these data, a tentative, paragenetic model is proposed for the Cu-Zn mineralization in the VBF (**Fig.** 20), and this model is discussed and argued for below.

Fault zone architecture, evolution and relation to Cu-Zn mineralization

The brittle VBF developed as a normal fault zone affecting Neoarchaean tonalite/gneisses in the footwall and down-faulted Palaeoproterozoic, meta-sedimentary rocks of the Skipsfjord Nappe/Vanna Group in the hanging wall (Bergh et al. 2007). These basement host rocks comprise a main ductile fabric/foliation which formed in a fold-thrust belt system during the Svecofennian orogeny at greenschist facies conditions (Bergh et al. 2007). A younger retrogressive, semi-ductile/brittle tectono-thermal event produced chlorite shear bands that may record the onset of Palaeozoic (Carboniferous-Permian) brittle faulting along the VBF (cf. Davids et al. 2013).

The brittle VBF is composed of two core zones surrounded by damage zones and undeformed host rocks, with fracture networks cemented by quartz-carbonate veins (**Figs.** 5 & 6). The structural evolution of the VBF included up to four stages of brittle normal faulting, hydrothermal veining (**Figs.** 7 & 11), and alteration of the crystalline bed rocks (**Fig.** 12). These events seem to have controlled the Cu-Zn mineralization (as summarized in **Figs.** 20B1-B3). To further, argue for the evolution and relative timing of textures and veins, the structures are discussed chronologically, in terms of pre-, syn-, or post-tectonic relative to the ore-forming processes.

The ductile, pre-ore fabrics of the host rock tonalitic gneisses and quartz-feldspatic schists in footwall and hanging wall of the VBF, respectively, are presumed to be Neoarchaean (ca. 2.7 Ga) to Palaeoproterozoic (c. 1.8 Ga) in age (Corfu et al. 2003; Myhre et al. 2013). These host rocks, however, were affected by networks of truncating chlorite-rich shear bands (**Fig.** 9) that may record the onset of brittle faulting along the VBF.

The initial stages of syn-ore brittle faulting along VBF generated massive proto/ortho-cataclasites in core zone A1 along the contact between the host tonalites and gabbroic dikes (**Figs.** 20A, B1). These

cataclasites were enclosed by a matrix of injected quartz-sphalerite (QS) hydrothermal veins, as evidenced by crosscut relationships (**Figs.** 7 & 11H-L). This early process of brittle fracturing and cataclasis may have increased the porosity of the fault rocks and created space for further hydrothermal fluid flow, and thus suggest that the fault core A1 at least initially acted as a fluid conduit. It is, however, reasonable to conclude that during successive injection of QS vein material, this fault core became partly or fully sealed, thus reducing the permeability and forcing the later fluids to flow into the damage zones (cf. Indrevær et al. 2014).

The next stage in the fault evolution was continued cataclasis and injection of quartz and chalcopyrite bearing (QCp) veins. This significantly more extensive syn-ore faulting and hydrothermal event produced ultra-cataclasites and QCp vein breccia infill that post-dated the QS veins in core zone A1. QCp veins are the first and dominant generation of vein material to be deposited in core zone A2, and also formed as stockwork and sheeted veins in fractures within damage zones B1 and B2 (**Fig.** 20B2), in close association with secondary chlorite, cookeite and microcline in the matrix of the ultra-cataclasites.

The presence of multiple generations of cataclasites and Cu-Zn bearing vein injections, as observed in core zone A2, suggests that the porosity of the fault rocks increased by continued fault movement, and allowed episodic flow of over-pressurised fluids capable of transporting fine-grained, crushed material from elsewhere along the fault. Episodic fluid flow is supported by several phases of injected flow-banded ultracataclasites (**Figs.** 11C, D & J-L) in close spatial relationships to zoned euhedral quartz with plumose textured rims (**Fig.** 8). The matrix between such zoned quartz grains were filled by new injected cataclasite and QCp veins. This abrupt change in texture from zoned quartz cores, where the rate of deposition is considered slow, to plumose quartz textures at the rims, indicating faster rate of silica deposition, may be caused by a change in pressure from lithostatic to hydrostatic due to fracturing along the fault (Fournier and Potter, 1982; Dong et al. 1995; Rimstidt 1997). This process with cyclic opening of a fault due to overpressured fluids is known as seismic pumping (Sibson et al. 1975).

The last main syn-tectonic hydrothermal events (stages iii) affecting the VBF included infill of calcite in QS and QCp veins, growth of calcite as the main gangue mineral in the late cross-cutting barren veins in all fault domains (Ca veins), and possibly also formation of sphalerite-calcite breccias near the rim of core zone A1, although timing of the latter is uncertain. However, textural observations suggest that sphalerite was deposited as part of the early QS vein phase, subsequently brecciated and cemented by latest-stage calcite (see **Fig.** 11B).

Post-ore brittle fault movements along VBF generated unconsolidated fault gauge (**Fig.** 10B) which is observed along the contact with Skipsfjord Nappe rocks, thus separating the Cu-Zn mineralized fault core-damage zones from the non-mineralized hanging wall (**Fig.** 20B3).

Our data show that the VBF acted as a fluid conduit infiltrating permeable fault rocks with reduced host rock strength, during several stages (i-iv) of brittle fracturing and cataclasis. The mapped VBF architecture, and close relation of microtextures and accumulated ore forming hydrothermal veins confirms that Cu-Zn mineralization was controlled by evolution of the fault rocks. The VBF also, clearly must have acted, at least intermittently and locally, as a barrier that helped localization and enrichment of Cu-Zn mineralization. Fluids migrating in the crust may effectively reduce the strength of the rock by increasing the pore pressure and decreasing the frictional resistance (Hubbert and Rubey 1959; Sibson et al. 1975). Changes in pore pressure and frictional characteristics may have occurred along the VBF. For example, the pore pressure may have approached lithostatic values during the syn-ore forming hydrothermal events (**Figs.** 20A, B), as inferred from: (i) growth of euhedral zoned quartz on fracture surfaces, and (ii) injections of multiple generations of flow-banded ultra-cataclasites, likely from reworked fault core rocks. One requirement for fluids to hold fractures open allowing euhedral quartz growth, is a pore pressure that at least, exceeds the confining pressure (Hubbert & Rubey 1959). Conversely, if over-pressurized fluids injected the fault zone, such fluids may have contributed to enhance faulting and further evolution of the fault architecture itself. Therefore, we favour a model of successive and/or repeated supply of over-pressurized hydrothermal fluids, from a variety of sources (**Fig.** 20C), in a tectonic environment characterised by crustal extension and normal faulting (cf. Indrevær et al. 2013, 2014) to explain the complex Cu-Zn mineralization in the VBF.

P-T-X conditions

Temperature constraints during brittle faulting and injection of Cu-Zn-bearing hydrothermal veins are indicated from chlorite geochemistry and by microthemometric measurements of primary fluid inclusions. Homogenisation temperatures measured from spahlerite-hosted inclusions range from 164 to 218°C, and represent the minimum fluid temperature for the ore-bearing fluids during the first mineralisation phases. Combining this data with chlorite geochemistry that indicate formation temperatures of 280-305°C ± 30°C, does provide some additional constraints. However, chlorite geochemistry is extremely sensitive to later overprints and temperature estimates should be treated with care (Vidal et al., 2006). This is exemplified by the prograde overprint shown in **Fig.** 13B (Table 2) where a c. 20°C increase in core to rim is suggests, likely as a result of seismic pumping allowing fluxes of hotter ore-bearing fluids through the fault.

Ideally, formation pressures could be constrained from isochores constructed based on mictrothermometric measurements of fluid inclusions combined with temperature estimates from chlorite geothermometry. However, the steepness of isochores from these highly saline (and dense) fluids, combined with the rather large temperature range (including uncertaincies) in the chlorite geothermometric estimates cannot provide adequate constrainst on the pressure/depth of ore formation. Previous work from Indrevær (2014) who studied several onshore Late Permian normal faults of the Vestfjord-Vanna fault complex in western Troms, containing hydrothermal quartz and K-

feldspar, yielded minimum P-T conditions of 300-275°C and 2.4-2.2 kbar. The temperature range overlap with that estimated from VBF, and we cautiously suggest that similar PT conditions could be used for VBF.

Fluid inclusion data microthermometric measurements suggest that the ore-bearing fluid is composed of H_2O-NaCl-$CaCl_2$ with a general NaCl/$CaCl_2$ ratio of c. 0.3 (Table 2). Regardless of the uncertainties in the accuracy of the salinity calculations, the various calculations show that the fluids are highly saline fluids (20-37 wt. % NaCl + $CaCl_2$). Analyses of evaporate mounds also suggested two different fluid compositions: one fluid with a significant proportion of sulphur, and one without. In addition, isocon diagrams suggests that sulphur was added to the mineralizing system, and we therefore suggest that the ore-bearing fluid also contained sulphur. In addition to sulphur and the ore-forming metals Zn and Cu, the isocon diagrams suggest that the ore-bearing fluid likely also contained (or remobilised) minor amounts of metals including Pb, As, Bi, Cd, Li and Ag (**Fig.** 18).

Redox potential of ore bearing fluids

As suggested above, the ore-bearing fluids at VBF contains sulphur (**Figs.** 16 & 17), but the speciation of sulphur is not known, and depends on whether the fluids have reducing or oxidizing properties. According to Zhong et al., (2015), given a high salinity fluid (>22.6 wt. % NaCl) sulphur would be present as sulphate (SO_4^-) in an oxidising fluid, and as H_2S in a reducing fluid.

At VBF, the alteration of host rock ilmentite to pyrite (**Fig.** 12), and general abundance of sulphide ore minerals suggests that the these minerals were formed under near neutral pH and reducing conditions, further implying that the ore-bearing fluids were reducing. However, fluids circulating in the upper crust with low water/rock ratios are commonly, at least in part, rock-buffered with sulphate is a common component - produced from oxidation of accessory sulphide minerals present in the basement (Bucher and Stober, 2010). In addition, sulphate is identified from the evaporate mounds (**Figs.** 16 & 17); this sulphate could have formed two ways, either it was already present in an oxidising ore-forming fluid, or the sulphur was oxidized to sulphate during the decrepitation process when exposed to atmospheric oxygen.

Two equations below exemplifies the two potential fluids (reducing fluid in equation 1 and oxidizing fluid in equation 2). In Equation 1, zinc is carried as a chloride complex in a reducing fluid and sulphur is present in the form of H_2S. The presence of H_2S in the fluid will destabilise the chloride complex carrying the zinc and significantly reduce the solubility of Zn (by shifting the equation to the right). However, higher salinities will increase the amount of H_2S the fluid can carry without precipitating sphalerite. Reversely, by diluting the fluid the decreasing Cl^- content will shift the equilibrium to the right, and sphalerite will precipitate.

Equation 1: $$ZnCl_{2\,(aq.)} + H_2S_{(aq.)} \rightleftharpoons ZnS_{(s)} + 2Cl^- + 2H^+$$

Equation 2: $ZnCl_{2\,(aq.)} + SO_4^{2-} + CH_4 \rightleftharpoons ZnS_{(s)} + CO_{2(aq.)} + 2Cl^- + 2H_2O$

Equation 2 describes an oxidising fluid that contains Zn as a chloride complex and sulphur as sulphate (SO_4^{2-}). However, to deposit sphalerite (ZnS) a reducing agent is needed, in this equation exemplified by CH_4. A reducing agent in this type of geological environment could be organic matter, however no evidence for such matter is found.

Ore-forming processes

Physicochemical properties of fluids control transport and deposition of metals in hydrothermal systems. In the upper crust these fluids are commonly, at least in part, rock-buffered. As a result of these buffering processes, the range in pH and oxygen fugacity of the fluid is relatively narrow and the major controls on metal solubility are temperature and concentration of ligands like chloride and sulphur (Yardley 2005; Zhong et al., 2015). At VBF, the ore-bearing fluids have a near neutral pH, have a salinity of c. 27-36 wt. % NaCl+$CaCl_2$, and a temperature estimated in the range of c. 250-335°C. The progressive enrichment of Zn in QS veins (first) followed by Cu in QCp veins (second), and the possible depositional mechanisms for each of these metals will be discussed below.

Zinc and copper in a highly saline fluid at a temperature of c. 300°C is likely transported as a chloride complex, regardless of the oxidation state of the fluid (Zhong et al. 2015). The positive correlation between T_h and salinity from fluid inclusions in sphalerite and in associated QS vein quartz (**Fig.** 15B) indicate mixing with a colder and less saline fluid, possibly originating as groundwater (table 2). Mixing and dilution of the fluid would efficiently precipitate sphalerite.

The progressive widening of the fault and repeated injections of fluid through the fault (and deposition of injected cataclasites) is associated with QCp vein deposition. Seismic pumping could lead to an increase in fluid flow, and also further influx of a colder and slightly less saline fluid. Such a process is supported by the salinity decrease observed in fluid inclusions from QS to QCp veins. It is further supported by the significant temperature decrease recorded in primary fluid inclusion in QCP vein quartz, and pseudosecondary inclusions in QS veins (**Fig.** 15B). It is likely that some of the solid material in the Type 2b fluid inclusions is accidentally entrapped microscopic minerals, like chlorite and microcline, from the material that deposited injected cataclasites.

A second contribution to the deposition of chalcopyrite is suggested by textural relationships; chalcopyrite have grown as a rim around clasts, or at the inner edges of the QCp veins, in direct contact with Fe-rich chlorite or pyrite, or chlorite-bearing cataclasite. This suggests that Fe was sourced locally from the host rocks, while sulphur could be sourced from the hydrothermal fluid (**Fig.** 17), and that chalcopyrite deposition was furthered by wall-rock interactions. Wall-rock interactions as a source of Fe may also explain why chalcopyrite mineralization is chiefly deposited in fractures

hosted by mafic (Fe-rich) dike host rock (domain B2) and in domains A1-A2 fault cores with chlorite (Fe-) rich injected ultracataclasites.

Stable isotopic composition of vein-forming fluids

The stable isotope data for hydrothermal calcite from the VBF (**Fig.** 19) yielded $\delta^{13}C$ values in the range of -5.7 to -4.0 ‰, and $\delta^{18}O$ values from +7.1 to +12.3 ‰, which plot close to that of igneous carbonates (Taylor et al. 1967). In general, alteration of igneous carbonate by oxygen-rich atmosphere (e.g. weathering) may cause an increase in the value of $\delta^{18}O$ at a fairly constant $^{13}C/^{12}C$ ratio (Taylor et al. 1967), and such a trend is apparent for hydrothermal calcite associated with the VBF (**Fig.** 19). Alternatively, the large spread in $\delta^{18}O$ values for the VBF calcite may reflect fluid mixing in the hydrothermal system (Savard and Kontak 1995; Kontak et al. 2006) and/or assimilation with sedimentary carbonates, as inferred from a pronounced increase of $\delta^{13}C$ in calcite veins of the diorite and matrix of the Vanna Group sedimentary rocks (**Fig.** 19). The narrow compositional range of $\delta^{13}C$ for VBF calcite, however, strongly supports a magmatic origin of CO_2, and also suggests that factors such as boiling, temperature, and oxidation state of the hydrothermal fluid did not influence the $\delta^{13}C$ signature (Rye and Ohmoto 1974). The fact that calcite from veins in the Skipsfjord nappe, and Vanna Group sedimentary rocks, display much higher values of $\delta^{13}C$ and $\delta^{18}O$, larger compositional variations, and more variable trends than calcite in the VBF (**Fig.** 19) suggests a different origin, and/or possibly more diverse enrichment history of these carbonates.

Potential origin of the ore-forming fluids

Fluids of the composition described above may have been sourced from several possible hydrological reservoirs, including sediment-derived or shallow marine brines and entrapped formation water, brine fluids from deeper in the crust, or magmatic and hydrothermal fluids (Yardley 2005). At Vanna, the relict sedimentary formations are represented by the Palaeoproterozoic Vanna Group rocks deposited in a shallow marine environment (Binns et al. 1980; Bergh et al. 2007; Johannessen 2012) and portions of the Skipsfjord Nappe (Opheim and Andresen 1989), in hanging wall of the VBF. Deeper brine sources may include the metamorphic tonalitic gneiss and mafic dike host rocks, or alternatively, magmatic fluids released from a hot magma and transported through faults, fractures, and/or along lithological contacts as pathways, and final emplacement in e.g. major faults/shear zones (**Fig.** 20C).

The role of basinal brines as ore forming fluids has been widely discussed (Yardley 2005) and two main models are suggested for their formation (Walter et al. 2016). In the first model, low salinity fluids circulating in the crust are modified by wall-rock interactions and enriched in solutes through hydrothermal alteration of e.g. feldspar and mica to clay. This model is questioned from experiments by Burisch et al. (2016), indicating that wall-rock interactions are not sufficient to produce brines over 28 wt. % salinities, and therefore, an additional source is required for highly saline fluids. The second model poses an external source of salinity, for example, dissolution of previously deposited evaporates

in a sedimentary rock sequence (Mississippi Valley Type deposits; Kesler et al. 1995), or the development and downward migration of so-called bittern brines, a residual brine produced by the precipitation of halite in shallow marine basins. This process is suggested for the formation of the continental basement brines at Schwarzwald (Walter et al. 2016). Although no evaporates have been observed within the relict shallow-water sedimentary sequences at Vanna, it is not unlikely that at least some of the salinity in the ore-forming fluid could be derived from this sequence. However, the $\delta^{13}C$ vs. $\delta^{18}O$ values of VBF calcite veins are distinctly different from those of the Skipsfjord Nappe and Vanna Group (**Fig.** 19), suggesting that a different source of CO_2 formed these carbonates.

Low Na/Ca ratios, like those at VBF, have been accredited to fluid-rock interactions by several workers. Banks et al. (1991) suggested a strong host rock control causing the fluid evolving to a lower Na/Ca ratio for brines analysed in the Central Pyrenees; Boiron et al. (2010) also suggested brine $CaCl_2$-enrichment caused by albitisation and Na-metasomatism, while Bucher and Stober (2010) show that brines may vary from NaCl-rich when residing in granites to $CaCl_2$-rich in mafic rocks like amphibolites and gabbros.

From the discussion above, a possible model for the Cu-Zn bearing fluid source in the VBF is that the first phase of fluids, associated with QS veins, originated as continent-internal basinal brines with Zn sourced mainly from the surrounding host rocks, possibly with some salinity derived from the meta-sedimentary sequence within the Skipsfjord Nappe. During continental rifting, the increasing amount of Cu associated with the second vein phase (QCp veins) was derived from either a Permian aged hot mafic melt/dike (see discussion below), or in combination with wall-rock interactions of a mafic component within the Neoarchaean host rock gneisses. A magmatic source for the CO_2 in the temporal late hydrothermal calcite veins (Ca veins) is suggested by the low $\delta^{13}C$ and $\delta^{18}O$ values (**Fig.** 19), indicating that the later fluids included some magmatic CO_2, possibly relating to Permian age rift-related magmatism.

Regional implications

A Palaeozoic (348-284 Ma) age of fault rocks along the VBF is well constrained from recent K-Ar dating of illite in late stage fault gouge (Davids et al. 2013). Such an age contrasts with previous workers arguing for a Palaeoproterozoic VMS stringer zone origin of the Cu-Zn mineralization, linked with the 2.4 Ga mafic dike swarm (Ojala et al. 2013; Monsen 2014) and subsequent spread of metals into sediments now present in the Skipsfjord Nappe (Opheim and Andresen 1989). The new dating results are consistent with formation of the VBF and enclosed Cu-Zn mineralized fault rocks/veins as part of an early Permian rifting event in the North Norwegian continental margin producing NE-SW striking brittle normal faults and associated fracture sets (Gabrielsen et al. 1990; Faleide et al. 2008; Smelror et al. 2009; Hansen et al. 2012), which later on evolved to major fault zones like the Vestfjord-Vanna and Troms-Finnmark fault complexes (Olesen et al. 1997; Indrevær et al. 2013,

2014; Koehl et al. 2018). Most of these Permian faults, including the VBF, contain features that indicate complex fluid flow and fault-rock interactions, however, yet very few of them seem to be accompanied by ore mineralization (cf. Koehl, 2013; Indrevær et al. 2014).

The wide K-Ar illite age range obtained for the VBF (Davids et al. 2013) could reflect a multiphase kinematic and very complex reactivation history of the fault rocks, as outlined in this work. If a minimum Early Permian age is linked to our post-ore movement unconsolidated fault gauge, the main fault zone movement may have initiated as early as in the Carboniferous, even Late-Devonian (cf. Koehl et al. 2018b). Carboniferous rifting is known to have produced mafic dike swarms on the Finnmark portion of the North Norwegian margin (Roberts et al. 2003, 2011; Nasuti et al. 2015) and numerous brittle normal faults with extensive hydrothermal alteration and cataclasis (Indrevær et al. 2013, 2014; Koehl et al. 2018a, b). Specifically, the Langfjorden-Vargsundet fault zone, which can be traced from Troms all along the coast of western Finnmark northward to Magerøya (**Fig.** 1), experienced multiphase movement and hydrothermal activity (Indrevær et al. 2013, 2014; Koehl et al. 2018a, b). In this fault zone early stage quartz- calcite- and laumontite-rich cataclasites initiated at a temperature of about 350-200°C and depth of 2-8 km, and were followed by a main, second period of faulting in the Mid-Permian (315–265 Ma) that exhumed basement rocks to shallow depths of 1-3.5 km (Koehl et al. 2018b). Similar results were obtained from several onshore Late Permian normal faults of the Vestfjord-Vanna fault complex in western Troms yielding minimum P-T conditions of 300-275°C and 2.4-2.2 kbar (Indrevær, 2014). These temperature estimates, as discussed above for PT conditions at VBF (this work) are altogether similar to those of the VBF, i.e. temperatures of 250-335°C. Based on the nature of the brittle faulting and the similar P-T conditions it is therefore likely that the hydrothermal Cu-Zn mineralization in the VBF was concurrent with the Carboniferous-Permian brittle extensional events that involved multiple brittle faulting, cataclasis, and hydrothermal Cu-Zn mineralization, coupled with a complex reactivation and exhumation history for the faults (cf. Davids et al. 2013).

Regarding a possible magmatic source for some of the hydrothermal fluids in the VBF (see **Fig.** 20C), no direct evidence of a corresponding hot Permian magmatic and/or volcanic source/dike for the fluids in the VBF have yet been observed in the Vanna island of western Troms. An exception is a lamproite dike in Kvaløya farther south, which yielded an Nd- and Sr-isotope age of ca. 333 Ma (Kullerud et al. 2011). Extensive rift-related mafic dike and sill intrusions of Carboniferous-Permian age, however, do exist at northern Atlantic Ocean margins (Kirstein et al. 2006), and also are recorded along portions of the Norwegian continental margin, including northern Finnmark (Lippard and Prestvik, 1997; Roberts et al. 2003, 2011; Rice et al. 2014; Nasuti et al. 2015). Thus, and since an increased geothermal gradient exceeding more than 50°C km^{-1} often accompanies incipient continental rifting events, we cannot rule out that a hidden subsurface, Carboniferous-Permian mafic magma source for hydrothermal Cu-Zn bearing fluids in the VBF may exist.

Conclusions

1) The Cu-Zn mineralization in the brittle, late Palaeozoic Vannareid-Burøysund fault on the island of Vanna, West Troms Basement Complex, is hydrothermal, epigenetic and localized within major core and damage zones, suggesting a strong structural (fault) control on the mineralization.
2) The brittle fault movement and cataclasis of the VBF created porosity allowing fluid flow and deposition of hydrothermal veins and Cu-Zn mineralization in the core and damage zones, possibly during two main stages of faulting/fracturing. Although the fault cores acted as the main fluid conduits, the fluids also weakened the strength of the fault damage zones and contributed to the complex fault architecture and development history.
3) A paragenetic model is developed for the successive deposition of i) quartz-sphalerite veins, ii) quartz-chalcopyrite veins and iii) calcite veins. Quartz-sphalerite veins deposited first in the core zone in conjunction with early brittle fracturing and cataclasis, increasing the porosity of the fault rocks and creating space for further hydrothermal fluid flow, confirming that the fault core at least initially acted as fluid conduit. With further fault movement and widening of the fault, quartz-chalcopyrite veins were deposited in fault core and damage zones. During successive injection of quartz-sphalerite vein material, the initial fault core became partly or fully sealed, thus reducing the permeability and forcing the later fluids to flow into the damage zones (cf. Indrevær et al. 2014).
4) The hydrothermal ore-bearing fluids in the VBF indicate temperature conditions of c. 250-335°C. Microtextural observations, including injected ultracataclasites, strongly indicate repeated phases of dilation, infill, and sealing of the fault. Such seismic pumping processes therefore indicate that the pressure conditions changed repeatedly between lithostatic and hydrostatic endmember values. Similar fault rock textures are documented from other Permian faults in the West Troms Basement Complex (Indrevær et al. 2014).
5) Ore forming fluids were near neutral, highly saline (c. 27-36 wt. % $NaCl+CaCl_2$) and composed of H_2O-NaCl-$CaCl_2$±S. A fluid with this high salinity is capable of transporting both Cu and Zn as chloride complexes. The ore-bearing fluid was likely a basinal brine with Zn sourced from tonalite gneiss host rocks. Sphalerite was deposited by fluid mixing with a colder and less saline fluid. Chalcopyrite in QCp veins deposited after sphalerite, likely by a combination of fluid mixing and wall-rock interactions. The stable isotope composition of calcite indicate a magmatic source of CO_2, suggests a later magmatic fluid influx, a common feature during continental extension/rifting.
6) The VBF comprises illite-bearing fault gouge yielding a Palaeozoic (Carboniferous) K-Ar age, thus linking the VBF to a period of incipient extensional faulting and rift basin formation in

the Norwegian–Greenland–Barents Sea. Several other faults in the west Troms Basement Complex are related to these early rifting events.

7) This study demonstrates that hydrothermal Cu-Zn mineralization in northern Norway may occur not only in old Precambrian and Caledonian basement rocks (Sandstad et al., 2015) but as well in much younger, Palaeozoic to Cretaceous (?), rift-related, brittle fault zones, and thus provides an additional mineral exploration model for structurally controlled ore deposits.

Acknowledgements

Tobias Bauer and Kristian Drivenes are kindly thanked for reviewing this manuscript. This work was funded by UiT – the Arctic University of Norway. We thank Øystein Rushfeld for access to assay data. Andrea Cobic with the University of Zagreb is thanked for XRD analyses. Kai Neufeld at UiT is acknowledged for his aid and input with SEM analyses. We also acknowledge Mattheus Lindgren at the Centre for Arctic Gas Hydrate, Environment and Climate at UiT for preforming stable isotope analyses.

Figures

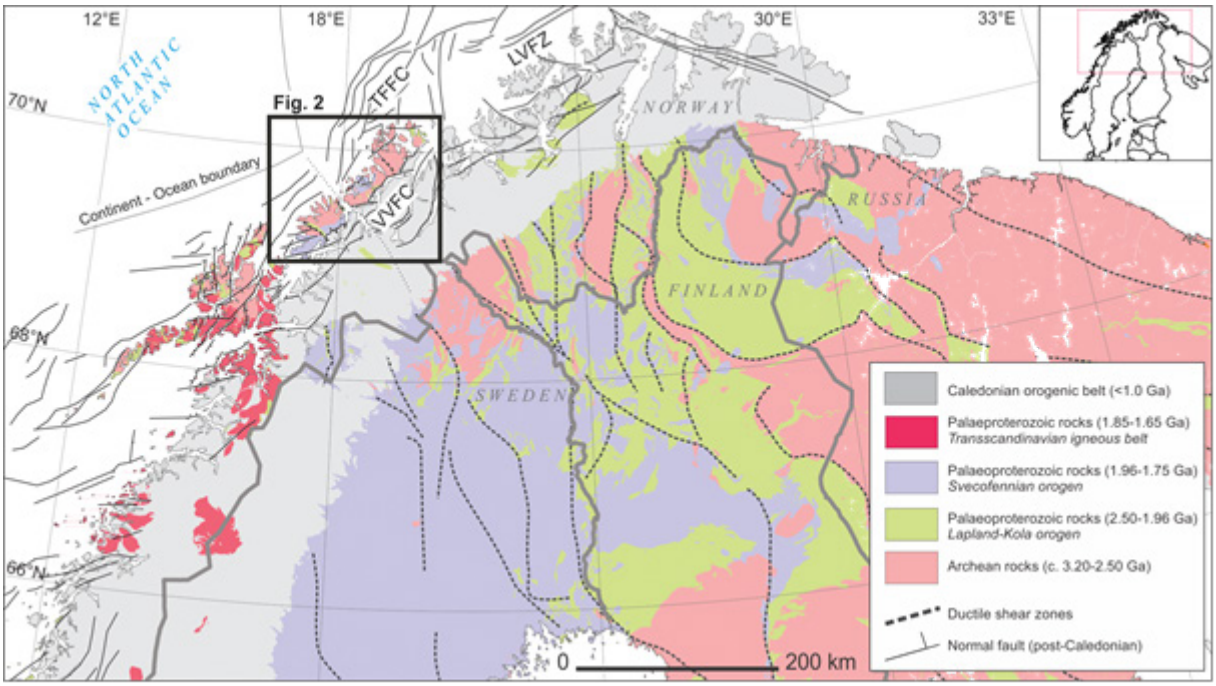

*Figure 1. Regional geological map of the northern Fennoscandian Shield (based on Koistinen et al. 2001; Olesen et al. 2002; Eilu et al. 2008; Bergh et al. 2010; Davids et al. 2013; and Koehl et al. 2018). The black frame outline the West Troms Basement Complex (**Fig.** 2), a basement horst controlled by the onshore Vestfjorden-Vanna fault complex (VVFC) that down faults the Caledonian rocks to the east. This Permian-Early Triassic rift related activity can also be correlated with offshore fault systems including Troms-Finnmark fault complex (TFFC) and Langfjorden-Vargsundet fault zone (LVFZ).*

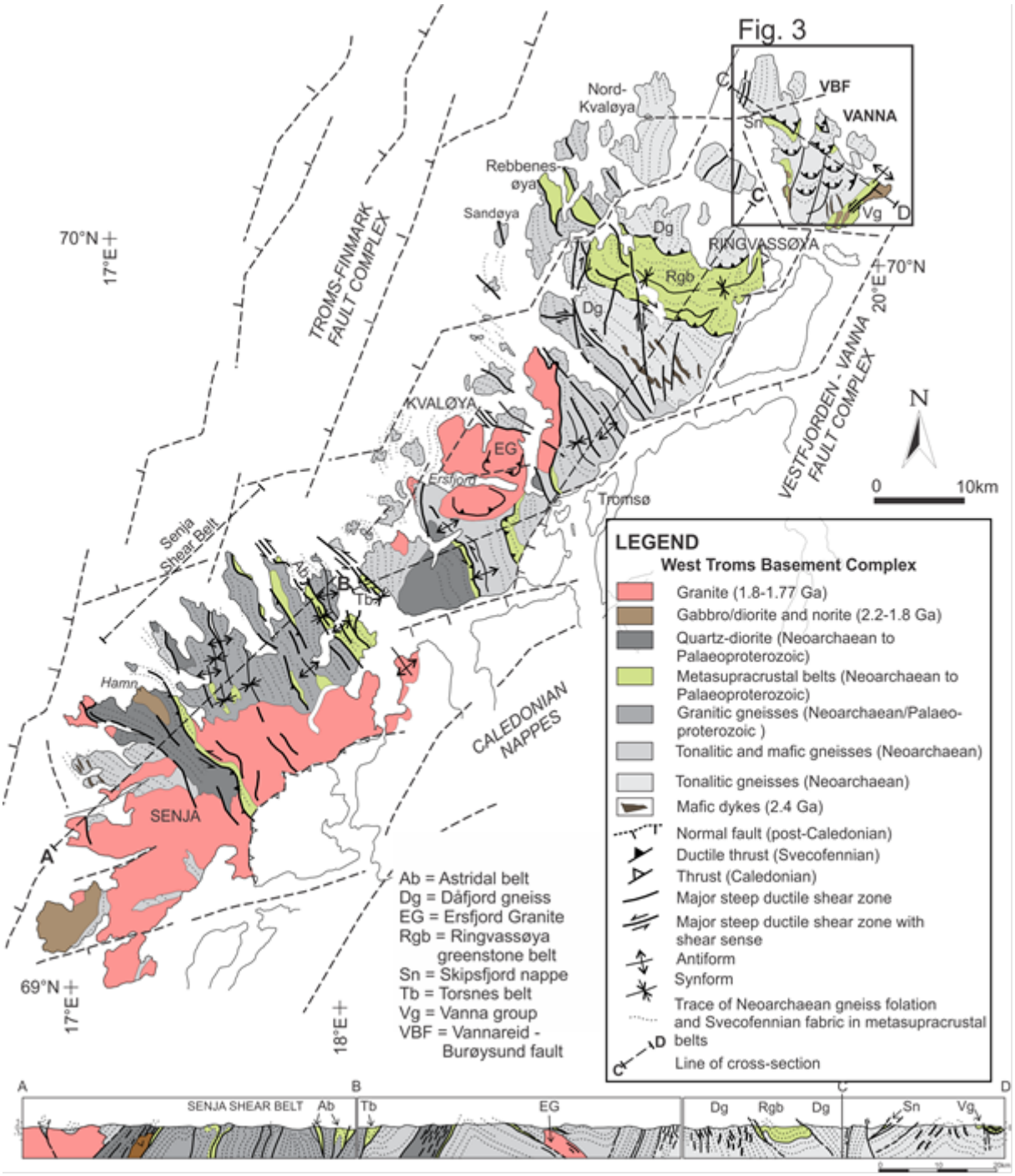

*Figure 2. Geology of the West Troms Basement Complex (Bergh et al. 2010; Thorstensen 2011; Davids et al. 2013; Haaland 2018). Vanna Island is located at the northern end of the complex. The location of the mineralized Vannareid-Burøysund fault (VBF) is marked on the map. The VBF is part of the Vestfjorden-Vanna and Troms-Finnmark Fault Complexes offshore and along fjords and sounds. Black frame outlines the island of Vanna (**Fig.** 3).*

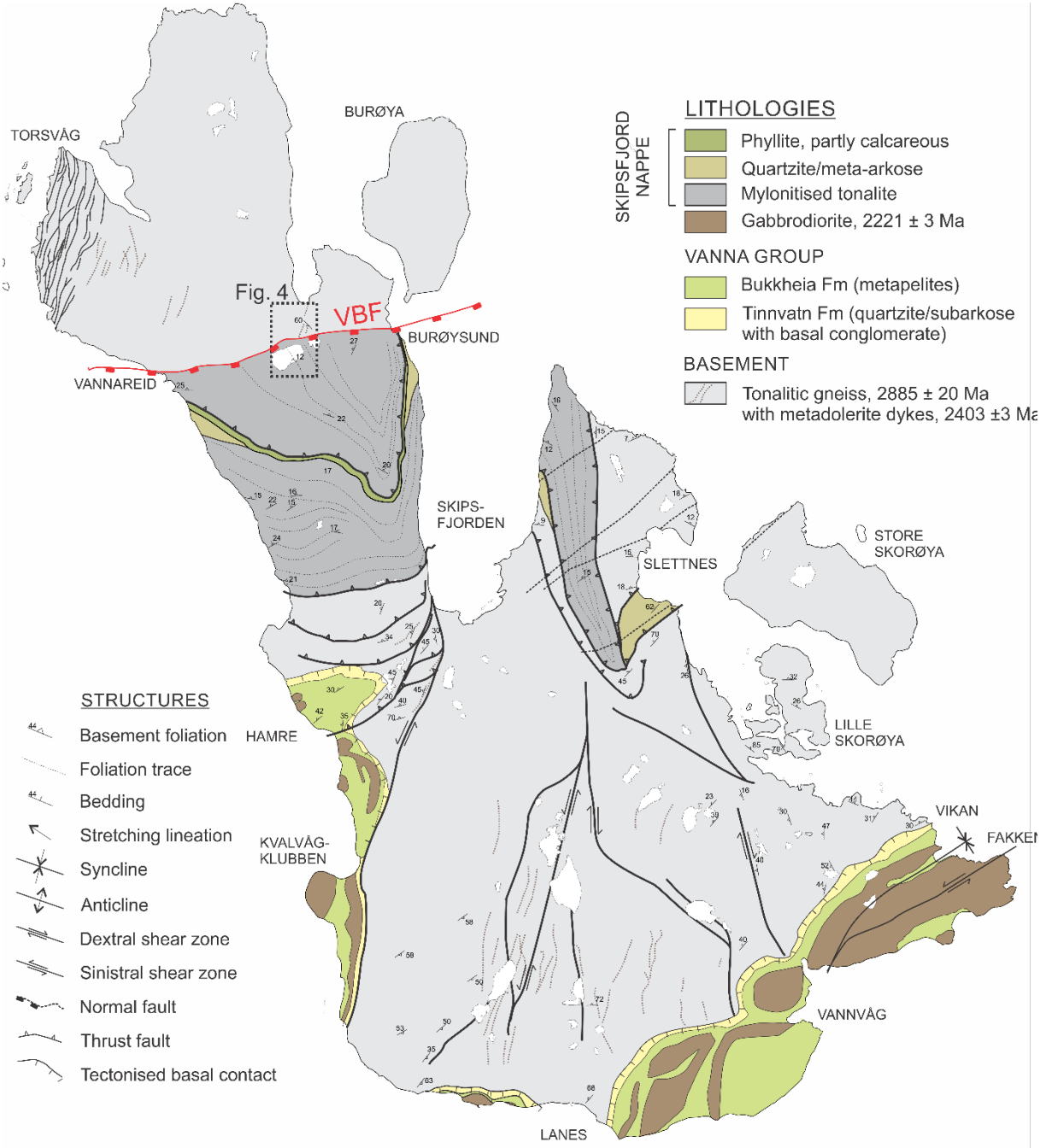

*Figure 3. Geological map of Vanna Island (Bergh et al. 2007). The mineralized Vannareid-Burøysund fault (VBF) separates variably deformed tonalite gneiss to the north from highly strained and mylonitized Skipsfjord Nappe rocks to the south. Black frame outlines the mineralized segment of the VBF (**Fig. 4**).*

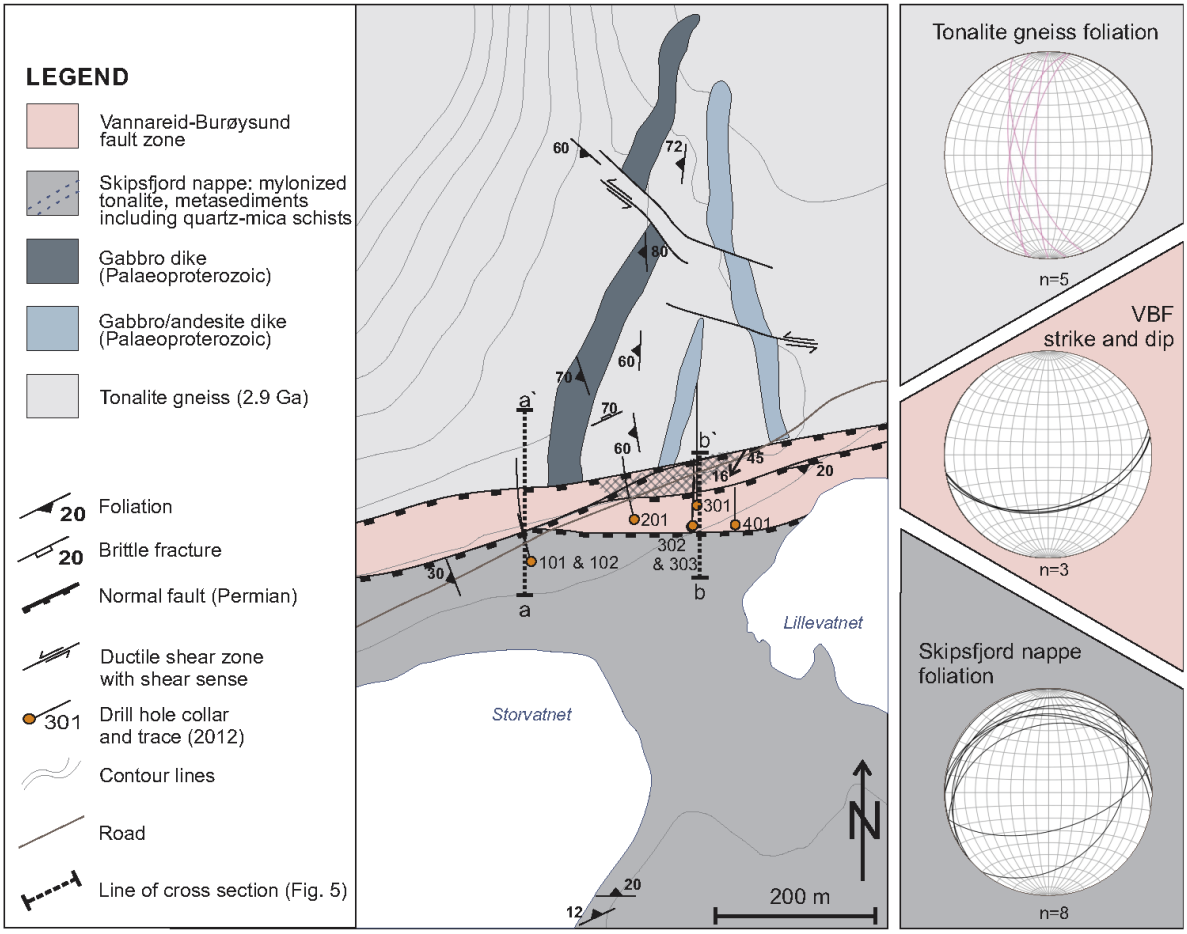

*Figure 4. Geological map of the mineralized segment of the VBF in the valley between Vannareid and Burøysund (see **Fig.** 3 for location), with enclosed fault details to the right outlined as great circles in lower-hemisphere stereo plots. Note several splay faults of the VBF, a gentle NW-dip of the foliation in Skipsfjord Nappe changing to a SE-dip close to the VBF. Map is modified after Monsen (2014). Existing drill core locations are marked on the map (Ojala et al. 2013). Profile lines a-a' and b-b' mark the location of profiles shown in **Fig.** 5.*

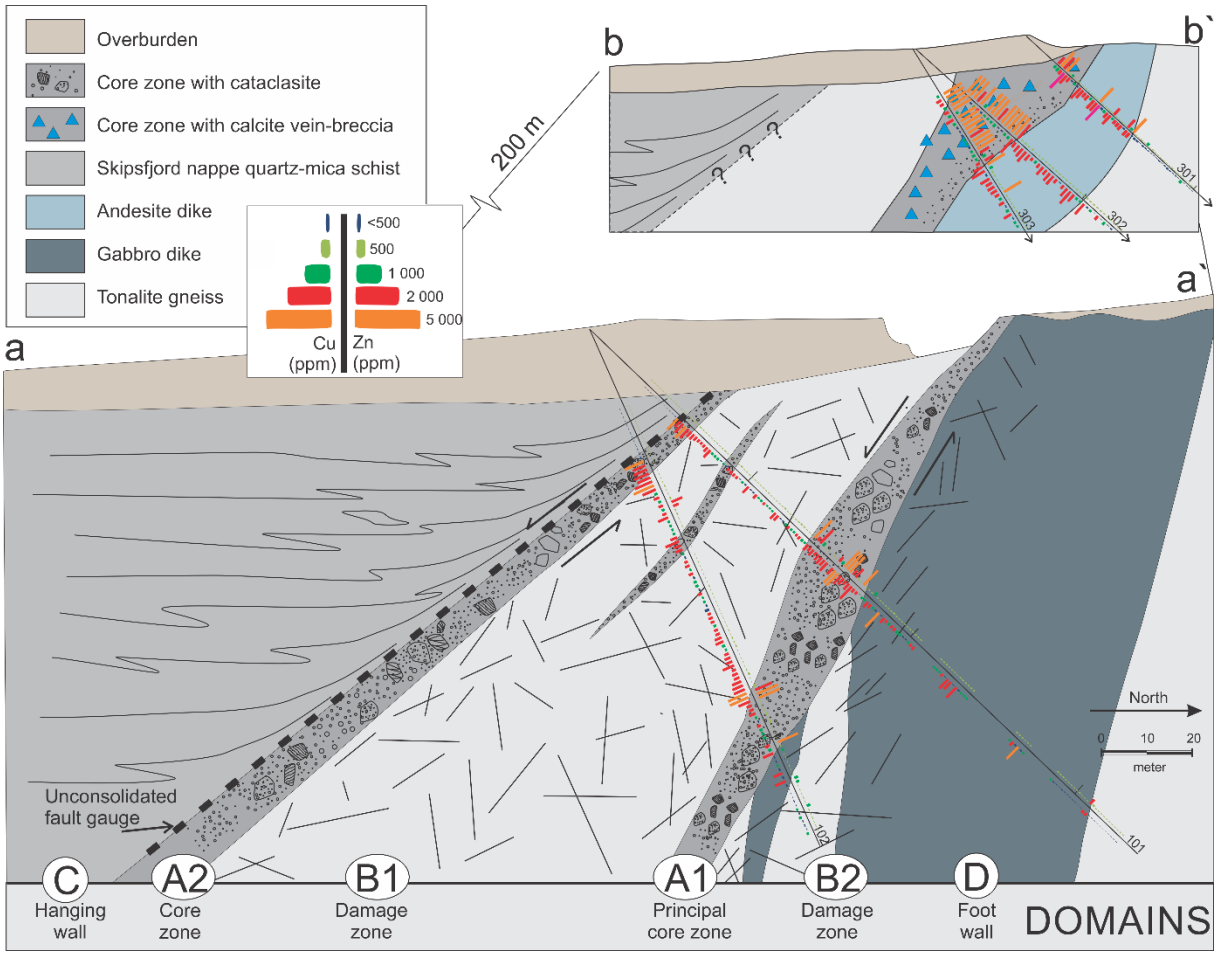

Figure 5. Cross-section a-a' through VBF showing the two drill cores and interpreted textural domains in mineralized fault rocks (core zone A1 and A2) and surrounding host rocks (damage zones B1 and B2; hanging wall domain C; and footwall domain D). The coloured assay data reflect amount of Zn (ppm), plotted on the right side of the drill core, and Cu (ppm) on the left side. Note enrichment of Cu-Zn in core zones A1 and A2, whereas lower values exist in damage zones B1 and B2. The down-dropped, non-deformed hanging wall rocks of the Skipsfjord Nappe are barren of ore mineralization. The inset figure on top right shows cross-section b-b' through VBF c. 200 m farther east, with thick calcite-breccias making up the fault core zone A1.

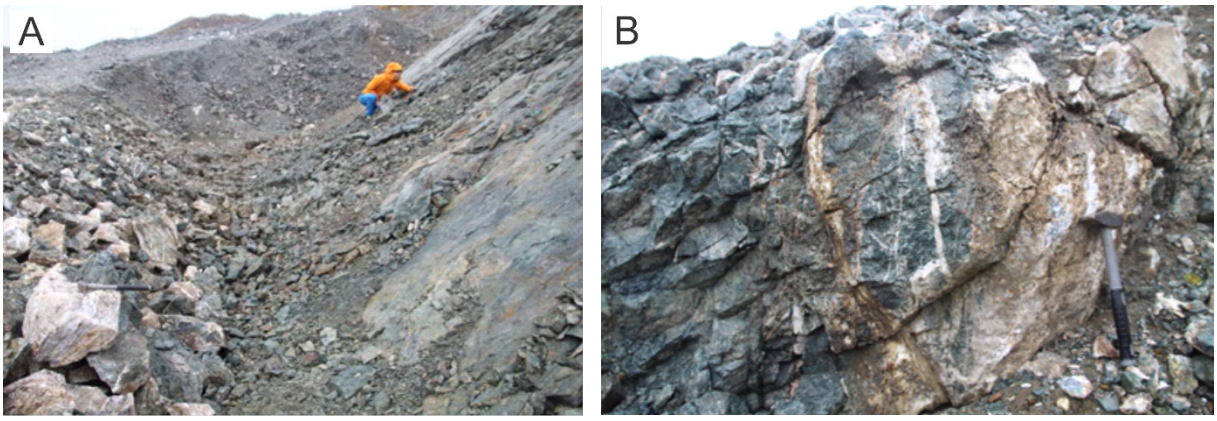

Figure 6. (A) Outcrop photo of the VBF, expressed as a planar, moderately dipping, locally striated surface, with malachite and epidote staining. Person for scale. (B) Outcrop photo of altered/chloritized (green colour) bed rocks and proto-cataclasites in damage zone B1 of the VBF. Note presence of abundant hydrothermal quartz and calcite veins as infill in brittle fractures.

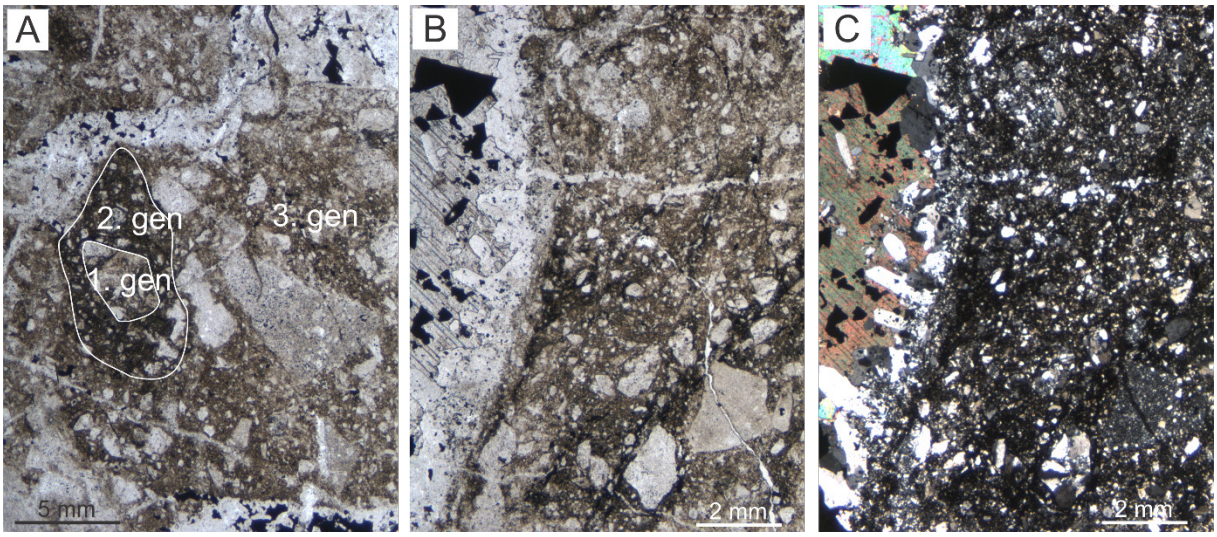

Figure 7. (A) Microphotograph (PPL) of three generations of cataclasite from core zone A1. These cataclasites are cross cut by a younger, hydrothermal chalcopyrite bearing quartz vein (top right to middle left). (B) Photomicrograph (PPL) from core zone A1 showing details several generations of cataclasite to the right and hydrothermal quartz-calcite vein to the left that is growing from the consolidated clast(s) of cataclasite. The rims of this vein is euhedral quartz with calcite infill. (C) Same as in B but as XPL.

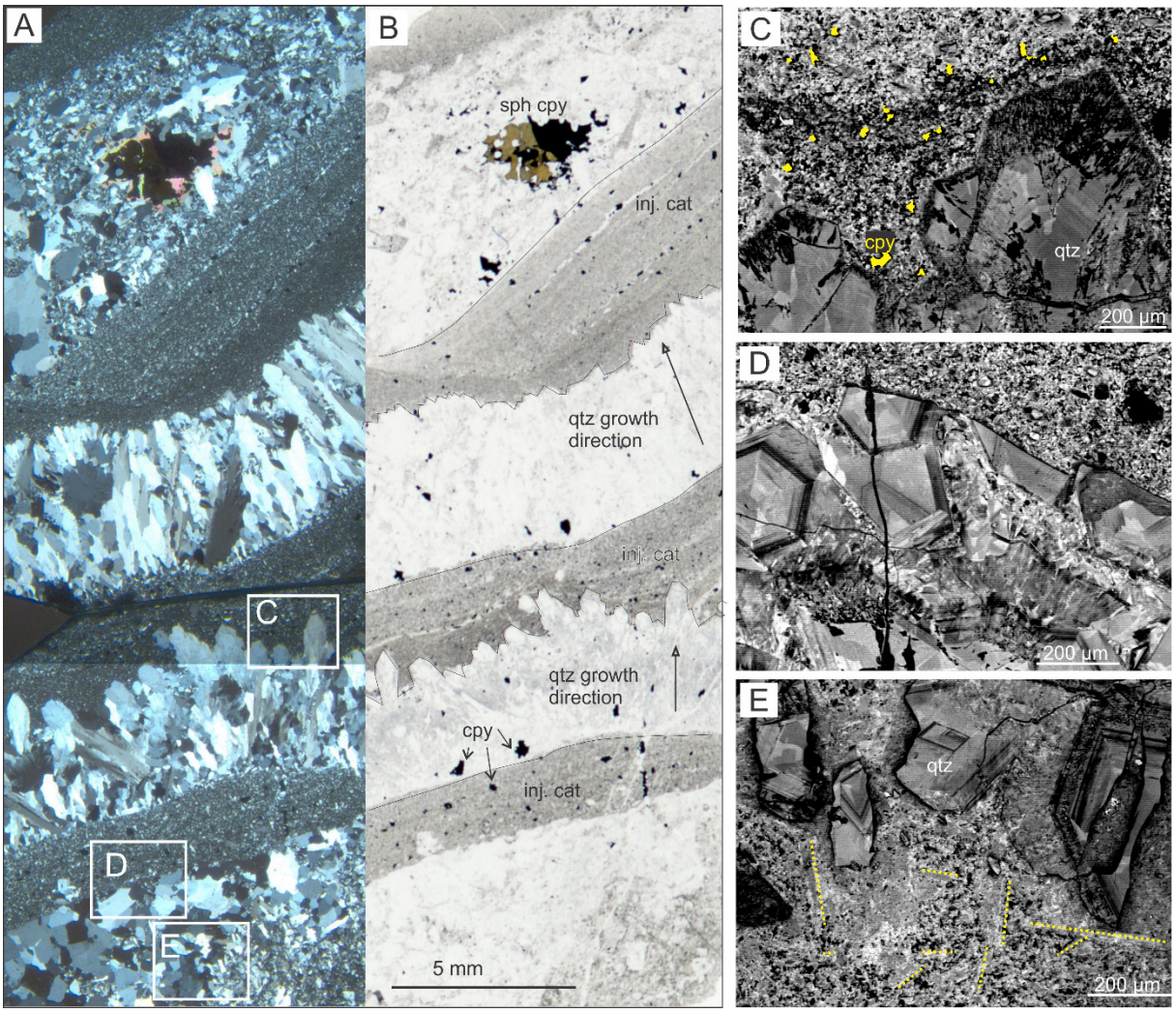

Figure 8. Microphotographs of hydrothermal veins and episodic injected ultracataclasites. XPL (A) and PPL (B) micrographs showing episodic quartz and injected cataclasites from core zone A2. Note location of C, D and E in frames. (C) Cathodoluminescence SEM image showing zoned euhedral quartz cores with plumose textured rims. Matrix between such quartz grains were then, later on filled by new injected cataclasite with chalcopyrite (yellow grains). (D) Cathodoluminescence SEM image showing fractured clasts of zoned quartz with fractures filled by injected ultracataclasite. (E) Fractured clasts of hydrothermal zoned quartz with plumose rims and surrounding infill of ultracataclasite with acicular new-grown minerals, in yellow (bottom half of photo. Abbreviations: inj. cat.-injected cataclasite, qtz -quartz, cpy -chalcopyrite, sph -sphalerite.

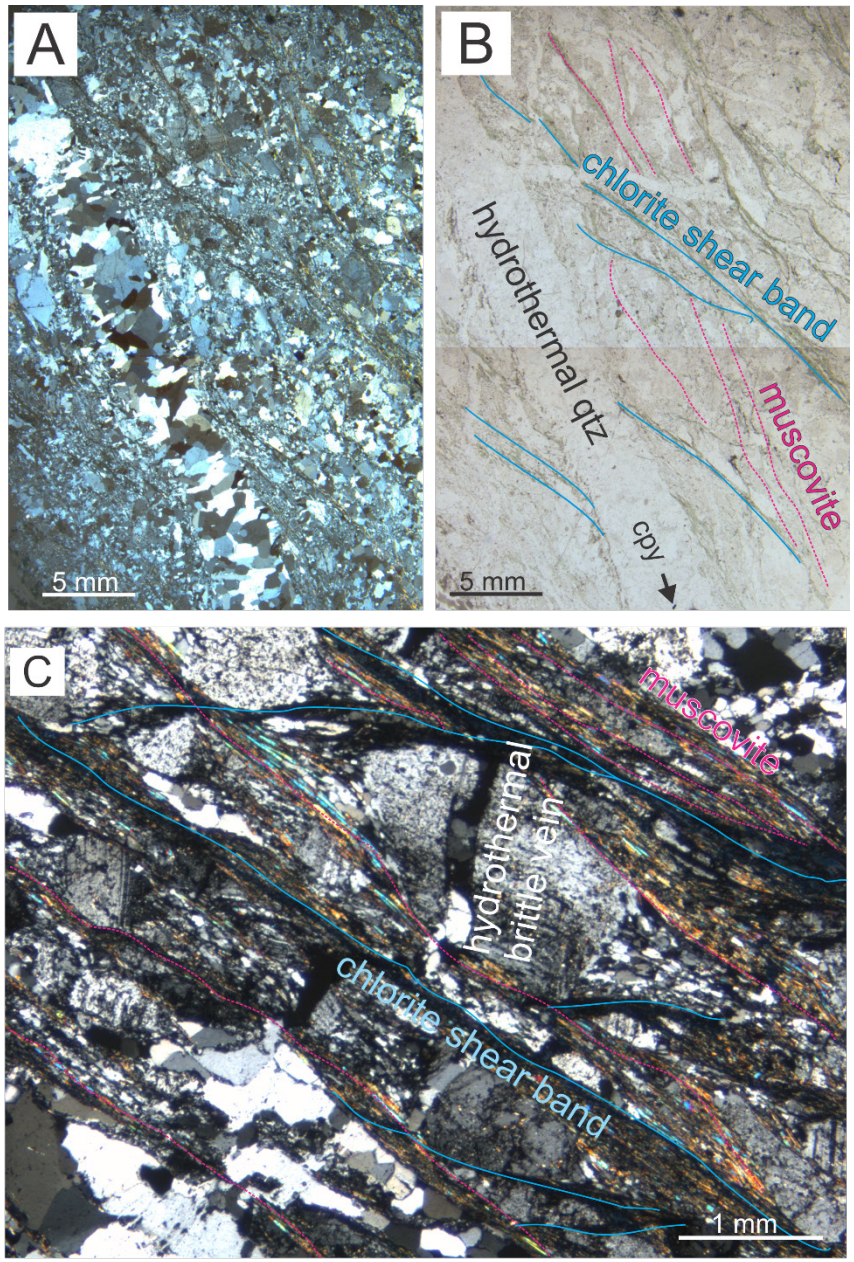

Figure 9. (A & B) XPL and PPL microphotographs from damage zone B1 showing weakly foliated tonalite gneiss with muscovite (pink) bands cut at a low angle by chlorite shear bands (blue). Younger hydrothermal quartz and chalcopyrite veins truncate, but are arranged parallel to the old, ductile fabric of the gneisses. (C) XPL micrograph of tonalitic gneiss with foliation composed mostly of aligned muscovite, which is superposed at low angle by chlorite shear bands in tonalite gneiss. Note the large, sigmoidal feldspar crystal in the middle of the micrograph which is fractured and dilated by quartz.

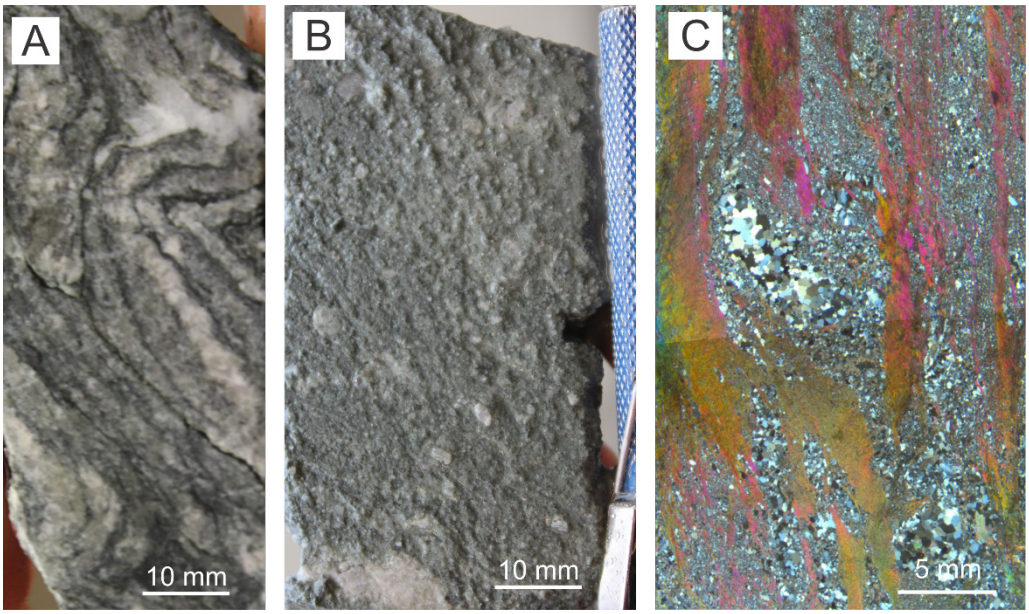

Figure 10. (A) Hand-specimen photo of folded, well-foliated, non-mineralized quartz-mica schist in Skipsfjord Nappe host rocks of the hanging wall to VBF. (B) Hand specimen photo of unconsolidated fault gouge (core zone A2) at the contact between quartz-schists in hanging wall and the mineralized footwall of VBF. (C) Photomicrograph (XPL) of quartz-mica schists from Skipsfjord Nappe rocks showing muscovite foliation and sigmoidal-shaped quartz crystal.

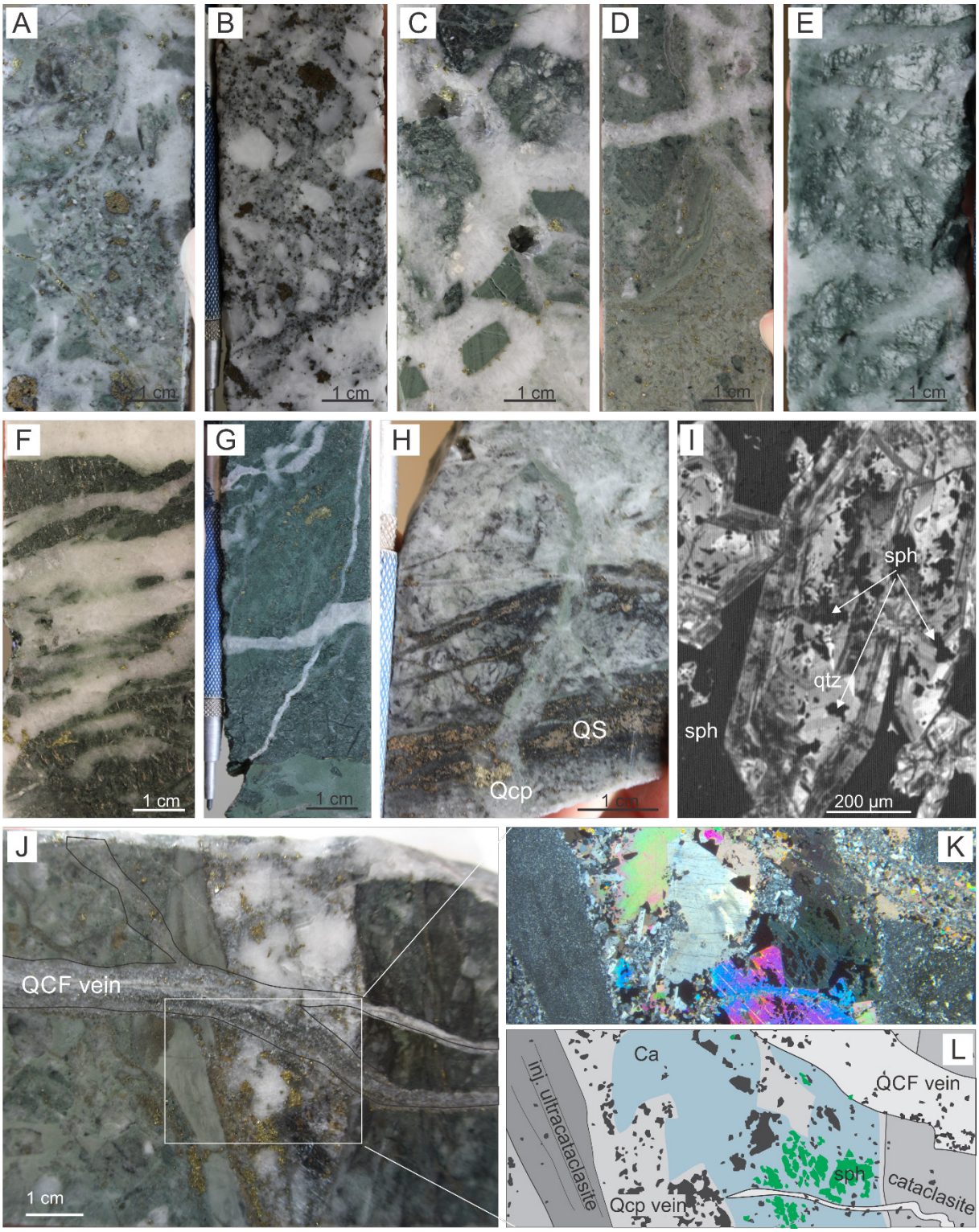

Figure 11. Drill core photographs (A-H and J) and microphotographs (I, K and L) of typical mineralization textures and quartz-carbonate veins. (A) Cataclasite with enclosed, early-stage sphalerite mineralization (QS) outlined as clasts cemented by a later phase of quartz-chalcopyrite veining material (QCp). From core zone A1. (B) Calcite-cemented sphalerite-rich breccia located at the top of core zone A1 (see Fig 5). (C) Clasts of banded ultracataclasites cemented by hydrothermal (QCp) veins in cataclasite of domain A2. Note that chalcopyrite is present as rims around chlorite-bearing clasts. (D) Cataclasite from core zone in domain A2, with clasts of quartz and several older generations of cataclasite, cemented by injected ultracataclasites, and cross cut by hydrothermal

quartz veins. (E) Damage zone B1 is characterised by fractured and weakly foliated tonalite gneiss cut by stock work QCp veins and chlorite alteration. (F) Chloritized gabbro in damage zone, domain B2, cut by parallel QCp veins. (G) Fine-grained cataclasite cut by QS veins in damage zone, domain B2. (H) Direct cross cutting relationship between early QS veins and later QCp veins, in core zone A1. (I) SEM cathodoluminescence image of a QS vein. Note zoned, euhedral quartz crystals with sphalerite occurring as small inclusions in quartz, and as interstitial sphalerite between quartz crystals. (J) Cross cutting relationships observed in core zone A1: Injected ultracataclasite is cut by QS and QCp veins, with a later infill of massive calcite. Early sphalerite grains are fractured in a jig-saw pattern by the later calcite infill. A narrow QCF vein with massive textures is the youngest vein observed. (K, L) Uninterpreted XPL (K) and interpreted (L) microphotograph of a portion (frame) of sample (J) outlining the relative timing (stages i-iv) of QS (green sphalerite), QCp (pale grey quartz and black chalcopyrite), Ca (pale blue calcite and black chalcopyrite), and QCF veins (palest white quartz-calcite-fluorite and black chalcopyrite and Pb-Ag-Bi sulphides), respectively. Injected cataclasites with apparent banding are outlined in darkest grey colour.

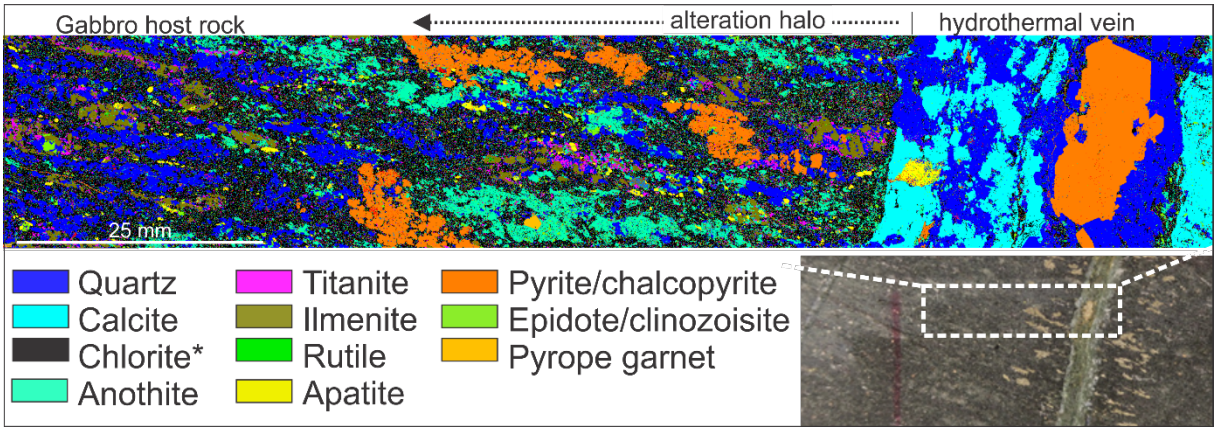

Figure 12. Secondary mineral growth expressed as alteration halo adjacent to a QCp vein, in gabbro from damage zone B2 (see inset photo of hand specimen and location of section, white stippled frame). SEM EBSD image (upper part) showing secondary alteration minerals replacing original minerals (in colour) along existing foliation in gabbro. The QCp vein is composed of quartz, calcite, and pyrite/chalcopyrite, with minor apatite and epidote. The mineral replacement is more pronounced close to the QCp vein where amphibole is replaced by chlorite; ilmenite/magnetite is replaced by pyrite/chalcopyrite and titanite; and feldspar is partly replaced by epidote.

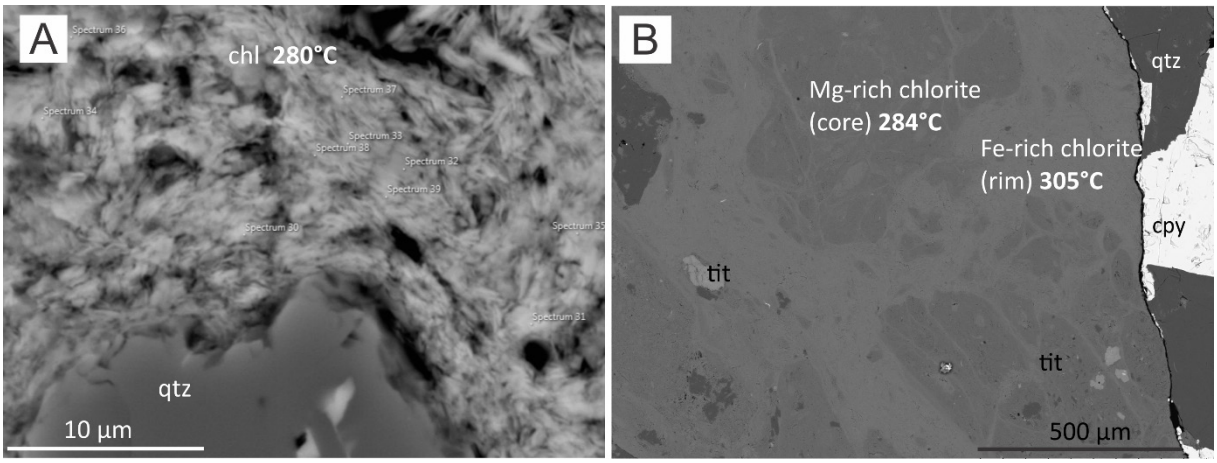

Figure 13. SEM images of different chlorite associations analysed for chlorite geothermometry. (A) Fine grained chlorite in cataclasite from top of core zone A1 (B) Two generations of cataclasite with chlorite alteration of amphibole in gabbro dike in damage zone B2.

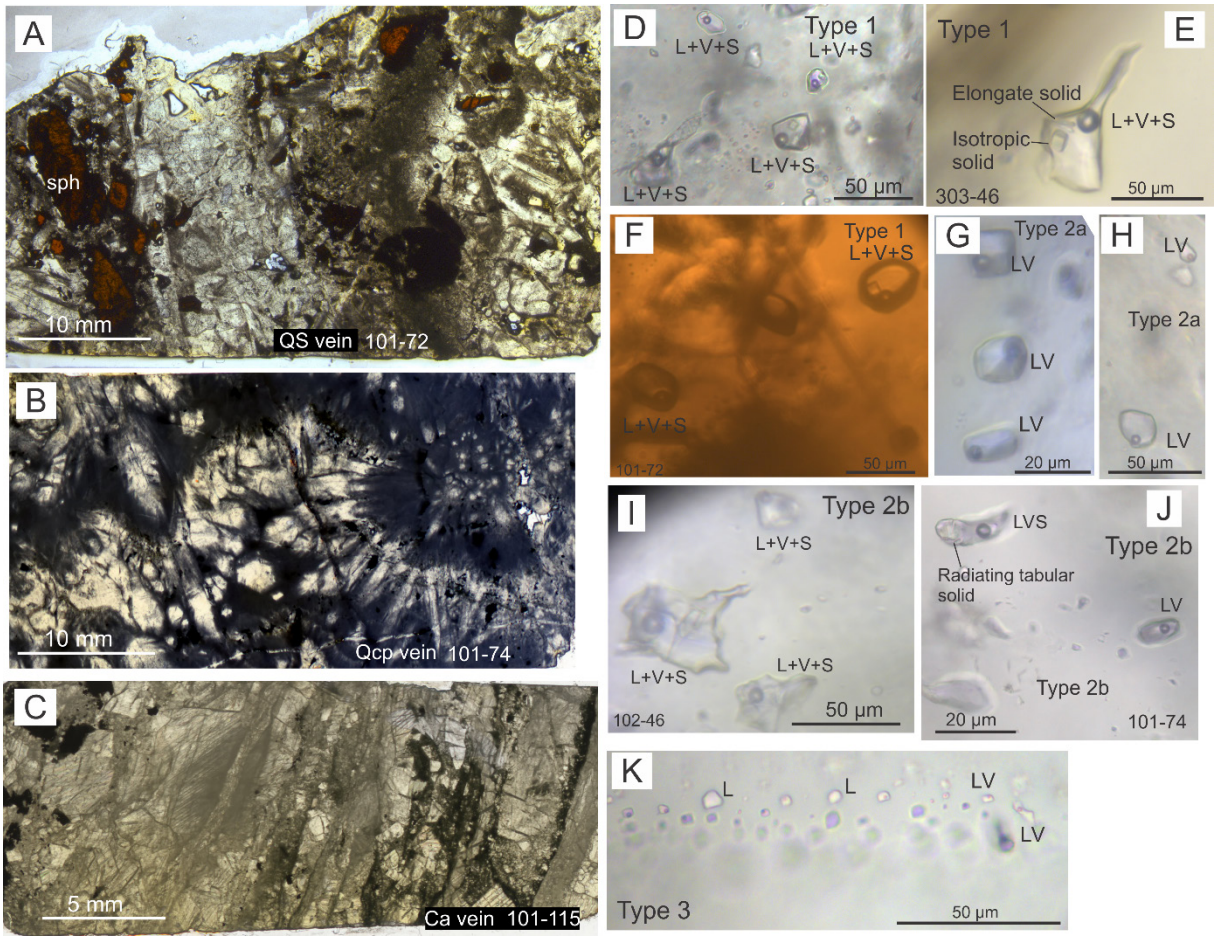

Figure 14. Compiled photographs double-polished wafers (A-C) and microphotographs of selected fluid inclusion types (D-K). A) Double polished wafer of QS vein from core zone A1. (B) Double polished wafer of typical textured QCp vein where quartz have zoned cores and feathery/plumose rims. C) Double-polished wafer of brecciated Ca vein. D) Composite photo of type 1 L+V+S fluid inclusion in quartz with cubic solid. E) Type 1 inclusion in quartz with two types of solids; an isotropic cubic solid which commonly melted around 70-200°C and a second, less common, elongate tabular crystal that did not melt when heated. The latter is possibly an incidentally entrapped solid. F) Type 1 L+V+S inclusions in sphalerite. G&H) Type 2a L+V inclusions in calcite. I) Type 2b L+V+S inclusions in quartz with <1-10% solids. J) Type 2b inclusion in quartz that contain a radiating tabular solid. K) Type 3 L+V and L-only pseudosecondary inclusions in quartz with negative crystal shapes. Note that L-inclusions lack vapour bubble at room temperature, but may develop vapour bubbles during freezing.

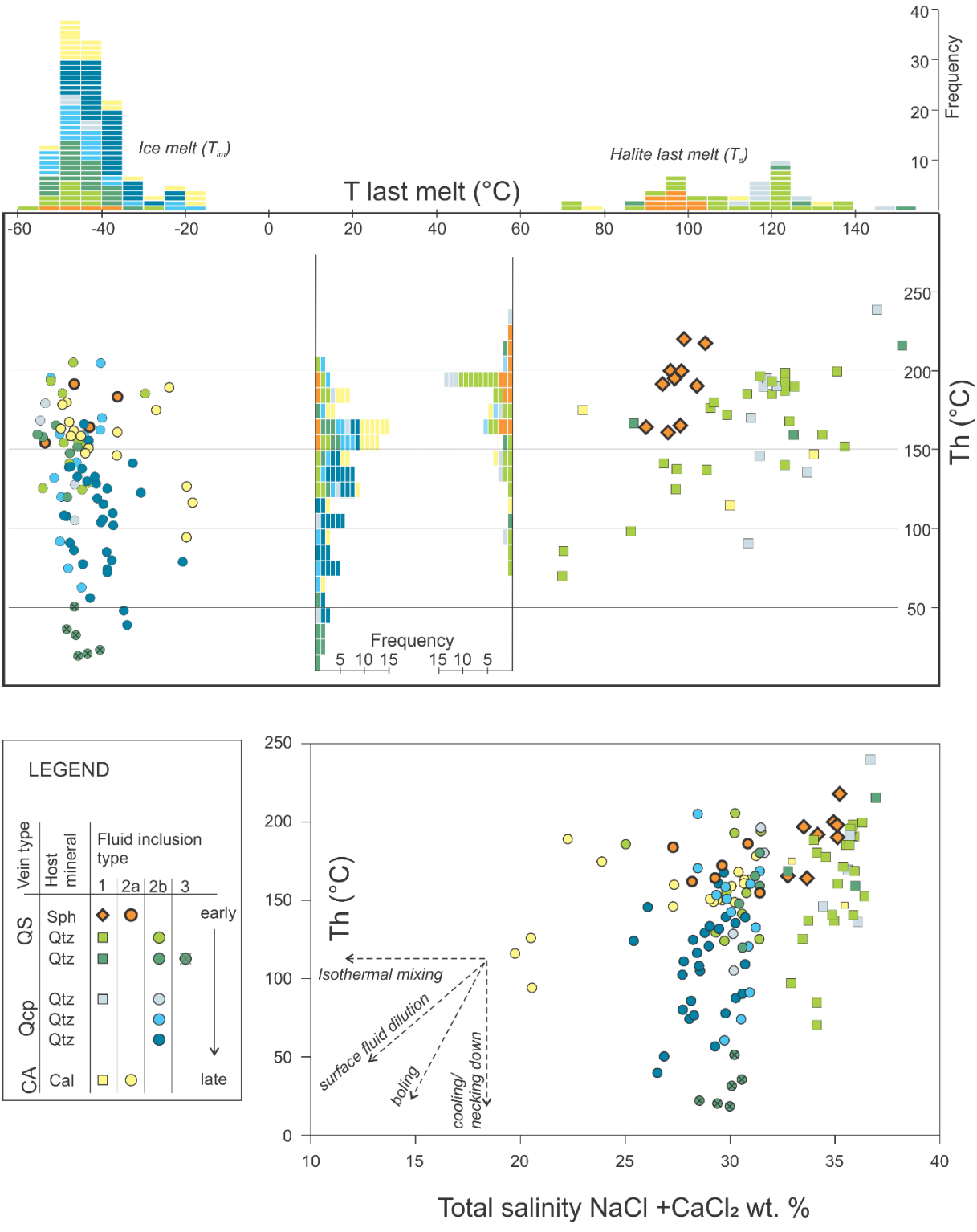

Figure 15. Summary of fluid inclusion microthermometric data. A) Measured ice melting temperatures ($T_{m\ Ice}$) for Type 2a, 2b and 3 inclusion are plotted on the X-axis. Halite melting temperatures for Type 1 inclusions are also plotted along the same axis. Homogenisation temperatures T_h (°C) is plotted on the Y axis. Note that frequency histograms are plotted separately for all measurements. B) Calculated total salinity ($NaCl+CaCl_2$) versus T_h (see also Table 2). The colours correspond to different vein samples from different vein types. Temporal relationships indicated in the legend is based on cross cutting relationships described in the text.

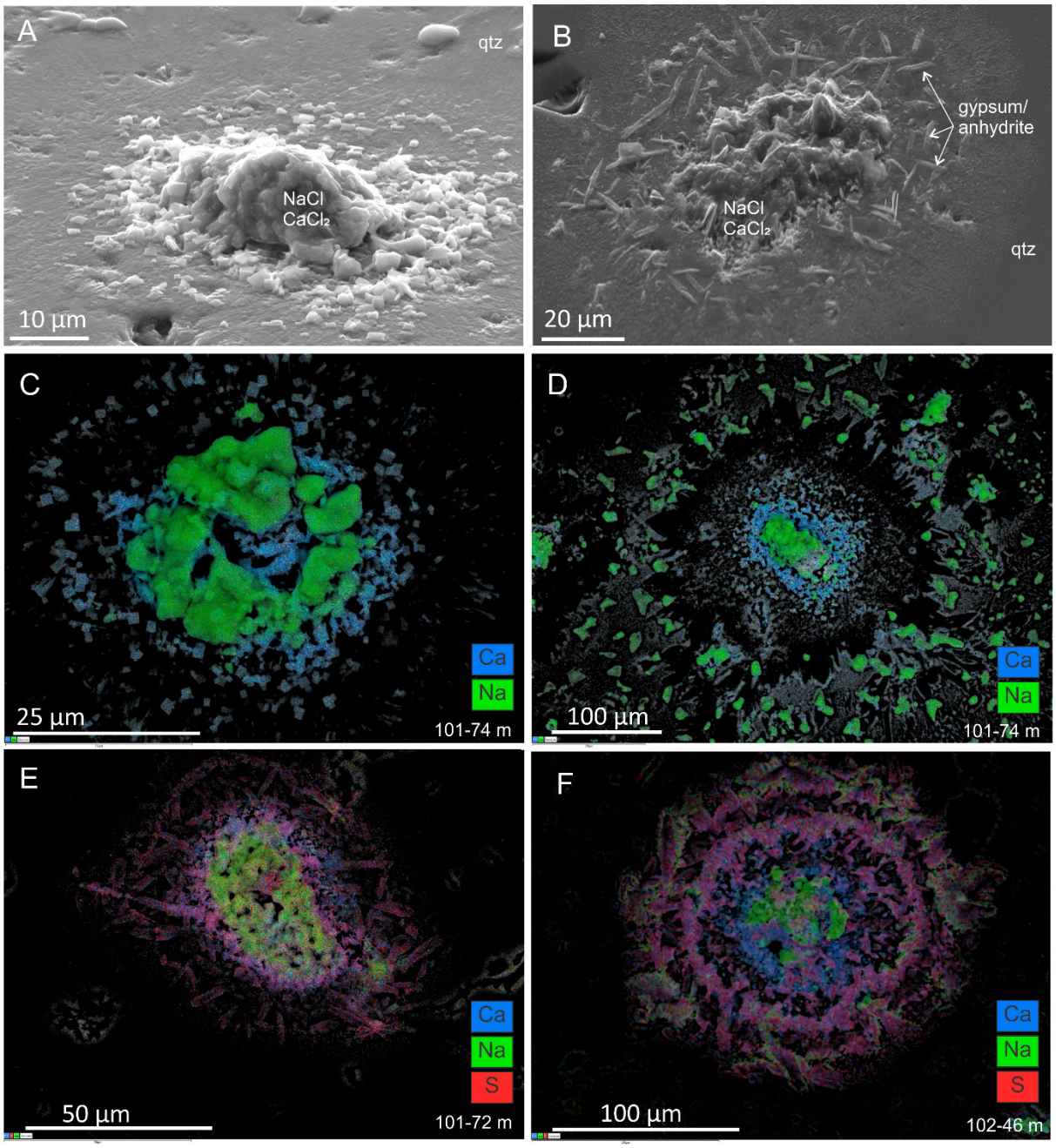

Figure 16. SEM images of evaporate mounds in quartz. (A) 3-D image of evaporate mound where cubic NaCl and $CaCl_2$ crystals from QCP vein (sample 101-74). (B) 3-D image of NaCl, $CaCl_2$ and $CaSO_4$ crystals (C & D) SEM-image with color code overlay, showing distribution of Na and Ca in QCp vein (sample 101-74). (E) NaCl, $CaCl_2$ and $CaSO_4$ in evaporate mounds from a QS vein (sample 101-72) F) NaCl, $CaCl_2$ and $CaSO_4$ in evaporate mounds from a QCp vein (sample 102-46)

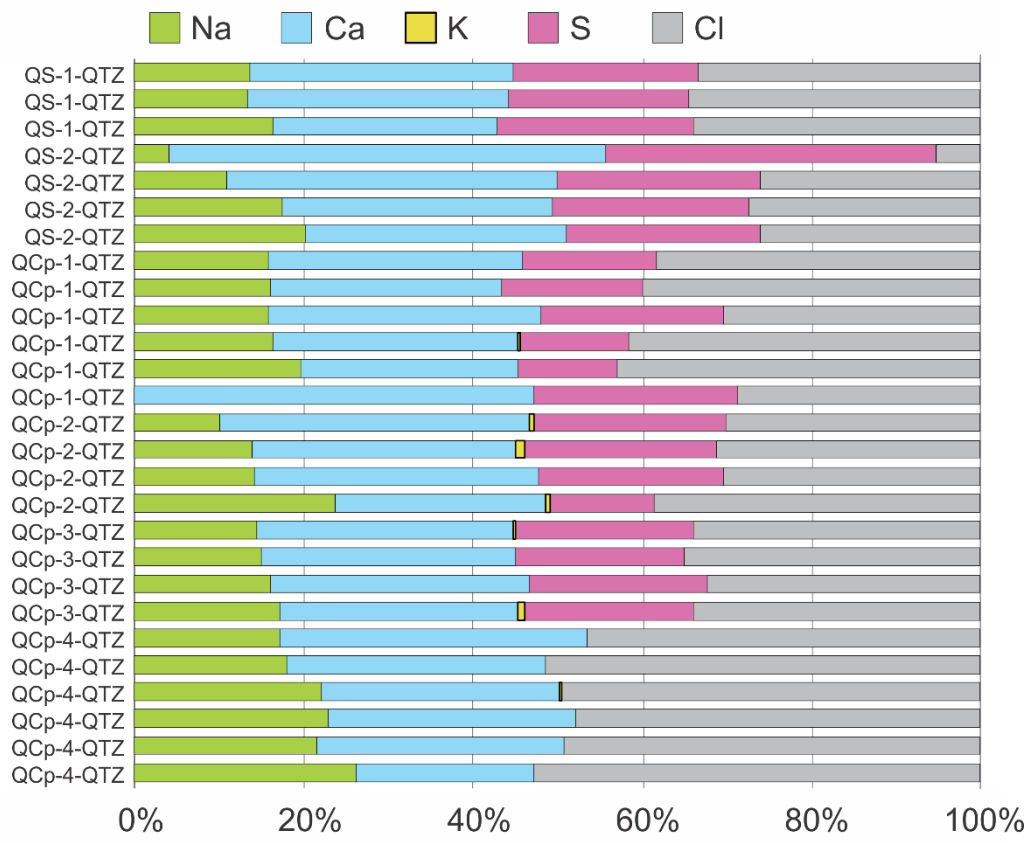

Figure 17. (A) Graphical presentation of relative proportions of Na, Ca, K, S, and Cl (in wt. %) measured in evaporate mounds from decrepitated fluid inclusions in quartz. The data are obtained by surface scanning of the evaporate mounds using a SEM.

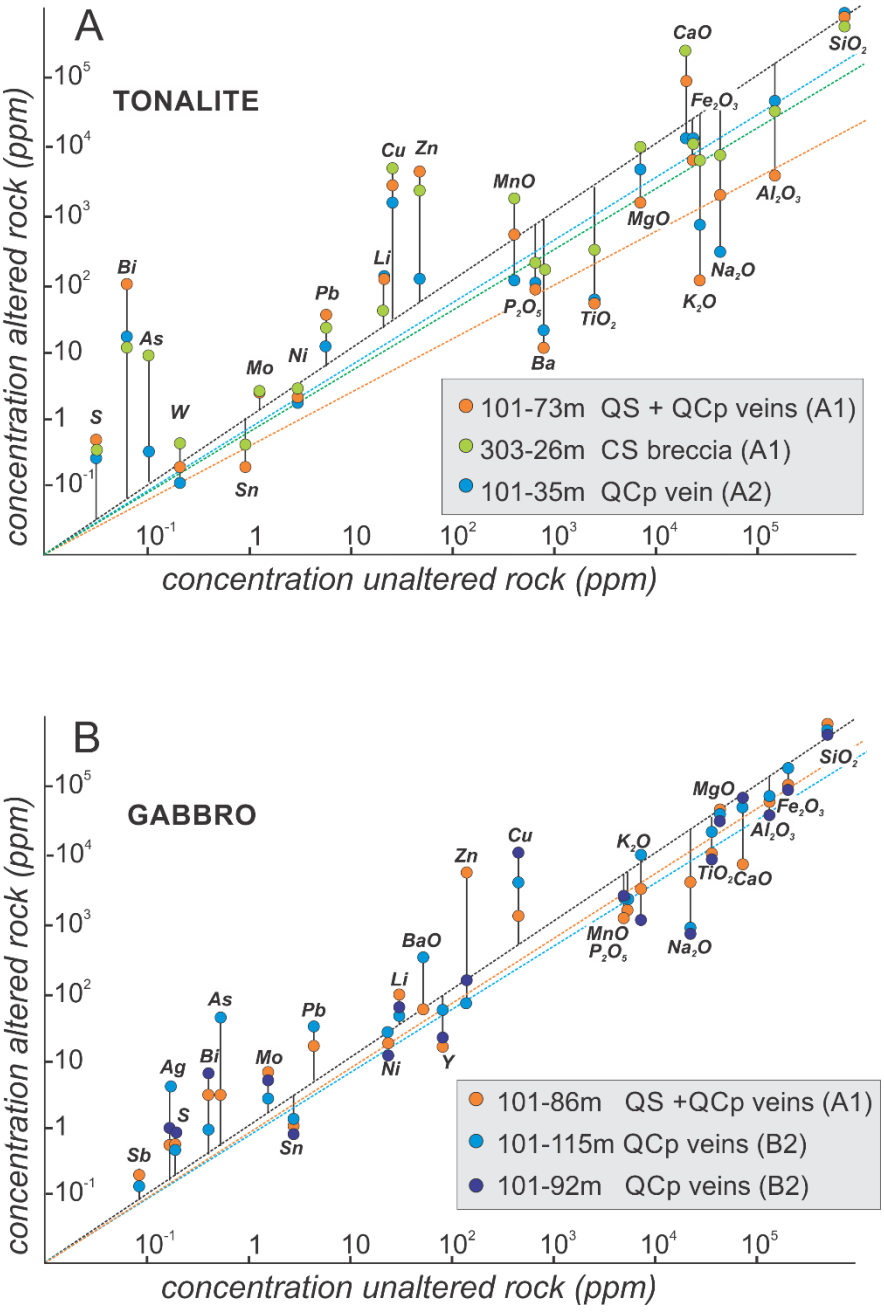

Figure 18. Isocon diagrams (after Grant, 1986) showing gains and losses of elements during fault-related hydrothermal alteration and mineralization. Applied geochemical whole rock data are from Store Norske Gull, drill core sections, of unaltered tonalite gneiss and gabbro, and altered host rocks, including veins and cataclasites in the core zones A1 and A2. For linear element correlations we used average line (Grant 1986) and additional, coloured line drawn between concentrations of presumed immobile Al_2O_3, TiO_2 and Zr. (A) Isocon diagram for altered tonalite gneiss in core and damage zones, domains A1, A2, and B1. (B) Isocon diagram for altered gabbro dike in domains A1 and B2. Note similar alteration trends for elements in both rock types (see main text for further details).

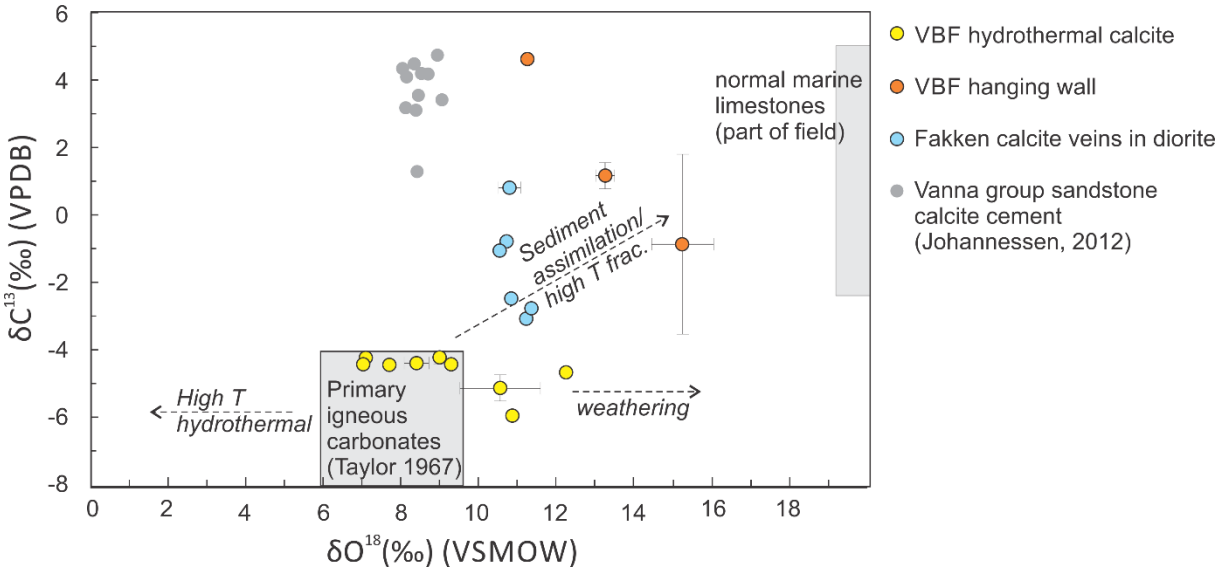

Figure 19. $\delta^{13}C$ and $\delta^{18}O$ diagram showing stable isotope composition of hydrothermal calcite from the VBF, Skipsfjord Nappe rock in hanging wall to the VBF, veins in intrusive diorite of the Vanna Group, and calcite cement from meta-sandstones in Vanna Group. Note that hydrothermal calcite from VBF overlap with primary igneous carbonates (Taylor, 1967).

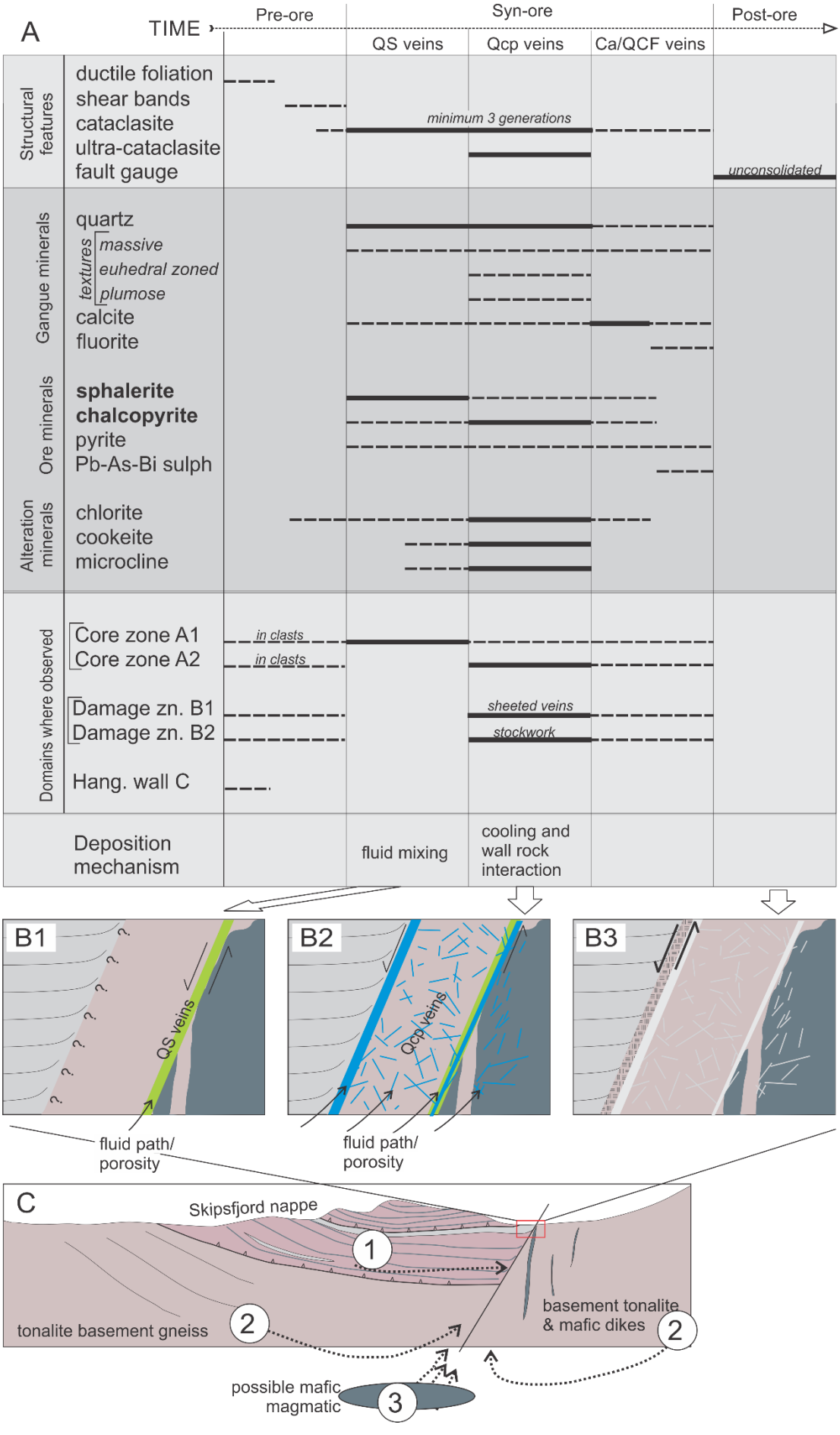
A
TIME
Pre-ore
Syn-ore
Post-ore
QS veins
Qcp veins
Ca/QCF veins
Structural features
ductile foliation
shear bands
cataclasite
ultra-cataclasite
fault gauge
minimum 3 generations
unconsolidated
Gangue minerals
quartz
textures
massive
euhedral zoned
plumose
calcite
fluorite
Ore minerals
sphalerite
chalcopyrite
pyrite
Pb-As-Bi sulph
Alteration minerals
chlorite
cookeite
microcline
Domains where observed
Core zone A1
Core zone A2
in clasts
in clasts
Damage zn. B1
Damage zn. B2
sheeted veins
stockwork
Hang. wall C
Deposition mechanism
fluid mixing
cooling and wall rock interaction
B1
QS veins
fluid path/ porosity
B2
Qcp veins
fluid path/ porosity
B3
C
Skipsfjord nappe
1
tonalite basement gneiss
2
basement tonalite & mafic dikes
2
possible mafic magmatic
3

Figure 20. Tentative para-genetic evolution model for the VBF and its Cu-Zn mineralization: (A) Summary of interpreted ore and gangue mineral growth in fault rocks and veins relative to the ore-forming events (pre-, syn-, post-), as seen within textural domains of the VBF. (B) Schematic illustration of the movement and mineralization history of the VBF, creating porosity and permeability contrasts that may have controlled the injection of QS and QCp veins, and final, post-ore movement (fault gouge). B1) The early movement caused fracturing, cataclasis and increased permeability in the core zone (domain A1), which acted as fluid conduit for later injections and cataclasis. B2) Reduced permeability forced later injections of QCp and Ca-veins into the damage zone and core zone (domain A2). B3) the final post-ore fault movement generated unconsolidated fault gouge in core zone A2. (C) Schematic representation of possible hydrothermal fluid sources of the mineralized VBF, including; the basinal brines from the cover-basement sequence represented by the meta-sedimentary Skipsfjord Nappe rocks and its lower contact with basement tonalite gneisses (1), the tonalite basement gneisses and enclosed mafic dikes (2), and a possible mafic intrusion (dike swarm) and/or deep magmatic source (3).

Table captions

Table 1. Chemical compositions of secondary chlorite formed in halos of injected QCp hydrothermal veins in core zone cataclasites of the VBF, associated with mineralization. Formula is calculated on the basis of 14 oxygens. Mdn±σ = median value plus/minus one standard deviation

** formation temperature calculated using the geothermometer of Cathelineau (1988).*

Sample - depth (m)	n	Material analysed	domain	Chlorite type	SiO_2 (%) ±σ	Al_2O_3 (%) ±σ	FeO (%) ±σ	MnO (%) ±σ	MgO (%) ±σ	Total ±σ	Temp (°C)*	Average structural formula
V6 - surface	8	cataclasite	A2	Clinochlore	27.4 ± 0.9	19.4 ± 0.7	22.9 ± 1.1	0.6 ± 0.1	14.5 ± 0.7	84.7 ± 2.1	**280°C**	$(Mg_{2.33}Fe_{2.06}Al_{1.40}Mn_{0.05})(Si_{2.94}Al_{1.06})O_{10}(OH)_8$
101-70.5	8	cataclasite	A1	Chamosite	28.9 ± 0.7	19.4 ± 0.6	28.3 ± 1.2	0.7 ± 0.1	15.7 ± 0.8	93.0 ± 1.0	**295°C**	$(Mg_{2.35}Fe_{2.37}Al_{1.18}Mn_{0.03})(Si_{2.89}Al_{1.11})O_{10}(OH)_8$
101-93	10	Mg-rich core cataclasite	A1	Clinochlore	27.5 ± 0.6	18.5 ± 0.6	19.4 ± 1.2	0.1 ± 0.1	18.3 ± 0.9	84.0 ± 1.4	**285°C**	$(Mg_{2.61}Fe_{2.00}Al_{1.26}Mn_{0.01})(Si_{2.93}Al_{1.07})O_{10}(OH)_8$
101-93	8	Fe-rich rim cataclasite	A1	Chamosite/ Clinochlore	25.7 ± 0.4	18.6 ± 0.3	24.9 ± 0.4	0.4 ± 0.2	13.8 ± 0.6	83.4 ± 1.1	**305°C**	$(Mg_{2.28}Fe_{2.31}Al_{1.30}Mn_{0.03})(Si_{2.86}Al_{1.14})O_{10}(OH)_8$

Table 2. Summary of fluid inclusion microthermometry from quartz, sphalerite and calcite in hydrothermal veins. Abbreviations; SPH = sphalerite; QTZ = quartz; CA = Calcite, Mdn±σ = median value plus/minus one standard deviation, n= number of fluid inclusion analyses

** melted at eutectic (-52°C)*

*** DNF - Did not freeze at -130°C for 5 minutes*

**** calculated wt. % $NaCl+CaCl_2$ (Steele-MacInnis et al., 2011)*

Host mineral	Vein type	Incl. type	P/PS	Microthermometric data										n
				T_{im} (°C)		T_s (°C)		T_h (°C)		Salinity ($NaCl+CaCl_2$)***		Ratio ($NaCl/CaCl_2$)		
				Range	Mdn±σ	Range	Mdn±σ	Range	Mdn±σ	Range	Mdn±σ	Range	Mdn±σ	
SPH	QS	1	P	-46.9 to -38.1	-43.1 ± 3.2	90 - 98	95 ± 3	164 to 197	179 ± 15.0	32.8 to 34.2	33.5 ± 0.5	0.27 to 0.34	0.29 ± 0.03	4
SPH	QS	1	P	-52*	-	96 - 104	100 ± 3	190 to 218	200 ± 10.2	34.9 to 35.2	35.1 ± 0.1	0.25 to 0.26	0.26 ± 0.01	4
SPH	QS	2a	P	-53.6 to -36.2	-42.8 ± 5.6	-	-	155 to 186	164 ± 11.0	27.3 to 31.4	29.3 ± 1.4	0.06*	-	7
QTZ	QS	1	P	-52.3 to -39.9	-44.2 ± 4.1	86 - 135	106 ± 15	97 to 199	177 ± 32.3	32.9 to 36.3	34.2 ± 1.0	0.29 to 0.36	0.31 ± 0.02	9
QTZ	QS	1	P	-52*	-	70 - 137	120 ± 19	70 to 198	171 ± 38.9	34.1 to 36.4	35.8 ± 0.7	0.21 to 0.32	0.29 ± 0.03	15
QTZ	QS	2b	P	-52.0 to -30.0	-46.7 ± 5.9	-	-	125 to 205	155 ± 29.5	25.0 to 31.4	30.2 ± 1.7	0.06*	-	10
QTZ	QS	3	PS	-48.2 to -40.3	-45.9 ± 2.6	-	-	19 to 36	22 ± 6.5	28.6 to 30.6	30.0 ± 0.7	0.06*	-	6
QTZ	QCP	1	P	-43.5 to -37.5	-41.9 ± 2.5	87 - 117	96 ± 13	146 to 167	161 ± 8.8	32.6 to 34.4	33.1 ± 0.8	0.29 to 0.34	0.33 ± 0.02	3
QTZ	QCP	1	P	-52*	-	115 - 151	121 ± 10	128 to 239	170 ± 30.3	35.6 to 36.9	35.8 ± 0.4	0.28 to 0.34	0.29 ± 0.02	15
QTZ	QCP	2b	P	-54.4 to -23.9	-44.9 ± 6.0	-	-	35 to 218	127 ± 41.6	22.5 to 31.4	29.8 ± 1.7	0.06*	-	51
QTZ	QCP	2b	P	DNF**	-	-	-	156 to 220	179 ± 20.5	-	-	-	-	15
CAL	CA	1	P	-47.5 to -43	-45.3 ± 2.3	75 - 130	103 ± 28	146 to 175	161 ± 14.4	33.0 to 35.5	24.1 ± 1.3	0.27 to 0.33	0.30 ± 0.03	2
CAL	CA	2a	P	-19.8 to -18.3	-19.7 ± 0.7	-	-	94 to 126	116 ± 13.4	19.8 to 20.6	20.5 ± 0.4	0.06*	0.06 ± 0.00	3
CAL	CA	2a	p	-50.3 to -23.5	-44.8 ± 8.3	-	-	146 to 189	161 ± 11.7	22.3 to 31.0	29.8 ± 2.6	0.06*	-	14

References

Armitage, P.E.B. & Bergh, S.G. 2005: Structural development of the Mjelde-Skorelvvatn Zone on Kvaløya, Troms: a metasupracrustal shear belt in the Precambrian West Troms Basement Complex, North Norway. *Norwegian Journal of Geology* 85, 117-133.

Augland, L.E., Andresen, A., Gasser, D. & Steltenpohl, M.G. 2014: Early Ordovician to Silurian evolution of exotic terranes in the Scandinavian Caledonides of the Ofoten-Troms area - terrane characterization and correlation based on new U-Pb zircon ages and Lu-Hf isotopes, *In*: Corfu, F., Gasser, D., Chew, D.M. (Eds.), *New perspectives on the Caledonides of Scandinavia and related areas.* The Geological Society of London, London, pp. 655-678.

Banks, D.A., Davies, G.R., Yardley, B.W.D., McCaig, A.M. & Grant, N.T. 1991: The chemistry of brines from an Alpine thrust system in the Central Pyrenees: An application of fluid inclusion analysis to the study of fluid behaviour in orogenesis. *Geochimica et Cosmochimica acta* 55, 1021-1030.

Bergh, S.G., Kullerud, K., Armitage, P.E.B., Zwaan, K.B., Corfu, F., Ravna, E.J.K. & Myhre, P.I. 2010: Neoarchean to Svecofennian tectono-magmatic evolution of the West Troms Basement Complex, North Norway. *Norwegian Journal of Geology* 90, 21-48.

Bergh, S.G., Kullerud, K., Corfu, F., Armitage, P.E.B., Davidsen, B., Johansen, H.W., Pettersen, T. & Knudsen, S. 2007: Low-grade sedimentary rocks on Vanna, North Norway: a new occurrence of a Palaeoproterozoic (2.4-2.2 Ga) cover succession in northern Fennoscandia. *Norwegian Journal of Geology* 87, 301-318.

Binns, R.E., Chroston, P.N. & Matthews, D.W. 1980: Low-grade sediments on Precambrian Gneiss on Vanna, Troms, Northern Norway. *Offprint NGU* 359, 61-72.

Blystad, P., Brekke, H., B., F.R., Larsen, B.T., Skogseid, J. & B., T. 1995: Structural elements of the Norwegian continental shelf. Part II: the Norwegian Sea Region. *Norwegian Petroleum Directorate Bulletin* 8, 1-45.

Bodnar, R.J. & Vityk, M.O. 1994: Interpretation of microthermometric data for H_2O-NaCl fluid inclusions, *In*: De Vivo, B., Frezzotti, M.L. (Eds.), *Fluid inclusions in minerals, methods and applications*. Virginia Tech, Blacksburg, VA, pp. 117-130.

Boiron, M.-C., Cathelineau, M. & Richard, A. 2010: Fluid flow and metal deposition near basement/cover unconformity: lessons and analogies from Pb-Zn-F-Ba systems for the understanding of Proterozoic U deposits. *Geofluids* 10, 270-292.

Braathen, A. & Davidsen, B. 2000: Structure and stratigraphy of the Palaeoproterozoic Karasjok Greenstone Belt, north Norway - regional implications. *Norsk Geologisk Tidsskrift* 80, 33-50.

Bucher, K. & Stober, I. 2010: Fluids in the upper continental crust. *Geofluids* 10, 241-253.

Burisch, M., Marks, M.A.W., Nowak, M. & Markl, G. 2016: The effect of temperature and cataclastic deformation on the composition of upper crustal fluids - an experimental approach. *Chemical Geology* 433, 24-35.

Cathelineau, M. 1988: Cation site occupancy in chlorites and illites as a function of temperature. *Clay Minerals* 23, 471-485.

Chu, H., Chi, G. & Chou, I-M. 2016: Freezing and melting behaviors of H2O-NaCl-CaCl2 solutions in fused silica capillaries and glass-sandwiched films: implications for fluid inclusion studies. *Geofluids* 16, 518-532.

Corbett, G.J. & Leach, T.M. 1998: Southwest Pacific Rim gold-copper systems; structure, alteration, and mineralization, *Special Publications. Society of Economic Geology*, p. 236.

Corfu, F., Armitage, P.E.B., Kullerud, K. & Bergh, S.G. 2003: Preliminary U-Pb geochronology in the West Troms Basement Complex, north Norway: Archean and Palaeoproterozoic events and younger overprints. *NGU Bulletin* 441, 61-72.

Dallmeyer, R.D. 1992: $^{40}Ar/^{39}Ar$ mineral ages within the Western Gneiss Terrane, Troms: evidence of polyphase Proterozoic tectonothermal activity (Svecokarelian and Sveconorwegian). *Precambrian Research* 57, 195-206.

Davids, C., Benowitz, J.A., Layer, P.W. & Bergh, S.G. 2018: Direct $^{40}Ar/^{39}Ar$ K-feldspar dating of Late Permian-Early Triassic brittle faulting in northern Norway. *Terra Nova* 30, 263-269.

Davids, C., Wemmer, K., Zwingmann, H., Kohlmann, F., Jacobs, J. & Bergh, S.G. 2013: K-Ar illite and apatite fission track constraints on brittle faulting and the evolution of the northern Norwegian passive margin. *Tectonophysics* 608, 196-211.

Dong, G., Morrison, G. & Jaireth, S. 1995: Quartz textures in epithermal veins, Queensland - classification, origin, and implication. *Economic Geology* 90, 1841-1856.

Dubois, M., Monnin, C., Castelain, T., Coquinot, Y., Gouy, S., Gauthier, A. & Goffè, B. 2010: Investigations of the H_2O-NaCl-LiCl system: a synthethic fluid inclusion study and thermodynamic modeling from -50° to +100°C and up to 12 mol/kg. *Economic Geology* 105, 10.

Faleide, J.-I., Tsikalas, F., Breivik, A.J., Mjelde, R., Ritzmann, O., Engen, Ø., Wilson, J. & Eldholm, O. 2008: Structure and evolution of the continental margin off Norway and the Barents Sea. *Episodes* 31, 82-91.

Forslund, T. 1988: *Post-kaledonske forkastninger i Vest-Troms: med vekt på Straumsbukta-Kvaløyslettaforkastningen, Kvaløya*. MSc thesis. UiT the arctic University of Tromsø, Tromsø, p. 160.

Fournier, R.O. & Potter, R.W. 1982: An equation correlating the solubility of quartz in water from 25° to 900°C at pressures up to 10,000 bars. *Geochimica et Cosmochimica acta* 46, 1969-1973.

Franklin, J.M., Lydon, J.W. & Sangster, D.F. 1981: Volcanic-associated massive sulfide deposits, *In*: Skinner, B.J. (Ed.), *Economic Geology 75th Anniversary Volume*, pp. 485-627.

Gabrielsen, R.H., B., F.R., Jensen, L.N., Kalheim, J.E. & Riis, F. 1990: Structural elements of the Norwegian continental shelf - Part I: the Barents Sea Region. *Norwegian Petroleum Directorate Bulletin* 6.

Gabrielsen, R.H. & Braathen, A. 2014: Models of fracture lineaments - joint swarms, fracture corridors and faults in crystalline rocks, and their genetic relations. *Tectonophysics* 628, 26-45.

Galley, A.G., Hannington, M. & Jonasson, I. 2007: Volcanogenic massive sulphide deposits, *In*: Goodfellow, W.D. (Ed.), *Mineral deposits of Canada: a synthesis of major deposit-types, district metallogeny, the evolution of geological provinces, and exploration method*. Geological Association of Canada, Mineral deposits division, pp. 141-161.

Grant, J.A. 1986: The isocon diagram - a simple solution to Gresens' equation for metasomatic alteration. *Economic Geology* 81, 1976-1981.

Griffin, B. J., Joy, D. C. & Michael, J. R. 2010: A comparison of a luminescence –based VPSE and an electron based GSED for SE and CL imaging in variable pressure SEM with conventional SE imaging. *Microscopy and Microanalysis* 16, 624-625.

Haaland, L.C. 2018: *Geometry and kinematic evolution of ductile shear zones in the Ersfjord Granite (1.79 Ga), West Troms Basement Complex: a Svecofennian accretionary thrust system*. MSc thesis, Department of Geosciences. UiT the arctic University of Norway, Tromsø, p. 79.

Hansen, J.-A., Bergh, S.G. & Henningsen, T. 2012: Mesozoic rifting and basin evolution on the Lofoten and Vesterålen margin, North Norway; time constraints and regional implications. *Norwegian Journal of Geology* 91, 203-228.

Hemley, J.J. & Cygan, C.L. 1992: Hydrothermal ore-forming processes in the light of studies in rock-buffered systems: iron-copper-zinc-lead sulfide solubility relations. *Economic Geology* 87, 1-22.

Hubbert, M.K. & Rubey, W.W. 1959: Role of fluid pressure in mechanics of overthrust faulting. *Bulletin of the Geological Society of America* 70, 115-166.

Indrevær, K., Bergh, S.G., Koehl, J.-B., Hansen, J.-A., Schermer, E.R. & Ingebrigtsen, A. 2013: Post-Caledonian brittle fault zones on the hyperextended SW Barents Sea margin: New insights into onshore and offshore margin architecture. *Norwegian Journal of Geology* 93, 167-189.

Indrevær, K., Stunitz, H. & Bergh, S.G. 2014: On Palaeozoic-Mesozoic brittle normal faults along the SW Barents Sea margin: fault processes and implications for basement permeability and margin evolution. *Journal of the Geological Society of London* 171, 831-846.

Ingebritsen, S.E. & Manning, C.E. 2010: Permeability of the continental crust: dynamic variations inferred from seismicity and metamorphism. *Geofluids* 10, 193-206.

Johannessen, H. 2012: *Tinnvatnformasjonen i Vannas proterozoiske lagrekke: Sedimentære facies og avsetningsmiljø*. MSc thesis, Department of Geology. University of Tromsø, Tromsø, p. 105.

Johansen, H. 1987*: Forholdet mellom det prekambriske underlaget og overliggende sedimentære bergarter sør-øst på Vanna, Troms*. Cand. scient thesis, Institutt for biologi og geologi. Universitetet i Tromsø, Tromsø, p. 136.

Kesler, S.E., Appold, M.S., Martini, A.M., Walter, L.M., Huston, T.J. & Kyle, J.R. 1995: Na-Cl-Br systematics of mineralizing brines in Mississippi Valley-type deposits. *Geology* 23, 641-644.

Kirstein, L.A., Davies, G.R. & Heeremans, M. 2006: The petrogenesis of Carboniferous–Permian dyke and sill intrusions across northern Europe. *Contributions to Mineralogy and Petrology* 152, 721-742.

Koehl, J.-B., Bergh, S.G., Henningsen, T. & Faleide, J.-I. 2018a: Middle to Late Devonian-Carboniferous collapse basins on the Finnmark Platform and in the southwesternmost Nordkapp basin, SW Barents Sea. *Solid Earth* 9, 341-362.

Koehl, J.-B., Bergh, S.G., Osmundsen, P.T., Redfield, T.F., Indrevær, K., Lea, H. & Bergø, E. 2018b: Late Devonian-Carboniferous faulting in NW Finmark and controlling fabrics. *Manuscript submitted to Norwegian Journal of Geology*.

Koistinen, T., Stephens, M.B., Bogatchev, V., Nordgulen, Ø., Wennerström, M. & Korhonen, J. 2001: Geological map of the Fennoscandian Shield, scale 1:2 000 000. *Geological surveys of Finland, Norway, Sweden, and the north-west department of ministry of Natural Resources of Russia.*

Kontak, D.J. 2004: Analysis of evaporate mounds as a complement to fluid-inclusion thermometric data: case studies from granitic environments in Nova Scotia and Peru. *The Canadian Mineralogist* 42, 1315-1330.

Kontak, D.J., Kyser, K., Gize, A. & Marshall, D. 2006: Structurally controlled vein barite mineralization in the Maritimes Basin of eastern Canada: geologic setting, stable isotopes, and fluid inclusions. *Economic Geology* 101, 407-430.

Kucha, H. & Pawlikoswki, M. 1986: Two-brine model of the genesis of strata-bound Zechstain deposits (Kupferschiefer type), Poland. *Mineralium Deposita* 21, 70-80.

Kullerud, K., Skjerlie, K.P., Corfu, F. & de la Rosa, J.D. 2006: The 2.40 Ga Ringvassøy mafic dykes, West Troms Basement Complex, Norway: The concluding act of early Palaeoproterozoic continental breakup. *Precambrian Research* 150, 183-200.

Kullerud, K., Zozulya, D., Bergh, S.G., Hansen, H. & Ravna, E.J.K. 2011: Geochemistry and tectonic setting of a lamproite dyke in Kvaløya, North Norway. *Lithos* 126, 278-189.

Lippard, S.J. & Prestvik, T. 1997: Carboniferous dolerite dykes on Magerøy; new age determinations and tectonic significance. *Norsk Geologisk Tidsskrift* 77, 159-163.

Meinert, L.D., Dipple, G.M. & Nicolescu, S. 2005: World skarn deposits, *In*: Hedenquist, J.W., Thompson, J.F.H., Goldfarb, R.J., Richards, J.P. (Eds.), *One hundred anniversary volume*. Society of Economic Geology, Littleton, pp. 299-336.

Monsen, K. 2014: *Hydrothermal Cu-Zn mineralization at Vanna, West Troms Basement Complex*. MSc thesis, Department of Geology. UiT the arctic University of Norway, Tromsø, p. 109.

Mosar, J. 2003: Scandinavias North Atlantic passive margin. *Journal of geophysical research* 108, 2360-2377.

Mosar, J., Eide, E.A., Osmundsen, P.T., Sommaruga, A. & Torsvik, T. 2002: Greenland-Norway separation: a geodynamic model for the North Atlantic. *Norwegian Journal of Geology* 82, 281-298.

Myhre, P.I., Corfu, F. & Bergh, S.G. 2011: Palaeoproterozoic (2.0-1.95 Ga) pre-orogenic supracrustal sequences in the West Troms Basement Complex, North Norway. *Precambrian Research* 186, 89-100.

Myhre, P.I., Corfu, F., Bergh, S.G. & Kullerud, K. 2013: U-Pb geochronology along an Archean geotransect in the West Troms Basement Complex, North Norway. *Norwegian Journal of Geology* 93, 1-24.

Nasuti, A., Roberts, D. & Gernigon, L. 2015: Multiphase mafic dykes in the Caledonides of northern Finnmark revealed by a new high-resolution aeromagnetic dataset. *Norwegian Journal of Geology* 95, 285-298.

Ojala, J.V., Hansen, H. & Ahola, H. 2013: Cu-Zn mineralisation at Vannareid, West Troms Basement Complex: a new Palaeoproterozoic VMS occurrence in the northern Fennoscandian Shield. *Abstracts and proceedings, 12th Biennial SGA Meeting*, p. 2.

Olesen, O., Lundin, E., Nordgulen, Ø., Osmundsen, P.T., Skilbrei, J.R., Smethurst, M.A., Solli, A., Bugge, T. & Fichler, C. 2002: Bridging the gap between the onshore and offshore geology in Nordland, northern Norway. *Norwegian Journal of Geology* 82, 243-262.

Olesen, O., Torsvik, T.H., Tveten, E., Zwaan, K.B., Løseth, H. & Henningsen, T. 1997: Basement structure of the continental margin in the Lofoten-Lopphavet area, northern Norway: Constraints from potential field data, on-land structural mapping and palaeomagnetic data. *Norwegian Journal of Geology* 77, 15-30.

Opheim, J.A. & Andresen, A. 1989: Basement-cover relationships on northern Vanna, Troms, Norway. *Norsk Geologisk Tidsskrift* 69, 67-81.

Oszczepalski, S. 1999: Origin of the Kupferschiefer polymetallic mineralization in Poland. *Mineralium Deposita* 34, 599-613.

Perelló, J., Clifford, J.A., Creaser, R.A. & A., V.V. 2015: An example of synorogenic sediment-hosted copper mineralization: geologic and geochronologic evidence from the Paleoproterozoic Nussir Deposit, Finnmark, arctic Norway. *Economic Geology* 110, 677-689.

Rice, A.H.N. 1990: A discussion: Basement-cover relationships on northern Vanna, Troms, Norway. *Norsk Geologisk Tidsskrift* 70, 179-186.

Rice, A.H.N. 2014: Restoration of the External Caledonides, Finnmark, North Norway. *Geological Society of London Special Publication* 390, 271-299.

Rimstidt, D., J. 1997: Gangue mineral transport and deposition, *In*: Barnes, H.L. (Ed.), *Geochemistry of hydrothermal ore deposits*, 3. ed. John Wiley & Sons, Inc, pp. 487-515.

Roberts, D. 2011: Age of the Hamningberg dolerite dyke, Varanger Peninsula, Finnmark: Devonian rather than Vendian - a revised interpretation. *Norges Geologiske Undersøkelse Bulletin* 451, 32-36.

Roberts, D. & Lippard, S.J. 2005: Inferred Mesozoic faulting in Finnmark: current status and offshore links. *NGU Bulletin* 443, 55-60.

Roberts, D., Torsvik, T., Andersen, T.B. & Rehnström, E.F. 2003: The Early Carboniferous Magerøy dykes, northern Norway; palaeomagnetism and palaeogeography. *Geological Magazine* 140, 443-451.

Roedder, E. 1984: *Fluid inclusions*. U S geological Survey, Blacksburg, Virginia, p. 644.

Rye, R.O. & Ohmoto, H. 1974: Sulfur and Carbon isotopes and ore genesis: a review. *Economic Geology* 69, 825-843.

Savard, M.M. & Kontak, D.J. 1995: $\delta^{13}C$-$\delta^{18}O$-$^{87}Sr/^{86}Sr$ covariations in ore-stage calcites at and around the Gays River Zn-Pb deposit (Nova Scotia, Canada) - evidence for fluid mixing. *Economic Geology* 93, 181-196.

Schmid, S.M. & Handy, M.R. 1991: Towards a genetic classification of fault rocks: geological usage and tectonophysical implications, *In*: Muller, D.W., McKenzie, J.A., Weissert, H. (Eds.), *Controversies in modern geology*. Academic press, London, pp. 339-361.

Seward, T.M. & Barnes, H.L. 1997: Metal transport by hydrothermal ore fluids, *In*: Barnes, H.L. (Ed.), *Geochemistry of hydrothermal ore deposits*, 3. ed. John Wiley & Sons, Inc, pp. 435-486.

Sheperd, T.J. 1985: *A practical guide to fluid inclusions*. Blackie &Son Ltd, p. 235.

Sibson, R.H. 1977: Fault rocks and fault mechanisms. *Journal of the Geological Society of London* 133, 191-216.

Sibson, R.H., Moore, J.M. & Rankin, A.H. 1975: Seismic pumping - a hydrothermal fluid transport mechanism. *Journal of the Geological Society of London* 131, 653-659.

Simmons, S.F., White, N.C. & John, D.A. 2005: Geological characteristics of epithermal precious and base metal deposits, *In*: Hedenquist, J.W., Thompson, J.F.H., Goldfarb, R.J., Richards, J.P. (Eds.), *One hundred year anniversary volume*. Society of Economic Geology, Littleton, pp. 485-522.

Smelror, M., Petrov, O., Larssen, G.B. & Werner, S. 2009: *Geological history of the Barents Sea*. Geological Survey of Norway, p. 135.

Steele-MacInnis, M., Bodnar, R.J. & Naden, J. 2011: Numerical model to determine the composition of H_2O-NaCl-$CaCl_2$ fluid inclusions based on microthermometric and microanalytical data. *Geochimica et Cosmochimica acta* 75, 21-40.

Taylor, H.P., Frechen, J. & Degens, E.T. 1967: Oxygen and carbon isotope studies of carbonatites from the Laacher See District, West Germany and the Alnö District, Sweden. *Geochimica et Cosmochimica acta* 31, 407-430.

Thorstensen, L. 2011: *Land-sokkel korrelasjon av tektoniske elementer i ytre del av Senja og Kvaløya i Troms*. MSc thesis, Department of Geology. University of Tromsø, Tromsø, p. 117.

Vanko, D. A., Bodnar, R. J. & Sterner, S. M. 1988: Synthetic fluid inclusions: VIII. Vapor-saturated halite solubility in part of the system NaClCaC12-H20, with application to fluid inclusions from oceanic hydrothermal. *Geochimica et Cosmochimica acta* 52, 2451-2456.

Vaughan, D.J. & Craig, J.R. 1997: Sulphide ore stabilities, morphologies, and intergrowth textures, *In*: Barnes, H.L. (Ed.), *Geochemistry of hydrothermal ore deposits*, 3. ed. John Wiley & Sons, Inc, pp. 367-434.

Vidal, O., De Andrade, V., Lewin, E., Munoz, M., Parra, T. & Pascarelli, S. 2006: P-T-deformation-Fe^{3+}/Fe^{2+} mapping at the thin section scale and comparison with XANES mapping: application to a garnet-bearing metapelite from the Sambagawa metamorphic belt (Japan). *Journal of Metamorphic Geology* 24, 669-683.

Walter, B., Burisch, M. & Markl, G. 2016: Long-term chemical evolution and modification of continental basement brines - a field study from the Schwarzwald, SW Germany. *Geofluids* 16, 604-624.

Wise, D.U., Dunn, D.E., Engelder, J.T., Geiser, P.A., Hatcher, R.D., Kish, S.A., Odom, A.L. & Schamel, S. 1984: Fault-related rocks: Suggestions for terminology. *Geology* 12, 391-394.

Yardley, B.W.D. 2005: Metal concentrations in crustal fluids and their relationship to ore formation. *Economic Geology* 100, 613-632.

Zhong, R., Brugger, J., Chen, Y. & Li, W. 2015: Contrasting regimes of Cu, Zn and Pb transport in ore-forming hydrothermal fluids. *Chemical Geology* 395, 154-164.